UNIVERSITY OF SOUTHAMPTON
FACULTY OF ENGINEERING AND THE ENVIRONMENT
INSTITUTE OF SOUND AND VIBRATION RESEARCH

SCAN-BASED SOUND VISUALISATION METHODS USING SOUND PRESSURE AND PARTICLE VELOCITY

by

Daniel Fernández Comesaña

Thesis for the degree of Doctor of Philosophy

July 2014

UNIVERSITY OF SOUTHAMPTON
Faculty of Engineering and the Environment
Institute of Sound and Vibration Research

Abstract

Doctor of Philosophy

SCAN-BASED SOUND VISUALISATION METHODS USING SOUND PRESSURE AND PARTICLE VELOCITY

by Daniel Fernández Comesaña

Sound visualisation techniques have played a key role in the development of acoustics throughout history. Progress in measurement apparatus and the techniques used to display sound and vibration phenomena has provided excellent tools for understanding specific acoustic problems. Traditional methods, however, such as step-by-step measurements or simultaneous multichannel systems, require a significant trade-off between time requirements, flexibility, and cost.

This thesis explores the foundations of a novel sound field mapping procedure. The proposed technique, Scan and Paint, is based on the acquisition of sound pressure and particle velocity by manually moving a p-u probe (pressure-particle velocity sensor) across a sound field, whilst filming the event with a camera. The sensor position is extracted by applying automatic colour tracking to each frame of the recorded video. It is then possible to directly visualise sound variations across the space in terms of sound pressure, particle velocity or acoustic intensity.

The high flexibility, high resolution, and low cost characteristics of the proposed measurement methodology, along with its short time requirements, define Scan and Paint as an efficient sound visualisation technique for stationary sound fields. A wide range of specialised applications have been studied, proving that the measurement technique is not only suitable for near-field source localisation purposes but also for vibro-acoustic problems, panel noise contribution analysis, source radiation assessment, intensity vector field mapping and far field localisation.

Keywords: sound visualisation, sound mapping, sound radiation, scanning methods, p-u intensity probes, panel contribution analysis, sound source ranking, operational deflections shapes, virtual phased arrays.

Contents

Abstract **iii**

Table of Contents **iv**

List of Figures **ix**

List of Tables **xiii**

Declaration of Authorship **xv**

List of Publications **xvi**

Acknowledgements **xxiii**

Abbreviations **xxv**

Symbols **xxvii**

1 Introduction **1**
1.1 Sound field visualisation 1
1.2 Sound and vibration transducers 2
1.3 Measurement procedures 4
1.4 Applications of acoustic imaging techniques 6
1.5 Research objective 6
1.6 Thesis organisation 7
1.7 Original Contributions 8

2 Literature review **11**
2.1 Introduction 11
2.2 Early experiments on sound and vibration imaging 11
2.3 Visualisation of wave propagation 14
2.4 Novel acoustic methods of the 20th century 16
2.4.1 Scan-based sound visualisation methods 17
2.4.2 Cymatics 17
2.4.3 Holographic interferometry 18
2.5 Current experimental sound visualisation methods 19
2.5.1 Acoustic holography 20

2.5.2 Acousto-optic mapping . . . 21
2.5.3 Beamforming . . . 22
2.5.4 Direct mapping methods . . . 24
2.5.5 Particle Image Velocimetry . . . 25
2.5.6 Schlieren and shadowgraph imaging . . . 26
2.6 Summary . . . 27

3 Fundamentals of Scan & Paint 29
3.1 Introduction . . . 29
3.2 Mathematical formulation . . . 31
3.2.1 Planar grid discretisation method . . . 31
3.2.2 Point discretisation method . . . 34
3.3 Sound received by a moving transducer . . . 35
3.3.1 The Doppler effect . . . 35
3.3.2 Sound pressure, particle velocity and velocity potential . . . 36
3.4 Statistical considerations . . . 38
3.4.1 Mean estimate . . . 38
3.4.2 Autospectral density estimate . . . 39
3.4.2.1 Bias of the estimate . . . 41
3.4.2.2 Variance of the estimate . . . 43
3.5 Practical considerations . . . 46
3.5.1 Tracking camera . . . 46
3.5.2 Video frame rate . . . 47
3.5.3 Reference sensor . . . 48
3.5.4 Manual scanning error . . . 49
3.5.5 Scanning speed . . . 52
3.6 Summary . . . 53

4 Sound mapping applications 55
4.1 Introduction . . . 55
4.2 Near-field source localisation . . . 55
4.2.1 Influence of background noise on sound mapping . . . 56
4.2.1.1 Sound emission . . . 56
4.2.1.2 Sensor directivity . . . 58
4.2.1.3 Background noise perceived near a rigid boundary . . . 60
4.2.2 Spatial resolution of direct mapping methods . . . 62
4.2.3 Experimental examples . . . 67
4.2.3.1 Small scale problems . . . 67
4.2.3.2 Vehicle interior noise . . . 67
4.2.3.3 Leak detection in building acoustics . . . 69
4.3 Acoustic vector field mapping . . . 71
4.3.1 Three dimensional sound intensity . . . 72
4.3.2 Experimental examples . . . 74
4.3.2.1 Loudspeaker in a room . . . 74
4.3.2.2 Vehicle exterior noise . . . 75
4.3.2.3 Unmanned Aerial Vehicles . . . 77
4.4 Summary . . . 77

5 Scanning Panel Contribution Analysis 79
5.1 Introduction . . . 79
5.2 Overview of panel contribution methods . . . 80
5.2.1 The windowing technique . . . 81
5.2.2 Surface velocity sampling methods . . . 82
5.2.3 Airborne Source Quantification (ASQ) . . . 82
5.2.4 Equivalent source methods (ESM) . . . 83
5.2.5 Near-field Acoustic Holography (NAH) based methods . . . 84
5.2.6 Pressure-velocity based reconstruction techniques . . . 84
5.3 Fundamentals of Panel Noise Contribution Analysis . . . 85
5.4 The Reference-Related method . . . 86
5.5 Measurement methodology . . . 88
5.5.1 Operational measurement . . . 88
5.5.2 Reciprocal transfer functions . . . 88
5.5.3 Camera positioning . . . 89
5.6 Experimental evaluation . . . 89
5.6.1 Experimental set-up and instrumentation . . . 90
5.6.2 Measurement process . . . 90
5.6.3 Measurement validation . . . 91
5.6.4 Analysis of results . . . 92
5.7 Comparison of scanning panel contribution analysis with current solutions 95
5.8 Summary . . . 96

6 Virtual Phased Arrays 97
6.1 Introduction . . . 97
6.2 Foundations of VPA . . . 98
6.2.1 Relative phase information . . . 98
6.2.2 Covariance matrix synthesis . . . 100
6.3 Source localisation and DOA algorithms . . . 102
6.3.1 Delay-and-sum beamforming . . . 102
6.3.2 MUSIC . . . 103
6.3.3 Least Squares Beamformer . . . 104
6.4 Deconvolution algorithms for VPA . . . 105
6.4.1 Fundamentals of iterative algorithms . . . 105
6.4.2 DAMAS . . . 106
6.4.3 Non-Negative Least Squares (NNLS) . . . 107
6.4.4 Iterative Sidelobe Cleaner Algorithm (ISCA) . . . 108
6.5 Simulations . . . 109
6.5.1 Relative phase information for DOA estimation . . . 110
6.5.2 Deconvolution algorithms . . . 111
6.5.2.1 Convergence of ISCA . . . 112
6.5.2.2 Localisation of sources with equal strength . . . 113
6.5.2.3 Localisation of sources with multiple strengths . . . 114
6.5.2.4 Localisation of sources including noise . . . 115
6.6 Practical implementation . . . 117
6.6.1 Measurement methodology and VPA configuration . . . 117
6.6.2 Instrumentation and experimental setup . . . 119

6.6.3 Data analysis . . . 121
6.6.4 Sound localisation maps . . . 122
6.6.5 DOA estimation . . . 123
6.6.6 Near-field pressure mapping versus VPA . . . 124
6.7 Comparison of different beamforming techniques for VPA . . . 125
6.8 Large multichannel arrays versus VPA . . . 126
6.9 Summary . . . 127

7 Conclusions and Recommendations 129
7.1 Summary of the main conclusions . . . 129
7.2 Recommendations for future work . . . 131

A Sound power measurements 133
A.1 Introduction . . . 133
A.2 Sound power estimation . . . 134
A.2.1 Direct intensity estimation . . . 135
A.2.2 Indirect intensity estimation . . . 135
A.3 Field indicators . . . 136
A.3.1 Temporal variability indicator (F_1) . . . 136
A.3.2 Surface pressure-intensity indicator (F_2) . . . 137
A.3.3 Negative partial power indicator (F_3) . . . 137
A.3.4 Field non-uniformity indicator (F_4) . . . 137
A.3.5 Reactivity error indicator (F_5) . . . 138
A.4 Sound power estimation with *p-p* and *p-u* probes . . . 138

B Mapping non-stationary sound fields 139
B.1 Introduction . . . 139
B.2 Theory . . . 140
B.3 Experimental evaluation . . . 143
B.3.1 Non-stationary mapping . . . 143
B.3.2 Directivity patterns . . . 144

C Scanning Operational Deflection Shapes 147
C.1 Introduction . . . 147
C.2 Background Theory . . . 148
C.2.1 Particle velocity sensors for vibro-acoustic applications . . . 148
C.2.2 Operational Deflection Shapes . . . 149
C.3 Experimental evaluation . . . 150
C.3.1 Measurement setup . . . 151
C.3.2 Surface velocity spectra . . . 151
C.3.3 Direct panel velocity mapping . . . 152
C.3.4 Operational Deflection Shapes . . . 152

Bibliography 155

List of Figures

1.1 First measurement setup (left) and sound map (right) obtained with the proposed scanning technique in 2009. 2
1.2 Features of the Scan & Paint method and other conventional measurement procedures. 5

2.1 Chladni patterns of a rectangular plate [40]. 12
2.2 Vibration microscope [45] (left) and example of Lissajous patterns (right). 13
2.3 The manometric flame apparatus of Rudolph Koenig (left) and an example of the device experimental output (right) [45]. 13
2.4 Toepler's original schlieren apparatus (left) [54] and Toepler's drawing of the schlieren image of a spherical shock wave from an electric spark in air (right) [52]. 14
2.5 Propagating sound waves 15
2.6 Sound wave entering into a model of a theatre 16
2.7 Sound propagation comparison using shadowgraphy techniques (left) and the water tank method (right) [48]. 16
2.8 Kock's scanning apparatus (left), sound pattern generated by two sound sources out of phase (top right), and wave radiation pattern generated by a telephone loudspeaker applying a subtraction technique at 4000 Hz (bottom right) [1]. 18
2.9 Several cymatics figures created by Hans Jenny [65]. 18
2.10 Deflection shapes of a violin plate using holographic interferometry [72]. . 19
2.11 Illustration of the general acoustic holography measurement principle. . . 20
2.12 Sketch of the setup of an an acousto-optic measurement. 22
2.13 Sketch of a far field source localisation problem evaluated using beamforming. 23
2.14 Illustration of direct mapping methods for simultaneous (left) or scanning (right) measurements. 24
2.15 Illustration of the particle image velocitmetry measurement principle. . . 26
2.16 Sketch of a typical Schlieren measurement setup. 27

3.1 Illustration of the basic steps undertaken with the Scan & Paint measurement method. 29
3.2 Sketch of the evaluated spatial domain. 32
3.3 Sketch of a simple scanning example. 35
3.4 Doppler effect for several scanning speeds depending upon the angle of incidence at two different frequencies: 5 kHz (left) and 10 kHz (right). . . 36
3.5 Illustration of the bias error introduced by the frequency band discretisation process of spectral density estimates. 41

3.6 Illustration of the variance error introduced by averaging several data blocks for the calculation of spectral density estimates. 43
3.7 Average estimation error (solid lines) and error intervals (shaded areas) introduced in the spectral estimates when the positioning error fluctuates by 0.01 (left) and 0.02 (right) metres for a harmonic excitation of 500 Hz. 50
3.8 Average spectra (solid lines) and error intervals (shaded areas) introduced in the spectral estimates of measurements performed at 0.05 m (left) and 0.1 m (left) with a 0.01 m positioning error. 51

4.1 Difference between normal particle velocity and sound pressure levels at 0.02 m (left) and 0.04 m (right) away from a sound source 58
4.2 Spatial distribution of the sound pressure and normal particle velocity produced by a point source at 1 kHz with a rigid boundary located at $y = 0$. 61
4.3 Difference between sound pressure and normal particle velocity levels produced by a noise source with a 45° (left) and 90° (right) angles of incidence. 62
4.4 Projection of the radial particle velocity on the normal sensor axis. 63
4.5 Sound field generated by two incoherent point sources in terms of sound pressure (left) and normal particle velocity (right) 64
4.6 Normalised acoustic levels of the two sources shown in Figure 4.5 in terms of sound pressure (left) and normal particle velocity (right) for several measurement distances d. 65
4.7 Spatial resolution (left) and resolution factor (right) of sound pressure and normal particle velocity mapping methods. 66
4.8 High spatial resolution of particle velocity mapping over 0.6 mm diametre holes with a 7 kHz excitation source behind the perforated plate. 68
4.9 Direct sound mapping of the helicopter cabin interior for a frequency range between 150 Hz and 1500 Hz. 69
4.10 Direct sound mapping for a frequency range between 50 Hz and 10 kHz. . 70
4.11 Spectra of the different elements (top) and normal particle velocity maps centred around different resonance frequencies of the window (A), door (B) and closet (C). 71
4.12 Schematic representation of the one dimensional complex acoustic intensity (left) and the three dimensional active intensity (right). 73
4.13 Acoustic intensity vector field of a loudspeaker at 4 kHz. 75
4.14 Acoustic intensity vector field of a static Nissan 350Z with a rotational engine speed fixed at 3000 RPM. 76
4.15 Acoustic intensity vector field of a radio control airplane. 77

5.1 Sketch of a typical Transfer Path Analysis problem regarding structural and airborne noise sources. 80
5.2 Sketch of the windowing measurement procedure. 81
5.3 Sketch of the surfaces involved in the derivation. 85
5.4 Sketch of the measurement procedure in operational conditions. 88
5.5 Sketch of the of the transfer paths measurement procedure. 89
5.6 Distribution of cameras across the car interior (left) and monopole source (right) used in the scan-based panel contribution analysis investigation. . 90
5.7 Average sound pressure of each scanning session recorded at the reference position in operational conditions. 91

5.8 Comparison of the measured and synthesised reference sound pressure. . . 92
5.9 Measurement results of the car's ceiling at 95 Hz each normalized to its highest value. 93
5.10 Example of source ranking of different areas at 95 Hz. 94

6.1 Sketch of a 3 x 3 square planar array (left) and its corresponding covariance matrix (right) representing the delay between the different element positions (green dots) with colours. 101
6.2 Schematic view of the simulation environment. The sensor array and sound sources are represented by a green line and circular markers, respectively. 110
6.3 Comparison of the beamformer output (left) and phase estimation (right) of data acquired with a static microphone array (solid line) and a virtual phased array (dotted line) for several frequencies. The arrows above the left figure indicate the real position of the sound sources. 111
6.4 Geometry of the simulated scenario. Evaluated source positions are plotted in green, array sensor positions are represented by red dots and the location of the noise sources are shown by blue circular markers. 112
6.5 Convergence of the method for different source strength ranges. 113
6.6 Comparison of several algorithms for localising multiple uncorrelated sources of equal source strength. The actual positions of the sources are indicated by circles. 114
6.7 Comparison of several algorithms for localising multiple uncorrelated sources for which the power is distributed along a 6 dB range. The actual positions of the sources are indicated by circles. 115
6.8 Signal received by the virtual array in terms of magnitude (left) and phase (right). 116
6.9 Comparison of several algorithms for localising multiple uncorrelated sources including random spectral estimation error. 117
6.10 Evaluation procedure of a VPA grid. 118
6.11 Virtual phased array PSF at 500 Hz (A) and 1 kHz (B) and 2D graph of the point spread function (PSF) at 500 Hz (C) and 1 kHz (D). 119
6.12 Pictures of the assessed measurement scenarios: outdoors experiments (left and bottom) and small anechoic chamber test (right) 120
6.13 Spectrogram sample of the scanning sensor (left) and 360° localisation map of the outdoor measurement (right) 121
6.14 Sum-and-delay beamforming localisation maps at several frequencies. . . . 122
6.15 Error between estimated and real source location for the outdoor test (left) and the anechoic chamber experiment (right) 123
6.16 Comparison of VPA output (bottom figures) and nearfield sound pressure map (top figures), each normalized to its highest value. 124

A.1 Sound power of a loudspeaker source, measured with a *p-p* and a *p-u* probes in two different measurement scenarios. 138

B.1 Sketch of the assessed problem 140
B.2 Example of a monopole radiattion measurements transformed to a spherical directivity pattern 142
B.3 Diagram of the positional discrimination procedure 143

B.4 Direct sound radiation mapping of a violin at 1340 Hz. 143
B.5 Experimental measurement setup (left) and spectrogram sample (right) . 144
B.6 Example of a monopole radiattion measurements transformed to spherical directivity pattern 145
B.7 Directivity patterns of a violin at third octave bands of 500 Hz (top left), 1000 Hz (top right), 1260 Hz (bottom left) and 1588 Hz (bottom right) [dB] 145

C.1 Front (left) and rear (right) view of the experimental setup. 151
C.2 Comparison of surface particle velocity at two different positions 152
C.3 Panel velocity mapping with step-by-step measurements using accelerometers (top of each sub-figure) and scanning measurements using a *p*-*u* probe (bottom of each sub-figure). 153
C.4 Operational deflection shapes of a vibrating plate obtained with scanning measurements using a *p*-*u* probe. 154

List of Tables

3.1 Summary of the effects of the scanning speed on the two discretisation methods for a fixed spectral bandwidth. 53

6.1 Location of sound sources used in the simulations. 111
6.2 Source strengths of the sound sources used in the simulation scenario. . . 114

Declaration of Authorship

I, Daniel Fernández Comesaña, declare that this thesis titled "Scan-based sound visualisation methods using sound pressure and particle velocity" and the work presented in it are my own. I confirm that:

- This work was done wholly or mainly while in candidature for a research degree at this University.
- Where any part of this thesis has previously been submitted for a degree or any other qualification at this University or any other institution, this has been clearly stated.
- Where I have consulted the published work of others, this is always clearly attributed.
- Where I have quoted from the work of others, the source is always given. With the exception of such quotations, this thesis is entirely my own work.
- I have acknowledged all main sources of help.
- Where the thesis is based on work done by myself jointly with others, I have made clear exactly what was done by others and what I have contributed myself.
- Parts of this work have been published, as listed in the following section.

Signed: _____

Date: _____

List of Publications

Below is presented a list of the publications written by the author during the study reported in this thesis

Journal papers

- Daniel Fernández Comesaña, Emiel Tijs and Kim Daewoon, "Direct sound radiation testing on a mounted car engine," *SAE International Journal of Passenger Cars - Mechanical Systems*, Vol. 7 (3), 2014.
- Daniel Fernández Comesaña, Keith R. Holland, Dolores García Escribano and Hans Elias de Bree, "An Introduction to Virtual Phased Arrays for Beamforming Applications," *Archives of Acoustics*, Vol. 39 (1), 2014.
- Daniel Fernández Comesaña, Steven Steltenpool, Graciano Carrillo Pousa, Hans-Elias de Bree and Keith Holland, "Scan & Paint: Theory and Practice of a Sound Field Visualisation Method", *ISRN Mechanical Engineering*, Vol. 2013, Article ID 241958, 11 pages, 2013.
- Daniel Fernández Comesaña, Dolores García Escribano and Hans-Elias de Bree, "Virtual Phased Arrays: nueva tecnica de medida para localizacion de fuentes de ruido," *Revista de Acústica*, Vol. 44 (1-2), 2013.
- Andrea Grosso, Daniel Fernández Comesaña and Hans-Elias De Bree, "Further Development of the PNCA: New Panel Noise Contribution Reference-Related (PNCAR)," *SAE International Journal of Passenger Cars - Mechanical Systems*, Vol. 5 (2), 2012.

Invited conference papers

- Daniel Fernández Comesaña, Edwin Jansen, Yolanda Rollán Seco and Hans-Elias de Bree, "Acoustic Multi-Mission Sensor (AMMS) system for illegal firework localisation in an urban environment," in *Proceedings of ICSV*, Beijing, China, July 2014. (Invited by Dr. Tom G.H. Basten; pending publication)
- Daniel Fernández Comesaña, Efrén Fernández Grande, Elisabet Tiana Roig and Keith Holland, "A novel deconvolution beamforming algorithm for virtual phased arrays," in Proceedings of Internoise, Austria, 2013. (Invited by Dr. Ning Xiang)
- Daniel Fernández Comesaña, Ibán Cereijo Graña and Andrea Grosso,, "Particle velocity sensors for enhancing vehicle acoustic simulations," in *Proceedings of AIA-DAGA*, Merano, Italy, February 2013. (Invited by Dr. Giuseppe Micoli)
- Daniel Fernández Comesaña, Keith Holland, Jelmer Wind and Hans-Elias de Bree, "Comparison of inverse methods and particle velocity based techniques for transfer path analysis," in *Proceedings of Acoustics*, Nantes, France, April 2012. (Invited by Dr. Filippo M. Fazi)

Papers presented at international refereed conferences

- Daniel Fernández Comesaña, Branko Zajamsek, Andrea Grosso and Keith R. Holland, "Assessing vehicle exterior noise using a virtual phased array (VPA)," *SAE 2013 Noise and Vibration Conference and Exhibition*, Michigan, USA, May 2013.
- Daniel Fernández Comesaña, Eduardo Latorre Iglesias, Malcolm Smith and Hans-Elias de Bree, "Experimental characterisation of a car window excited by turbulent flow using scanning sound intensity techniques," *ASME NCAD*, New York, USA, August 2012.
- Daniel Fernández Comesaña, Andrea Grosso, Hans-Elias de Bree, Jelmer Wind and Keith Holland, "Further development of velocity-based airborne TPA: Scan & Paint TPA as a fast tool for Sound Source Ranking," in *Proceedings of iSNVH*, Graz, Austria, June 2012.
- Daniel Fernández Comesaña, Jelmer Wind and Hans-Elias de Bree, "A scanning method for source visualisation and transfer path analysis using a single probe," *SAE 2011 Noise and Vibration Conference and Exhibition*, Grand Rapids (Michigan), USA, May 2011.

- Emiel Tijs, Jelmer Wind and Daniel Fernández Comesaña, "Fast, high resolution panel noise contribution method," *SAE 2011 Noise and Vibration Conference and Exhibition*, Grand Rapids (Michigan), USA, May 2011.

Papers presented at international unrefereed conferences

- Daniel Fernández Comesaña and Hans-Elias de Bree, "Sound visualisation tools for investigating acoustic fields based on scanning measurements," in *Proceedings of Forum Acusticum*, Krakow, Poland, September 2014. (Pending publication)
- Daniel Fernández Comesaña and Hans-Elias de Bree, "Exploring the properties of acoustic particle velocity sensors for near-field noise source localisation applications," in *Proceedings of Forum Acusticum*, Krakow, Poland, September 2014. (Pending publication)
- Daniel Fernández Comesaña, Bilen Oytun Peksel and Hans-Elias de Bree, "Expanding the sound power measurement criteria for sound intensity *p-u* probes," in *Proceedings of ICSV*, Beijing, China, July 2014. (Pending publication)
- Graciano Carrillo Pousa, Marcin Korbasiewicz and Daniel Fernández Comesaña, "Fault Detection System Using Acoustic Particle Velocity based on Gaussian Mixture Models and Mel-Cepstral Parameters," in *Proceedings of DAGA*, Oldenburg, Germany, March 2014.
- Amaya López-Carromero García, Daniel Fernández Comesaña and Keith R. Holland, "Evaluación acústica de prototipo para escenario portátil,"[Acoustic performance evaluation of a portable stage] in *Proceedings of Tecniacustica*, Valladolid, Spain, October 2013.
- Daniel Fernández Comesaña and Steven Steltenpool, "Mapping stationary sound fields using scanning techniques: the fundamentals of Scan & Paint," in *Proceedings of ICSV*, Bangkok, Thailand, July 2013.
- Peter Cats, Emiel Tijs and Daniel Fernández Comesaña, "Differences between the PU and reverberant room method," in *Proceedings of ICA*, Montreal, Canada, May 2013.
- Daniel Fernández Comesaña, Andrea Grosso and Keith R. Holland, "Loudspeaker cabinet characterisation using a particle-velocity based scanning method," in *Proceedings of AIA-DAGA*, Merano, Italy, February 2013.

- Daniel Fernández Comesaña, Emiel Tijs, Peter Cats and Douglas Cook, "Visualisation of acoustic intensity vector fields using scanning measurement techniques," in *Proceedings of Internoise*, Innsbruck, Austria, September 2013.
- Daniel Fernández Comesaña, Dolores Garcia Escribano and Hans-Elias de Bree, "Virtual Phased Arrays, nueva tcnica de medida para localizacin de fuentes de ruido," in *Proceedings of Acustica*, Evora, Portugal, October 2012.
- Branko Zajamsek, Daniel Fernández Comesaña and Andrea Grosso, "Experimental evaluation of an optimum amount of probes used in PNCAR methodology for assessing airborne transfer path analysis," in *Proceedings of ISMA*, Leuven, Belgium, September 2012.
- Daniel Fernández Comesaña, Dolores Garcia Escribano and Hans-Elias de Bree, "Helicopter cabin interior noise assessment using Scan & Paint Transfer Path Analsyis," in *Proceedings of ERF*, Amsterdam, the Netherlands, September 2012.
- Marcos Felipe Simón Gálvez, Antonio Mínguez Olivares and Daniel Fernández Comesaña, "Passive and active noise control of a low power diesel generator," in *Proceedings of Internoise*, New York, USA, August 2012.
- Daniel Fernández Comesaña, Takashi Takeuchi, Sandra Morales Cervera and Keith Holland, "Measuring musical instruments directivity patterns with scanning techniques," in *Proceedings of ICSV*, Vilnius, Lithuania, July 2012.
- Daniel Fernández Comesaña, Eduardo Latorre Iglesias, Keith Holland, Jelmer Wind and Hans-Elias de Bree and Malcolm Smith, "Measuring operational deflection shapes with a scanning PU probe," in *Proceedings of ICSV*, Vilnius, Lithuania, July 2012.
- Daniel Fernández Comesaña, Jelmer Wind, Hans-Elias de Bree and Keith Holland, "Characterising directivity patterns of non-stationary sound sources with scanning techniques," in *Proceedings of DAGA*, Darmstadt, Germany, March 2012.
- Daniel Fernández Comesaña, Jelmer Wind, Hans-Elias de Bree and Keith Holland, "Adapting beamforming techniques for virtual sensor arrays," in *Proceedings of BeBeC*, Berlin, Germany, February 2012.
- Daniel Fernández Comesaña, Sandra Morales Cervera, Takashi Takeuchi and Keith Holland, "Measuring under non stationary conditions with scanning techniques," in *Proceedings of NOVEM*, Sorrento, Italy, April 2012.
- Daniel Fernández Comesaña, Jelmer Wind, Hans-Elias de Bree and Keith Holland, "Virtual Arrays", a novel broadband source localisation technique," in *Proceedings of NOVEM*, Sorrento, Italy, April 2012.

- Dolores Garcíia Escribano, Daniel Fernández Comesaña and Hans Elias de Bree, "Sistemas de monitorización sonora basados en sensores Microflown," [Monitoring sound systems based on Microflown sensors] in *Proceedings of Tecniacustica*, Caceres, Spain, October 2011.

- Emiel Tijs, Daniel Fernández Comesaña and Dolores Garcíia Escribano, "Caracterización de absorbentes acústicos in-situ," [In-situ characterisation of acoustical absorbing materials] in *Proceedings of Tecniacustica*, Caceres, Spain, October 2011.

- Daniel Fernández Comesaña, Keith Holland, Hans-Elias de Bree and Dolores Garcíia Escribano, "Evaluación y deteccin de pérdidas de aislamiento acústico en edificación,"[Evaluation and detection of acoustic leakage] in *Proceedings of Tecniacustica*, Caceres, Spain, October 2011.

- Daniel Fernández Comesaña, Jelmer Wind, Keith Holland and Andrea Grosso, "Performance of *p-p* and *p-u* probes using Scan& Paint," in *Proceedings of ICSV*, Rio de Janeiro, Brasil, July 2011.

- Daniel Fernández Comesaña, Jelmer Wind, Keith Holland and Andrea Grosso, "Far field source localisation using two transducers: a "virtual array" approach," in *Proceedings of ICSV*, Rio de Janeiro, Brasil, July 2011.

Acknowledgements

I gratefully acknowledge the financial support for my PhD study provided jointly by Microflown Technologies and by the University of Southampton. Besides economic matters, without the support, patience and guidance of the following people, this study would not have been completed. It is to them that I owe my deepest gratitude,

- My supervisors, Hans-Elias de Bree and Keith Holland, whose encouragement enabled me to develop the work presented here. I also would like to thank my initial supervision Jelmer Wind for his great input and helpful assistance. I have been amazingly fortunate to have advisers who gave me not only the freedom to explore on my own but also the guidance to focus on the right targets.
- The Microflown managing director Alex Koers, who had faith in me and provided inspiration and enthusiasm, and at the same time, great resources for getting involved in a wide range of projects and frequent trips abroad.
- The examiners of this thesis, Phil Joseph and Michael Vorländer, who have kindly agreed to review the thesis and provided useful input that greatly improved the work hereby presented.
- My dear friends and colleagues Emiel Tijs and Jaime Wild, for their immense support and advice writing the thesis, I could not find words that suffice to express my gratitude, I have learned so much from their suggestions and comments.
- My dear friends and colleagues Grachi Carrillo and Antonio Linares, for the daily discussions, their big support and help, encouraging me to continue working hard to solve every problem and therefore pushing me towards success.
- My dear company colleagues from Microflown, who has created an open-minded and creative working atmosphere but also they have been there to listen and give advice. I will never forget what supposed working, learning from Branko, Oytun, Andrea, Iban, Lola, Marcin, Steven, David, Yoli, Jeroen, Ivan, Rien, Timo, Erik-Jan, Arjan, Martin, Wei, Rick, Michael, Ray, Olga, Peter... and many others.

- The people who has contributed to this work with their advice, that in some cases resulted in fruitful collaborations for which I am greatly indebted to Efren Fernandez Grande, Elisabet Tiana Roig, Antoni Torras, Takashi Takeuchi, Filippo Fazi, Manuel Sobreira, Antonio Pena, Soledad Torres, Daewoon Kim, Sandra Morales, Amaya Lopez, Peter Cats, Thomas Kletschkowski and Malcolm Smith.

- My dear friends and colleagues Paul Rodriguez Garcia, Eduardo Latorre Iglesias, Hessam Alavi, Marcos Simon Galvez, Josebaitor Luzarraga, Ajit Bhuddi, Luis Tafur Jimenez, Halil Yetgin, Hector Garcia Mayen, Joan Serra Tur, Jonathan Zapatero, Alicia Costalago Meruelo, Juan Rodriguez, Pablo Peso, Begoña Fuentes, Mario Maruenda, Alberto Muiño, Martin Bueno, Daniel Docal, Vitor Domingues, Carlos Prieto, Alicia Alonso, Xavier Valero... and many others, who have inspired me and helped in many occasions and, sometimes, even spent days and nights with me in labs.

- My dear friends from Arnhem, who have made my life in the Netherlands an enjoyable and fun experience, becoming an important part of my life; especially Noortje, who has been an invaluable source of strength and inspiration.

- All my friends from Southampton and Spain. Life is happiness only if you have support from all people around you. I feel lucky of always finding excellent friends since me childhood, such as Xoel Chamorro, Andoni Garrido, David Ferro, Javi Costas, Pablo Alvarez, Silvia Perez, Eva and Aaron Fernandez, Joel Barreiro... and many others.

- Most importantly, none of this would have been possible without the love and patience of my family, to whom this thesis is dedicated to. Not only my parents and brother but also my whole extended family have been a constant source of concern and support. I also would like to express my heart-felt gratitude for given me the chance of studying abroad, sacrificing themselves to give me an opportunity to grown in knowledge, enhancing my future life.

Abbreviations

ASQ	**A**irborne **S**ource **Q**uantification
CBF	**C**onventional **B**eam-**F**orming
CPSD	**C**ross-**P**ower **S**pectral **D**ensity
CSLDV	**C**ontinuous **S**can **L**aser **D**oppler **V**ibrometry
DAMAS	**D**econvolution **A**pproach for the **M**apping of **A**coustic **S**ources
DOA	**D**irection **O**f **A**rrival
EMA	**E**xperimental **M**odal **A**nalysis
ESM	**E**quivalent **S**ource **M**ethods
FDTD	**F**inite-**D**ifference **T**ime-**D**omain
FEM	**F**inite **E**lement **M**ethod
FIR	**F**inite **I**mpulse **R**esponse
FRF	**F**requency **R**esponse **F**unction
IBEM	**I**nverse **B**oundary **E**lement **M**ethod
ISCA	**I**terative **S**idelobe **C**leaner **A**lgorithm
ISVR	**I**nstitute **S**ound and **V**ibration **R**esearch
LS	**L**east-**S**quares
LDV	**L**aser **D**oppler **V**ibrometer
LSV	**L**aser-**S**peckle **V**ibrometer
MUSIC	**MU**ltiple **SI**gnal **C**lassification
NAH	**N**ear-field **A**coustic **H**olography
NLLS	**N**on-**L**inear **L**east **S**quares
NPL	**N**ational **P**hysical **L**aboratory
NVH	**N**oise, **V**ibration and **H**arshness
ODS	**O**perational, **D**eflection **S**hape
PIV	**P**article **I**mage **V**elocimetry

PSD	**P**ower **S**pectral **D**ensity
PSF	**P**oint **S**pread **F**unction
RAOS	**R**apid **A**cousto-**O**ptic **S**canning
RMS	**R**oot-**M**ean-**S**quare
SAR	**S**ynthetic **A**perture **R**adar
SAS	**S**ynthetic **A**perture **S**onar
SLDV	**S**canning **L**aser **D**oppler **V**ibrometry
SMT	**S**ubstitution **M**onopole **T**echnique
SNR	**S**ignal-to-**N**oise **R**atio
SPL	**S**ound **P**ressure **L**evel
STSF	**S**patial **T**ransformation of **S**ound **F**ields
TBT	**T**oeplitz-**B**lock-**T**oeplitz
TPA	**T**ransfer **P**ath **A**nalysis
UAV	**U**nmanned **A**erial **V**ehicle
VASM	**V**ehicle **A**coustic **S**ynthesis **M**ethod
VPA	**V**irtual **P**hased **A**rray
VVS	**V**olume **V**elocity **S**ource

Symbols

Greek symbols

β	adaptive parameter that controls source amplitude
γ	scaling factor
γ_{xy}	linear coherence between x and y
Γ	position associated with a signal segment
Δ	spatial segment
Δ_f	frequency bandwidth
Δr	microphone spacing
Δ_x	cell width
Δ_y	cell height
ϵ	normalised mean square error
ϵ_0	initialisation parameter
ϵ_b	normalised bias error
ϵ_r	normalised random error
$\zeta^{\boldsymbol{\sigma}}$	unitary vector $\zeta^{\boldsymbol{\sigma}}$ oriented to $\boldsymbol{\sigma}$
η_p	ratio between sound pressure resolution and measurement distance
η_u	ratio between particle velocity resolution and measurement distance
θ	azimuth angle
Θ	Distance between two parallel planes
ι	Number of time segments associated to a grid cell
λ	optimal step factor
μ_c	contour mean
μ_y	mean of the signal y
$\xi_{m,n}$	VPA element cross-spectrum created by a synthetic source
Π	sound power

ρ	air density
ϱ	positioning error
σ	variance
σ_{dipole}	variance perceived by a sensor with a figure-of-eight directivity
σ_n	variance of the noise subspace
σ_{omni}	variance perceived by a omni-directional sensor
σ_{PW}	power variance
σ_s	signal subspace variance
σ_y	variance of y
$\boldsymbol{\sigma}$	steering vector
τ	time length
τ_i	time interval i
$\tau_{m,n}$	time segment inside a grid cell
$\Upsilon_{m,n}$	coordinates of a grid cell centre
φ	elevation angle
φ_{pe}	sound pressure phase shift induced by calibration errors
φ_{ue}	particle velocity phase shift induced by calibration errors
ψ	parameter estimator
Ψ	velocity potential
ω	radial frequency
Ω_T	space-time domain
Ω_h	spatial domain
$\Omega_h^{m,n}$	cell domain

Roman symbols

a	piston or source radius
$a_{m,n}^l$	cell index
$A^{(m)}$	area of panel m
$\mathbf{A_s}$	eigen value matrix
$b[.]$	bias error
$b_{m,n}^l$	cell index
$B(\theta,\omega)$	beamformer output
B	bandwidth

B_{NF}	near-field acoustic beamformer
B_{FF}	far-field acoustic beamformer
c	speed of sound
C	contour path
$\mathbf{C}$	covariance matrix
$\mathbf{C}^{\mathrm{rel}}$	relative covariance matrix
d	distance from to a source
D	source directivity
D_r	resolution distance
e_{RMS}	root-mean-square error
f	frequency
f_s	sampling frequency
f_v	video frame rate
h_m	Hankel function of order m
H_{xy}	Transfer function between x and y
H_1	Transfer function estimator
$\mathbf{H}$	Transfer function matrix
i	index
$\mathbf{I}$	identity matrix
j	imaginary unit
J	reactive intensity
k	wavenumber
l	index
L	array elements
L_{eff}	effective structural wavelength
L_p	sound pressure level
L_u	acoustic particle velocity level
m	index
M	number of grid rows or panels
n	index
n_d	number of averages
$\mathbb{N}$	natural numbers
N_b	sample block width

o_d	percentage of overlap
$\mathbf{O}$	origin of coordinates
p	sound pressure
p_{ref}	sound pressure reference
p^{TF}	sound pressure during transfer function measurements
P	Fourier transform of sound pressure
P_m	Legendre transform of order m
$P_{m,n}$	Average sound pressure power spectral density in the cell m, n
q	temporal signal driving a sound source
q_i^n	partial source strength of a deconvolution map
Q	source strength
r	radial distance to a source
$\mathbf{r}$	source trajectory
R_{xy}	cross-correlation function between x and y
R_{yy}	auto-correlation function of y
s	source index
S	number of sources or spatial domain of integration
$Spp_{m,n}^{(l)}$	partial sound pressure of the cell m, n
$Suu_{m,n}^{(l)}$	partial particle velocity of the cell m, n
S_{xy}	cross-power spectral density between x and y
S_{yy}	auto-power spectral density of the signal y
t	time variable
T	time length
T_d	length of a data segment
T_p	propagation time between a sound source and a sensor
u_n	normal particle velocity
u_r	radial particle velocity
$\mathbf{u}$	particle velocity
$U_{m,n}$	Fourier transform of the normal particle velocity at cell m, n
U_0	speed of a vibrating piston
v	sensor speed
$\mathbf{V}$	eigenvector matrix
$\mathbf{V_s}$	signal subspace eigenvectors

$\mathbf{V_n}$	noise subspace eigenvectors
x	spatial variable
$\mathbf{x}$	point in three dimensional space
y	spatial variable
z	spatial variable
Z	specific acoustic impedance

Operators

$E[.]$	expectancy
$H(.)$	Hessian of a matrix
$(.)^H$	Hermitian of a matrix
$J(.)$	Jacobian of a matrix
$(\hat{.})$	estimated value
$\bigtriangledown$	gradient operator
$\bigtriangledown^2$	Laplace operator
$< . >_t$	time-average

Dedicated to my parents

Chapter 1

Introduction

1.1 Sound field visualisation

The transformation of physical phenomena into something visual has provided fundamental insight to the develop of many fields of science throughout history. Particularly, in acoustics, sound visual representations have been thought of as a key to aid in understanding [1]. Ever since Newton expressed sound as colours more than 300 years ago [2], many different methods have been developed to express sound in terms of a visual representation. As is remarked in [3], visualisation methods offer a classical approach to physical research: "they report practical observations and building-block experiments designed to reveal a phenomenon or prove a concept."

Transducers that sense acoustic excitations are required to visualize sound, specifically, it is essential to characterise the two fundamental building blocks of acoustics: sound pressure and particle velocity[1]. As human beings, our perception of sound comes from our ears, a pair of natural sensors which transform acoustic pressure waves into mechanical vibrations, ultimately interpreted by the brain as what we call "sound". It is not surprising that since the introduction of the microphone in the 1870s by Edison [4], his device, able to mimic what we hear, became the most widely employed instrument in experimental acoustics.

The exclusive use of sound pressure microphones, either a single sensor or a large transducer array, provides insufficient data to evaluate the complete behaviour of a sound field. Consequently, many signal processing techniques were developed as an aid to

[1] An interesting analogy can be explored to understand the duality between sound pressure and particle velocity, as in, it is similar to how energy can be distinguished between kinetic and potential. The same concept could be applied to associate the vector quantities which carry directional information (particle velocity and kinetic energy) and the two scalar magnitudes (sound pressure and potential energy)

extract the largest amount of information out of a reduced dataset of sound pressure measurements. Misleadingly definitions are commonly found in the literature, describing sound visualisation as "a typical inverse problem, simply because we attempt to get more information than we measure or is available" [5] disregarding then direct field mapping techniques or indirect optic methods, the historical starting point of this field, as we shall see in the following chapter. In contrast, the research presented throughout this thesis uses both microphones and acoustic particle velocity transducers, triggering the development of a wide range of applications and therefore demonstrating the great potential of combined sensor solutions.

Acoustic measurements provide information of the assessed physical quantity at a given location. For visual purposes, a link is established between the signal level of each transducer and a colour within a certain scale, associating for instance warm colours with loud sounds and cool colours with low excitations. After data is gathered across the sound field, it is then possible to create a direct representation of the distribution of sound throughout the space by superimposing a colourmap over a photo of the measurement area. Figure 1.1 presents an example of the first measurement made with the proposed methodology, showing clearly a loud "hot spot" (indicated with red) when measuring directly in front of the loudspeaker.

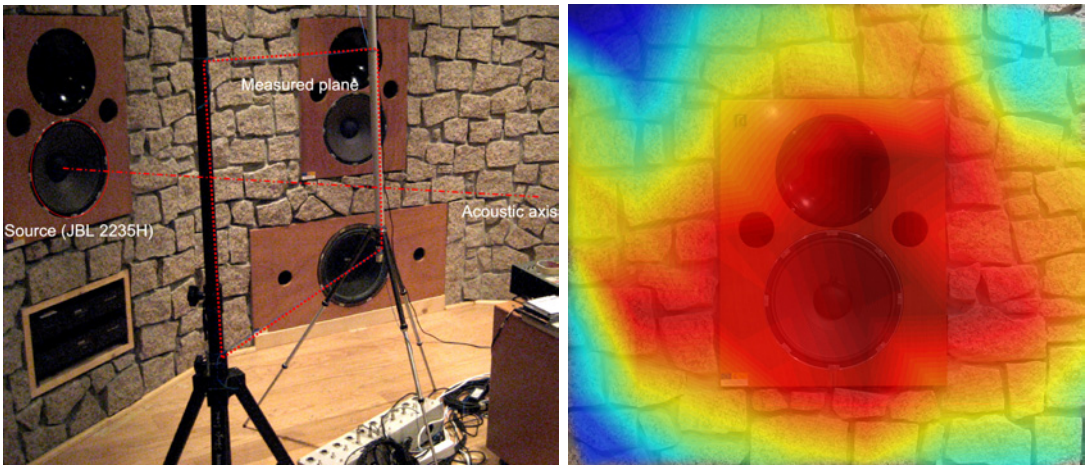

FIGURE 1.1: First measurement setup (left) and sound map (right) obtained with the proposed scanning technique in 2009.

1.2 Sound and vibration transducers

Sound field mapping methods require the use of transducers that enable the capture of a desired physical quantity. The main sensors currently available for acoustic and vibration measurements are described as follows:

- Pressure microphones are the most common devices used to measure sound pressure. They have an internal membrane which responds to pressure fluctuations in air in the same way as our eardrum, moving backwards and forwards as the pressure force acts over the membrane surface. The motion of the membrane is converted into an electric signal by a transducing element.

- Acoustic particle velocity sensors, or Microflowns, are transducers which are able to capture the particle velocity in air. The transducers were inspired by hot wire anemometers: a wire is heated up by an electrical current and is cooled down when exposed to an acoustic flow. Due to the temperature change in the wire, its resistance changes accordingly, producing a variable electrical signal proportional to the incident flow. Using two closely-spaced heated wires, a measure of the acoustic particle velocity can be estimated from the difference in temperature between them. The small size of this device allows three orthogonal sensors to be placed close to each other to characterise the acoustic particle velocity vector of the sound field.

- Accelerometers are sensors that can be fixed to a structure to measure its surface acceleration. The device senses the acceleration of a test mass inside its frame. Single and multi-axis models of accelerometer are available to detect magnitude and direction of the acceleration as a vector quantity. Although the reasonably low cost of this technology makes it attractive, the fact that it has to be directly attached to the vibrating structure is one of the main disadvantages, limiting its application in experimental cases.

- Laser Doppler Vibrometers (LDV) can measure the instantaneous surface velocity of a structure with a non-intrusive approach. The velocity is characterised by directing a laser beam at the target point and measuring the Doppler-shift of the light reflected back from the moving surface using an interferometer. Therefore, a clear reflection from the surface must be achieved to guarantee the success of the measurements. Continuous Scan Laser Doppler Vibrometry (CSLDV) and Scanning Laser Vibrometry (SLDV) are often the measurement methods implemented[2]. The high cost and low flexibility of this technology limits their use in most practical applications.

- Sound intensity probes are able to provide acoustic intensity information, that is the time averaged product of pressure and particle velocity. This makes it possible to locate acoustic sources wherever a significant net energy flow is injected

[2]In CSLDV the laser beam is swept across the surface of a test subject to capture the motion of a surface at many points simultaneously; in SLDV the laser beam is kept at a fixed point during each measurement and quickly moved to a new position to acquire the next measurement.

into the medium. A direct way of measuring the two quantities, required for calculating the sound intensity, uses a probe which is comprised of a pressure and a particle velocity transducer, i.e. the p-u intensity probe. Alternatively, an indirect estimation of the intensity can arise from the measurement of two pressure microphones placed close to each other. The extended use of the pressure microphone over the years, and the relatively recent invention of the Microflown sensor (1994), has increased the popularity of p-p probes, despite the intrinsic limitations of the indirect method used, as discussed in Chapter 4 and Appendix A.

1.3 Measurement procedures

Many techniques and apparatus have been proposed over time with the aim of obtaining a visual representation of sound [6], as can be seen in the following chapters. Regardless of the post-processing techniques applied, the current measurement procedures for characterising sound fields can be classified by three major categories: step-by-step, simultaneous and scanning measurements. Each of these techniques can be evaluated using three main features: measurement time, flexibility and total cost of the equipment.

Step-by-step is one of the most common techniques to create spatial representations of stationary sound fields. It is based upon the acquisition of data at a set of discrete positions. The flexibility of this method is one of its main advantages since the number of transducers and their spatial distribution are customizable. The number of sensors used is directly related to the cost of the experiment but inversely proportional to the time needed to undertake the measurements. In the case that all positions are characterised at the same time, it is necessary to use a large multichannel system, and hence to perform simultaneous measurements.

Conventionally, systems based upon sensor arrays are expensive and have low flexibility derived from their complexity. Alternatively, scanning methods can be used to reduce the measurement time and cost providing the sound field is time-stationary. Scan-based techniques have a fundamental difference to the previously cited procedures: data is no longer acquired at discrete spatial positions since the sensor, or set of sensors, is moved during the acquisition stage[3]. The recorded acoustic signal will have an associated tracking path which determines the sensor position during the measurement. The evaluation of a short time interval, when the sensor is passing over the area of interest, will give an estimate of the spectral content at that specific location. Traditionally, scan-based

[3]Whereas most "scanning" methods or apparatus are based upon acquiring data along a continuous path, Scanning Laser Doppler Vibrometer (SLDV) differs from this principle since data is measured at a set of discrete positions forming a step by step approach.

techniques require costly and complex tracking systems, which has led to this approach being avoided for industrial applications.

Far too little attention has been paid to scan-based measurement techniques despite their capabilities. Several attempts have been made to expand their potential by using scanning microphone arrays in combination with acoustic holography algorithms [7–12]. However, the high cost of the tracking systems used and the complex setup needed for experimentation has limited the application of this powerful measurement technique.

The novel sound visualisation technique proposed in this thesis is called "Scan & Paint". The acoustic signals of the sound field are acquired by manually moving a single transducer across a measurement plane whilst filming the event with a camera. In the post-processing stage, the sensor position is extracted by applying automatic colour detection to each video frame. It is then possible to split the long recording into multiple segments by applying a spatial discretisation algorithm (Chapter 3). Each fragment of the signal is linked to position depending upon the location of the probe during the measurement. Spectral variations across the measurement area are computed by analysing the signal segments of each grid section. A link between the 2D coordinates of the image space and the 3D coordinates of the measurement scenario is later established by defining the correspondence between pixels and meters. Additionally, a fixed reference pressure microphone can be used to preserve the relative phase information across the sound field at the different grid positions.

Figure 1.2 illustrates with a simple diagram a feature comparison of the conventional measurement procedures against the proposed method "Scan & Paint". As is shown, the step-by-step method offers the cheapest solution and simultaneous measurements provide the fastest acquisition time, whilst "Scan & Paint" has the best overall performance, a good compromise between measurement and setup time, and system cost.

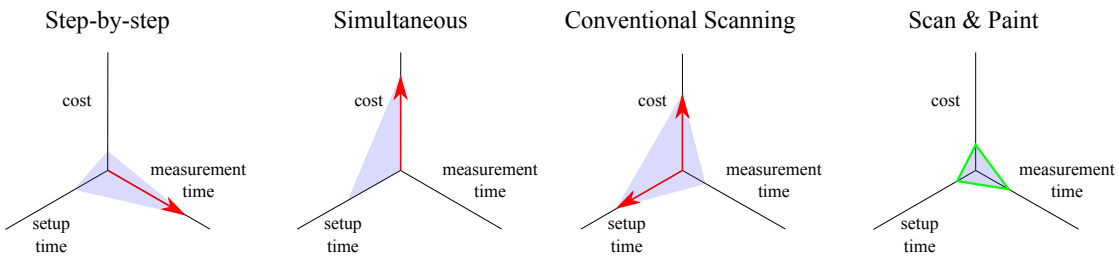

FIGURE 1.2: Features of the Scan & Paint method and other conventional measurement procedures.

1.4 Applications of acoustic imaging techniques

Most problems relating to acoustics require a detailed understanding and representation of an observed sound field. As is shown in the following chapters, acoustic measurement data used along with a suitable processing method can provide an extensive acoustic characterisation of a device, machine or environment.

It is important to remark that no prior knowledge of the source or acoustic environment are required for most of the near field investigation techniques proposed. Many alternative inverse methods, such as Near-field Acoustic Holography (NAH), involve applying models of the source or propagation features in order to estimate the response at certain points. Conventional inverse visualisation methods rely upon the inversion of the measurement data, which limits the resolution and accuracy of the results primarily due to constrained signal-to-noise ratio. In contrast, direct sound field mapping provides straightforward information about the real acoustic behaviour of a sound field without making any assumptions.

The novel sound visualisation technique proposed is attractive mainly because of its simplicity, ease of calculation, prompt results, flexibility and low cost. For these reasons, the current commercial software which implements the scanning method "Scan & Paint" has become a popular tool in recent years. For instance, Lumnitzer and Farkasovska describe it as "a revolutionary solution to the localisation of noise emissions and their quantitative evaluation" [13]. Parallel to this research, other companies around the world (Belgium, Canada and China) have developed their own scanning systems following a similar philosophy but using pressure transducers only.

Many practical applications have been investigated using the proposed methodology. As is illustrated in the following sections, noise source assessments have been carried out in various scenarios, such as: vehicle acoustics (both interior [14] and exterior noise [15]), building acoustics [16], musical instruments [17], loudspeaker design [18], aerodynamic noise [19], material characterisation [20], vibro-acoustic assessment [21] and far field source localisation [22].

1.5 Research objective

The idea of developing a novel scanning measurement technique was first proposed by the author as an MSc Project at the end of 2009. The promising preliminary results achieved in the first stage triggered the creation of a PhD proposal based upon the development of all capabilities for different scenarios and applications. Searching for an

industrial sponsor, it was discovered that the Dutch company Microflown Technologies was developing a similar scan-based methodology. With a clear shared interest, this study eventually took place as a collaboration between the University of Southampton (United Kingdom) and Microflown Technologies (the Netherlands) who kindly funded the project with five main aims:

- Create the theoretical basis for characterising magnitude and phase variations of sound pressure, particle velocity and acoustic intensity across a stationary sound field using scan-based methods.
- Explore the theoretical and practical limitations of the use of p-p and p-u intensity probes performing scan-based measurements.
- Investigate the potential of scanning measurement techniques for assessing acoustic emission problems in both free field and reverberant environments.
- Develop a panel noise contribution measurement method to evaluate real scenarios of the automotive and aviation industry efficiently.
- Exploit the capabilities of scanning measurement techniques for far field localisation and environmental noise problems.

1.6 Thesis organisation

This chapter gives a brief overview of the field of acoustic imaging, clarifying the motivation and research objectives of this work. The following chapter presents a detailed literature review of sound visualisation methods. It begins by introducing the historical development of sound visualisation techniques and follows with a brief overview of the current measurement and processing methodologies.

The theoretical framework of the proposed sound visualisation method "Scan& Paint" is presented in Chapter 3. The mathematical formulation used, the definition of the sound received by a moving transducer and some general statistical considerations for scan-based methods are introduced along with important practical remarks regarding the data acquisition process.

Next, Chapter 4 explores the use of sound pressure and particle velocity for source localisation purposes. Fundamental properties of the method, such as the influence of background noise or the spatial resolution achieved, are studied from a theoretical and practical point of view.

A new methodology for applying panel noise contribution analysis to data acquire using scanning measurements is given in Chapter 5. The theoretical and practical foundations of this technique are presented along with an experimental validation of the method.

A novel approach for far field problems is introduced in Chapter 6, where data obtained by scanning is used instead of traditional large multichannel systems. The theoretical foundations, simulations and experimental validation are presented along with the beamforming and deconvolution algorithms developed to localise sound sources in an acoustic environment.

Finally, Chapter 7 contains a summary of what has been accomplished and to what extent the research goals have been achieved. In addition, a brief outlook for future development to enhance the novel measurement method is presented.

1.7 Original Contributions

The main, original contributions of this thesis are listed below:

- An extensive overview of the historic development of sound visualisation methods is presented for the first time. It contains a review of more than 200 years of acoustic innovation, instrumentation and novel measurement methods that cover, for example, the first scanning visualisation method of Winston Kock in the 1960's - work that is almost forgotten in the recent literature.
- Two novel algorithms to process scan-based measurement data are introduced [23]. Not only the mathematical foundations but also the theoretical spectral estimation errors are studied in detail. New analytical solutions are derived to construct a solid base, ensuring the reliability and accuracy of the proposed technique from a fundamental point of view.
- The relationship between the fundamental features of scan-based methods (measurement distance, spatial and spectral resolution, scanning speed and spectral estimations errors) are explored in detail. In addition, a set of practical recommendations are given to ensure the quality of the data acquisition process.
- Several acoustic transducers are assessed from a theoretical and practical point of view, leading to the definition of the advantages, disadvantages and limitations associated with each device. In order to obtain a complete characterisation of a sound field both pressure and particle velocity need to be acquired, resulting in the use of intensity probes for gathering data across the sound field. The limited

frequency range, the poor performance in reverberant spaces and the high noise floor in the the low frequency region make *p-p* probes unsuitable for most scanning measurements [24]. *p-u* probes have been proven to give a far better performance in most practical conditions due to the direct acquisition of pressure and particle velocity using two different transduction principles.

- A fast and intuitive method for characterising the vibro-acoustic behaviour of machinery is proposed [19, 21]. Particle velocity acquired close to the vibrating surface provides acoustic data that is directly proportional to the surface displacement. The use of an accelerometer attached to the structure enables the computation of relative phase information, and ultimately, the operational deflection shapes of the vibrating body.

- A novel processing method for assessing non-stationary sound radiation is developed using a combination of moving and static reference sensors [25]. A positional discrimination algorithm is created based upon the evaluation of the signal to noise ratio and transfer function estimation of the measurement data, resulting in a frequency dependent spatial grid. The proposed method is tested experimentally in an anechoic chamber yielding directivity patterns of several musical instruments [17].

- A novel scanning method for panel noise contribution analysis is introduced and validated based upon a single moving sensor and a static reference transducer [14, 26–29]. The application of scanning panel contribution analysis quantifies the sound pressure contribution of problematic airborne or structure-borne sound sources distributed across a cavity [18]. The successful results achieved convinced several car manufacturers for employing the proposed technique to assess cabin interior noise problems.

- Acoustic intensity vector fields of several complex scenarios are investigated using scanning measurement techniques [30]. The proposed method allows the acquisition of acoustic data across large areas in a fast and efficient way. The measurement time is reduced from hours to minutes, revealing the acoustic energy flow around several vehicles and common devices [31].

- "Virtual Phased Array" technology (VPA) is successfully validated as a novel broadband source localisation technique for assessing environmental noise problems under stationary conditions from both a theoretical and practical point of view [15, 22, 32, 33]. The simulations of conventional multichannel phased arrays and VPAs show a good agreement between the two technologies, supporting the robustness of the introduced theoretical basis. An experimental validation has also

been undertaken successfully. Notably, good results are obtained even at lower frequencies, which conventional multichannel solutions are not able to assess due to size limitations of the arrays. The measurement technique presented reduces the number of transducers, measurement time and cost of regular microphone arrays, provided that the sound field is time stationary. Moreover, the remarkable flexibility of a VPA makes it a powerful tool for the assessment of broadband noise localisation problems.

- Several deconvolution methods are adapted and tested with VPAs for source localisation purposes [34]. Improvements in the spatial resolution, dynamic range and accuracy are achieved by applying deconvolution techniques to a conventional delay-and-sum beamforming output. A novel iterative sidelobe cancellation algorithm (ISCA) is introduced and compared with conventional deconvolution methods such as DAMAS and NNLS. Noise localisation experiments with multiple uncorrelated sources have been undertaken under different excitation conditions, with and without artificial noise in the virtual array data acquired. It is shown that the performance of the new method proposed exceeds that of conventional iterative deconvolution algorithms due to the nature of the investigation process: ISCA mainly interacts with the data at the points where the energy is maximised along a limited dynamic range, avoiding problems caused by the noise floor of the measurement data.

Chapter 2

Literature review

2.1 Introduction

The necessity to represent sound and vibration information visually triggered many investigations with a common goal: to create tools to build intuition and understanding upon specific problems. Before going into detail on the proposed scanning measurement technique, it is worth highlighting the importance of developing devices for displaying sound phenomena, and how it has evolved thus far. This will allow us to understand the value of the proposed method within the current state of the art and previous techniques.

This chapter starts by addressing the evolution of the main acoustic methods and apparatus introduced throughout history. The early experiments on sound and vibration imaging during the 18th and 19th centuries are reviewed. Next, the development of methods to visualise sound propagation phenomena is assessed. This is followed by the description of the main acoustic measurement techniques introduced in the last century. Then, the last part of this chapter is focused on the description of the main current direct and indirect measurement methodologies.

2.2 Early experiments on sound and vibration imaging

Although the interest in acoustics is considered to have its origins in ancient Greece with studies concerning vibrating strings and musical sounds were undertaken by Pythagoras [35], it was not until 1787 when the first technique for visualising vibration in plates was introduced. Ernst Chladni, based on the previous work of Robert Hooke and Simeon Poisson, introduced his method of using sand sprinkled on vibrating plates to show modal lines [36]. He generated the so called *Chladni patterns* by strewing sand on a vibrating

plate excited with a violin bow, causing the sand to collect along the nodal lines [37], as can be seen in Figure 2.1. Interest in his success went beyond the scientific community of his time, amusing even Napoleon Bonaparte, who ordered a translation of his major work *Die Akustik* [38] into French and offered a reward[1] to whomever would be able to explain the *Chladni patterns* mathematically.

FIGURE 2.1: Chladni patterns of a rectangular plate [40].

During the 19th century several acoustic apparatus were designed to measure and visualise sound phenomena [41]. In 1827, Sir Charles Wheatstone coined the term microphone that was initially associated with a purely acoustical device, similar to a stethoscope; nonetheless, his most successful invention was the kaleidophone [42]. Although his apparatus helped him to understand that the modal behaviour of a structure is linked to the superposition of transversal waves, the kaleidophone only provided a visual demonstration of the complex motion of a vibrating body.

Around forty years later, Hermann von Helmholtz invented a vibration microscope for sound and vibration visualisation of violin strings and human speech [43]. The device reveals the frequency of a tuning fork or other vibrating object with respect to a fork of known frequency by way of Lissajous figure analysis [44]. By viewing the patterns for a bowed violin string, von Helmholtz was able to determine the actual motion of the string, which is still referred to nowadays as the Helmholtz motion. A picture of the device is shown along with some examples of Lissajous patterns in Figure 2.2.

In 1866, closely related to von Helmholtz' work, the German scientist August Kundt first proposed a way of visualising standing acoustic waves, ultimately allowing him to measure the speed of sound in different gasses [46]. He used seeds of lycopodium and corkdust to show periodic patterns when standing waves were created in the tube. Similar work was developed in England by John Tyndall, who created several apparatus to illustrate sound phenomena [47]; for instance, he made use of ripples for the demonstration of wave phenomena in connection with the propagation of light. As we shall see, his experiments established a starting point for novel sound visualisation techniques based in wave propagation on water developed during the next century [48].

The use of burning gases for sound visualisation purposes was explored extendedly by the Russian scientist Rudolph Koenig, who devoted more than 40 years to creating a

[1] Sophie Germain was awarded the prize offered by the French emperor Napoleon for writing a fourth-order equation to describe plate vibrations, although Kirchhoff later proposed a more accurate description of the boundary conditions [39].

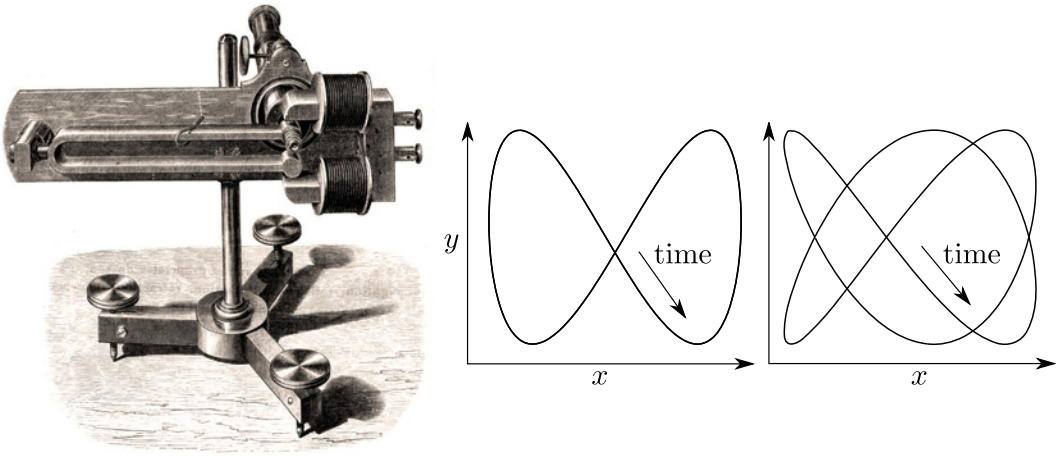

FIGURE 2.2: Vibration microscope [45] (left) and example of Lissajous patterns (right).

large collection of innovative acoustical equipment [49]. His most famous contribution, the manometric flame, allowed him to study the nature of all kind of acoustic signals in a visual way. The manometric capsule is divided into two parts by a thin flexible membrane. Sounds waves are collected by a funnel and cause the membrane to vibrate. The oscillations cause a periodic change in the supply of gas to a burner, so the flame moves up and down at the frequency of the sound. A rotating mirror allows one to view the flame variations caused by the sound. By incorporating Helmholtz resonators it was even possible to use this apparatus as a Fourier analyser, expanding its capabilities for a wide range of applications. Figure 2.3 shows a picture of the device (left) along with an example of the output produced by the apparatus (right).

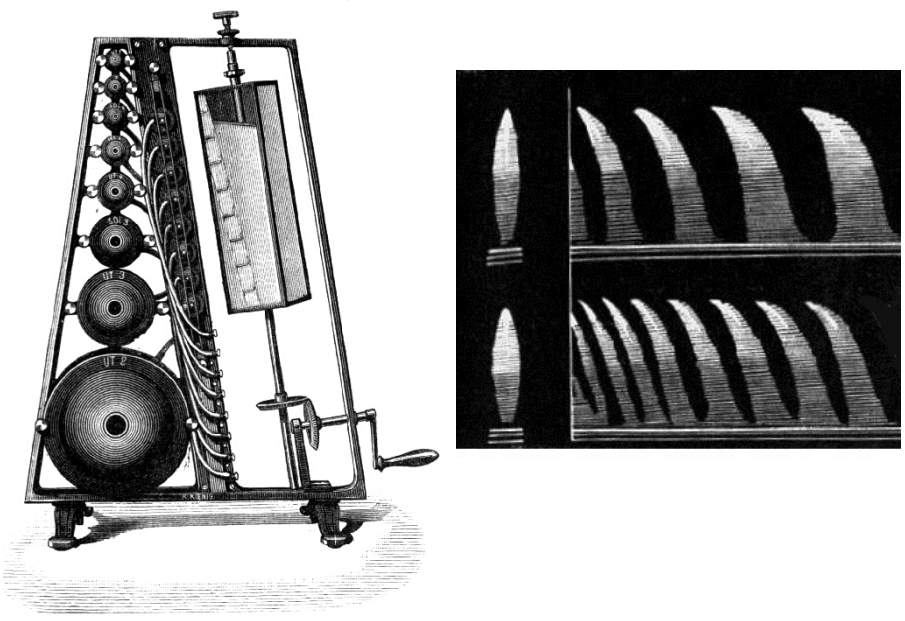

FIGURE 2.3: The manometric flame apparatus of Rudolph Koenig (left) and an example of the device experimental output (right) [45].

2.3 Visualisation of wave propagation

At the beginning of the 19th century, in optics literature it was pointed out that it was impossible to accomplish a stroboscopic observation of an expanding spherical wave [50]. Nevertheless, August Toepler between 1859 and 1964 realised that a probing wave of pulsed light is able to freeze an expanding spherical sound wave, since the velocity ratios are about one million to one. Thus, he invented a technique to see travelling waves: the schlieren method [51–53]. The schlieren method entails "amplifying" small differences in the optical refraction index of the medium through which the sound wave travels. This amplification therefore increases the contrast between transparent objects having extraordinary small index differences. Figure 2.4 shows a sketch of the original aparatus (left) along with a drawing of the results obtained with it (right).

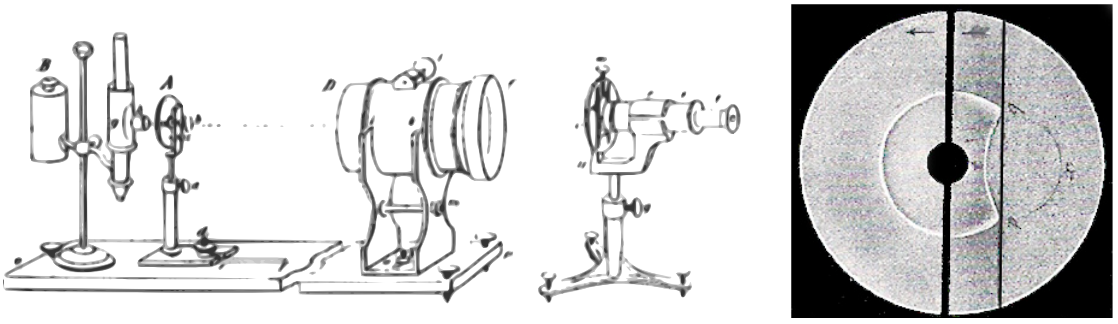

FIGURE 2.4: Toepler's original schlieren apparatus (left) [54] and Toepler's drawing of the schlieren image of a spherical shock wave from an electric spark in air (right) [52].

The impressive results obtained by Toepler encouraged other scientists to research this area and also expand upon the method for other fields of science[2]. A remarkable example of a prolific career linked to schlieren imaging is that of Ernst Mach. During his early life, Mach enhanced the initial device of Toepler to achieve a synchronised delay circuit for visualising *sound* waves from sparks. The combination of his developments with the latest technology of photographic film enabled precise wave-speed measurements. His findings ultimately lead him to discover that the waves from sparks were not mere sound waves, they were *supersonic* [55]. Unfortunately for Toepler, he did not live long enough to become aware of Mach discoveries and on his epitaph still remains the misleading sentence "He was the first to see sound," referring to his schlieren images of weak shock waves [52].

[2] The dutch scientist Friest Zernike presented a new perspective of the schlieren method which won him a Nobel Prize in 1953. The conventional schlieren methods were applied from a geometrical-optics point of view and, in contrast, he analysed the method with a wave-optics point of view [50]. He improved the method but constrained to microscopy, introducing the phase contrast microscope.

Another remarkable optic-based sound visualisation method was created by one of Mach's assistants, Vincenz Dvorak, who published the first traditionally-recognised account of the simplest sound observation method in 1880[3], the so called shadowgraph technique [57]. Dvorak used sunlight focused on a 1 mm aperture to project a diverging light beam across his darkened lab onto a white wall. As a result, refractive phenomena in the middle of the beam appeared as shadows on the wall.

Some decades later, in 1912, Foley and Souder [58] reinvented the Dvorak's shadow method as a new alternative to schlieren devices. Surprisingly, Foley and Souder referenced the previous devices of Toepler and Mach, but did not mention anything about Dvorak's first apparatus of shadowgraph photography. They created a device which generates a shock wave from an electric spark followed by a light flash. Depending on the time gap between the flash and the spark, it is possible to capture the outcoming supersonic wave at different stages after generation. Figure 2.5 displays three main experiments: free radiation from a point source, reflection of a wave at a plane surface, and simultaneous reflection and transmission by a diffraction grating plate, illustrating with remarkable clarity the Huygens principle.

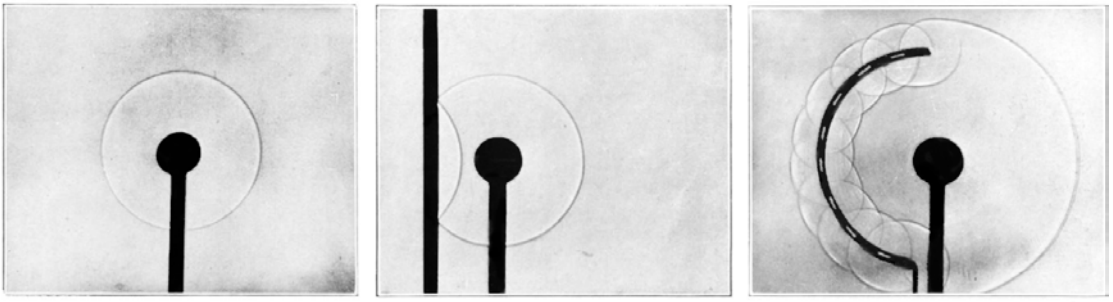

FIGURE 2.5: Photographs of propagating waves using shadowgraph techniques [58].

Shadowgraph techniques were extensively used by many scientists throughout history such as W. C. Sabine (1868 -1919). He built models of concert halls, fired sparks and sent weak shock waves reverberating around them. These weak shocks, almost sound waves, revealed themselves in direct shadowgraphs, allowing for the study of the emitted waves at different stages in their propagation through the room, as can be seen in Figure 2.6. Sabine brought forth the first real understanding of sound in auditoriums at the beginning of the 20th century [59–61], for which he is nowadays considered the father of modern architectural acoustics.

In addition, shadowgraphy was also used as a key aid to study the analogy between cylindrical sound waves and waves on the surface of a liquid. Ripples in a small tank are

[3]There are remarkable similarities with previous research done by Robert Hooke throughout the 17th century and Marat's forgotten "helioscope" shadowgraph apparatus [56] introduced in 1780. The lack of popularity of both works left only recognition for Dvorak's "novel" device.

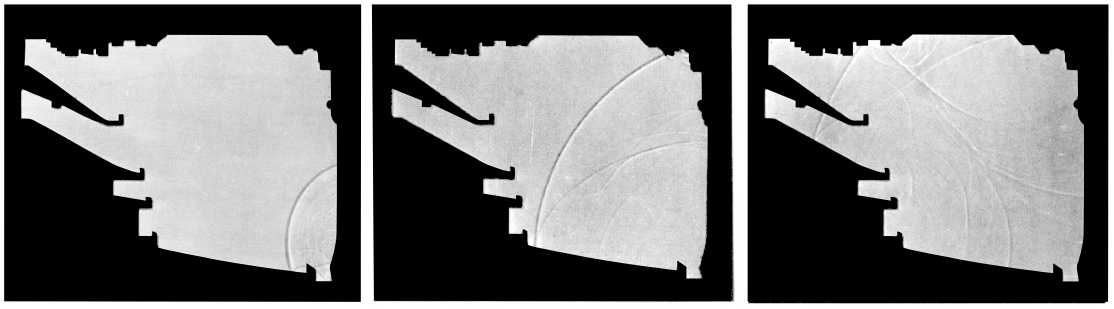

FIGURE 2.6: Sabine's shadowgrams of wave motion in a model of the new theatre of New York City [61].

suitable for illustrating acoustical phenomena when the wavelength is comparable to the size of any objects used. Although the potential for using a water tank to study sound propagation inside enclosures was already discussed in 1844 [62], and later demonstrated by Tyndall [48], it would not be until 1925 when extensive research was undertaken by A. Davis. His work established the limitations of the use of water tanks to study sound propagation phenomena [48]. Figure 2.7 illustrates the results obtained with the experimental setup of Davis compared with conventional shadowgraph methods. As can be seen, even though the use of the optic-based technique results in clearer images, the similarities between the two experiments show the possibility of using wave propagation in water as a simple alternative technique to study sound.

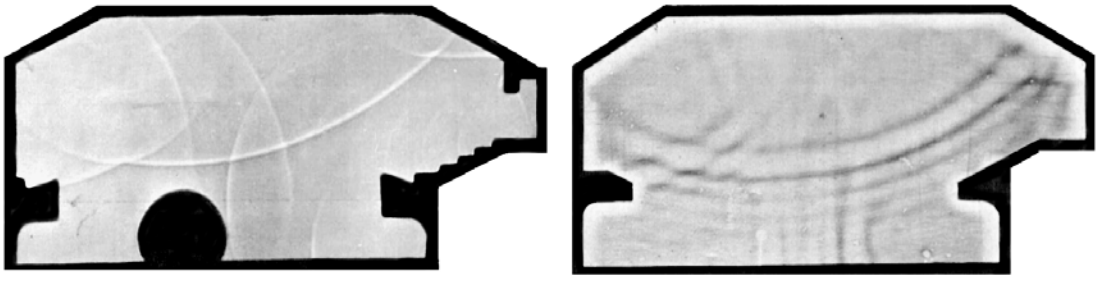

FIGURE 2.7: Sound propagation comparison using shadowgraphy techniques (left) and the water tank method (right) [48].

2.4 Novel acoustic methods of the 20th century

The beginning of the 20th century brought the first effective attempts to introduce modern and precise measuring instruments into the field of acoustics, primarily by Arnold and Crandall of the American Telephone and Telegraph and Wente from Western Electric Laboratories [63]. Unfortunately, World War I and II caused large change to the trends of the scientific production; sound visualisation was no longer a primary goal. A large number of government sponsored laboratories were formed in addition to already

existing industrial groups focused upon communication and military purposes. This new trend caused worry in the scientific community, as was recorded for instance by Eccles in 1928, who stated: "new acoustics is Baconian, that is to say, it is being prosecuted with a view to rendering services to mankind rather than from the motive of scientific curiosity" [63].

2.4.1 Scan-based sound visualisation methods

It was not until the 1960's that new methods for sound visualisation were introduced. The first scanning technique to display sound was presented by Winston Kock in 1965 [64]. He worked extensively on improving his apparatus which lead him to later publish the book *Seeing sound* [1]. Kock's method was not directly based upon visual observation like Toepler's technique but rather indirect visual observation. The electrical signal of the microphone can be made visible by causing it to light an electric neon bulb. The brightness of the lamp at a particular spot is then indicative of the loudness of sound at that point. In order to photographically record the brightness pattern, he set a camera with a long time exposure aimed at the area of interest. Consequently, as the microphone-light device scans the area with a fixed speed, the camera records the light intensity variations from point to point. In addition, he also developed a subtraction technique for visualising the wave patterns across a sound field. The addition of the microphone signal with the excitation signal results in a coherent summation of both waves. This reinforces the light output when the two signals are in phase, whereas the brightness is very low when they have opposite phase. A picture of the device is displayed in Figure 2.8 along with few loudness patterns.

2.4.2 Cymatics

Completely independent of Kock's work, Hans Jenny attempted to redefine the study of visible sound and vibration during the 60's by the term "cymatics" [65]. Inspired by the work of Ernst Chladni, he delved deeper into the many types of periodic vibro-acoustic phenomena in a similar fashion to Chladni. He tested the vibrating surface of plates, diaphragms and membranes by applying a thin coating of particles, paste and liquids. Those materials reorganize depending upon the level of vibration across different areas, therefore displaying different patterns (as shown in Figure 2.9). His holistic approach to science, his claims of the ability to "bring matter to life with sound" and his fascination for occultism, divided opinions between those affirming his responsibility for the "history of bad acoustics" [66] and those who believe that his patterns hide something beyond science, something that could lead to the understanding of the healing power of audible

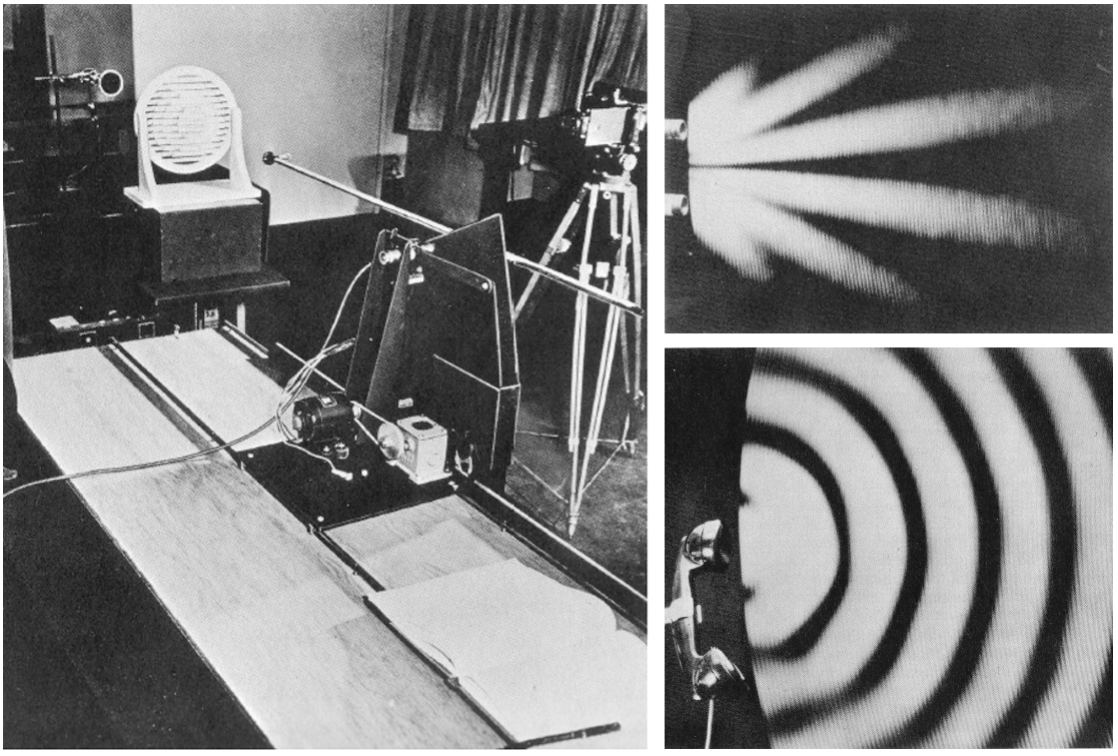

FIGURE 2.8: Kock's scanning apparatus (left), sound pattern generated by two sound sources out of phase (top right), and wave radiation pattern generated by a telephone loudspeaker applying a subtraction technique at 4000 Hz (bottom right) [1].

sound [67]. The credibility of the second group is undoubtedly questionable, and it is a shame that the supporters of the hidden power of sound can argue that their beliefs are based upon "scientific work".

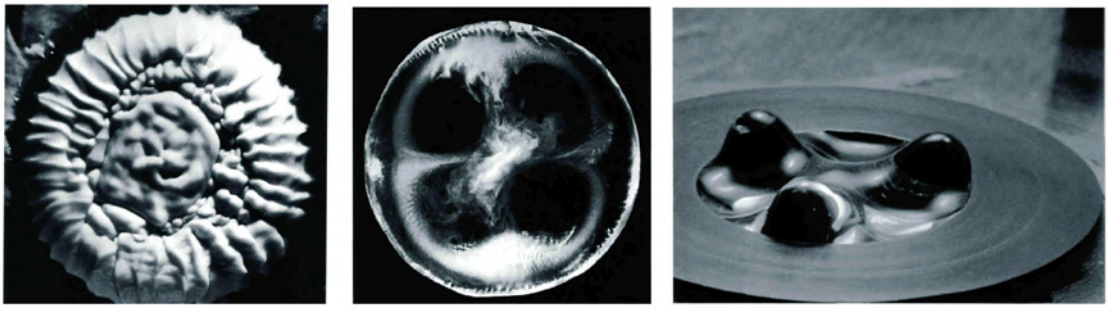

FIGURE 2.9: Several cymatics figures created by Hans Jenny [65].

2.4.3 Holographic interferometry

Another alternative measurement technique which emerged during the same period is holographic interferometry. In the forties Dennis Gabor [68] presented a technique that allowed the recording of both amplitude and phase information of a wave front at any

point in space. With this technique, which Gabor named holography (from the Greek *holos*, or *the whole*), it was possible to reconstruct, from one hologram measurement plane, the complete field generated. But, according to [69], it was not until the 60's when some independent works revealed that this technique can be very useful for experimental mechanics applications if interferometry between holograms were used to detect phenomena that can be encoded in a wave front [70, 71].

One of the earliest practical studies investigated using holographic interferometry can be found in [72], where the use of this technology was employed to produce visualisations of the vibrating behaviour of a violin body. A sample of such holograms is shown in Figure 2.10.

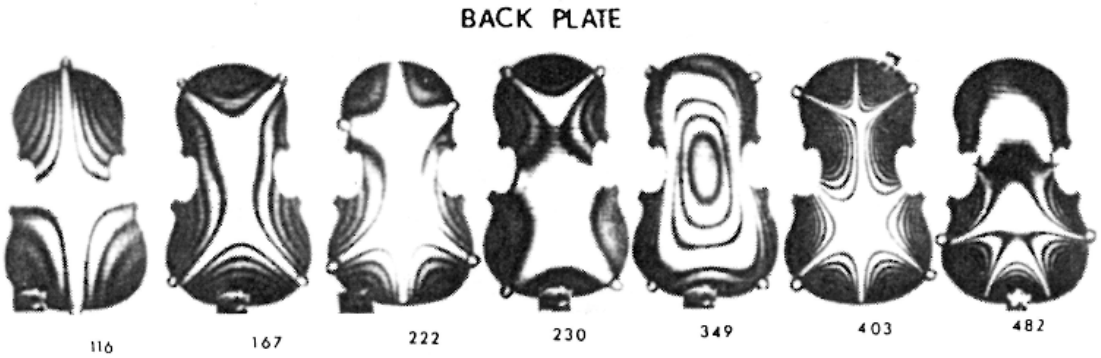

FIGURE 2.10: Deflection shapes of a violin plate using holographic interferometry [72].

2.5 Current experimental sound visualisation methods

Over the past forty years there has been a dramatic increase in the development of sound measurement methods and processing techniques. Transducers based upon mechanical, thermal or optical principles have provided a wide technological basis to determine the acoustic properties of a sound field. It is often necessary to describe not only the location and nature of the sound sources, but also the behaviour of the sound field they generate. The direct representation of the quantity being measured (direct methods) and the application of signal transformations to expand the data acquired (indirect methods) have vastly contributed to the development of the field of acoustic imaging. In this section the most common measurement methods are briefly introduced with the aim of noting the basic differences between the scan-based technique proposed in this thesis ("Scan & Paint") and other current sound visualisation methods.

2.5.1 Acoustic holography

Theoretical and numerical means to visualise sound fields have been attempted via acoustic holography, first adapted from optics [68, 73, 74] to acoustics during the 1980s [75–78]. Maynard et al. justified the potential of the proposed technique by stating that "the great utility of holography arises from its high information content, since data recorded on a two-dimensional surface (the hologram) may be used to reconstruct an entire three-dimensional wave field" [77]. The initial limitation of a planar geometry was removed in 1989, when Veronesi and Maynard introduced the inverse boundary element method (IBEM) [79].

Acoustic holography can be classified as an indirect technique for sound source identification and visualisation. It enables the rendering of a full description of the sound field to provide insight into how the acoustic output or the structural vibration of a source is coupled to the surrounding fluid medium. Generally, a discrete number of acoustic observations are measured over a two-dimensional plane or "aperture". A full three-dimensional representation of the field can be obtained by using the data acquired together with a sound propagation model. Figure 2.11 shows a sketch of the measurement principle.

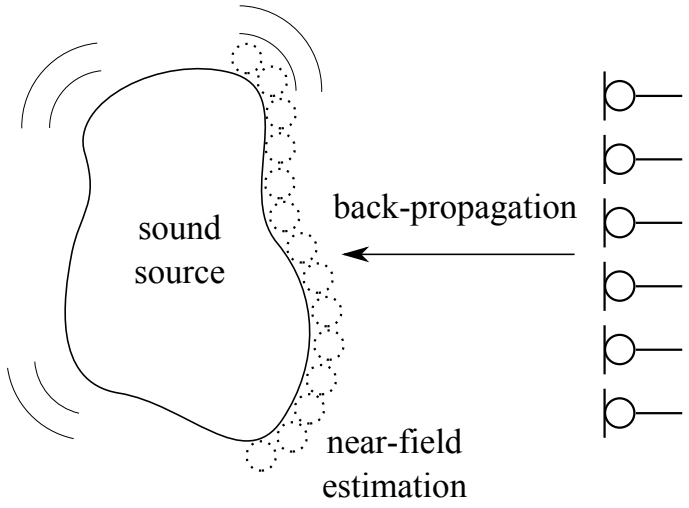

FIGURE 2.11: Illustration of the general acoustic holography measurement principle.

In the specific case of near-field acoustic holography (NAH), the measurements are undertaken in the vicinity of the sound source. As a result, the proximity allows for the capture of its "complete" radiation into the medium, avoiding the otherwise inherent truncation error of far-field holography [80]. In addition, near field measurements enable the capture of waves that propagate ineffectively and exponentially decay when the distance from the source is increased, i.e. the evanescent waves. By acquiring this high spatial-frequency information, NAH reduces the wavelength resolution problem that

conventional acoustic holography or other indirect sound visualisation techniques, such as beamforming methods have.

In spite of the strong theoretical basis, acoustic holography poses several challenges in its practical implementation. The back-propagation from the observation plane toward the source, which cannot always be placed in the near field, is ill-posed due to the presence of evanescent waves. Furthermore, the propagation model used may not suit the real experimental scenario, as is often the case in non-anechoic conditions. Regarding the real measurement aperture, it is discrete, finite and has associated positioning errors. Moreover, the data acquired is biased by sensor calibration errors. Practical limitations together with the high cost and complexity of these systems limit the range of applications where acoustic holography is able to provide meaningful and accurate results.

2.5.2 Acousto-optic mapping

One of the typical problems with determining quantities of an acoustic field is the influence of the transducer itself on the actual properties being measured. Contrary to most conventional sensors, optical transducers offer a non-intrusive approach to acquire data. Optical techniques, which rely on exploiting the acousto-optic effect in the audible range, assess the interaction between sound and light by measuring the phase modulation effect of a laser beam exposed to acoustic excitation. According to [81], a laser beam travelling throughout a sound field is able to capture the acoustic properties along the path it follows in the compressed form of a line integral. The dependency of the speed of light upon the refractive index of the medium produces a modulation effect on the phase of light: it travels slightly faster through a high pressure field whereas its speed reduces in the presence of lower pressure. In practice, these phenomena can be detected via laser interferometry by monitoring the laser light phase changes. This measurement procedure can provide a detailed insight of the sound field which can be used either for visualisation purposes or in combination with other advance processing methods. Figure 2.12 presents a diagram of the measuring principle.

The acousto-optic effect has been investigated extensively to characterize ultrasonic waves in water and other dense fluids for more than twenty years [82–84]. Nonetheless, very few studies have been reported for audible sound [85–87]. Recently, an important step forward has been made by A. Torras-Rosell et al. who successfully combined the acousto-optic effect with beamforming [88], holographic [89] and tomographic techniques [90]. In addition, the National Physical Laboratory (NPL) reported in commercial media that a rapid sound field evaluation is now available via a novel method

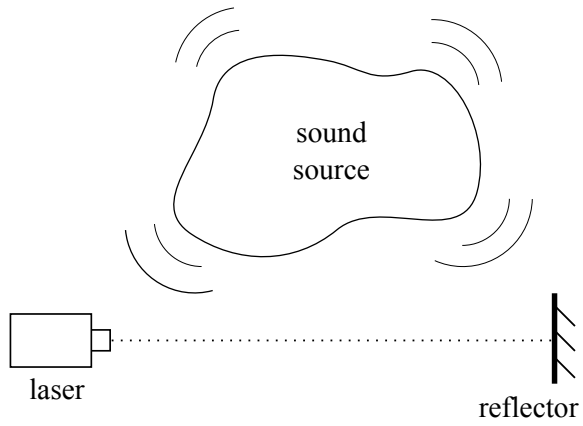

FIGURE 2.12: Sketch of the setup of an an acousto-optic measurement.

called Rapid Acousto-Optic Scanning (RAOS). This method uses the direct display of the Radon transform and cannot be used as a pressure reconstruction technique, it can only be used for visualisation purposes.

2.5.3 Beamforming

In the 1970's, multichannel microphone arrays were first applied to sound source localisation, although the idea of developing such a device was first proposed during the World War I [91]. The first microphone antenna, or so called "acoustic telescope", was invented by Billingsley in 1974 [92]. Since then, the use of multichannel products has grown substantially with the improvement of data acquisition systems, computing hardware and localisation algorithms. Since 1999, a set of apparatus catalogued as "acoustic camera" has been presented as a solution for detecting and localising noise sources in a sound field [93].

Spatial filtering operations, known as beamforming, are applied to the sensor data to extract the localisation information of the noise sources. An array of transducers captures certain acoustic properties of the sound field at a set of discrete positions. Next, data is processed using wave propagation models to estimate their direction of arrival, acting as a spatially discriminating filter [94]. The resulting maps are computed almost in real time and often overlaid on a video picture, enabling the visualisation of the noise emitted by a noise source. It has had a large impact in the media and also impressed the general public, helping to spread the use of microphone arrays as an interesting and intuitive acoustic testing method. Figure 2.13 shows a sketch of a measurement scenario.

Beamforming and the previously mentioned Near-field Acoustic Holography (NAH) have some fundamental common background (e.g. they often share the basis functions in which the sound field is decomposed), and are somewhat complementary to each

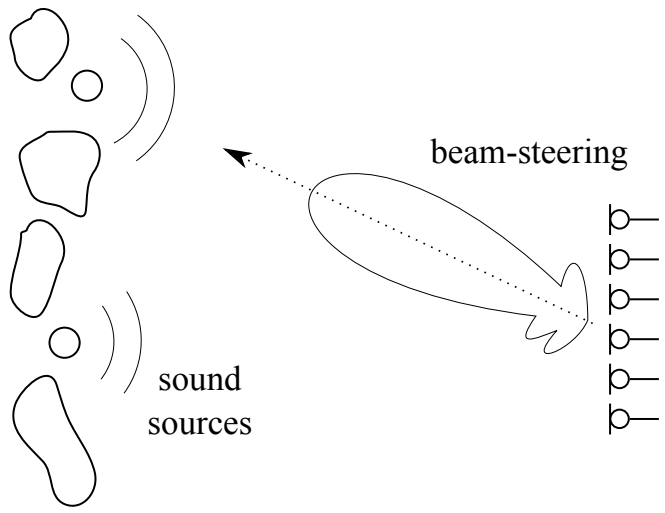

FIGURE 2.13: Sketch of a far field source localisation problem evaluated using beamforming.

other [80]. Beamforming is mostly a far-field sound source localisation technique, which implies that the evanescent sound field is not captured. Consequently, beamforming cannot be considered as a sound field reconstruction technique, it simply provides an approximate relative "source strength" map and not a quantitative reconstruction. The resolution of conventional beamforming is limited by the spatial wavelength. Therefore, the size of the array must be proportional to the largest wavelength evaluated. On the other hand, beamforming can easily handle incoherent sources, but it presents some difficulties dealing with coherent sources, such as reflections, which can lead to corrupt results. In near-field acoustic holography, the coherence assumptions are different, coherent sources are easily assessed, whilst incoherent sources require the use of complex processing methods.

Similarly to NAH, acoustic beamforming systems have several practical limitations. The wave propagation models used in the algorithms may not suit the real measurement scenario, making the method face difficulties in non-anechoic conditions [95]. The aperture or observation plane is finite, discrete and has positioning error associated to it. Moreover, the sensors are not ideal, the data acquired is affected by transducer calibration errors. These practical limitations together with the high cost and complexity of commercial systems limit the range of suitable applications for conventional beamforming solutions[4].

[4] A novel approach for applying beamforming algorithms to data acquired by scan-based techniques is presented in Chapter 6.

2.5.4 Direct mapping methods

It is difficult to trace the origin of direct sound field mapping. The idea of linking sound with colour had already been in use from the days of Newton at the beginning of the 18th century [2]. But, it was not until the 19th century when the first attempts to obtain pictorial representations of sound were performed successfully. Initially, indirect demonstrations of sound propagation and vibro-acoustic behaviour were achieved via visual observation and optic techniques. However, to the author's knowledge, the generation of colourful images of level distribution throughout the measurable area was impossible until approximately the 1980's when computer technology had sufficient processing power to handle multichannel audio recordings and complex graphical representations.

The methodology followed by direct methods, as explained in Chapter 1, relies on the representation of signals acquired by a single transducer or set of sensors placed across the measurement area. The transformation of each signal to the frequency domain enables the access of the maximum excitation of a particular spectral region, which in practical cases can show a resonance, leakage or defective area. The technique proposed in this thesis, "Scan & Paint", is based upon this direct mapping procedure. Multiple application examples are presented in the following chapters, where the final output of the system will generally be a colourful image in which the loudest areas are highlighted. This methodology delivers acoustic colormaps in a fast and efficient way; it is the first step towards solving a specific noise problem based upon building intuition and understanding from experimental evidence. A sketch of the measurement procedure is presented in Figure 2.11 for the case of simultaneous (left) or scanning (right) acquisition.

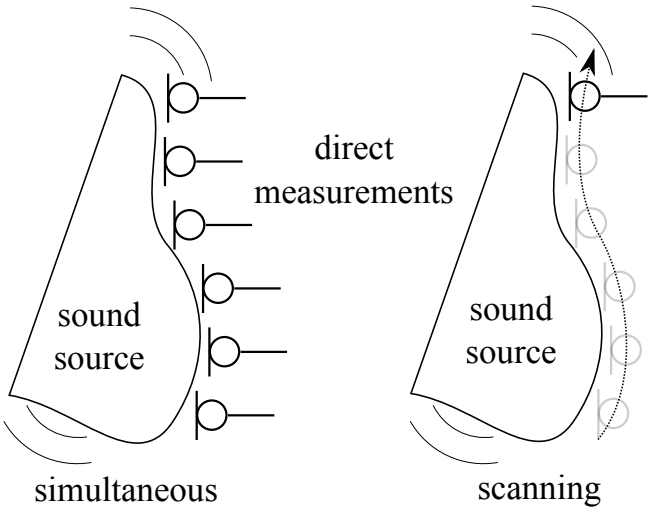

FIGURE 2.14: Illustration of direct mapping methods for simultaneous (left) or scanning (right) measurements.

The indirect methods described so far "attempt to obtain what is not available based on what is available," [96] which often means that a quantity is estimated indirectly and that a reduced dataset is enlarged by calculating the missing data. The main problem with these approaches is the strong dependency on the accuracy of both the theoretical models used and the the signal to noise ratio of the experimental data. On the contrary, direct observation is often the most straightforward way to get an accurate and reliable characterisation of a discrete point.

There are three fundamental ways to acquire data across a sound field depending on how the phase information is gathered. Firstly, in order to obtain a complete characterisation of the phase information it is necessary to place sensors at every single point aimed to be assessed (simultaneous measurement, see Section 1.3). This is, a costly and impractical solution for most applications. Secondly, as shall be seen in Chapter 4 and Chapter 5, there are many situations where the use of relative phase information is sufficient. Consequently, a single or set of fixed reference sensors can be used in order to preserve the relative phase linked to a certain position in the field. In this case, either scan-based or point by point measurements can be performed. Thirdly, if the phase information can be considered irrelevant, it is then possible to use a point by point or scan-based measurement to acquire data asynchronously, hence capturing only magnitude variations across the measurement area.

In summary, direct mapping measurement techniques are attractive because they do not require a propagation model or basis functions that mimic the measurement environment. Indirect acoustic methods are convenient if direct measurements are expensive, inapplicable or difficult to use. The main advantage of the proposed scan-based technique, "Scan & Paint", is that the quantity of interest is captured directly, avoiding the traditional drawbacks of inverse sound field mapping methods.

2.5.5 Particle Image Velocimetry

Particle Image Velocimetry (PIV) is a non-intrusive technique for simultaneously measuring velocities at many points in a fluid flow. To the author's knowledge, there is no a clear starting point of this methodology, since it grew out of Laser-Speckle Velocimetry (LSV) during the 1970's [97]. An extensive review of the development of PIV can be found in [98]. The technological evolution of the last decades together with some recent developments have extended PIV to the study of acoustic problems [99], specifically focused on the determination of acoustic particle velocity vector fields [100]. The principle of the PIV measurement technique relies on the physical definition of velocity as a differential quotient. The trajectory of many tracer particles which follow the flow

faithfully can be captured with an optical camera by illuminating a plane in the flow with two very short light pulses (of a few nanoseconds) within a time difference of a few microseconds. The particle images captured at two instants are stored by the imaging sensor. This allows a cross-correlation between the two pictorial distributions, which is used to determine the local displacement of many positions of the observation field locally. Using an image magnification factor, this method typically enables the measurement of more than 10000 instantaneous velocity vectors for each double-image of the tracer particles inside the light sheet plane. Extending the PIV system to a stereo camera setup allows all three components of the velocity vectors in the plane of the flow field to be determined instantaneously. A simple drawing of the measuring principle is shown in Figure 2.11.

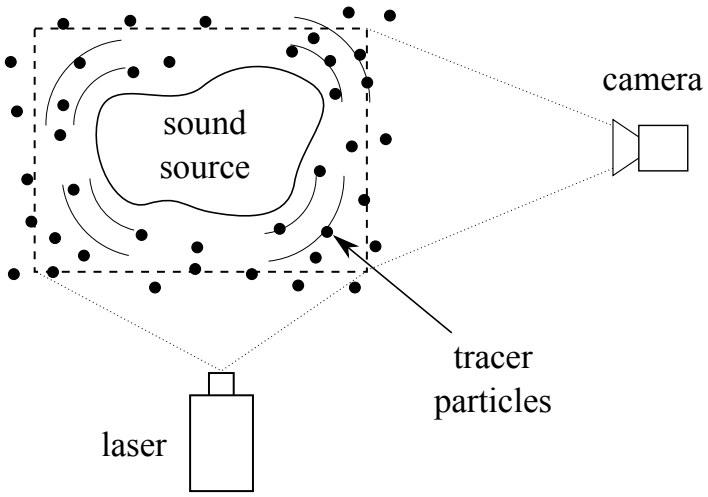

FIGURE 2.15: Illustration of the particle image velocitmetry measurement principle.

An important feature of PIV is that a reliable basis of experimental flow field data can be obtained for direct comparison with numerical calculations and hence, for the validation of computer codes [101]. During the last years an increasing number of scientists have started to utilise the PIV technique to investigate the instantaneous structure of velocity fields in various areas of fluid mechanics. Nowadays PIV is not only used in microscale planes but also in areas of several square meters and in flows with velocities from a few mm/s up to km/s.

2.5.6 Schlieren and shadowgraph imaging

The history of Schlieren and shadowgraph techniques has always been closely related to flow and shock wave visualisation (see Section 2.2). Nonetheless, in 2005 Hargather et al. [102] demonstrated that these methods can also be used to obtain a visual impression of a sound field, as long as the sound level and frequency are sufficiently high. Despite

the lack of research in the development of these imaging methods for sound visualisation purposes, future improvements in the sensitivity of measuring devices could enhance the current capabilities of Schlieren-based imaging techniques. Both Schlieren and shadowgraph methodologies exploit the deflection of light by the local variations of the medium's refractive index. When sound travels through air it causes the air's refractive index to change locally. This change influences light travelling through it, slightly varying its trajectory. Using a double mirror system with a sharp blocking object, or "knife-edge", positioned almost at the focusing point, a shadow pattern can be created and projected onto a screen. The shadow pattern corresponds to a light-intensity representation of the expansions (low density regions) and compressions (high density regions) that take place between the mirrors. Extensive descriptions of these techniques are given in several books and articles on flow visualisation, e.g. [3, 103–105]. Figure 2.11 shows a sketch of the basic Schlieren measurement setup.

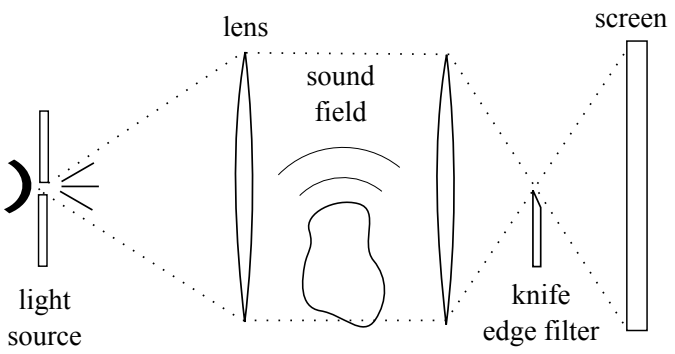

FIGURE 2.16: Sketch of a typical Schlieren measurement setup.

2.6 Summary

It has been shown that there is notable interest in the development of instruments to assess sound and vibration phenomena in both qualitative and quantitative terms. Sound visualisation methods are powerful tools for gaining understanding in specific experiments and to ultimately step forwards toward solutions for acoustic problems. In this chapter many examples of prolific scientific careers linked to the employment of sound imaging techniques have been described, along with the numerous acoustic apparatus introduced throughout history. Furthermore, the most common measurement methods have been reviewed. Despite the great variety of measurement methodologies available, the introduction of a straightforward and cost effective technique is highly valuable for a wide range of real-life experimental scenarios; the scan-based technique proposed in this thesis "Scan & Paint" aims to provide a simple, flexible and effective tool to visualise sound.

Chapter 3

Fundamentals of Scan & Paint

3.1 Introduction

The novel scan-based sound visualisation technique proposed in this thesis is called "Scan & Paint". Most disadvantages of complex hardware systems can be avoided by employing a simple acquisition procedure. The sensor, or probe, is manually moved across a measurement plane. A video camera is used to film the measurement process; this information is later used in a post-processing stage to extract the position of the sensor for each video frame. The recorded signals are split into multiple segments using a spatial discretisation algorithm, assigning a spacial position based upon the tracking information. A colour representation of the acoustic variations across the sound field can then be computed using a discrete mesh of values and applying a linear interpolation between them. The results are finally combined with a background picture of the measured environment to obtain a visual representation, allowing to ''see'' the sound.

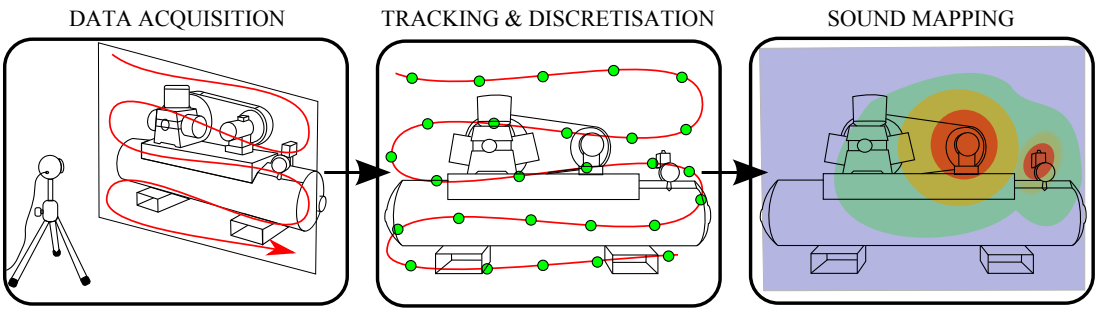

FIGURE 3.1: Illustration of the basic steps undertaken with the Scan & Paint measurement method.

Scan-based methods were introduced by Kock [1, 64] during the 1960's, for creating visual representations of sound pressure fields. However, it was not until the late 1980's when acoustic data acquired with moving transducers was first used to obtain quantitative results, following the development of the Spatial Transformation of Sound Fields (STSF) technique by Hald and Ginn [7, 106, 107]. This method combines Near-field Acoustic Holography (NAH) for the investigation of a sound field in the vicinity of the source with the Helmholtz' integral equation to determine the noise radiated in the distant field.

Alternative approaches that use moving microphone arrays and holography methods were also introduced over the following years [8–12]. However, the common aspect of all these methods, the implementation of inverse techniques to provide a complete characterisation of the sound field, often leads to poor estimates if the transducer response, location, measurement conditions and testing environment are defined inaccurately. These constraints, together with the practical limitations of hardware systems, limited the application of commercial scan-based solutions.

In recent years, the introduction of ''Scan & Paint'' and several alternative commercial sound imaging devices have made a strong impact in the industrial acoustic market. Scan-based solutions offer an effective approach to display sound phenomena, which can ultimately help to solve a wide range of acoustic and vibro-acoustic problems. Nevertheless, there is a current knowledge gap in the theoretical foundations of scanning measurement procedures.

This chapter presents the fundamental theory of the proposed acoustic imaging technique along with some statistical considerations for scan-based systems. The mathematical formulation of the problem is outlined along with two novel spatial discretisation methods. Next, the theoretical implications of the sensor movement on the acquired data are examined. The fundamentals of statistical signal processing of the proposed method are then introduced, providing novel derivations for the spectral estimation error. This section is followed by the practical considerations of "Scan& Paint", not only general guidance for the measurement procedure but also the influence of tracking errors introduced by the manual movement of the probe and an assessment of the link between scanning speed and accuracy of the resulting maps. The chapter ends by summarising the main concepts presented.

3.2 Mathematical formulation

One of the key steps of the sound visualisation method proposed is the fragmentation of the continuously acquired data. It is essential to define a method that guarantees the robustness and accuracy of the data splitting process. In this section, the formulation of the Scan & Paint basis is defined for the two discretisation methods developed: a decomposition of the measurement space into a set of spatial areas (planar grid method) and the fragmentation of the signal along the tracking path (point method).

3.2.1 Planar grid discretisation method

The regular discretisation of a continuous spatial domain is often used by many computational acoustic techniques, such as FEM [108] or FDTD [109]. It provides a decomposition of a continuous domain into a finite set of equal sized elements. As a result, the resolution and accuracy are preserved across the space, achieving homogeneous estimations across the entire grid. This discretisation criteria can also be applied to the proposed measurement technique with some practical and theoretical considerations. The tracking system implemented in Scan & Paint estimates the position of the sensor by analysing individual video frames, i.e. images that contain a projection of the environment in a two dimensional space. This transformation prevents the tracking of the exact location of the probe since slight variations along the camera axis (the depth of the image) cannot be perceived. Tracking errors may ultimately have a significant impact in the resulting sound maps [110], but this effect can be minimized by positioning the video camera perpendicular to the measurement surface and maintaining a constant measurement distance. In this way, resolution and accuracy limits of the sound maps produced can be maintained.

The formal derivation of the method begins by defining a continuous 2D dimensional spatial domain, the image space, with an additional time dimension associated with it. The discretisation of the spatial domain and the definition of the evaluated time signal of length T (the measurement time) can be expressed as

$$\Omega_T = \Omega_h \times [0, T] \in \mathbb{R}^3 \tag{3.1}$$

where Ω_h is the union of M by N non-overlapping subspaces $\Omega_h^{m,n}$, i.e.

$$\Omega_h = \bigcup_{m=1}^{M} \left(\bigcup_{n=1}^{N} \Omega_h^{m,n} \right) \tag{3.2}$$

where $\bigcup_{m=1}^{M}$ denotes the union operator of the elements $m = 1$ to M. The area covered by each block $\Omega_h^{m,n}$ can be delimited using a regular planar grid of cell size Δ_x by Δ_y. Figure 3.2 illustrates this scenario.

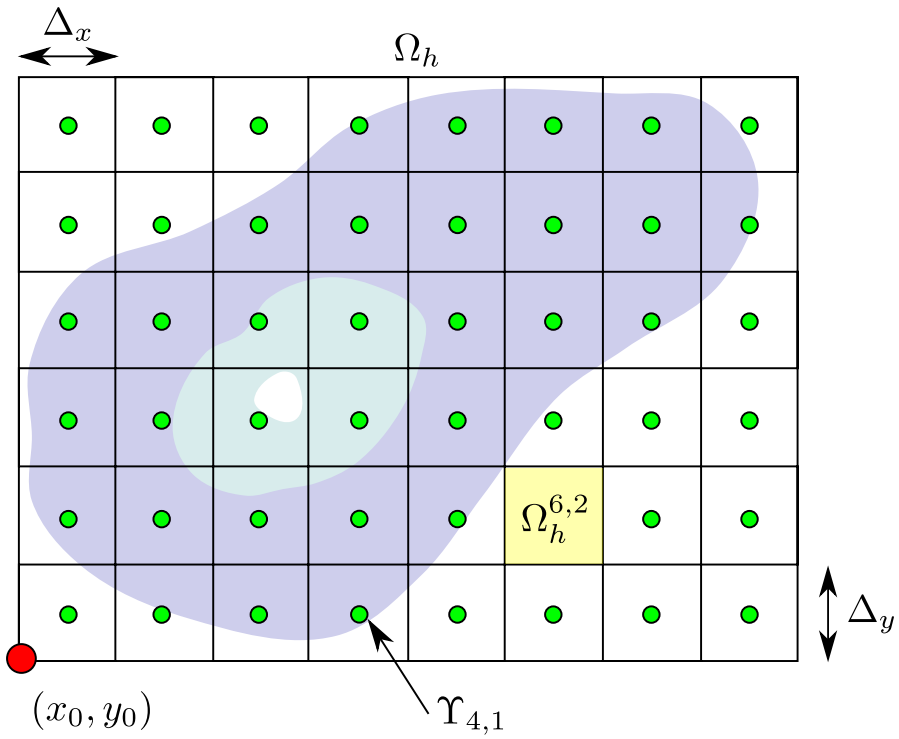

FIGURE 3.2: Sketch of the evaluated spatial domain.

The centre of each grid cell $\Omega_h^{m,n}$ can be defined with respect to the starting point of the discretisation grid (x_0, y_0), the cell size (Δ_x, Δ_y) and their row and column index (m, n)

$$\boldsymbol{\Upsilon}_{\mathbf{m,n}} = (x_m, y_n) \ / \ \boldsymbol{\Upsilon}_{\mathbf{m,n}} \in \Omega_h^{m,n} \tag{3.3}$$

with

$$x_m = x_0 + \Delta_x(m - 1/2) \tag{3.4}$$

$$y_n = y_0 + \Delta_y(n - 1/2) \tag{3.5}$$

$$m = 0, 1, ..., M \ \text{ and } \ n = 0, 1, ..., N \tag{3.6}$$

where M and N are the total number of rows and columns of the planar grid. Therefore, each cell will be defined spatially as

$$\begin{aligned} \Omega_h^{m,n} = (x_m - \Delta_x/2, x_m + \Delta_x/2) \times (y_n - \Delta_y/2, y_n + \Delta_y/2) = \\ \left\{(x, y) \in R^2 \ / \ x_m - \Delta_x/2 < x < x_m + \Delta_x/2 \ , \ y_n - \Delta_y/2 < y < y_n + \Delta_y/2\right\} \end{aligned} \tag{3.7}$$

Once the spatial domain of interest has been discretised, a link can be then established between measurement data acquired with a moving transducer and the defined grid. The continuous path $\mathbf{r}(t)$ followed by the sensor is fragmented into several segments using the grid structure of Ω_h, hence dividing the original signal and assigning each segment a position on the measurement area. As a result, each grid cell will have a list of associated segments such as

$$\xi_{m,n} = \mathbf{r}(t) \cap \Omega_h^{m,n} = \left\{ \mathbf{r}(\tau_{m,n}^{(1)}), \mathbf{r}(\tau_{m,n}^{(2)}), ...\mathbf{r}(\tau_{m,n}^{(\iota)}) \right\} \tag{3.8}$$

where $\tau_{m,n}^{(l)}$ is a time interval which connects a section of the original time signal to a certain grid element $\Omega_h^{m,n}$, and ι is the number of sweeps within the cell. Each signal segment $\tau_{m,n}^{(l)}$ has certain time boundaries $a_{m,n}^{(l)}, b_{m,n}^{(l)}$, i.e.

$$\tau_{m,n}^{(l)} = \left[a_{m,n}^{(l)}, b_{m,n}^{(l)} \right] \ / \ a_{m,n}^{(l)}, b_{m,n}^{(l)} \in [0, T] \tag{3.9}$$

According to Equation 3.8, one grid cell can have multiple associated sections of the original signal if the sensor crosses the same area several times. The use of a sound probe which combines a sound pressure microphone and a particle velocity sensor (a p-u probe) enables the measurement of both acoustic quantities across the space. Consequently, the application of the grid method to a scanning measurement yields the relationship between measured time data and the different grid cells. As a result, each cell of a sound pressure $\mathbb{P} \in \Omega_T$, and particle velocity $\mathbb{U} \in \Omega_T$ signal array can be defined as

$$\mathbb{P}(\boldsymbol{\Upsilon}_{\mathbf{m,n}}) = \left\{ p(\tau_{m,n}^{(1)}), p(\tau_{m,n}^{(2)}), ..., p(\tau_{m,n}^{(\iota)}) \right\} \tag{3.10}$$

$$\mathbb{U}(\boldsymbol{\Upsilon}_{\mathbf{m,n}}) = \left\{ u_n(\tau_{m,n}^{(1)}), u_n(\tau_{m,n}^{(2)}), ..., u_n(\tau_{m,n}^{(\iota)}) \right\} \tag{3.11}$$

where p and u_n are the recorded sound pressure and normal particle velocity signals, respectively. The route followed by the probe will determine which grid cells have data assigned to them and which, if any, will be empty. Averaging is therefore required if multiple time signals are associated to a single cell. Since data is acquired asynchronously at different cells, the averaging process must be applied in the frequency domain, thus

$$\hat{P}_{m,n}(f) = \frac{1}{\iota} \sum_{l=1}^{\iota} \hat{S}pp_{m,n}^{(l)}(f) \tag{3.12}$$

$$\hat{U}_{m,n}(f) = \frac{1}{\iota} \sum_{l=1}^{\iota} \hat{S}uu_{m,n}^{(l)}(f) \tag{3.13}$$

where each $\hat{S}pp_{m,n}^{(l)}(f)$ and $\hat{S}uu_{m,n}^{(l)}(f)$ denotes the autospectral density estimate of a

given segment of the sound pressure and particle velocity signals, respectively. Averaging spectral density estimates calculated from uneven time series results in a complex definition of the achieved spectral accuracy. It is however possible to derive the limits of this approach provided that sufficient data is acquired within one cell. Further details about the calculation of autospectral estimates and their associated error are given in Section 3.4.2.

3.2.2 Point discretisation method

An alternative discretisation process can also be introduced, based upon the segmentation of the tracking data available along the scanning path. A unidimensional discretisation approach is used instead of the two dimensional decomposition of the Cartesian space implemented in the grid method. Since a finite number of tracking points are recorded, it is then possible to define a set of positions $\mathbf{\Gamma}_i$ associated with the acquired audio signal

$$\mathbf{\Gamma}_i = (x_i, y_i) / \ \mathbf{\Gamma}_i \in \Omega_h \tag{3.14}$$

where $i \in \mathbb{N}$ indicates the position index. Each of the tracking samples or spatial points $\boldsymbol{\Gamma_i}$ has an associated time interval τ_i. With the spatial point method, the discretisation process is performed along the scanning route $\mathbf{r}(t)$ depending upon three main user parameters: number of averages (n_d), sample block width (N_b) and overlap ratio between sample blocks (o_d). Each time interval is defined as

$$\tau_i = \left[\frac{i}{f_v} - \frac{n_d N_b (1 - o_d)}{2 f_s}, \frac{i}{f_v} + \frac{n_d N_b (1 - o_d)}{2 f_s} \right] \tag{3.15}$$

where f_v and f_s denote the video and audio sampling frequencies, respectively. The pressure and particle velocity levels representative of each spatial position $\mathbf{\Gamma}_i$ are then obtained by evaluating the audio signal in the assigned time interval, i.e.

$$\mathbb{P}(\mathbf{\Gamma}_i) = p(\tau_i) \tag{3.16}$$

$$\mathbb{U}(\mathbf{\Gamma}_i) = u_n(\tau_i) \tag{3.17}$$

Finally, a scattered grid of data is obtained with an amount of points equals to the total number of video frames. Similar to the planar grid method, the calculation of the spectral density functions associated with each segment also enables the assessment of the acoustic map in the frequency domain. The point method does not require a link to be established between the image space and the real measurement environment. As such, this method can be more robust than the grid method if the visible area of the source differs drastically from a planar geometry or if the axis of the video camera is

not normal to the surface under assessment. Nevertheless, the lack of averaging between autospectral estimates of closely spaced positions results in a larger variance error of the sound maps, often losing the visual "smoothness". Therefore, the selection of the most suitable discretisation method mainly depends upon the measurement conditions and accuracy.

3.3 Sound received by a moving transducer

In most of the literature reviewed so far regarding scan-based methods it is considered that a fraction of the acquired signal is representative of a discrete position, disregarding any possible errors induced by the scanning process. Nonetheless, non-linearities appear in an acoustic signal recorded with a moving transducer due to the Doppler effect. Some acoustic holography measurement methods proposed simplified analytical expression to compensate for a constant sensor speed [7, 8]. This section not only evaluates the impact of the Doppler shift but also presents a definition of the sound pressure and particle velocity data acquired, accounting for the arbitrary movement of the measuring probe.

3.3.1 The Doppler effect

A non-linear effect is introduced due to the relative motion between an emitting sound source and a receiving transducer, known as the Doppler effect. The acquired signal presents a shift in frequency that is directly dependent upon the wavelength. A sketch of the problem can be seen in Figure 3.3, where $\mathbf{v} = [v_x, v_y, v_z]$ denotes the speed of the probe, $\mathbf{c} = [c_x, c_y, c_z]$ is the velocity of the sound wave in the direction of the propagation and φ is the angle of incidence.

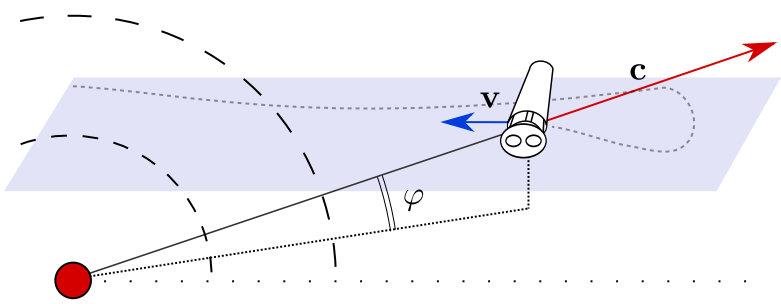

FIGURE 3.3: Sketch of a simple scanning example.

The frequency shift Δf recorded by the moving transducer can be defined as [111]

$$\Delta f = \left| \frac{\|\mathbf{v} + \mathbf{c}\|}{\|\mathbf{c}\|} - 1 \right| f \tag{3.18}$$

The maximum frequency shift occurs when the norm of the propagation and scanning speed is maximal, i.e. when both vectors are parallel. On the other hand, scanning data acquired in front of the sound source presents an insignificant non-linear shift.

Several scanning speeds have been simulated in order to have a quantitative assessment of the impact of the Doppler effect. Figure 3.4 shows the frequency shift introduced into the recorded signal for different angle of incidences and frequencies. As is shown, non-linear effects are insignificant (average frequency shift is below 1 Hz) up to 10 kHz if the scanning speed is less than 5 centimetres per second (0.05 m/s). An interesting derivation is given in [112] where it is shown that the Doppler shift is always smaller than the spectral bandwidth providing a good frequency resolution is preserved.

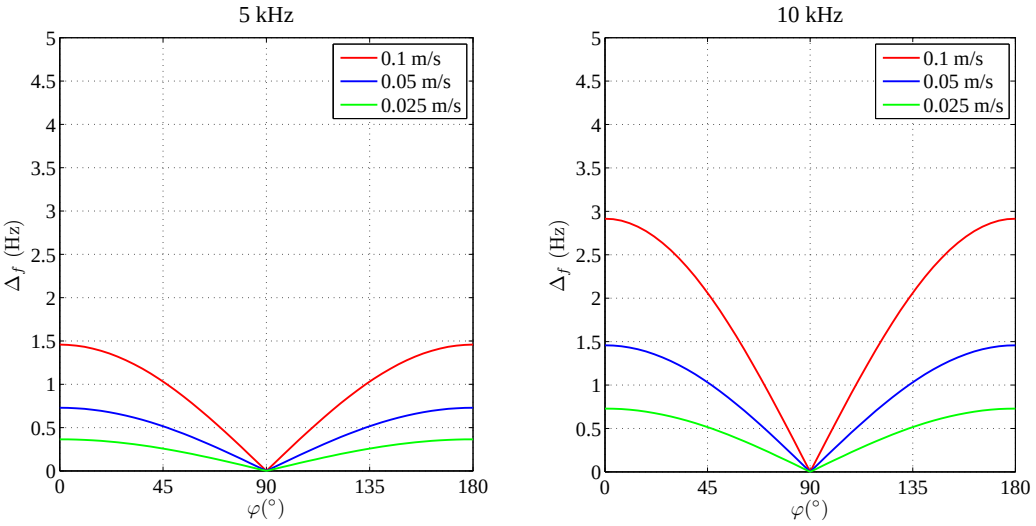

FIGURE 3.4: Doppler effect for several scanning speeds depending upon the angle of incidence at two different frequencies: 5 kHz (left) and 10 kHz (right).

3.3.2 Sound pressure, particle velocity and velocity potential

The derivation presented below is based upon the solution of an analogue problem in electromagnetism [113] which has recently been adapted for acoustic moving sources by Camier et al. in [114]. The current work evaluates a reciprocal problem to Camier's study since, in our case, a point sound source remains static while the receiving microphone is moving.

The derivation begins by defining the excitation of the system by a punctual sound source $Q(\mathbf{x_0}, t)$ located at an arbitrary position $\mathbf{x_0} = [x_0, y_0, z_0]$ at which temporal behaviour varies according to a function $q(t)$

$$Q(\mathbf{x_0}, t) = q(t)\delta(\mathbf{x_0}) \tag{3.19}$$

In order to study the sound field produced by $Q(\mathbf{x_0}, t)$ it is crucial to define the associated velocity potential Ψ. This allows the sound pressure and particle velocity to be derived at any point in the evaluated environment. The wave equation for free field conditions in the presence of a punctual source is defined as

$$\Delta\Psi - \frac{1}{c^2}\frac{\partial^2\Psi}{\partial t^2} = Q(\mathbf{x_0}, t) \tag{3.20}$$

where $\Delta\Psi$ indicates the Laplacian of the velocity potential and c is the speed of sound in air. In order to introduce position changes of source or receiver in the analytical model, it is necessary to define the associated Green functions and convolve them with the excitation produced by $Q(\mathbf{x_0}, t)$. Following the derivation proposed by Camier et al. it is possible to define the velocity potential as a function of the excitation source q, the distance between source and receiver r, the speed of the moving sensor $\mathbf{v}$ and its trajectory $\mathbf{x}$. The expression is defined for a time instant which depends upon the propagation time T_p from the sound source to the receiver such as

$$\Psi(\mathbf{x}, t) = \frac{q(t-\chi)}{4\pi(r(t-T_p) - \mathbf{v}(t-\chi)\cdot(\mathbf{x}(t-T_p) - \mathbf{x}_0))} \tag{3.21}$$

where

$$\chi = \frac{r(t-T_p)}{c} \tag{3.22}$$

Finally, the sound pressure p and the particle velocity vector $\mathbf{u}$ are obtained by deriving the velocity potential temporally and spatially, hence

$$p = -\rho\frac{\partial\Psi}{\partial t} \tag{3.23}$$

$$\mathbf{u} = \nabla\Psi \tag{3.24}$$

In conclusion, the sound pressure and particle velocity acquired by a moving sensor have been defined. In later sections, the implementation of the above analytical expressions will allow for the evaluation of how the measurement conditions impact upon the spectral estimation.

3.4 Statistical considerations

Most acoustic problems are not of a deterministic nature. Since properties of a random variable cannot be exactly determined from a finite set of samples [115] it is necessary to implement statistical signal processing techniques to process the data. Only estimates of the parameters of interest can be calculated from a finite amount of observations. This section presents the basic operations required to estimate various properties of random data based on either a static or moving acquisition process. Attention in this section is focused on the errors that are solely statistical, since data acquisition and processing errors are covered in the following section.

3.4.1 Mean estimate

The first statistical quantity of interest is the ensemble mean value. The unbiased mean estimate of a signal y of finite length T acquired with a fixed sensor measuring a time stationary excitation can be expressed as

$$E[\hat{\mu}_y] = E\left[\frac{1}{T}\int_0^T y(t)dt\right] = \frac{1}{T}\int_0^T \mu_y dt = \mu_y \tag{3.25}$$

where $\hat{\mu}_y$ is the mean estimate of y, and $E[.]$ denotes the expected value operator. The influence of a sound field on a moving sensor can be quantified using a line integral (sometimes called a path or contour integral). This operation is often used to measure the effect of a field along a given trajectory or path. The mean estimate of a moving sensor $\hat{\mu}_c$ can be defined by combining a line integral with the second mean value theorem of integration. For a sensor which follows a smooth path $C \subset \Omega_h$, the mean estimate can be defined as

$$\hat{\mu}_c = \frac{1}{\Delta}\int_C y\left(\mathbf{x}(t), t\right)\, dS \tag{3.26}$$

where Δ is the total distance of the path

$$\Delta = \int_C dS \tag{3.27}$$

and dS is the infinitesimal path segment covered during a time interval dt at velocity $|\partial\mathbf{x}(t)/\partial t|$. It is convenient to change the integration domain from space to time in order to obtain a similar definition of a fixed position measurement to that shown in Equation 3.25, thus

$$\hat{\mu}_c = \frac{1}{\Delta}\int_0^T y\left(\mathbf{x}(t), t\right)\left|\frac{\partial\mathbf{x}(t)}{\partial t}\right| dt \tag{3.28}$$

In the special case that the moving speed is constant (e.g. $|\partial \mathbf{x}(t)/\partial t| = \mathbf{v}$), Equation 3.27 then becomes

$$\Delta = \int_0^T \mathbf{v}\, dt = \mathbf{v}\, T \tag{3.29}$$

leading to an equivalent expression to that found in Equation 3.25, i.e.

$$\hat{\mu}_c = \frac{1}{T} \int_0^T y(\mathbf{x}(t), t)\, dt \tag{3.30}$$

This last expression implies that the application of an averaging process to several signal segments acquired with moving sensors (the spectral averaging process shown in Equation 3.12 and Equation 3.13) will only lead to an unbiased estimation of the mean when the speed is constant. Otherwise, if there are large fluctuations in scanning speed within a cell, it is necessary to consider the changes in velocity of the transducer during the sweep. Despite the manual sensor movement, this condition is often fulfilled by the Scan & Paint measurement procedure since the signal segments belonging to one grid cell are usually sufficiently short to avoid large scanning speed fluctuations.

3.4.2 Autospectral density estimate

The evaluation of discrete frequency components is an unsuitable spectral analysis method for the assessment of non-deterministic signals [116]. Instead, it is more convenient to study the power distribution in the frequency domain via autospectral density functions. Most current digital data analysis procedures use finite Fourier transforms in order to estimate autospectral density functions [115]. Given a sample time history $y(t)$ of infinite length T, the autospectral density function, also known as one-sided power spectral density, is defined as

$$S_{yy}(f) = 2 \lim_{T \to \infty} \frac{1}{T} E[\, |Y(f,T)|^2 \,] \tag{3.31}$$

where $Y(f,T)$ is the finite Fourier transform of $y(t)$, thus

$$Y(f,T) = \int_0^T y(t) e^{-j2\pi f t} dt \tag{3.32}$$

The definition given in Equation 3.31 holds for signals of infinite length. In practice, autospectral density functions are often calculated by splitting the total length of the recorded signal T into n_d independent data segments of length T_d, and averaging the

discrete Fourier transforms of each portion as such

$$\hat{S}_{yy}(f) = \frac{2}{n_d T_d} \sum_{i=1}^{n_d} |Y_i(f, T_d)|^2 \tag{3.33}$$

Therefore, usually

$$E[\hat{S}_{yy}] \neq S_{yy} \tag{3.34}$$

The mean square error of the estimate $\hat{S}_{yy}$ can be calculated

$$\text{mse}[\hat{S}_{yy}] = E[(\hat{S}_{yy} - S_{yy})^2] = \text{Var}[\hat{S}_{yy}] + b^2[\hat{S}_{yy}] \tag{3.35}$$

where $\text{Var}[\hat{S}_{yy}]$ is the variance of the estimate[1] as defined by

$$\text{Var}[\hat{S}_{yy}] = E[(\hat{S}_{yy} - E[\hat{S}_{yy}])^2] \tag{3.36}$$

and $b[\hat{S}_{yy}]$ is the bias of the estimate as defined by

$$b[\hat{S}_{yy}] = E[\hat{S}_{yy}] - S_{yy} \tag{3.37}$$

For the sake of clarity, it is convenient to define the error of an estimate in terms of a fractional portion of the quantity being estimated. A normalised error can be computed by dividing the error by the quantity being estimated [115], i.e.

$$\text{normalised random error} = \varepsilon_r[\hat{S}_{yy}] = \frac{\sqrt{\text{Var}[\hat{S}_{yy}]}}{S_{yy}} = \frac{\sqrt{E[(\hat{S}_{yy})^2] - E[\hat{S}_{yy}]^2}}{S_{yy}} \tag{3.38}$$

$$\text{normalised bias error} = \varepsilon_b[\hat{S}_{yy}] = \frac{b[\hat{S}_{yy}]}{S_{yy}} = \frac{E[\hat{S}_{yy}]}{S_{yy}} - 1 \tag{3.39}$$

$$\text{normalised rms error} = \varepsilon[\hat{S}_{yy}] = \frac{\sqrt{E[(\hat{S}_{yy} - S_{yy})^2]}}{S_{yy}} \tag{3.40}$$

The following sections present formal definitions of the autospectral estimate error in terms of bias, variance and mean square error for two different conditions: measurements taken by fixed and moving transducers. In the case of a static measurement at a fixed position, these expressions are well known and the derivations below follow those of Bendat and Piersol [115]. However, the use of moving sensors implies that the signals recorded are acquired over a region of the space, introducing additional error in the autospectral estimates. From a theoretical point of view, the signal received from a

[1] Note that the square root of the variance is the standard deviation $\sigma(\hat{S}_{yy})$ of the estimator

moving microphone cannot be considered stationary in time and therefore the results of conventional Fouier analysis are not striclty valid. Nevertheless, according to Fahy [117] this fact does not have serious practical implications except at scan speeds "greatly in excess of 1 ms^{-1} in very complex intensity fields". Consequently, the novel definitions of the statistical errors proposed aim to establish the accuracy limits for scan-based measurement methods under such conditions.

3.4.2.1 Bias of the estimate

The bias of an estimate (in our case the autospectral density function) is the difference between the mean value given by the estimate and the true value of the function being estimated. When this difference vanishes, the estimate is considered unbiased. Figure 3.5 illustrates the bias error definition of an autospectral density function for a given bandwidth B.

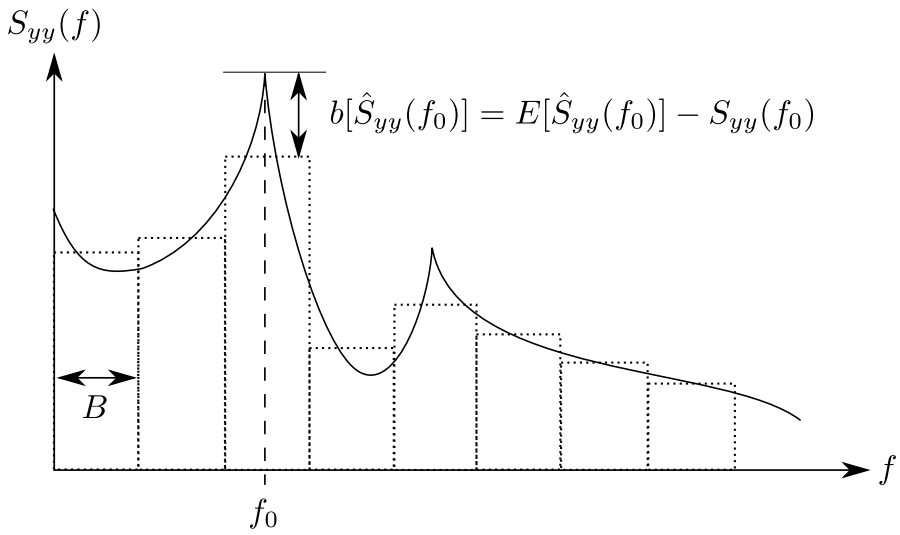

FIGURE 3.5: Illustration of the bias error introduced by the frequency band discretisation process of spectral density estimates.

Fixed position An approximate expression to describe the bias error can be derived by defining the true spectrum at $S_{yy}(f)$ about the frequency $f = f_0$ using a Taylor series expansion, retaining only the first three terms [115], i.e.

$$S_{yy}(f) \approx S_{yy}(f_0) + (f - f_0)\frac{\partial S_{yy}(f_0)}{\partial f} + \frac{(f - f_0)^2}{2!}\frac{\partial^2 S_{yy}(f_0)}{\partial f^2} \tag{3.41}$$

The estimated value of the spectrum can be obtained from the normalised integral of the area under the curve within a certain bandwidth B around the frequency of interest

f_0, hence

$$E[\hat{S}_{yy}(f_0)] \approx \frac{1}{B}\int_{f_0-B/2}^{f_0+B/2} S_{yy}(f)df \tag{3.42}$$

Substituting Equation 3.41 into Equation 3.42 leads to

$$E[\hat{S}_{yy}(f_0)] \approx S_{yy}(f_0) + \frac{B^2}{24}\frac{\partial^2 S_{yy}(f_0)}{\partial f^2} \tag{3.43}$$

Therefore, the bias term is approximated by the second derivative of the function inside the band, thus

$$b[\hat{S}_{yy}(f)] \approx \frac{B^2}{24}\frac{\partial^2 S_{yy}(f)}{\partial f^2} \tag{3.44}$$

According to [115], Equation 3.44 is an approximation of the bias error, which is suitable for cases where the product of the second derivative and the square bandwidth is lower than the value of the function at that particular frequency. Equation 3.44 will therefore exaggerate the degree of bias of the estimate because autospectra, in practice, frequently display sharp peaks, indicating large second derivatives. Nevertheless, it represents a useful first-order approximation that correctly describes important qualitative results.

Moving sensor A signal acquired with a moving sensor can be considered stationary over a suitable time providing that it moves at sufficiently low scanning speed. Such signal can be approximated using a generalised Taylor series expansion of the spectrum $S_{yy}(\mathbf{x}, f)$ about the position $\mathbf{x_0}$ and frequency f_0. Preserving the first three terms of the Taylor series and given that $\mathbf{Y} = \begin{bmatrix}\mathbf{x}\\ f\end{bmatrix}$ and $\mathbf{Y_0} = \begin{bmatrix}\mathbf{x_0}\\ f_0\end{bmatrix}$ yields

$$S_{yy}(\mathbf{Y}) \approx S_{yy}(\mathbf{Y_0}) + J(\mathbf{Y_0})(\mathbf{Y}-\mathbf{Y_0}) + \frac{1}{2!}(\mathbf{Y}-\mathbf{Y_0})^T H(\mathbf{Y_0})(\mathbf{Y}-\mathbf{Y_0}) \tag{3.45}$$

where $J(.)$ represents the Jacobian matrix and $H(.)$ is the Hessian matrix. As has been shown in Section 3.4.1, the mean of the autospectral estimate can be calculated using linear integration, providing the scanning speed is constant during the data acquisition process. Given that the sensor travels a distance Δ from the point $[x_0 - \Delta/2; y_0; z_0]$ to $[x_0 + \Delta/2; y_0; z_0]$ and the autospectral estimate is integrated over bandwidth B, then

$$\hat{S}_{yy}(\mathbf{Y_0}) = \frac{1}{B\Delta}\int_{x_0-\Delta/2}^{x_0+\Delta/2}\int_{f_0-B/2}^{f_0+B/2} S_{yy}(\mathbf{Y})df\,dx \tag{3.46}$$

Substituting with the generalised Taylor series expansion presented in Equation 3.45 gives

$$\hat{S}_{yy}(\mathbf{Y_0}) \approx S_{yy}(\mathbf{Y_0}) + \frac{1}{24}\begin{bmatrix}B^2\,\partial^2/\partial^2 f & \Delta^2\,\partial^2/\partial^2 x\end{bmatrix} S_{yy}(\mathbf{Y_0}) \tag{3.47}$$

Thus the bias term can be approximated by

$$b[\hat{S}_{yy}(\mathbf{Y})] \approx \frac{1}{24}\left[B^2\frac{\partial^2 S_{yy}(\mathbf{Y})}{\partial f^2} + \Delta^2\frac{\partial^2 S_{yy}(\mathbf{Y})}{\partial x^2}\right] \tag{3.48}$$

It is worth remarking on the similarities between the bias error previously presented for a fixed sensor (Equation 3.44) and the result now derived for moving transducers (Equation 3.48). Since frequency and spatial domains are both independent, the bias can be expressed as the sum of the errors induced by the discretisation process performed in each dimension, which is proportional to the second spatial and temporal derivative of the autospectrum.

3.4.2.2 Variance of the estimate

The variance of an estimate is an averaged measure of how far a set of realisations are spread out from the mean value. The autospectral density function is often calculated using a time averaging process of several data segments (Equation 3.31). Therefore, the variance will give an estimation of the variability between them. A graphical description of the variance error is shown in Figure 3.6.

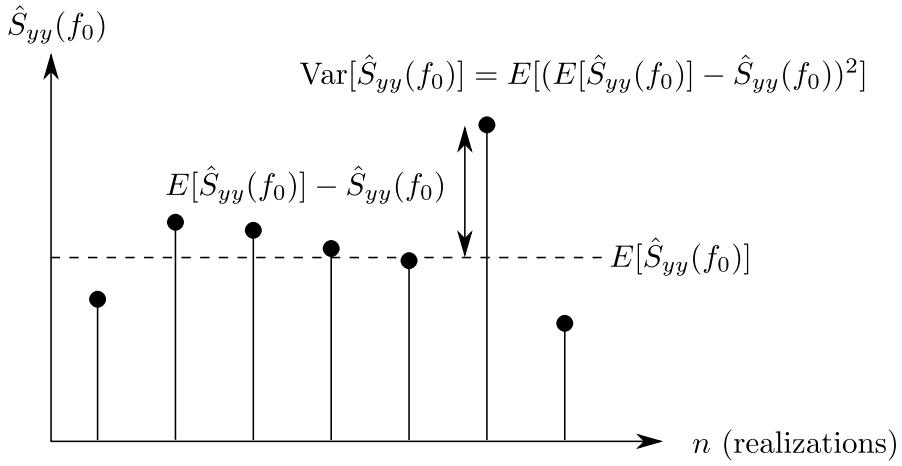

FIGURE 3.6: Illustration of the variance error introduced by averaging several data blocks for the calculation of spectral density estimates.

Fixed position The most direct way to obtain a variance expression for autospectral density estimates is through its relationship with the mean square value of the signal[2], i.e.

$$\hat{\psi}^2(f, B) = B\hat{S}_{yy}(f) \tag{3.49}$$

[2]A detailed derivation of mean square value estimates is given in Bendat and Piersol [115]

where $\hat{\psi}^2(f, B)$ is an unbiased estimate of the mean square value of $y(t)$ within the bandwidth B centred at f. The true value is given by $\psi^2(f, B) = BS_{yy}(f)$ when $S_{yy}(f)$ is constant over the bandwidth B. This will approximately be the case if B is sufficiently small. For a zero-mean process the variance of the mean square estimator can be defined as

$$\mathrm{Var}[\hat{\psi}^2] \approx \frac{\psi^4}{BT} \tag{3.50}$$

The substitution of Equation 3.49 into Equation 3.50 leads to

$$\mathrm{Var}[\hat{\psi}^2] = \mathrm{Var}[B\hat{S}_{yy}(f)] \approx \frac{B^2 S_{yy}^2(f)}{BT} \tag{3.51}$$

The definition of the variance, given in Equation 3.36, for a time invariant bandwith B results in the following relationship

$$\mathrm{Var}[B\hat{S}_{yy}(f)] = B^2 \mathrm{Var}[\hat{S}_{yy}(f)] \tag{3.52}$$

Thus, the combination of Equation 3.51 and Equation 3.52 gives an approximate expression for the variance of autospectral estimates

$$\mathrm{Var}[\hat{S}_{yy}(f)] \approx \frac{S_{yy}^2(f)}{BT} \tag{3.53}$$

Moving sensor The variance error of data acquired with a moving sensor can be derived by exploring the relationship between the mean square and the autospectral estimate. For a constant scanning speed, the mean square estimator $\hat{\psi}_c$ is defined by the temporal average of the recorded signal squared, i.e.

$$\hat{\psi}_c = \frac{1}{\Delta} \int_C y^2\left(\mathbf{x}(t), t\right)\, dS = \frac{1}{T} \int_0^T y^2(\mathbf{x}(t), t) dt \tag{3.54}$$

In this case, the variance definition (Equation 3.36) yields

$$\begin{aligned} \mathrm{Var}[\hat{\psi}_c] &= E[(\hat{\psi}_c - E[\hat{\psi}_c])^2] = E[\hat{\psi}_c^2] - E^2[\hat{\psi}_c] \\ &= \frac{1}{T^2} \int_0^T \int_0^T (E[y^2(\mathbf{x}(t_1), t_1) y^2(\mathbf{x}(t_2), t_2)]) dt_1 dt_2 - E^2[\hat{\psi}_c] \end{aligned} \tag{3.55}$$

The rather involved integrand presented above can be simplified by assuming that the signals perceived have a Gaussian distribution. If the random variables $y(\mathbf{x_1}, t_1)$ and

$y(\mathbf{x_2}, t_2)$ are jointly Gaussian, it can be shown that [112]

$$E[y^2(\mathbf{x}(t_1), t_1)y^2(\mathbf{x}(t_2), t_2)] = E[y^2(\mathbf{x}(t_1), t_1)]E[y^2(\mathbf{x}(t_2), t_2)] + 2E[y(\mathbf{x}(t_1), t_1)y(\mathbf{x}(t_2), t_2)]^2 - 2E[y(\mathbf{x}(t_1), t_1)]^2 E[y(\mathbf{x}(t_2), t_2)]^2 \tag{3.56}$$

It is now necessary to establish the relationship between the expectancy of the signal combinations and their equivalent statistical operators, i.e. the autocorrelation function

$$\hat{R}_{yy}(t_2 - t_1) = E[y(\mathbf{x}(t_1), t_1)y(\mathbf{x}(t_2), t_2)] \tag{3.57}$$

Assuming that $y(\mathbf{x}, t)$ is a random process with zero mean and substituting the relationships presented above leads to

$$\mathrm{Var}[\hat{\psi}_c] = \frac{1}{T^2}\int_0^T\int_0^T \Big(E[y^2(\mathbf{x}(t_1), t_1)]E[y^2(\mathbf{x}(t_2), t_2)] + 2\hat{R}^2_{yy}(t_2 - t_1))\Big)\, dt_1 dt_2 - E^2[\hat{\psi}_c] \tag{3.58}$$

Splitting the last expression into a set of integrals leads to

$$\begin{aligned}\mathrm{Var}[\hat{\psi}_c] = \frac{1}{T^2}\int_0^T E[y^2(\mathbf{x}(t_1), t_1)]dt_1 \int_0^T E[y^2(\mathbf{x}(t_2), t_2)]dt_2 \\ + \frac{1}{T^2}\int_0^T\int_0^T 2\hat{R}^2_{yy}(t_2 - t_1)dt_1 dt_2 - E^2[\hat{\psi}_c]\end{aligned} \tag{3.59}$$

The fist part of the last equation represents the estimator expectancy, therefore cancelling with the last term, hence

$$\mathrm{Var}[\hat{\psi}_c] = \frac{2}{T^2}\int_0^T\int_0^T R^2_{yy}(t_2 - t_1))dt_1 dt_2 \tag{3.60}$$

Next, it is possible to redefine the domain of integration by changing the integration variables

$$\mathrm{Var}[\hat{\psi}_c] = \frac{2}{T}\int_{-T}^T \left(1 - \left|\frac{\tau}{T}\right|\right) R^2_{yy}(\tau)d\tau \tag{3.61}$$

Considering the special case of bandwith-limited Gaussian white noise, the autospectral density function can be defined as

$$\hat{S}_{yy}(x(t), f) = \begin{cases} \frac{\hat{\sigma}^2}{B} & 0 \leq f \leq B \\ 0 & f > B \end{cases} \tag{3.62}$$

The autocorrelation function is then expressed as

$$\hat{R}_{yy}(\tau) = \int_0^\infty \hat{S}_{yy}(f)\cos(2\pi f\tau)df = \hat{\sigma}_y^2\left(\frac{\sin(2\pi B\tau)}{2\pi B\tau}\right) \tag{3.63}$$

Substituting the the autocorrelation function of band limited white noise into Equation 3.61 gives

$$\mathrm{Var}[\hat{\psi}_c] \approx \frac{\hat{\sigma}_y^4}{BT} \tag{3.64}$$

Finally, applying the relationship between the mean square and autospectrum estimates shown in Equation 3.49, Equation 3.64 can be formulated as such

$$\mathrm{Var}[\hat{S}_{yy}(\mathbf{Y})] \approx \frac{\hat{S}_{yy}^2(\mathbf{Y})}{BT} = \frac{(S_{yy}(\mathbf{Y}) + b[\hat{S}_{yy}(\mathbf{Y})])^2}{BT} \tag{3.65}$$

This equation is similar to the mean square variance expression derived for a fixed position. The main difference is caused by dependency upon the biased estimator.

3.5 Practical considerations

Despite the robustness of the theoretical foundations of any measurement technique, it is essential to follow a series of practical aspects in order to guarantee the quality of the data acquisition process. The understanding of the primary features related to the measurement protocol is undoubtedly helpful for achieving reliable results. This section covers the main practical considerations which should be understood in order to achieve an effective and successful experimental design using Scan & Paint. Practical aspects such as camera positioning, video frame rate selection, reference sensor capabilities, the error introduced by the manual movement of the probe and scanning speed are studied in this section.

3.5.1 Tracking camera

The proposed measurement technique uses a video camera to capture the location of the moving sensor. Therefore, one of the crucial steps during experiment preparation is the positioning of the camera. The usage of a single-lens imaging device has great advantages such as flexibility and usability; however, it also has a significant drawback for tracking: it constrains the spatial information to two dimensions, being unable to track movement along the camera axis. Consequently, the camera should be placed perpendicular to the measurement area to minimize the visual errors caused by the camera image projection.

The misalignment of the imaging device has an impact on calculations depending upon the discretisation method used, as it has been explained in Section 3.2. The lack of an automatic 3D tracking system can be compensated for by the knowledge and skill of the operator performing the measurements, who becomes responsible for the reliability of the results.

Additional visual aids, such a cross-laser, can be used if the measurement area intends to cover a planar slice of the sound field. Nevertheless, this is not the case for most practical scenarios, where a constant separation between the probe and the surface of the noise source under assessment is recommended to be maintained. If the surface curvature is too large, it may be convenient to split the total area into a subset of measurements using several camera positions, thus minimising visual errors (see Section 3.2.1).

The position of the probe in the video images is determined by localising a coloured marker attached to the probe with (automatic) colour tracking algorithms. Large measurement areas should be assessed using higher resolution settings in order to guarantee that a significant amount of pixels correspond to the probe marker. Alternatively, a bigger marker, such as a coloured wind screen, might be used to improve the robustness of the tracking process applied later.

The measurement area should be sufficiently lit to ensure that the probe's colour marker can be distinguished from other objects in the image. On the other hand, back-lighted measurement scenarios may overload the image sensor, reducing the video colour quality and ultimately hindering the probe tracking process.

Only the 2D location relative to the background image is computed automatically. For some tests where dimensions are important, such as sound power calculations (see Appendix A), it is required to establish the size of an image pixel. This can be undertaken by delimiting an object that appears at the measurement plane, such as the probe size or the height of the operator in the case of a large area, and defining its real size.

3.5.2 Video frame rate

As mentioned previously, a camera is used to film the scanning measurement. The recorded video is composed of a series of images, or frames, which are individually analysed to extract the position of the probe. The total number of frames per second, or video frame rate, can easily be adjusted to the user's preferences. This parameter can have a different effect depending on the spatial discretisation method which is later applied. The point discretisation method (see Section 3.2.2) associates a fixed time window for each tracked position, and thus each video frame. As a result, high video

frame rates require the calculation of a large number of data points, resulting in heavy computational effort and a lot of redundant data. A high frame rate likely implies that the tracking points are closely spaced. In that case, the use of the point discretisation method will suffer from redundant calculations, as there will be slight differences between each of the calculation points. In summary, the video frame rate should be set rather low (about 5 to 10 frames per second) to avoid the aforementioned problems. In contrast, the planar grid method (see Section 3.2.2) is unaffected by this parameter since it does not rely on the individual tracking points but the time interval within a region of space. Furthermore, the tracking data points are always interpolated up to a high rate to accurately determine the time in a cell.

3.5.3 Reference sensor

A fixed reference sensor can be used to preserve the phase information across the sound field. The location of the linking sensor should be a position close to the main excitation source within the measurement area covered in order to obtain as high coherence values as possible. Sound pressure microphones or particle velocity transducers are convenient references for most acoustic problems, whereas accelerometers or particle velocity sensors are more suitable for vibro-acoustic applications.

The use of a reference sensor enables the synchronisation of the measurement data in a relative sense via cross-spectral or transfer function estimates. The quality of these functions can be measured by assessing the coherence between the signals from the fixed and moving transducers. Therefore, high values of coherence ensure the reliability of the relative phase estimations. Sound sources that are only perceived at certain areas of the measurement plane or the presence of correlated sources is likely to result in coherence drops. In practice, the measurement conditions encountered for indoor scenarios limit the usage of a reference sensor. However, it is possible to quantify the quality of the relative phase acquired by computing the coherence of each data block, and thereby select the representative data acquired. Following [118], the linear coherence between any two measurement points x and y can be computed by dividing the cross-spectra by the product of the squared root of each individual auto-spectra, i.e.

$$\gamma_{xy}(\omega) = \frac{S_{xy}(\omega)}{\sqrt{S_{xx}(\omega)}\sqrt{S_{yy}(\omega)}} \tag{3.66}$$

It should be noted that Equation 3.66 contains the phase of the cross-spectrum but it is usually the modulus that is of interest.

A static sensor can be also used to verify that the sound field is stationary[3]. The

[3] A temporal variability indicator is given in Appendix A

evaluation of the spectrogram of a fixed reference transducer permits the tracking of unexpected acoustic changes during the acquisition process. This information can be used to exclude time intervals from the calculations which do not meet the stationary requirements. In addition, for the particular case of rotating machinery, the spectrogram can also be used to control the working regime, ensuring that the measurement is performed with a constant rotational speed.

3.5.4 Manual scanning error

The scan-based sound mapping system proposed relies on video tracking to extract the position of the probe during measurements. Despite its flexibility and simplicity, the use of a single camera limits the tracking capabilities to the image space, a two dimensional spatial domain. This indirectly implies that the probe movement along the camera axis is untraceable and the distance between the probe and the radiating surface is unknown. Consequently, manual imprecisions introduces an error to the perceived spectral level. Although there are alternative tracking systems available which do not have those limitations, they do have other disadvantages such as their high cost, complex setup and unsuitability for many applications.

The influence of the positioning error caused by the user can be studied by asessing a point source model. The following expressions define the sound pressure and particle velocity modulus at a given distance r from a source of amplitude A considering certain position inaccuracy ϱ

$$|\hat{p}| = \frac{A}{r+\varrho} \tag{3.67}$$

$$|\hat{u}_r| = \frac{A}{\omega\rho(r+\varrho)}\left(k^2 + \frac{1}{(r+\varrho)^2}\right)^{1/2} \tag{3.68}$$

The derivation of expressions which describe how the above equations differ from an ideal measurement can be used to define the impact of the distance error introduced. Firstly, for the pressure

$$|\hat{p}| = \frac{A}{r+\varrho} = \frac{A}{r} + \frac{-A\varrho}{r(r+\varrho)} = |p| + |\hat{p}|_e \tag{3.69}$$

where $|\hat{p}|$ is an estimate of $|p|$ with an error represented by the term $|\hat{p}|_e$ of which the normalised version can be expressed by

$$\frac{|\hat{p}|_e}{|p|} = \frac{-\varrho}{r+\varrho} \tag{3.70}$$

On the other hand, the same procedure can be applied to the measured particle velocity in order to find the relationship between the estimator $|\hat{u}_r|$ and the real value $|u_r|$, thus

$$|\hat{u}_r| = \frac{A}{\omega\rho}\frac{1}{r+\varrho}\left(k^2+\frac{1}{(r+\varrho)^2}\right)^{1/2} = \frac{A}{\omega\rho r}\left(k^2+\frac{1}{r^2}\right)^{1/2} + \frac{A}{\omega\rho}\left(\frac{\sqrt{k^2+1/(r+\varrho)^2}}{r+\varrho} - \frac{\sqrt{k^2+1/r^2}}{r}\right) = |u_r| + |\hat{u}_r|_e \tag{3.71}$$

therefore $|\hat{u}_r|$ is a estimate of $|u_r|$ with a normalised error term $|\hat{u}_r|_e$ associate with the non dimensional quantities kr and ϱ/r as such:

$$\frac{|\hat{u}_r|}{|u_r|} = \frac{1}{(1+\varrho/r)^2}\sqrt{\frac{(kr)^2(1+\varrho/r)^2+1}{(kr)^2+1}} - 1 \tag{3.72}$$

These definitions offer a useful measure of the positioning error produced when the sensor is moved away from the expected location. It is generally more convenient to represent the estimation error relative to the quantity being estimated, as defined in Equation 3.39. Figure 3.7 illustrates how both quantities change for a harmonic excitation of 500 Hz depending on the distance to the sound source r and the positioning error ϱ. The blue and red shaded areas show the range where the error is defined. However, it is more representative to study the average error introduced (solid lines) since the distance to the source will vary during the measurement and several data segments will be averaged (see Section 3.2).

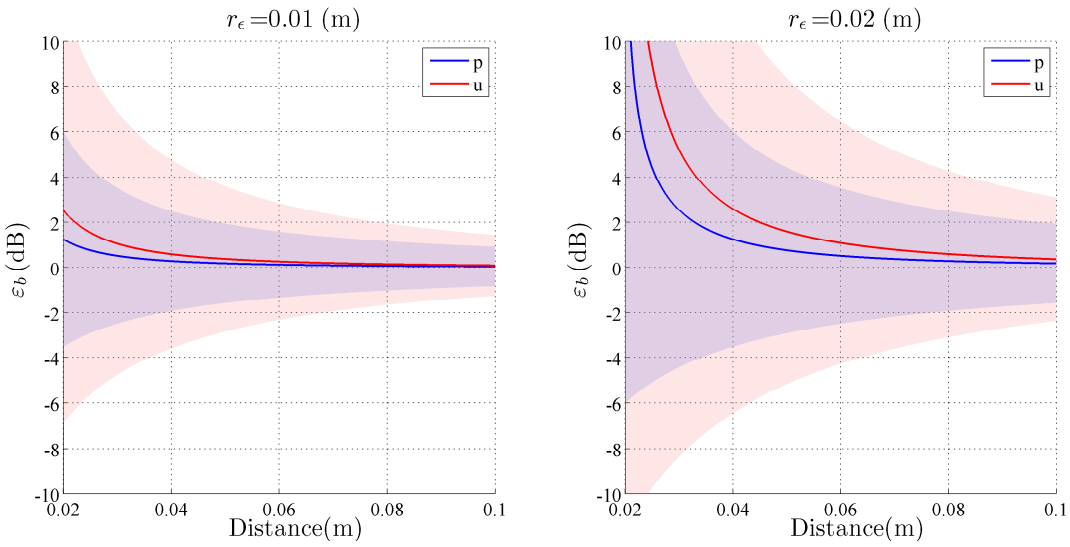

FIGURE 3.7: Average estimation error (solid lines) and error intervals (shaded areas) introduced in the spectral estimates when the positioning error fluctuates by 0.01 (left) and 0.02 (right) metres for a harmonic excitation of 500 Hz.

It is apparent from these results that the average error becomes critical when the measurements are performed very close to the excitation point. It is also shown that the positional error is higher for particle velocity than for pressure measurements, mainly due to the larger level differences when measurements are performed in the vicinity of the sound source. Nonetheless, as is shown in the following chapter, the large dynamic range of the perceived normal particle velocity causes particle velocity colour maps to be proportionally less affected by the manual error than pressure maps for source localisation purposes.

Basically, the average error becomes insignificant when data is acquired at a distance from the source larger than 0.04 metres, providing the position error due to the manual movement of the probe is approximately 0.01 metres. It should be emphasised that the point source model utilised in the derivation represents a simple theoretical approach but, in practice, the level difference is less severe in the near-field of real sources (especially for industrial machinery), as is the estimation error.

As shown in Equation 3.72, the estimation error of the particle velocity is frequency dependent, it grows slightly at lower frequencies. Figure 3.8 shows the influence of spectral estimation upon an arbitrary signal when the distance fluctuates by 0.01 m (left) and 0.02 m (right). As it can be seen, the error range is fairly constant across the whole spectrum, proving that the increase in error at lower frequencies has a minor effect on the overall results.

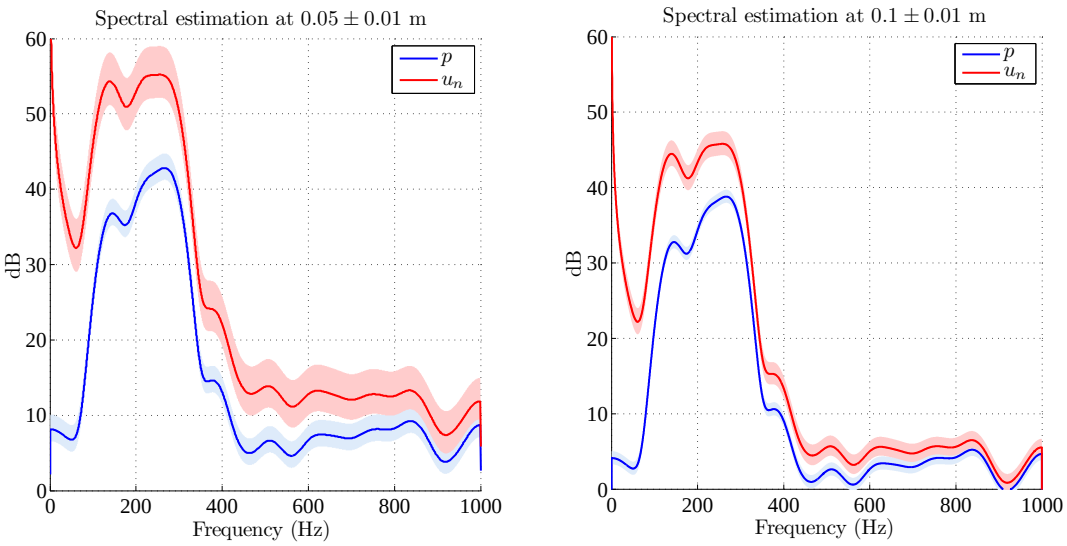

FIGURE 3.8: Average spectra (solid lines) and error intervals (shaded areas) introduced in the spectral estimates of measurements performed at 0.05 m (left) and 0.1 m (left) with a 0.01 m positioning error.

3.5.5 Scanning speed

The velocity of a sensor during a scanning measurement has an impact upon the accuracy[4] and spectral resolution[5] of the sound maps produced later. Assuming that non-linear Doppler shift can be disregarded for low scanning speeds (see Section 3.3.1), the influence that speed has on the measurement results mainly depends upon the discretisation method applied. For Scan & Paint, two different discretisation techniques are studied: the point method and the planar grid method. To evaluate how the scanning speed affects the two methods it can be started by defining two average speeds $\mathbf{v}$ and $\mathbf{v}'$, related by a factor β as such

$$\mathbf{v}' = \beta\mathbf{v} = \frac{1}{T'}\int_0^{T'} \left|\frac{\partial \mathbf{x}(t)}{\partial t}\right| dt \tag{3.73}$$

For the grid discretisation method (see Section 3.2.1), the length of a signal segment depends upon the position of the probe, i.e. for how long the probe is moved inside one grid cell. Therefore, increasing speed reduces the time within a grid cell. Recalling the definition of the autospectral density estimate given in Equation 3.33, the length of each time segment is divided into n_d sub-records, for which Fourier Transforms are later averaged. A relationship between the spectral resolution and the time length of the signal segments can be established as

$$B = \frac{1}{T_d} = \frac{n_d}{T} \tag{3.74}$$

where T_d denotes the time length of each block used in the autospectral calculations. The preservation of a constant spectral resolution, thus a fixed bandwith B, reduces the number of averages when the speed is doubled ($n'_d = n_d/\beta$). From Equation 3.65 and Equation 3.74 can be inferred that the variance of spectral estimates is inversely proportional to the number of averages n_d. Hence, the variance error of the autospectral estimate grows as the speed is increased.

On the other hand, the use of the point discretisation method (see Section 3.2.2) associates a fixed time window to each tracked position. Hence, the time length of each segment analysed is independent of sensor velocity during the measurement. Nonetheless, the speed determines the distance between tracking points. This has a direct impact on the bias error of the autospectral estimation since data representing one fixed position is gathered along the path followed by the moving sensor. According to the derivation

[4]In the literature, Jacobsen analysed the error introduced by different scanning speeds in the determination of sound power, concluding that it is recommeded that $v/c << B/f_0$ [119].

[5]It is worth to emphasising the difference between spectral and spatial resolution: while the former is the ability to distinguish two closely spaced spectral components, the latter is the ability to identify two sound sources in space

given in Section 3.4.2.1, the bias will depend upon the second spatial derivative of the sound field multiplied by the square of the distance travelled along the tracking path. Thus, the faster the probe is moved, the larger the bias.

In conclusion, Table 3.1 presents a brief summary of the influence of speed on both discretisation methods. As shown the variance error of the grid method is directly proportional to an increase in speed. In contrast, for the point method it is the bias error which strongly increases as the scanning transducer is moved faster.

TABLE 3.1: Summary of the effects of the scanning speed on the two discretisation methods for a fixed spectral bandwidth.

	Time length	Averages	Spectral error
Grid Method	$T' = T/\beta$	$n'_d = n_d/\beta$	$\mathrm{mse}'[\hat{S}_{yy}] \approx b^2[\hat{S}_{yy}] + \beta \mathrm{Var}[\hat{S}_{yy}]$
Point Method	$T' = T$	$n'_d = n_d$	$\mathrm{mse}'[\hat{S}_{yy}] \approx \beta^4\, b^2[\hat{S}_{yy}] + \mathrm{Var}[\hat{S}_{yy}]$

3.6 Summary

The theoretical foundations of the scanning sound visualisation method "Scan & Paint" have been presented. The mathematical formulation is given along with the implementation of two different spatial discretisation methods: the planar grid method and the point method.

Several fundamental principles common to all scan-based techniques have been investigated. The assessment of the Doppler effect and the time-domain formulation of the sound field perceived by a moving sensor provide a detailed description of scanning measurement techniques.

Statistical considerations for the data analysis process have been studied exhaustively, introducing novel analytical expressions for the bias and variance error of scanning measurements. The derivation proposed allows for a quantitative assessment of the spectral estimation error depending upon the measurement conditions.

In addition, multiple practical considerations regarding the tracking camera, reference sensor, scanning speed and manual errors have also been presented.

Chapter 4

Sound mapping applications

4.1 Introduction

Sound visualisation is a powerful tool for investigating a great variety of acoustic and vibro-acoustic problems. As shown in this chapter, the direct mapping of acoustic quantities, obtained by means of scan-based methods, provides a simple and effective approach to solve a wide range of problems. The direct acquisition of sound pressure and particle velocity enables extensive analysis of any sound field without traditional frequency constraints imposed by most inverse methods.

This chapter explores the use of sound pressure and normal particle velocity for source localisation purposes. The influence of background noise, the spatial resolution properties and the usability of the resulting sound maps are studied from a theoretical and practical point of view. In addition, three dimensional vector field mapping of sound intensity is introduced. Several examples have been evaluated to demonstrate the capabilities of Scan & Paint as a flexible and efficient sound visualisation method for a wide range of applications.

4.2 Near-field source localisation

One of the main challenges arising from noise and vibration problems is how to identify the areas of a device, machine or structure that produce significant acoustic excitation, i.e. the localisation of main noise sources. Many techniques can provide an accurate answer if the geometry is known and the testing process is undertaken in a controlled environment such as an anechoic chamber. Nevertheless, conventional pressure-based

source localisation methods often require more elaborate, and ultimately more expensive, systems to study complex scenarios, without necessarily guaranteeing accurate results. This is especially true for low frequency problems, when there are multiple noise sources or for measurements performed in a reverberant environment. Theoretical simplifications may not be viable for unfavourable scenarios, possibly leading to ambiguous results. In contrast, the direct visualisation of normal acoustic particle velocity is a robust approach to locate sound sources regardless of frequency range or the reverberation of the measurement environment [16, 19, 120].

The following sections explore the main characteristics of acoustic sensors for source localisation purposes, such as their signal-to-noise ratio in the presence of background noise and the ability to distinguish closely spaced sound sources. For the sake of clarity, a frequency domain analysis is used assuming harmonic excitation; however, the sources of errors discussed in Chapter 3 still apply. Furthermore, some practical examples of acoustic mapping are shown, demonstrating the theoretical principles introduced.

4.2.1 Influence of background noise on sound mapping

Sound visualisation techniques often encounter difficulties adapting from controlled experiments to industrial application cases. Laboratory tests are helpful to prove theoretical concepts and demonstrate novel technologies, but the measurement conditions are usually favourable and far different from those in regular industrial scenarios. In most real applications the presence of background noise reduces signal-to-noise ratio, increasing the estimation error, ultimately limiting the capabilities for resolving noise sources accurately. Therefore, it is necessary to determine the impact of extraneous noise sources upon the two fundamental acoustic quantities: sound pressure and particle velocity. In this section, the influence of the background noise is studied by exploring three main concepts: the sound levels perceived close to a sound source, the noise reduction achieved with a directive sensor and the sound field produced in the proximity of a rigid surface.

4.2.1.1 Sound emission

The impact of background noise is relative to the signal emitted by the device under assessment. Near a sound source, the particle velocity level is usually higher than the sound pressure level. This discrepancy is commonly described by their ratio, i.e. acoustic impedance. For a point source in free field, the acoustic impedance can be defined as [121]

$$Z_{point} = \frac{p}{u_r} = \rho\, c \left(\frac{jkr}{jkr + 1} \right) \tag{4.1}$$

where ρ is the air density, c is the speed of sound in air, k is the acoustic wavelength and r is the distance from the source to the measurement position. For far field conditions ($kr >> 1$), Equation 4.1 becomes the characteristic acoustic impedance of the medium ($\rho\, c$). However, the influence of the imaginary part grows as the distance to the source is reduced, introducing a phase shift between sound pressure and particle velocity. The above expression can also be formulated in terms of levels[1], i.e.

$$L_u \approx L_p + 20 \log \left(\left| 1 + \frac{1}{jkr} \right| \right) \tag{4.2}$$

where L_u and L_p are the acoustic particle velocity and sound pressure level, respectively. Since wavenumber k and source distance r are both positive in this case, Equation 4.2 shows that the particle velocity level produced by a point source is always larger than the sound pressure level, particularly when $kr < 1$, in the near field.

There are other expressions to model the acoustic behaviour of different sound sources. In the case of a circular piston mounted in an infinite baffle, the on-axis impedance can be expressed as [122]

$$Z_{piston} = \frac{\rho\, c \left(1 - e^{-2j\gamma}\right)}{1 - \alpha e^{-2j\gamma}} \tag{4.3}$$

where a is the radius of the piston and

$$\alpha = \frac{r}{\sqrt{a^2 + r^2}} \quad , \quad \gamma = k \frac{\sqrt{a^2 + r^2} - r}{2} \tag{4.4}$$

An alternative expression can be used to model a point source encapsulated in a rigid sphere. In practice, this can be achieved by creating a small hole in a hollow rigid sphere driven by a loudspeaker inside it [123]. The on-axis specific acoustic impedance can be defined as [124]

$$Z_{MonopoleB} = -j\rho c \frac{\sum_{m=0}^{\infty} (m + 1/2) \frac{h_m(kr)}{h'_m(kb)}}{\sum_{m=0}^{\infty} (m + 1/2) \frac{h'_m(kr)}{h'_m(kb)}} \tag{4.5}$$

where b is the radius of the sphere, h_m is the spherical Hankel function of the second kind and order m, and h'_m is its derivative. In addition, a piston source can also be enclosed inside a rigid sphere, leading to the following on-axis impedance expression [125]

$$Z_{sphere} = -j\rho c \frac{\sum_{m=0}^{\infty} (P_{m-1}(\cos\beta) - P_{m+1}(\cos\beta)) \frac{h_m(kr)}{h'_m(kb)}}{\sum_{m=0}^{\infty} (P_{m-1}(\cos\beta) - P_{m+1}(\cos\beta)) \frac{h'_m(kr)}{h'_m(kb)}} \tag{4.6}$$

[1]It should be noted that the standard reference sound pressure is 20 μPa whereas the reference particle velocity is 50 nm/s. The ratio between them approximately equals the characteristic acoustic impedance, i.e. $\rho c \approx p_{ref}/u_{ref}$

where $\beta = \sin^{-1}(a/b)$, b is the radius of the sphere, a is the radius of the loudspeaker, P_m is the Legendre function of the order m.

The level differences between sound pressure and normal particle velocity can be estimated using the aforementioned acoustic impedance expressions. These models provide a good approximation of the acoustic behaviour perceived in the vicinity of a sound source although, in practice, more aspects should also be considered, such as complex surfaces, evanescent waves or edge effects.

Since particle velocity level tends to be higher than sound pressure, the inverse form of the acoustic impedance, i.e. the acoustic admittance, is represented instead. Figure 4.1 shows the simulation results for measurement distances of 0.02 m and 0.04 m, a piston radius of 0.0375 m (3 inch speaker), and a sphere radius of 0.05 m.

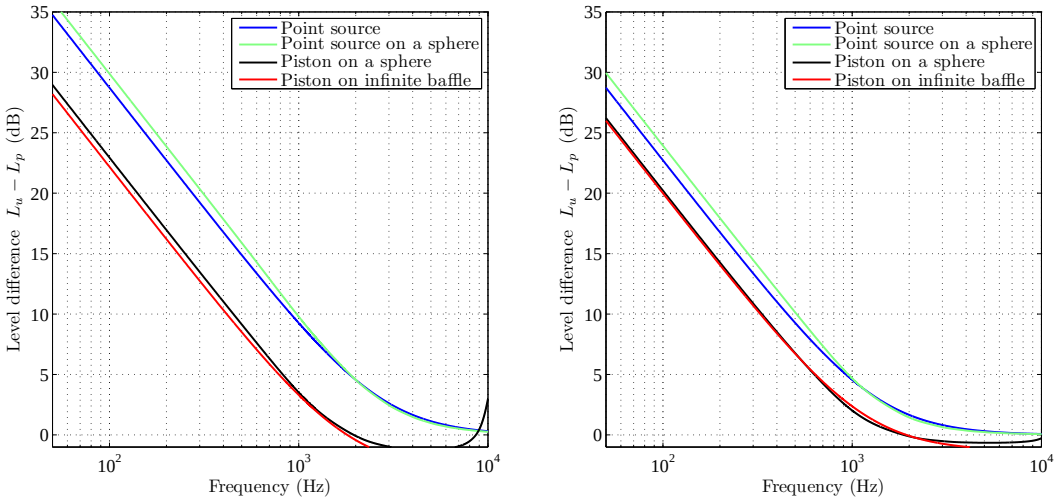

FIGURE 4.1: Difference between normal particle velocity and sound pressure levels at 0.02 m (left) and 0.04 m (right) away from a sound source

As can be seen, the level difference between sound pressure and normal particle velocity is significant in the acoustic near field. The admittance grows proportionally to the source distance and wavelength, the kr product. Therefore, the high particle velocity level perceived in near field conditions gives particle velocity transducers an advantage over sound pressure microphones for source localisation.

4.2.1.2 Sensor directivity

The directional properties of a sensor are linked to the measurement signal-to-noise ratio. Free-field and pressure microphones have a sensitivity response which is not dependent upon the direction of arrival of the incident sound, i.e. they have an omni-directional

directivity pattern. On the other hand, particle velocity transducers are equally sensitive to sound arriving from the front or back, but are insensitive[2] to sound arriving from the sides, following a figure-of-eight directivity pattern.

Directivity can be a useful feature for sound source localisation if the sensor is aimed appropriately. The transducer can be steered towards an area of interest to maximise the sound perceived from the aimed direction. For industrial applications, the long reverberation time and the presence of multiple disturbance sources causes the background noise to be distributed fairly homogeneously. As a result, there is an equal probability of sound waves arriving from any direction, condition that precisely defines a "diffuse" sound fields.

Assuming that there are uncorrelated plane waves of equal power arriving at the sensor from all directions, the temporally averaged variance $\overline{\sigma_s^2}$ of the signal output can be calculated by integrating the individual contributions from all directions weighted by the directivity pattern $D(\theta, \phi)$, i.e.

$$\overline{\sigma_s^2} = \int_0^{\pi} \int_0^{2\pi} \overline{\sigma_{PW}^2} D^2(\theta, \phi) \sin(\theta)\, d\phi\, d\theta \tag{4.7}$$

where θ and ϕ denote azimuth and elevation angles, respectively. For an omni-directional microphone with unitary gain, Equation 4.7 simplifies to

$$\overline{\sigma_{omni}^2} = \int_0^{\pi} \int_0^{2\pi} \overline{\sigma_{PW}^2} \sin(\theta)\, d\phi\, d\theta = 4\pi \overline{\sigma_{PW}^2} \tag{4.8}$$

On the other hand, the figure-of-eight directivity pattern of a particle velocity transducer can be modelled using the function $cos(\theta)$. Substituting this term into Equation 4.7 leads to

$$\overline{\sigma_{dipole}^2} = \int_0^{\pi} \int_0^{2\pi} \overline{\sigma_{PW}^2} \cos^2(\theta) \sin(\theta)\, d\phi\, d\theta = \frac{4}{3}\pi \overline{\sigma_{PW}^2} \tag{4.9}$$

The ratio between Equation 4.8 and Equation 4.9 defines the effect caused by the directivity in the variance of output signal, thus

$$\overline{\sigma_{dipole}^2} / \overline{\sigma_{omni}^2} = 1/3 \tag{4.10}$$

The result presented in Equation 4.10 is in agreement with an alternative derivation introduced in [127]. It shows that, in a diffuse sound field, where uncorrelated wave-fronts arrive homogeneously from all directions, omnidirectional microphones capture three

[2]In practice, particle velocity sensors attenuate the sound arriving at the less sensitive direction for about 50 dBs. [126]

times more energy than transducers with a figure-of-eight directivity pattern. Consequently, the directivity of particle velocity sensors acts as a spatial filter which reduces 66% of the background noise. In terms of sound level, it results in approximately 5 dB improvement in the noise floor of the measurement data.

4.2.1.3 Background noise perceived near a rigid boundary

The signal-to-noise ratio plays a key role in the accuracy of acoustic emission estimations. In the absence of background noise, sound pressure and acoustic particle velocity are generally high close to the vibrating areas of a structure, whereas the level is strongly reduced near the rigid sectors. In such a way, the dynamic range is maximised between vibrating and non-vibrating areas. Nonetheless, industrial machinery is often surrounded by other devices which cannot be removed or silenced during the acoustic test. Furthermore, the emitted acoustic energy will be partially reflected back, acting as an additional set of partially correlated sources. The signal-to-noise ratio is therefore greatly reduced, as is the quality of the experimental data. The background noise effectively limits the dynamic range of the sound maps, masking weak sources. It is then desirable to minimise its influence in order to avoid errors in locating the noise emission points.

The sound field produced near a rigid boundary has been simulated to study the impact of background noise upon both sound pressure and normal particle velocity. The rigid surface represents a non-vibrating and fully reflective part of a device, whilst a source produces noise that disturbs the measurements. As it has been mentioned above, the level close to a non-moving surface should be as low as possible to maximize the dynamic range of the sound map. Figure 4.2 presents a contour plot of the spatial distribution of sound pressure (A) and normal particle velocity[3] (B) levels for a harmonic excitation of 1 kHz.

This simulation shows that the pressure level close to a rigid surface is always high. Incident and reflected sound pressure waves sum coherently resulting in reinforcements close to the boundary. This effect can cause ambiguous results since high levels could be interpreted as radiated sound from the machinery instead of reflected sound from a external source.

On the other hand, Figure 4.2 shows that the normal particle velocity field is minimised close to the rigid boundary. In contrast to sound pressure, particle velocity is a vector quantity with an associated direction. Consequently, the incident and reflected wavefronts will have a 180 degrees phase shift, cancelling each other out and creating a

[3]The acoustic particle velocity displayed is normal to the x-axis, where the rigid surface is defined.

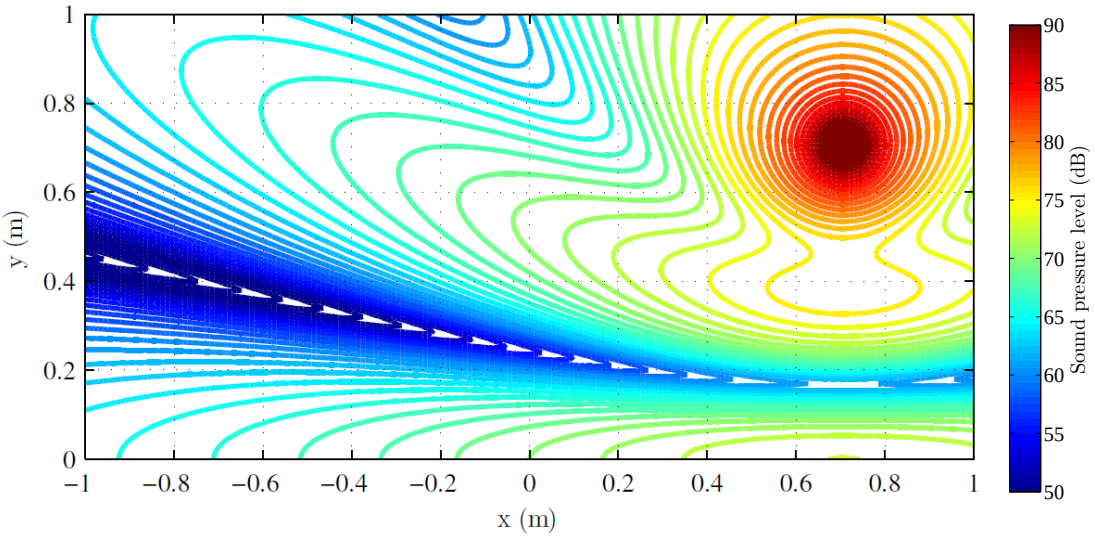

(A) Sound pressure

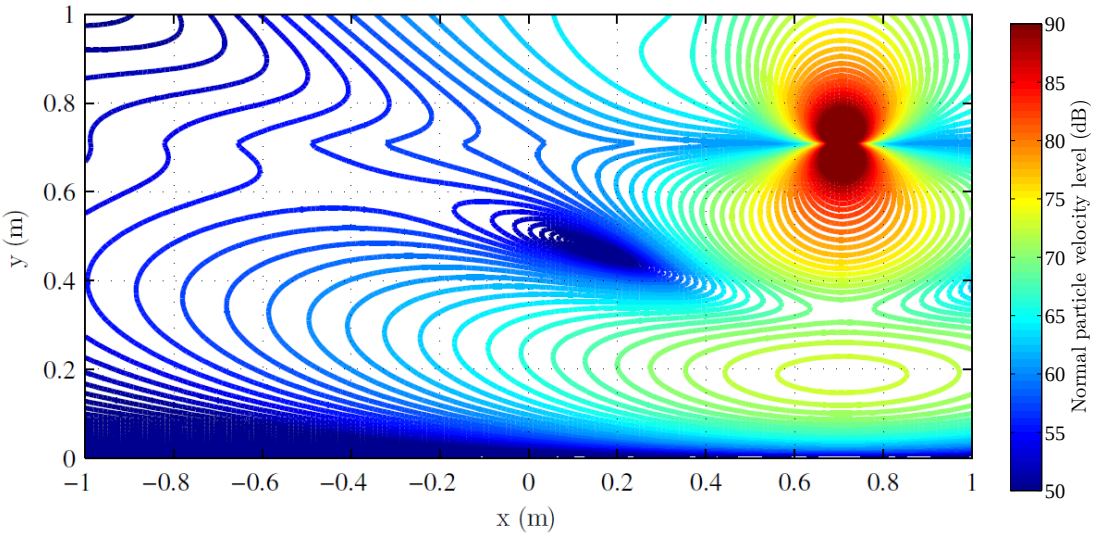

(B) acoustic particle velocity y-component

FIGURE 4.2: Spatial distribution of the sound pressure and normal particle velocity produced by a point source at 1 kHz with a rigid boundary located at $y = 0$.

particle velocity minima. This effect is useful for source localisation purposes because the influence of background noise will be significantly reduced if measurements are performed sufficiently close to a rigid surface.

The region where normal particle velocity measurements achieve a substantial reduction of background noise is determined by the wavelength and location of the noise source. Figure 4.3 presents the level difference[4] between the sound pressure and normal particle velocity measured along the y axis with a noise source at one metre distance from the surface and 45° (left) and 90° (right) angles of incidence[5].

[4]The quantity displayed is equivalent to the specific acoustic impedance level using ρc as reference.

[5]Following the nomenclature used in Section 4.2.1.1, the sound field was calculated for $x = 0$ and $x = 1$

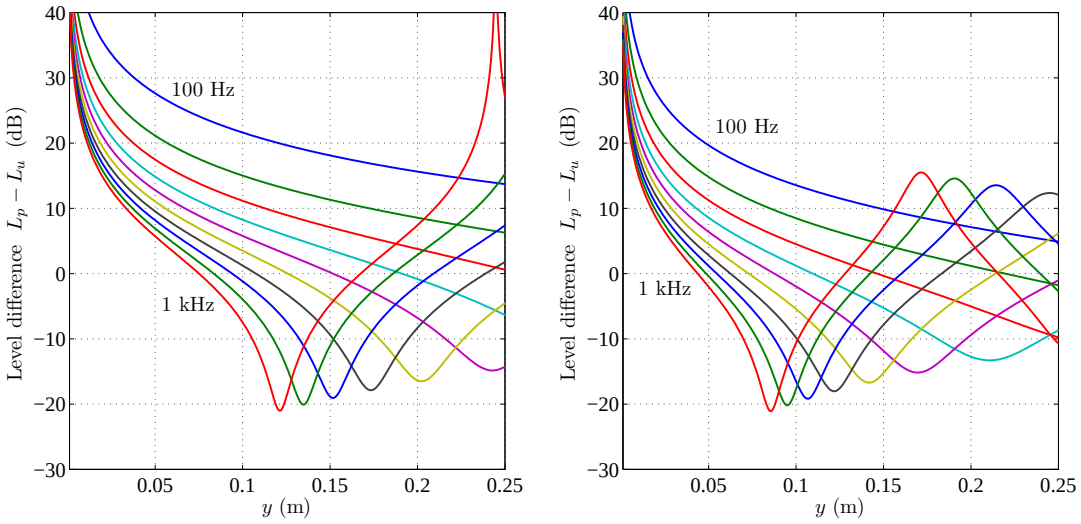

FIGURE 4.3: Difference between sound pressure and normal particle velocity levels produced by a noise source with a 45° (left) and 90° (right) angles of incidence.

These figures give quantitative information about how noise generated by external sources can be reduced if particle velocity transducers are used instead of sound pressure microphones. As shown, the main benefit appears at the lower frequency range, where the minimisation achieved is higher. At mid and high frequencies it is necessary to measure as close as possible to ensure a reduction in background noise, and to avoid measuring in a region of minimum normal particle velocity. In addition, further investigation should be undertaken in order to clarify the effect of measuring close to non-rigid materials.

4.2.2 Spatial resolution of direct mapping methods

The selection of an appropriate measurement distance is crucial to accurately determine the location of a noise source. This section details the resolution properties of both sound pressure and particle velocity mapping procedures in the vicinity of a source. The sound field generated by a harmonic point source can be defined as [117]

$$p(r,t) = \frac{A}{r}\, e^{j(\omega t - kr)} \tag{4.11}$$

$$u_r(r,t) = \frac{A}{\omega \rho r}\left(k - \frac{i}{r}\right) e^{j(\omega t - kr)} \tag{4.12}$$

where $p(r,t)$ and $u_r(r,t)$ are the sound pressure and radial particle velocity, respectively; A is determined by the point source features[6], r is the distance to the source, k is the wavenumber and ω is the angular frequency. Taking the absolute value of the previous

[6] A detailed description of this variable is later given in Chapter 6

expressions yields

$$|p| = \frac{|A|}{r} \tag{4.13}$$

$$|u_r| = \frac{|A|}{\omega\rho r}\left(k^2 + \frac{1}{r^2}\right)^{1/2} \tag{4.14}$$

Sound intensity probes enable the acquisition of a one dimensional particle velocity vector component, namely the projection of the radial velocity u_r on the normal sensor axis. Using Equation 4.14, the normal component of particle velocity can be defined as

$$|u_n| = \sin(\theta)\cos(\varphi)\,|u_r| = \sin(\theta)\cos(\varphi)\frac{|A|}{\omega\rho r}\left(k^2 + \frac{1}{r^2}\right)^{1/2} \tag{4.15}$$

where θ and φ are azimuth and elevation angles, respectively. Figure 4.4 gives an illustration of the relationship between radial and normal particle velocity components caused by the source $S_0(\mathbf{x_0})$.

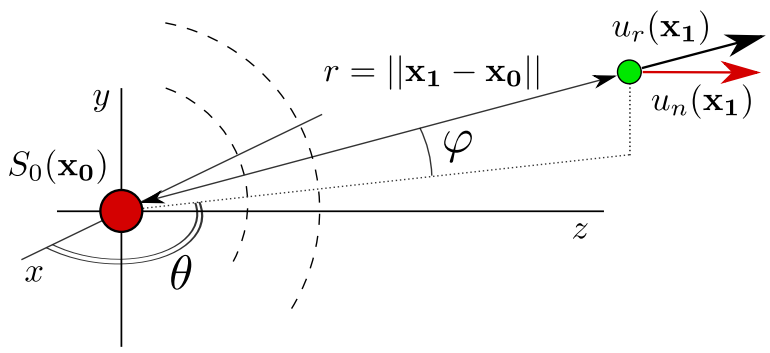

FIGURE 4.4: Projection of the radial particle velocity on the normal sensor axis.

The spatial resolution of a sound localisation method determines the ability to distinguish two closely spaced noise sources. It can be considered as the closest distance between sources which guarantees that the power between them halves, ensuring a signal to noise ratio of at least 3 dB. The superposition principle states that the total acoustic fluctuation caused by multiple sound sources can be calculated by summing the modulus of the individual contributions, providing the sources are uncorrelated. Therefore, the sound field produced by several uncorrelated sources can be simulated by implementing Equation 4.13 and Equation 4.15 and applying this principle. Figure 4.5 presents a simulation of the sound pressure and normal particle velocity field generated by two uncorrelated monopole sources excited at 500 Hz in free field conditions and separated by 0.2 metres. As can be seen in this example, there are large level differences between sound pressure and normal particle velocity in the near field, which has a significant impact in the resolution of both quantities.

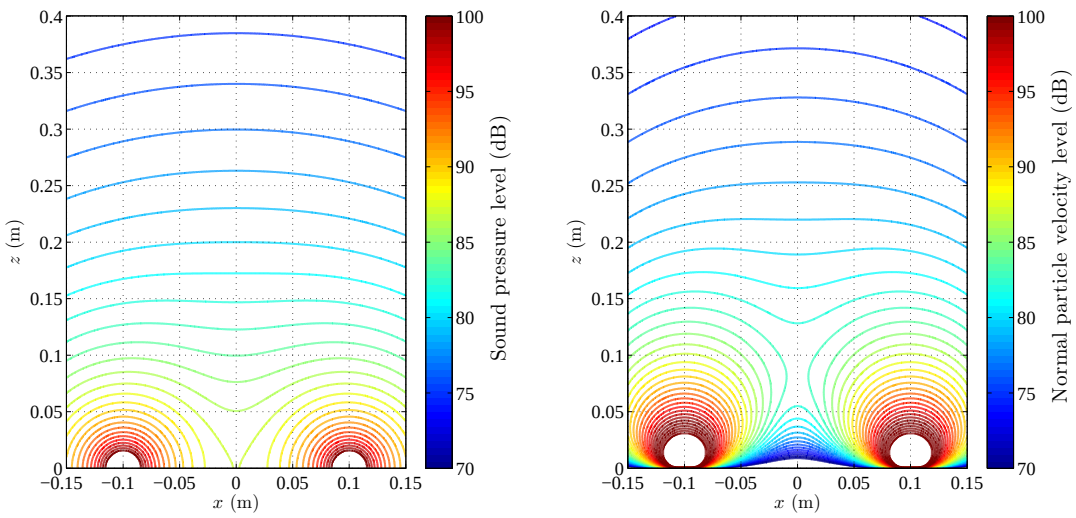

FIGURE 4.5: Sound field generated by two incoherent point sources in terms of sound pressure (left) and normal particle velocity (right)

The sound level perceived at a certain distance d along the z axis[7] is displayed in Figure 4.6. It is shown how the normalised sound pressure (left) and normal particle velocity (right) vary on the measurement plane. These results demonstrate that there is a substantial difference in dynamic range between both acoustic quantities. Large normal particle velocity level variations allow for resolving closely spaced sources, especially when measurements are performed near the source plane. Consequently, large level variations are an advantage of using particle velocity transducers for source localisation purposes in the near-field.

The relationship between a measurement distance d and a resolution distance D_r (the minimum separation at which sources are distinguishable) establishes the precise limitations of near-field mapping methods. Given a free-field scenario with two uncorrelated point sources located at $(-D_r/2, 0, 0)$ and $(D_r/2, 0, 0)$, the assessment of the resulting sound field will lead to an expression for the spatial resolution. Firstly, the resolution of near-field sound pressure mapping can be derived using Equation 4.13 given the condition that the total excitation decreases by half at the midpoint $(0, 0, d)$ located on the measurement plane Ω_h, yielding the following expression

$$\left(\frac{A}{d}\right)^2 + \left(\frac{A}{\sqrt{d^2 + D_r^2}}\right)^2 = 4\left(\frac{A}{\sqrt{d^2 + D_r^2/4}}\right)^2 \tag{4.16}$$

[7]The separation d denotes the distance between a plane containing the sources Θ and a parallel measurement plane Ω_h. It is defined by the Euclidean norm between them, such as $d = ||\Theta - \Omega_h||$.

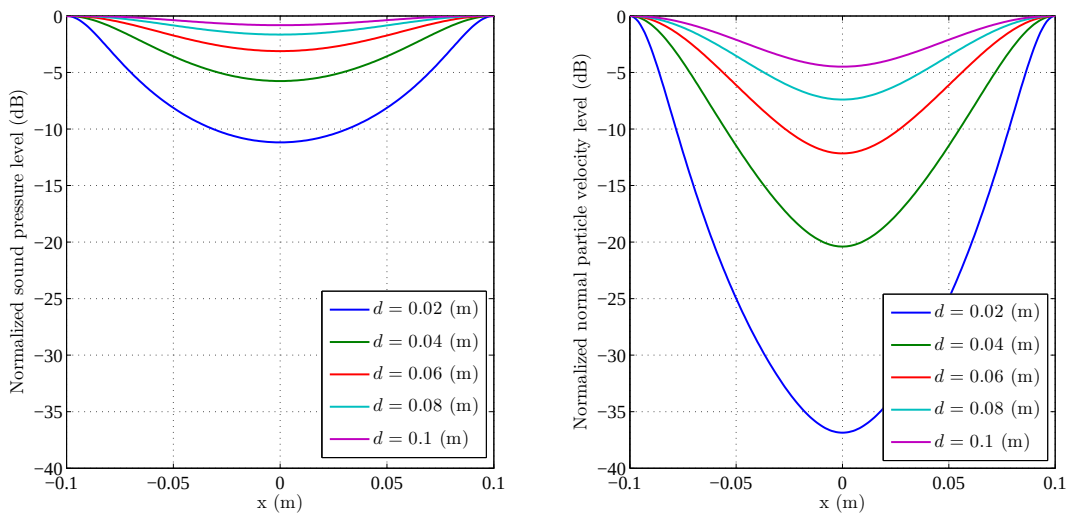

FIGURE 4.6: Normalised acoustic levels of the two sources shown in Figure 4.5 in terms of sound pressure (left) and normal particle velocity (right) for several measurement distances d.

Solving Equation 4.16 yields a parameter η_p which relates resolution D_r to measurement distance d, i.e.

$$d = \eta_p D_r = \frac{\sqrt{\sqrt{33}-5}}{2\sqrt{2}} D_r \approx 0.3\, D_r \tag{4.17}$$

Recalling the previous example simulation shown in Figure 4.5, it would be necessary to perform sound pressure measurements at a distance of 0.06 metres or closer in order to distinguish two sound sources separated by 0.2 metres with a 3 dB signal-to-noise ratio (SNR).

On the other hand, for normal particle velocity, the relationship between measurement distance and source separation is not straightforward. Frequency dependency along with the vector nature of particle velocity leads to a rather complex initial equation, i.e.

$$\begin{aligned}\left(\frac{A}{d}\right)^2\left(k^2+\frac{1}{d^2}\right)+\left(\frac{A}{\sqrt{d^2+D_r^2}}\right)^2\left(k^2+\frac{1}{d^2+D_r^2}\right)\frac{d^2}{d^2+D_r^2} = \\ 4\left(\frac{A}{\sqrt{d^2+D_r^2/4}}\right)^2\left(k^2+\frac{1}{d^2+D_r^2/4}\right)\frac{d^2}{d^2+D_r^2/4}\end{aligned} \tag{4.18}$$

The last expression can be rearranged to polynomial form as such:

$$\begin{aligned}(d^2k^2+1)D_r^{12}+(15d^4k^2+15d^2)D_r^{10}+(24d^6k^2+87d^4)D_r^8+(-190d^8k^2-10d^6)D_r^6+ \\ (-552d^{10}k^2-408d^8)D_r^4+(-480d^{12}k^2-480d^{10})D_r^2-128d^{14}k^2-128d^{12}=0\end{aligned} \tag{4.19}$$

According to the Abel-Ruffini theorem, the above equation is analytically unsolvable since there are no general algebraic solutions to fifth order polynomial equations or higher [128]. Hence, the above expression must instead be evaluated using numerical methods. An unconstrained non-linear optimisation has been performed using the square of Equation 4.19, to ensure that the minima are located at the roots of the function. The application of an optimisation procedure throughout the audible frequency range (20 Hz - 20 kHz), and substituting $D_r = d/\eta_u$ in Equation 4.19, yields the following relationship for normal particle velocity measurements

$$d = \eta_u \, D_r \quad \text{where} \;\; 0.51 < \eta_u < 0.66 \tag{4.20}$$

The results found for both sound pressure and normal particle velocity mapping are compared in Figure 4.7 (left) along with the variation of the resolution factor depending on the measurement distance (right).

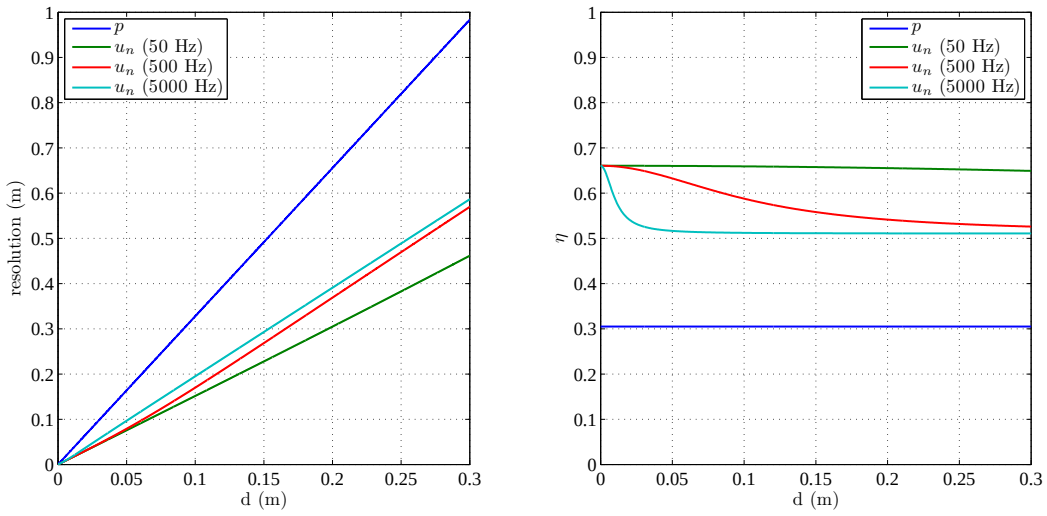

FIGURE 4.7: Spatial resolution (left) and resolution factor (right) of sound pressure and normal particle velocity mapping methods.

As illustrated, normal particle velocity measurements provide much better resolution than sound pressure. Despite the simplicity of the simulation scenario, the superiority of particle velocity transducers for source localisation purposes is clear, especially when measurements are carried out in the near-field. In fact, the inclusion of additional factors such as background noise, rigid boundaries or reverberation time would only increase the resolution difference between sound pressure and particle velocity mainly due to directivity of the sensor [120].

In addition, the parameter which relates measurement distance d to resolution distance D_r is displayed on the right hand side of Figure 4.7. In spite of the complexity of the equations used in the case of normal particle velocity, a bounded interval where this parameter is defined can be established.

The ratio between the expressions which describe the spatial resolution of the studied acoustic quantities (Equation 4.17 and Equation 4.20) leads to the conclusion that normal particle velocity mapping can achieve double the spatial resolution of sound pressure.

4.2.3 Experimental examples

Direct sound mapping techniques, particularly the visualisation of the normal acoustic particle velocity, provide a flexible and robust approach for localising sound sources in a variety of environments. This section presents several practical examples illustrating the results of the proposed scanning technique "Scan & Paint" for direct sound mapping.

4.2.3.1 Small scale problems

Most current pressure-based methods lack sufficient resolution to distinguish a set of closely spaced sound sources, such as noisy electronic components, mechanical parts or micro-perforations that act as acoustic leakages. As demonstrated in Section 4.2.2, the mapping of normal particle velocity allows for the identification of neighbouring noise sources with a high spatial resolution, particularly when the measurements are undertaken in the near-field. A miniature version of a p-u probe (the so called p-u match probe) can be used for the investigation of acoustic scenarios of very small dimensions. Figure 4.8 gives an example of the high spatial resolution achievable with the proposed mapping system when the scanning measurements are performed very close to the noise sources (about 0.5 mm). The probe was mounted on a stand which was moved carefully to keep a constant separation between the radiating plane and the sensor. As shown, the proposed scanning technique is able to provide a detailed sound map that reveals local acoustic excitation. In this case, it is possible to distinguish between 0.6 mm holes with 4 mm spacing between them.

4.2.3.2 Vehicle interior noise

There are many sound sources and reflections contributing to the sound pressure at a particular position inside a vehicle cabin. Even close to the radiating surface, it is

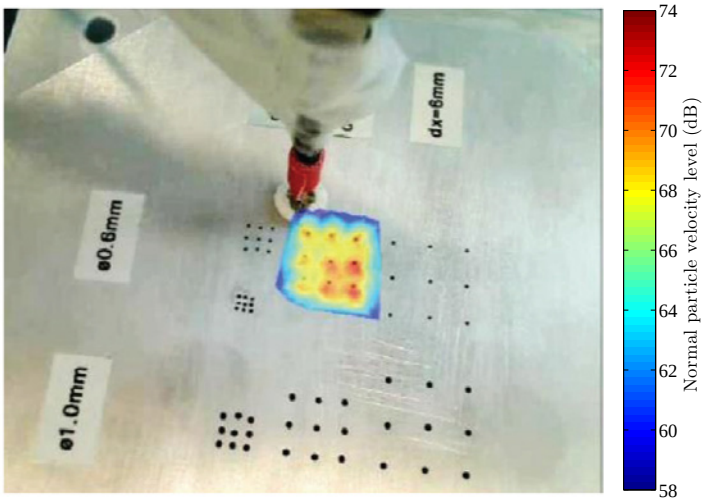

FIGURE 4.8: High spatial resolution of particle velocity mapping over 0.6 mm diametre holes with a 7 kHz excitation source behind the perforated plate.

hard to distinguish the direct contribution from other disturbances. A reliable method to identify the main noise sources is often required to improve the overall acoustic performance. Pressure-based measurement methods and processing techniques often fail to provide proper results in such conditions due to high levels of background noise and the high surface impedance of most of enclosure materials. Alternatively, direct normal particle velocity mapping benefits from the intrinsic properties of this quantity (see Section 4.2), enabling the characterisation of acoustic excitations across the vehicle despite the harsh measurement conditions. In addition, a quantification of the noise contribution of each part of the cabin interior to a particular position can be implemented using panel contribution analysis, as will be introduced in Chapter 5.

The cabin interior of a helicopter was investigated to provide experimental evidence showing the advantages of using sound maps of normal particle velocity for noise source localisation in an adverse environment. For the case studied, the measurements were carried out at Lelystad Airport (the Netherlands) during the conventional 10 minute warm-up time of a helicopter. Figure 4.9 presents the experimental scenario and the broadband sound pressure and normal particle velocity maps obtained.

As can be seen, no particular excitation can be identified on the pressure map. It is likely that the background noise caused by the multiple sound sources distributed across the cabin is masking the pressure emitted by specific areas of the vibrating structure. However, the normal particle velocity map shows that the ceiling window is the most powerful excitation source in the evaluated frequency band. Further details of this test, the application of a scanning panel contribution approach and the validation procedure of the acquired data can be found in [27].

(A) Measurement scenario

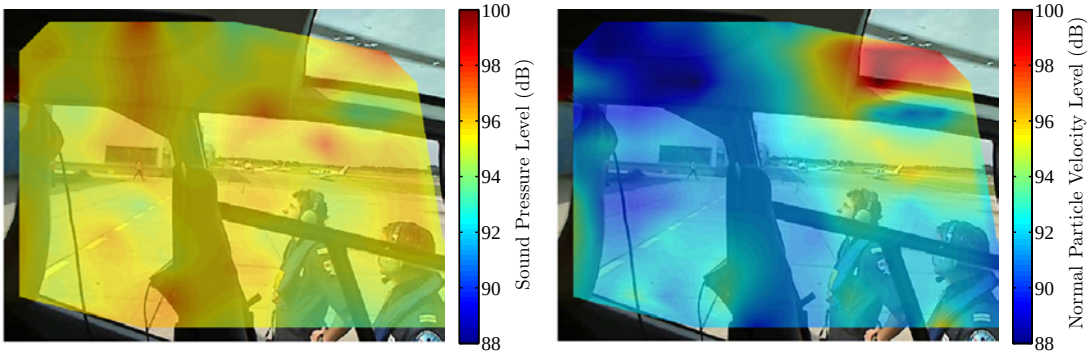

(B) Sound pressure (C) Normal particle velocity

FIGURE 4.9: Direct sound mapping of the helicopter cabin interior for a frequency range between 150 Hz and 1500 Hz.

4.2.3.3 Leak detection in building acoustics

A sound field cannot be completely confined to an enclosed space; sound generally propagates throughout air or the structural paths exciting neighbouring rooms. The acoustic features of those rooms are determined not only by the properties of their construction materials but also by the way they are installed. Sound insulation losses often appear after the mounting process and should therefore be tested *in situ*.

The insulation properties of several constructive elements of a large room were investigated, based on the previous work presented in [16]. Two loudspeakers were used to produce a stationary acoustic excitation outside the room being assessed. White noise was used in order excite any possible resonance frequency within the audible range. A 10 minutes scanning measurement was undertaken, moving the probe across an area of 3.2 metres by 1.4 metres approximately 0.03 metres from the surface of the constructive elements. Figure 4.10 shows the measurement setup (A) and experimental examples of leakage detection in constructive materials using a broadband mapping of sound pressure

(B) and normal particle velocity (C). As can be seen, the spatial distribution of the normal particle velocity has a larger dynamic range than the sound pressure, enabling the localisation of weak noise sources. While the pressure roughly indicates where the noise emission areas are, the normal particle velocity map even reveals the acoustic leakage introduced by the door profile.

(A) Measurement scenario

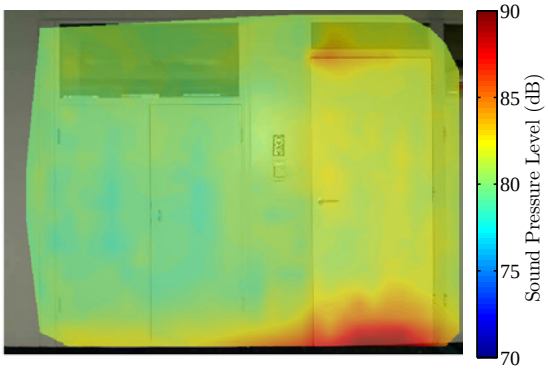

(B) Sound pressure

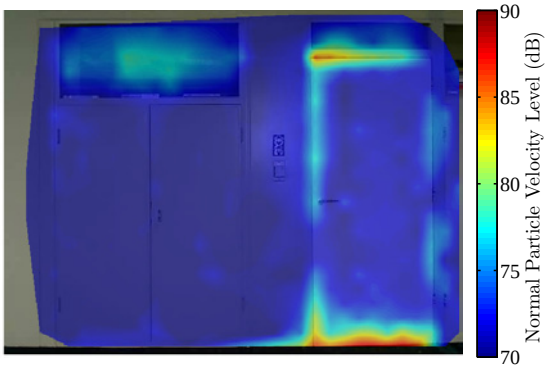

(C) Normal particle velocity

FIGURE 4.10: Direct sound mapping for a frequency range between 50 Hz and 10 kHz.

The scanning method proposed also allows for the evaluation of acoustic behaviour in several areas of interest. In the case studied, the door, closet and window were the main components investigated. The mean acoustic excitation perceived near each element is calculated by averaging the signals recorded at a specific region. Since normal particle velocity is proportional to surface displacement [129], the summation of the spectra over a particular component often shows the structural resonant frequencies, i.e. the main insulation weaknesses of each component. Figure 4.11 illustrates the normal particle velocity spectra over the three constructive elements studied along with the sound maps at three particular frequency bands. As shown, most of the noise goes through the door frame, mainly through the top and bottom junctions, becoming the dominant source across almost the entire spectra. The low frequency noise transmitted to the room is dominated by the first modes of the window. Appendix C shows that detailed vibro-acoustic analysis can be performed by means of scanning operational deflection shapes. On the other hand, the noise emitted by the closet is only significant at the second axial

mode of the cavity, when the maximum pressure is located at the middle of the door frame [16].

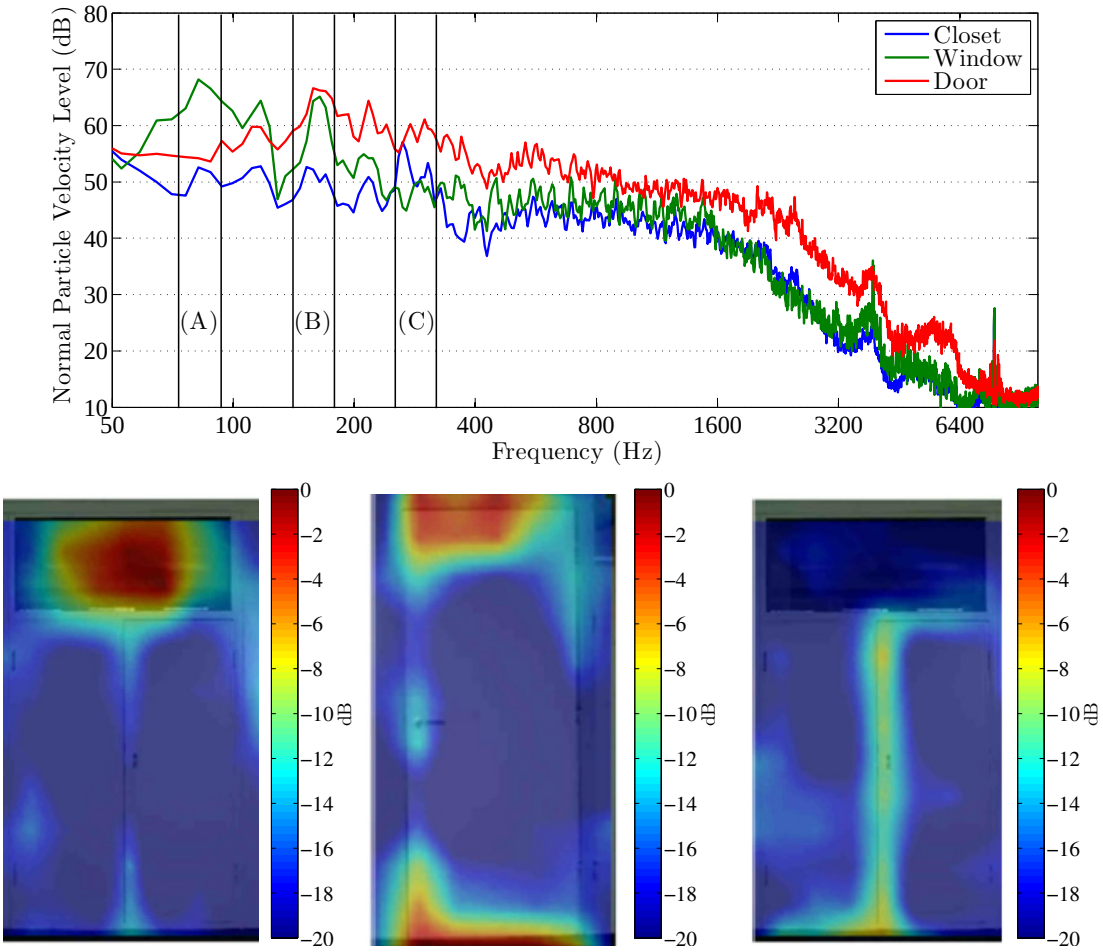

(A) 87 Hz (B) 165 Hz (C) 265 Hz

FIGURE 4.11: Spectra of the different elements (top) and normal particle velocity maps centred around different resonance frequencies of the window (A), door (B) and closet (C).

In summary, the visualisation of the sound field close to constructive elements can show the distribution of the local excitations, data that can ultimately be used to enhance the acoustic insulation of a room. This experiment demonstrates the high spatial resolution achievable even for large measurement areas in non-anechoic conditions.

4.3 Acoustic vector field mapping

The combination of acoustic energy maps and energy flow measurements is uncommon in acoustic metrology [130]. Traditionally, the analysis of acoustic fields concerns only the distribution of sound pressure levels. The ability to measure sound intensity has

changed the approach to examining many acoustic phenomena. The visualisation of the vectorial field has been applied to various studies, greatly simplifying research methods.

Visualisation of sound intensity can be used to depict various acoustic phenomena, depending on the test purpose. In sound engineering, it may be an acoustic wave power density distribution, wave dissipations or the evaluation of wave motion within a medium. For experimental acoustics, the directional characteristics of industrial sources and variables associated with reflection, scattering and diffractions due to obstacles could prove interesting. It can be used to draw maps of noise levels and evaluate the effectiveness of noise solutions applied in industrial facilities.

The Scan & Paint scanning methodology can also be used with a three dimensional sound probe which incorporates three orthogonal particle velocity sensors and a pressure microphone. The intensity vector field of the evaluated scenario can be acquired by moving the probe across a plane and keeping its orientation constant during the scanning process.

4.3.1 Three dimensional sound intensity

Sound pressure and acoustic particle velocity elements have a phase difference which depends upon the sound direction of arrival and source distance [111]. This implies that the instantaneous products of the sound pressure and each orthogonal particle velocity component yields a complex vector: the complex acoustic intensity $\mathbf{C}$. The imaginary part of this quantity is known as the reactive intensity $\mathbf{J}$, which represents the non-propagating acoustic energy. It is, however, more common to study acoustic sound fields in terms of the active, or propagating, part of the complex intensity [117], i.e.

$$\mathbf{I} = \{I_x, I_y, I_z\} =< p\,\mathbf{u} >_t = \frac{1}{2} Re\{p\,\mathbf{u}\} \tag{4.21}$$

where $< . >_t$ indicates time averaging, and the latter expression is based on the complex representation of harmonic variables. Figure 4.12 shows a schematic representation of the one dimensional complex acoustic intensity and the modulus of the three-dimensional active intensity vector.

Since both sound pressure and particle velocity are measured simultaneously, the calculation of the three dimensional acoustic intensity can be performed directly, without any approximation. This quantity provides directional information about the flow of acoustic energy. In addition, a scalar term can be extracted for visualisation purposes

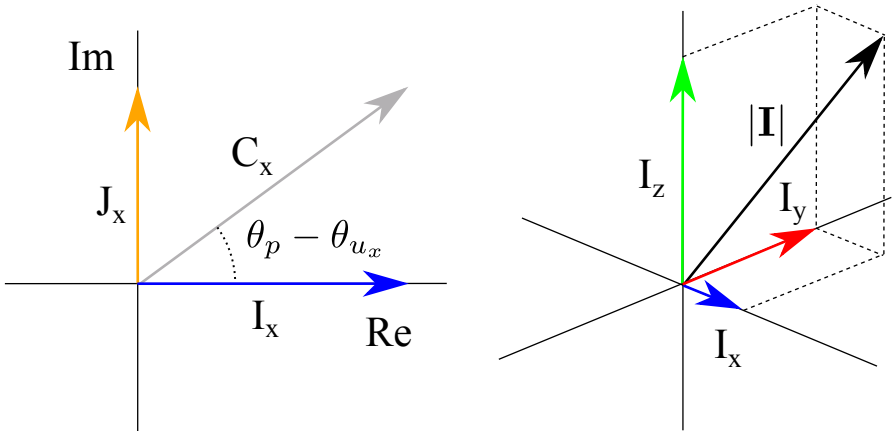

FIGURE 4.12: Schematic representation of the one dimensional complex acoustic intensity (left) and the three dimensional active intensity (right).

by taking the modulus of the active intensity vector, hence

$$|\mathbf{I}| = \frac{1}{2}\sqrt{\left(Re\left\{p\,u_x\right\}^2 + Re\left\{p\,u_y\right\}^2 + Re\left\{p\,u_z\right\}^2\right)} \tag{4.22}$$

Pressure-based measurement methods cannot be utilised when the pressure-intensity index (the ratio of sound pressure squared to active intensity) is high, which in practice limits the use of *p-p* intensity probes in environments with high levels of background noise or reflections (see Appendix A for further details). In contrast, direct intensity measurements using a combination of pressure and particle velocity transducers, the so called *p-u* intensity probes, are unaffected by this index, enabling the estimation of propagating acoustic energy despite unfavourable conditions [131, 132]. On the other hand, the error of the intensity calculations using *p-u* probes mainly depends upon the reactivity of the sound field (the ratio of reactive to active intensity J/I). If the reactivity is high, for example in the near field of a source, a small phase mismatch in the transducer's calibration may lead to considerable error in the intensity estimate. In [133] it is stated that in practical situations the reactive intensity should not exceed the active intensity by more than 5 dB, which corresponds to a ± 72 degree phase difference between sound pressure and particle velocity. Although active intensity may be biased in a highly reactive field, the phase difference between pressure and particle velocity can still be measured accurately. Therefore, it is still possible to detect which measurement positions are exposed to high reactivity.

4.3.2 Experimental examples

Energy wave phenomena around radiating structures can be studied by means of acoustic intensity field visualisation. Using a vector quantity directly acquired by a three dimensional sound intensity p-u probe contributes to a more comprehensive interpretation of acoustic radiation mechanisms. Experimental evidence can be used to understand how the acoustic field is excited, potentially helping to improve the source design or positioning.

Several experimental cases are presented in this section. The sound fields are illustrated using a picture of the setup overlaid with a measured vector field and a colormap of the acoustic intensity norm (Equation 4.22). As mentioned above, an intensity measurement is only valid if the reactivity is not too high, consequently, all signal segments with a phase exceeding ± 72 degrees were omitted.

4.3.2.1 Loudspeaker in a room

Loudspeaker cabinet design aims to provide the appropriate acoustic loading for the drive units while ensuring a good performance of the complete system [134]. The vibrations induced by the driver frame and moving airmass within the enclosure should therefore be controlled in order to minimise radiation from the cabinet itself. There are several methods for capturing and visualising the vibro-acoustic behaviour of a radiating sound source, but often they are tedious or impractical. In contrast, direct sound field visualisation offers a more flexible approach to display sound phenomena. This section shows some of the results presented in [18] concerning the sound radiation of a loudspeaker in a conventional room. Figure 4.13 shows the acoustic sound field at the third octave frequency band of 4 kHz.

It is worth taking the impact of diffracted sound into account to correctly assess the structure-borne noise from the loudspeaker cabinet. When wavefronts generated at the speaker driver reach the sharp edge of the cabinet there is a sudden increase in the rate of expansion [135]. There are two consequences to this effect. Firstly, part of the acoustic energy radiated effectively turns around the edge and continues propagating in the region behind the plane of the source. Secondly, a new sound wave appears to emanate from the edge, the so called diffracted wave. As a consequence, particle velocity measured on the sides of the loudspeaker is a combination of structure-borne sound radiated by the vibrating cabinet and airborne sound originating from the speaker driver. Additional structural transfer function measurements would be required in order to separate both structure-borne and airborne noise. An extended analysis of this data can be found in [18].

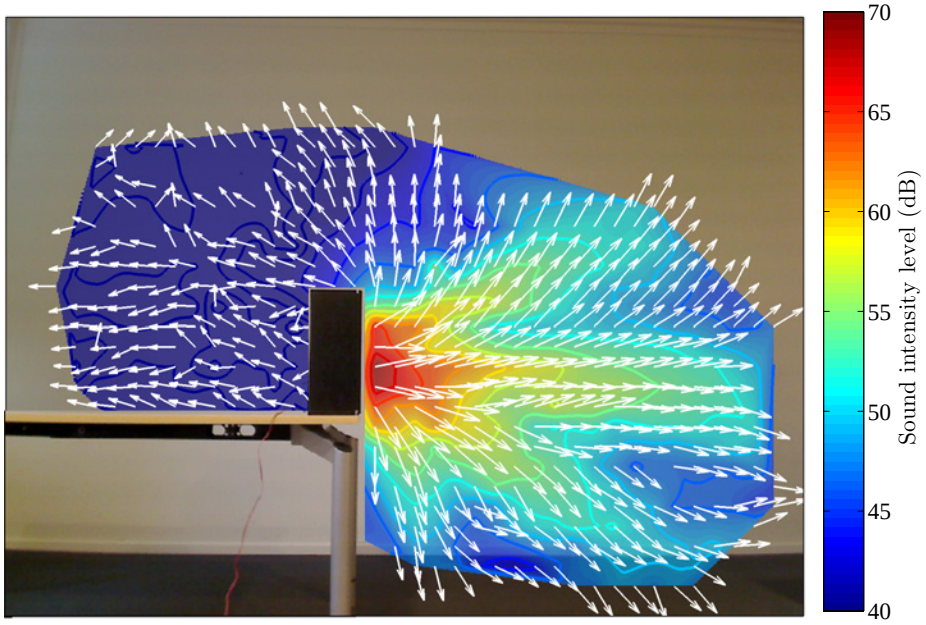

(A) Side view

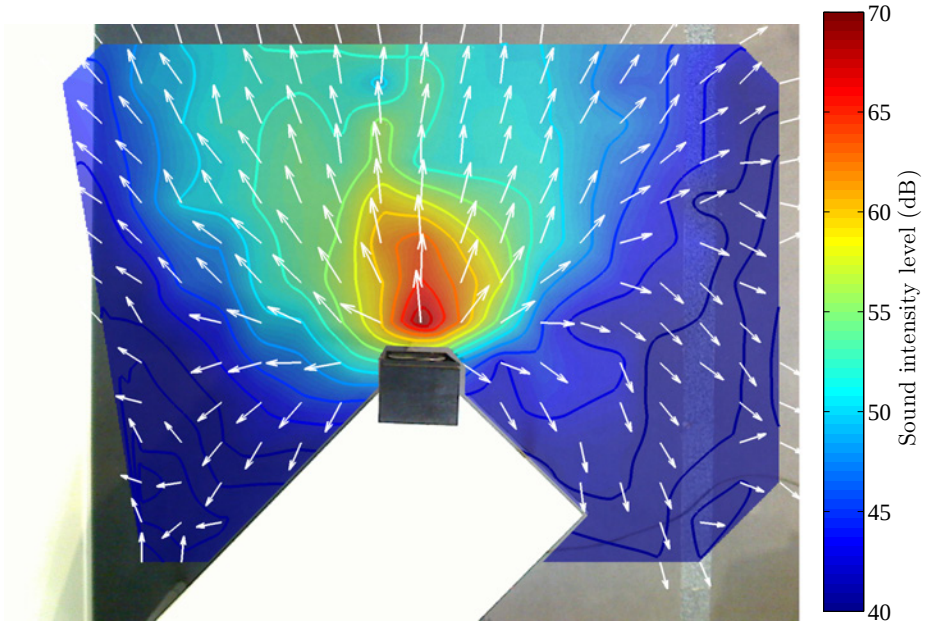

(B) Top view

FIGURE 4.13: Acoustic intensity vector field of a loudspeaker at 4 kHz.

4.3.2.2 Vehicle exterior noise

Standardised exterior noise tests are commonly used to determine the sound quality of vehicles in development. The combination of static tests and on-road measurements is essential to undertaking a successful refinement process. Beamforming techniques, using phased microphone arrays, are common tools for localising and quantifying noise sources

across the vehicle body. However, such devices have some well-known disadvantages regarding, for instance, their high cost, limited performance at low frequencies and transducer calibration problems. In contrast, a direct sound intensity mapping method offers an alternative approach to assess vehicle exterior noise in an efficient way.

With the latter technique, the sound field produced by a static Nissan 350Z has been evaluated in an open outdoors area. The noise radiation from the front and the back of the vehicle was mapped by positioning the camera twice. The camera itself was placed at a height of 3 metres. Figure 4.14 presents the results obtained at 250 Hz and 1260 Hz. As shown, the intake and exhaust systems are the main noise sources at lower frequencies, situated on the left side of the vehicle body. Furthermore, an almost symmetric pattern can be seen at the front of the vehicle at higher frequencies; the ventilation areas of the engine bay act as the main radiation sources.

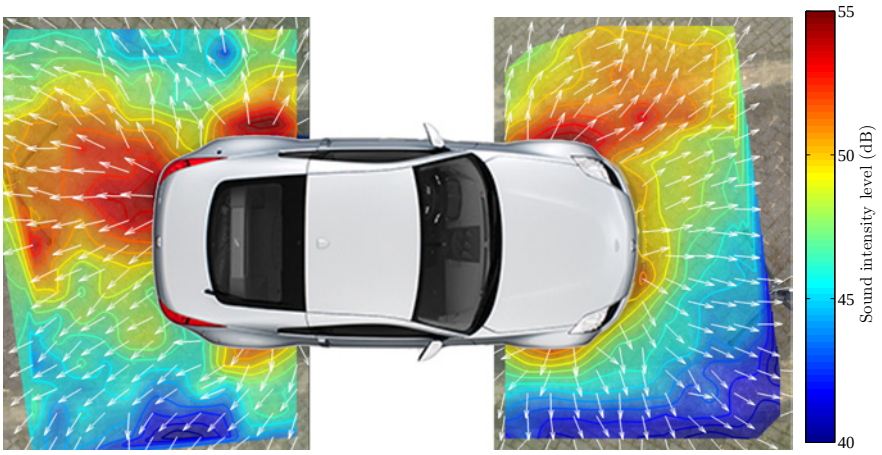

(A) 250 Hz

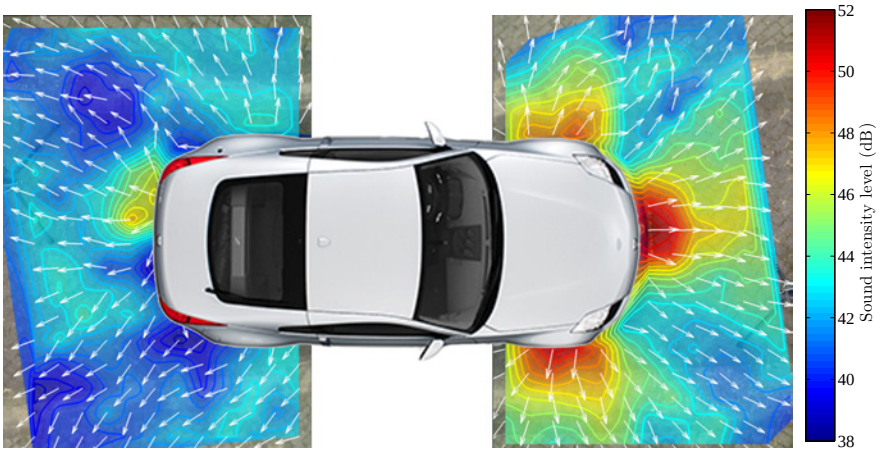

(B) 1260 Hz

FIGURE 4.14: Acoustic intensity vector field of a static Nissan 350Z with a rotational engine speed fixed at 3000 RPM.

4.3.2.3 Unmanned Aerial Vehicles

Interest in the development of Unmanned Aerial Vehicles (UAV) has rapidly increased in recent years. One current discussion topic is reduction of the acoustic signature of UAVs, ideally to achieve acoustic stealth. For this purpose, the sound field produced by the jet engine of a radio-controlled plane has been measured on land in a fixed position with idle engine conditions. Figure 4.15 presents the results of the test. The intake noise produced by the fan becomes dominant at 5 kHz, as can be seen in the left hand side of the figure. In contrast, the noise produced at the exhaust is dominant for the rest of the spectrum, having a radiation maximum at a specific angle from the exhaust axis, as expected for most jet engines [136].

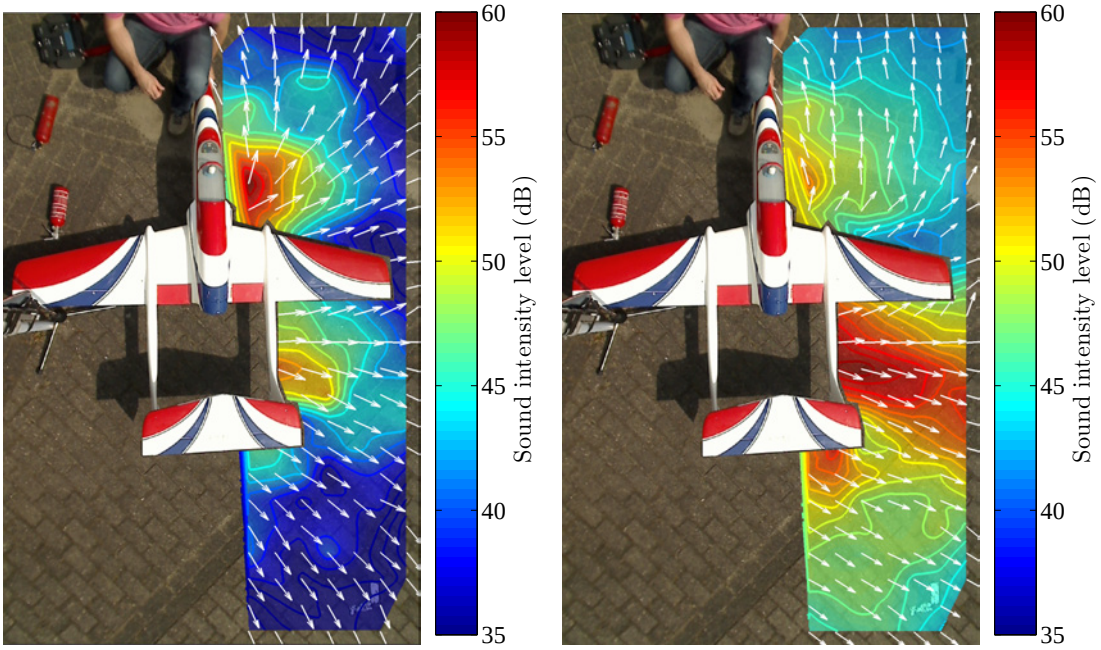

(A) 5 kHz (B) 8 kHz

FIGURE 4.15: Acoustic intensity vector field of a radio control airplane.

4.4 Summary

The main characteristics of sound pressure and particle velocity mapping have been studied for source localisation purposes. It has been proven that external noise sources have little effect on normal particle velocity measurements near a vibrating surface since:

- The particle velocity level caused by vibrating surfaces is higher than the sound pressure level because of near field effects.

- The normal particle velocity close to a non-vibrating structure is very low since it is proportional to the surface displacement, thus achieving a strong reduction in the noise generated by other sources.
- Particle velocity sensors have a figure-of-eight directivity pattern that is pointed towards the vibrating surface, reducing the noise contributions from other directions.

Furthermore, novel expressions describing the spatial resolution of direct mapping methods for sound pressure and normal particle velocity have been derived. It has been shown that particle velocity yields better results for identifying closely spaced noise sources. Moreover, experimental evidence using both one dimensional and three dimensional acoustic intensity maps has been presented, proving the theoretical foundations introduced. It can be concluded that the proposed scanning mapping method can be used for machine diagnostics, vibroacoustic characterisation and sound radiation assessment in real-life conditions. The short time required to undertake Scan & Paint measurements allows for the evaluation of detailed acoustic data from small to large areas in a fast and efficient way.

Chapter 5

Scanning Panel Contribution Analysis

5.1 Introduction

Direct sound visualisation is not always the most suitable way to assess complex noise problems. An apparently loud spot in a near-field sound map may have an insignificant contribution to another position outside the measurement plane. Detailed information about the acoustic environment and the sound sources is required to tackle this problem. Several pressure contribution techniques, often referred to as "Panel (Noise) Contribution Analysis" methods, aim to determine the influence of local excitations upon one reference point in the sound field. The summation of individual contributions yields the sound pressure at the specified location. These techniques allow for the areas of local excitation to be ranked; information is essential for designing effective noise control strategies.

Most conventional methods require complicated and time consuming measurement procedures. For instance, according to Wolff "a complete investigation of a vehicle takes typically two to four weeks" [137]. In contrast, a scan-based solution relying upon the direct acquisition of sound pressure and acoustic particle velocity can potentially improve results and, at the same time, speed up the measurement procedure. This chapter introduces a new scan-based method that applies the principles of panel noise contribution analysis to data acquired using a p-u intensity probes. It begins with an overview of the most popular measurement methods. The theoretical and practical fundamentals are then presented along with an experimental study of a car interior. This is followed by a discussion focused on the advantages, disadvantages and limitations of the novel method proposed.

5.2 Overview of panel contribution methods

One current requirement for the noise, vibration and harshness (NVH) sector is the development of efficient measurement techniques to evaluate the contribution of sound sources to specific locations. A general approach is to take into account operational forces acting over a structure, acoustic excitation sources and the corresponding structural and acoustic propagation paths [138]. Measurement methods seeking a solution to the complete coupled vibro-acoustic problem are usually based upon the principles of Transfer Path Analysis (TPA). Figure 5.1 presents a sketch of the problem commonly addressed in the automotive or aerospace industry.

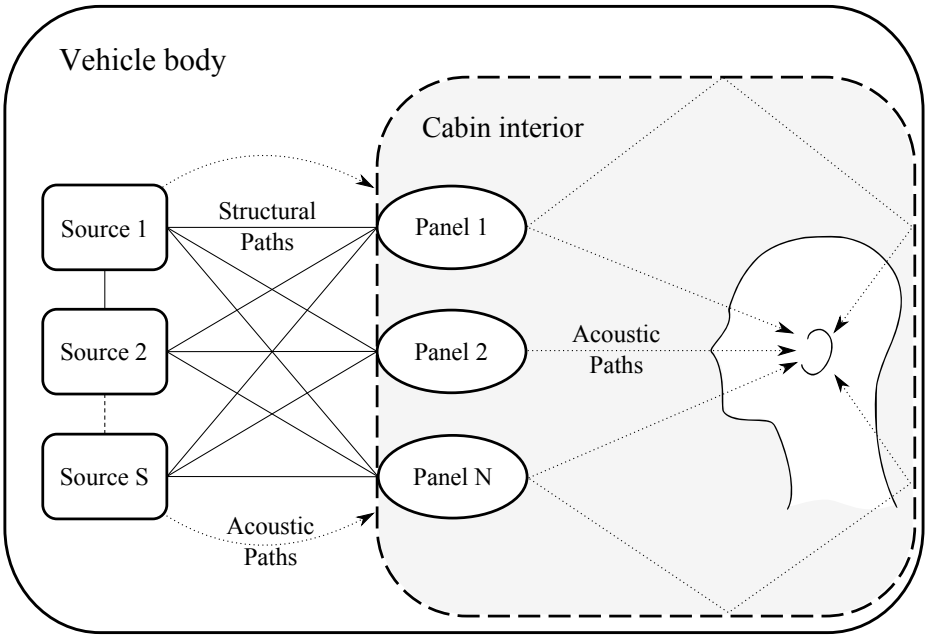

FIGURE 5.1: Sketch of a typical Transfer Path Analysis problem regarding structural and airborne noise sources.

The optimisation of a vehicle cabin can also be undertaken by only considering the airborne contributions of different surface areas to a reference position. This problem is often studied with panel noise contribution analysis techniques. Most techniques begin with the application of spatial discretisation to a complex radiating structure, dividing it into multiple vibrating surface areas denoted as *panels*. Their degree of *contribution* should then be defined in order to rank which parts have a stronger influence on the sound pressure at the evaluated position. In the technical literature, several experimental methods have been developed to address this problem. An overview of the most relevant techniques is given below following [137, 139–141].

5.2.1 The windowing technique

One of the most traditional measurement methods for quantifying the noise emitted by a particular region of a complex structure is the popular 'windowing' or 'masking' technique. A very heavy acoustic treatment, known as *maximum package*, is installed across the entire cabin in order to prevent sound from penetrating into the vehicle interior. Next, the sound pressure perceived at a reference position is measured when a small area, or *window*, of the insulation is uncovered. It is assumed that noise from others parts of the vibrating structure is completely muffled by the acoustic treatment, and therefore the sound pressure perceived at the reference position corresponds to the contribution of the uncovered area. A sketch of the measurement technique is shown in Figure 5.2

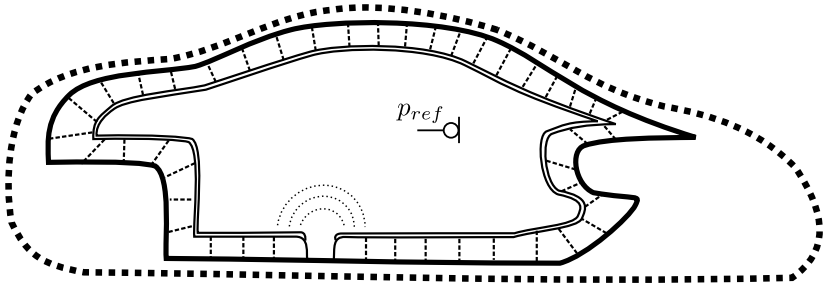

FIGURE 5.2: Sketch of the windowing measurement procedure.

Despite the intuitive and pragmatic nature of this approach, it has several well known drawbacks. Firstly, the preparation of the maximum package is very time consuming; it can take up to 3 weeks. Furthermore, the application of such a heavy treatment[1] can significantly alter both dynamic and acoustic properties of the vehicle. The top layer of the maximum package has higher impedance than the interior walls in regular conditions, which causes the sound pressure produced by a *window* to be reinforced by the acoustic environment, hence leading to overestimations of the pressure contribution that need to be corrected.

In addition, phase information is lost during the asynchronous data acquisition process, limiting the applicability of the method at low frequencies. Regardless of these disadvantages, the method has proven useful in practice, yielding reasonable results when the number of dominant contributions is low.

[1]The weight of the maximum package can be up to 150 kg [71]

5.2.2 Surface velocity sampling methods

There are several panel noise contribution techniques that rely on the direct acquisition of panel vibrational velocities [142]. The measurement process is often performed by either attaching light accelerometers to the vibrating structure or using laser vibrometers. Accelerometers may add a mass load that significantly influences the panel surface vibration. Although a non intrusive approach with laser vibrometers may seem more attractive, it requires the laser beam to be perpendicular to the vibrating surface. Furthermore, non-reflecting or fibrous materials may cause difficulties during the measurement process.

The accuracy of the results obtained from surface velocity sampling methods is highly dependent upon the number of measurement positions. Previous studies have shown that spatial aliasing of the vibration field, due to point sampling, can result in large errors in radiated field estimates [143]. In principle, the total number of sampled points should be able to describe the entire structural vibration pattern. It can be shown that even relatively simple study cases require a very high density of measurement positions, especially when assessing mid or high frequencies. In addition, external noise introduced into the cabin through small leaks or imperfect seals is disregarded with this measurement approach.

5.2.3 Airborne Source Quantification (ASQ)

The ASQ method uses sound pressure measurements to estimate panel surface velocities and ultimately sound pressure contributions [144]. This technique is based upon the fundamental principles of matrix inversion methods for vibro-acoustic applications, originally proposed by Verheij in [145]. ASQ begins by acquiring a number of 'indicator' pressure responses near the radiating surfaces in operating conditions. The volume velocity of each panel is then estimated by using inverse methods upon the near-field transfer functions between indicator positions and panels. The transfer function matrix is measured in a reciprocal way by placing a volume velocity source (VVS) at the location of the 'indicators' whilst microphones are positioned very close to the radiating surface.

Experimental inverse procedures suffer from numerical difficulties inherent to the computation of matrix inverses. The accuracy of the method strongly depends upon the transfer function matrix. Ideally, it should be comprised of at least as many pressure indicators as surface panels, but the inclusion of more indicators is recommended to improve the quality of the inversion process [144]. This requirement results in a substantial increase in the number of measurement points.

The ASQ method relies on the assumption that all cabin interior surfaces have high acoustic impedance, i.e. panels are acoustically reflective. This 'hard-wall' assumption does not account for the acoustically absorbent materials distributed across the cabin interior. In practical cases, such a simplification can lead to poor results at high frequencies [28].

5.2.4 Equivalent source methods (ESM)

The reconstruction of a complex sound field by means of a finite set of monopole sources has triggered the development of equivalent source methods (ESM) for multiple applications [146]. One of the first implementations incorporated in industry was the "Substitution Monopole Technique" (SMT) [145, 147]. The SMT calculates a set of equivalent monopole volume velocities from intensity measurements performed in free-field conditions. The sound pressure at a reference position is then reconstructed by combining the *substitution monopoles* with their corresponding transfer functions and adding them, assuming they are uncorrelated.

The free-field requirement for estimating monopole volume velocities is a major disadvantage that limits the application for studying complex scenarios such as vehicle compartments. This was also stated in [147], where it is proposed to apply an acoustic treatment in order to improve the measurement conditions for *p-p* intensity probes. The installation of additional acoustically absorbent material is an elaborate and time consuming task, another important disadvantage of this method.

An alternative equivalent source approach that overcomes the practical limitations of the SMT is the "Vehicle Acoustic Synthesis Method" (VASM) [148, 149] which substantially reduces the measurement time whilst increasing the accuracy of the results. The VASM incorporates an array of *p-u* intensity probes to measure the *in-situ* sound intensity with less acoustic restrictions in the measuring environment.[2]

The fundamental principles of panel noise contribution implemented by SMT and VASM are similar to the ASQ method mentioned above, i.e. they all rely upon the "hard-wall" assumption, which may limit the accuracy of the results at high frequencies. Furthermore, as reported in [145, 148, 149], both uncorrelated ESM methods often suffer from errors at low frequencies since phase information is not taken into account. However, this limitation could be mitigated by using reference sensors for acquiring relative phase information, similarly to the proposed method shown in Section 5.4.

[2]The limitations of *p-p* and *p-u* probes for intensity measurements are discussed in Appendix A

5.2.5 Near-field Acoustic Holography (NAH) based methods

A reduced dataset can be used to obtain to a full sound field reconstruction by means of acoustic holography [124]. Several panel contribution approaches based on NAH can be found in literature that use either single layer [150–152] or double layer [152, 153] microphone arrays in the near-field of a vibrating structure. The array pressure data is used to estimate the sound pressure and particle velocity at the vibrating surface via inverse methods. The acoustic power flow from each panel is later related to the radiated acoustic pressure at the reference position.

NAH presents some advantages over the previous techniques since it does not necessarily require a transducer to be mounted on the panels or for the original cabin structure to be modified; it also avoids the "hard-wall" assumption in its theoretical formulation. Nevertheless, NAH is often limited to the evaluation of local acoustic behaviour and does not cover the full interior simultaneously. This implies that phase relationships between panels are lost, potentially leading to poor results at low frequencies.

Moreover, a very high number of transducers is required in order to obtain reliable results. Further discussion of the drawbacks of holography solutions for industrial applications is given in Section 2.5.1.

5.2.6 Pressure-velocity based reconstruction techniques

There is a group of techniques based on the direct acquisition of sound pressure and particle velocity which applies the fundamental panel noise contribution relationship without the "hard-wall" assumption. The main difference with respect to the NAH approaches mentioned above is that both fundamental quantities involved in the calculations, i.e. sound pressure and normal particle velocity, are acquired directly using a p-u intensity probe near the radiating structure instead of back-propagating the data [139].

The scan-based implementation of panel noise contribution principles introduced in this chapter belongs to this group of methods. The scanning approach was originally proposed by the author in [14] and later validated in complex measurement scenarios such as a car interior [27] and a helicopter cabin [29]. The same approach was also used to link several measurements performed using small sensor arrays [26]. The key to this novel method is the utilisation of a reference sensor to preserve phase information, which acts as a link connecting the signals in a relative sense. A detailed description of the proposed theoretical foundations are given in the following section.

5.3 Fundamentals of Panel Noise Contribution Analysis

This section considers the theoretical framework for deriving the fundamentals of panel noise contribution analysis. It is assumed that the continuous surface of a complex structure, denoted by **S**, excites the sound field under operating conditions. An infinitesimal area **M** can be defined to study how different areas of the structure *contribute* to the position of **M**. Figure 1 shows a sketch of the described scenario.

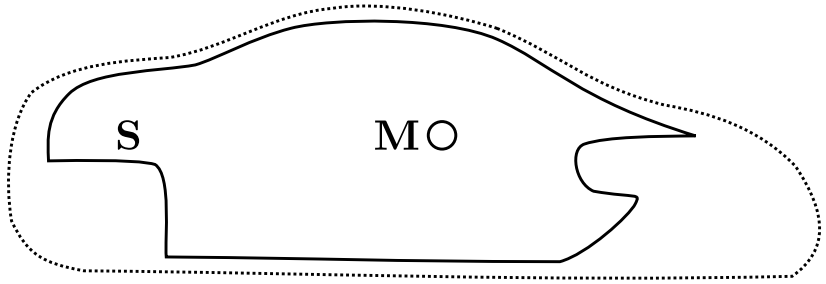

FIGURE 5.3: Sketch of the surfaces involved in the derivation.

The derivation of an expression that defines the pressure contribution at **M** follows Hald [152] and Kinsler [111]. As pointed out by Hald, the fundamental expressions of panel noise contribution can be derived from the definition of acoustic reciprocity. The reciprocity theorem establishes a link between two different conditions given in the same time-invariant spatial domain [154]. Each measurement state has its own set of time-invariant variables. Generally, two different excitation sources are used to create those conditions: a monopole source at **M** (reciprocal transfer function measurements) and the noise generated by the machine or structure **S** (noise measurements).

Two acoustic variables can be defined for each measurement state: p^{TF} and u_n^{TF} are the sound pressure and normal particle velocity during the reciprocal transfer function measurements, and p and u_n are the sound pressure and normal particle velocity during the noise measurements. Both sets of variables are initially defined at any point of the sound field but, as shown below, the measurement position for acquiring those quantities will depend upon the integration domain.

The acoustic reciprocity theorem states that [111]

$$\int_{\mathbf{M}} (p^{TF} u_n - p u_n^{TF}) d\mathbf{M} + \int_{\mathbf{S}} (p^{TF} u_n - p u_n^{TF}) d\mathbf{S} = 0 \tag{5.1}$$

The integral of the normal particle velocity u_n across the entire surface **M** will be zero since there is no net energy throughout **M** during the noise measurements. Furthermore, sound pressure p can be integrated over **M** during the noise measurements obtaining the reference pressure p_{ref}. The integration of normal particle velocity over **M** during the

transfer function measurement yields the volume velocity of the monopole source Q[3]. Consequently, the previous expression simplifies to

$$-p_{ref}Q + \int_{\mathbf{S}} (p^{TF}u_n - pu_n^{TF})d\mathbf{S} = 0 \tag{5.2}$$

The pressure at the reference position can then be defined as

$$p_{ref} = \int_{\mathbf{S}} \left(\frac{p^{TF}}{Q}u_n - p\frac{u_n^{TF}}{Q} \right) d\mathbf{S} \tag{5.3}$$

It can be shown that the second term of the integral vanishes when data is acquired directly at a rigid boundary [137]. Such an approximation, often referred as the "hard-wall assumption", is used by most of the panel contribution methods (see Section 5.2). In the case that sensors are not directly attached to the surface or the materials are non-rigid, such a simplification is no longer applicable and the whole of Equation 5.3 should be considered.

In summary, Equation 5.3 presents the fundamental equation for most panel noise contribution methods. It relates the sound pressure at the reference position p_{ref} to the normal particle velocity u_n and sound pressure p measured near the structure $\mathbf{S}$ combined with their correspondent acoustic transfer function p^{TF}/Q and u_n^{TF}/Q.

5.4 The Reference-Related method

The general definition of the sound pressure at a reference position shown in Equation 5.3 implies that the entire distribution of sound pressure and normal particle velocity should be acquired simultaneously. Otherwise, the phase information would be lost, resulting in large estimation errors in the presence of correlated or partially-correlated sources. This condition becomes critical at low frequencies. In order to overcome this problem, a novel approach called the "Reference-Related method" was proposed by the author in [14]. The main idea is to use a fixed reference sensor to synchronise data at multiple locations during the noise radiation test. The technique involves solving Equation 5.3 using relative phase information instead of absolute phase. For this purpose, Equation 5.3 is first multiplied by the complex conjugate version of the pressure reference p_{ref}^*, as such

$$p_{ref}p_{ref}^* = \int_{\mathbf{S}} \left(\frac{p^{TF}}{Q}u_n p_{ref}^* - pp_{ref}^* \frac{u_n^{TF}}{Q} \right) d\mathbf{S} \tag{5.4}$$

[3]The volume velocity of a source is defined by the product of the radiating area and the particle velocity normal to it

So far only arbitrary signals have been considered in the derivation. However, a statistical approach should be performed to account for the random nature of the data acquired in a real measurement scenario [116]. As such, taking the expected values $E[.]$ of the previous expression yields

$$E[p_{ref}p^*_{ref}] = \int_{\mathbf{S}} \left(E\left[\frac{p^{TF}}{Q}\right] E[u_n p^*_{ref}] - E[pp^*_{ref}] E\left[\frac{u_n^{TF}}{Q}\right] \right) d\mathbf{S} \tag{5.5}$$

Equation 5.5 can be now expressed by a combination of auto spectra, cross-spectra and transfer functions, i.e.

$$S_{p_{ref}p_{ref}} = \int_{\mathbf{S}} \left(H_{Qp^{TF}} S_{u_n p_{ref}} - H_{Qu_n^{TF}} S_{pp_{ref}} \right) d\mathbf{S} \tag{5.6}$$

where $S_{p_{ref}p_{ref}}$ is the autospectrum of the pressure reference; $H_{Qp^{TF}}$ and $H_{Qu_n^{TF}}$ are the transfer functions between the sound pressure p^{TF} and normal particle velocity u_n^{TF} and the monopole source Q during the transfer function measurements; $S_{pp_{ref}}$ and $S_{u_n p_{ref}}$ are the cross-spectra of the sound pressure p and normal particle velocity u_n with the reference pressure sensor p_{ref} measured in operational conditions.

In practice the amount of measurement points must be limited. As a result, the surface $\mathbf{S}$ has to be discretised into M sub-areas or *panels*. Equation 5.6 hence becomes

$$S_{p_{ref}p_{ref}} = \sum_{m=1}^{M} \left(H^{(m)}_{Qp^{TF}} S^{(m)}_{u_n p_{ref}} - H^{(m)}_{Qu_n^{TF}} S^{(m)}_{pp_{ref}} \right) A^{(m)} \tag{5.7}$$

where $A^{(m)}$ is the area of each panel m. For most practical applications, it may be more suitable to refer to the outcome of the above expression as $S_{p_{syn}p_{ref}}$, a mix between the measured reference and the synthesised, or reconstructed, sound pressure. The pre-multiplication by the conjugated reference signal undertaken at the beginning of this derivation biases the estimation of individual panel contributions. An estimate of the synthesised pressure level $S_{p_{syn}p_{syn}}$ can be reconstructed by normalising the last expression with the reference signal as such:

$$S_{p_{syn}p_{syn}} = \frac{|S_{p_{syn}p_{ref}}|^2}{S_{p_{ref}p_{ref}}} \tag{5.8}$$

The use of a single reference sensor has been proven to enable the reconstruction of a sound field created by a reduced number of sound sources. However, it may be necessary to increase the number of reference sensors in order to improve the accuracy of the relative phase reconstruction in the presence of multiple uncorrelated sound sources. Further investigation should be performed to establish the limitations of the method in such conditions.

5.5 Measurement methodology

The Reference-Related method in combination with the measurement technique Scan & Paint yields a scanning panel contribution approach that allows for the identification of individual source contributions. Each sound pressure contribution can be calculated according to Equation 5.7 and Equation 5.8. As shown in this section, the input datasets are determined via two independent measurement steps: the acquisition of the acoustic excitation in operational conditions and the characterisation of the sound propagation from the structure surface toward a reference position. In addition, the use of a single video camera for conventional Scan & Paint may not be suitable to locate the probe during the measurements of a complex environment such as a cabin interior. This issue is addressed in the last part of this section.

5.5.1 Operational measurement

The first measurement step aims to evaluate the acoustic excitation of the vibrating structure in stationary operational conditions. Scanning measurements are performed near the vibrating panels following the Scan & Paint procedure previously introduced in Chapter 3. An additional reference microphone is needed in order to apply the Reference-Related method. The reference sensor establishes a relative link between all data captured along the scanned paths. Figure 5.4 shows an sketch of this procedure.

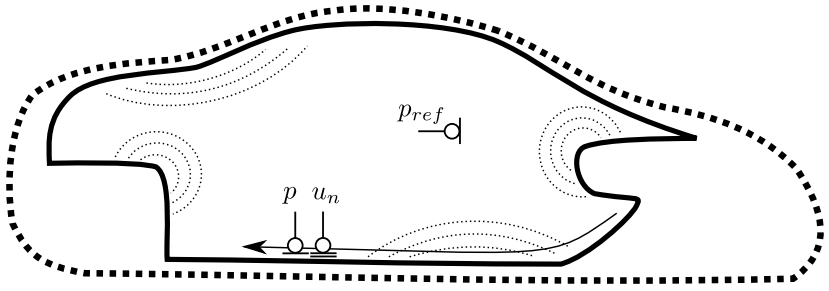

FIGURE 5.4: Sketch of the measurement procedure in operational conditions.

5.5.2 Reciprocal transfer functions

The second measurement step involves the assessment of acoustic propagation paths from each part of the structure to a reference position. For this purpose, the assessed noise radiation object should be switched off. This measurement follows a reciprocal approach: the sound field is excited by a volume velocity source (VVS), i.e. a source of controlled acoustic output that has an omni-directional radiation pattern, while scanning

measurements are performed near the structure. Figure 5.4 illustrates the evaluated scenario.

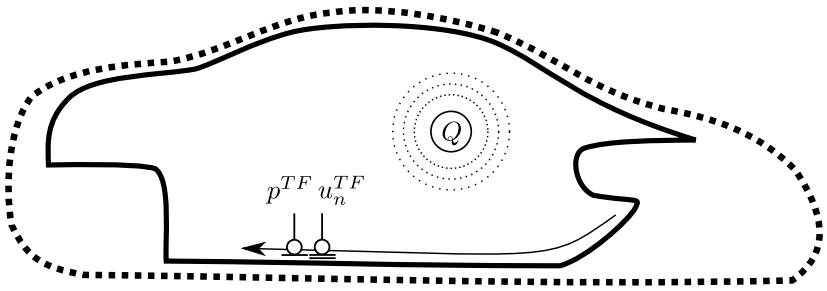

FIGURE 5.5: Sketch of the of the transfer paths measurement procedure.

Frequency limitations of reciprocal transfer function measurements are constrained by the effective working range of the monopole source used to excite the sound field. In practice, the dimensions of the source should be proportional to the wavelength of the emitted sound field. Therefore, depending on the application, it may be necessary to combine the results of measurements with multiple VVSs in order to cover a broad frequency range.

5.5.3 Camera positioning

A single camera is sufficient to locate the probe during the scanning process providing excitation sources are visible within a plane. However, this is not necessarily the case for many industrial applications. Even using a 360° camera the view may be obstructed by obstacles. Moreover, the camera should be placed perpendicular to the measurement area to minimise visual errors, as shown in Section 3.5. Therefore, complex structures usually require the use of multiple cameras, the number and configuration of which will depend upon the dimensions and shape of the evaluated scenario.

5.6 Experimental evaluation

Several validation experiments were undertaken in [14] proving that the proposed scan-based panel contribution methodology works well in laboratory conditions. Diverse practical cases were also successfully investigated, such as a helicopter cabin interior [18] and a loudspeaker cabinet [27]. Given the importance of the automotive industry among the NVH sector, this section is focused on the evaluation of a test performed in a car interior, initially introduced in [29].

5.6.1 Experimental set-up and instrumentation

The cabin interior of a family class car "Toyota Avensis" has been investigated. The vehicle was studied using 10 cameras distributed as follows: rear and front doors (4 cameras); dashboard, front window and front floor (1 camera); ceiling (1 camera); trunk door, sides and bottom (4 cameras). As mentioned, the probe position is calculated relative to the video, hence obtaining two dimensional image coordinates which cannot be directly related to the actual position of the probe in the three dimensional space inside the cabin. Therefore, the cameras were fixed during the testing process in order to combine operational data and transfer function measurements. Figure 5.6 shows two pictures of the measurement setup: distribution of cameras across the cabin interior (left) and positioning of the volume velocity source (VVS) used in the reciprocal transfer function measurements (right).

FIGURE 5.6: Distribution of cameras across the car interior (left) and monopole source (right) used in the scan-based panel contribution analysis investigation.

Each camera was used individually for filming the measurement process of different car areas. All scanning data was acquired using a sound intensity p-u probe which was moved near the cabin interior surfaces. In addition, a reference particle velocity sensor at the VVS and a GRAS random incidence microphone fixed at the driver's seat were required to measure the volume velocity of the source Q and the reference sound pressure p_{ref}, respectively. The total time taken for the test, including set-up and data acquisition, was approximately one day.

5.6.2 Measurement process

Operational measurements were performed on a highway whilst driving at a constant speed of approximately 80 km/h. Figure 5.7 shows the sound pressure levels recorded during the different scanning sessions. As can be seen, the variability at low frequencies is acceptable but increases with frequency, potentially limiting the accuracy of the results at high frequencies.

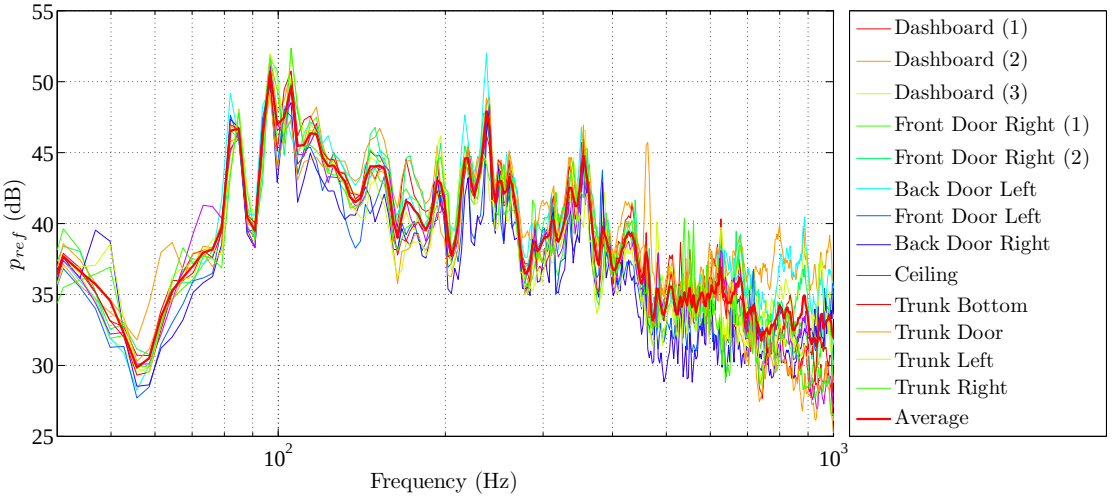

FIGURE 5.7: Average sound pressure of each scanning session recorded at the reference position in operational conditions.

The transfer paths between all the surface areas and the reference sensor were measured reciprocally, i.e. placing a volume velocity source at the same spot of the previously used reference microphone. Since the frequency region of interest was below 500 Hz, the use of a single low-frequency monopole source served the purpose. It should be noted that it would be necessary to place a new monopole at additional reference positions and scan all the surfaces once more in order to calculate the synthesised sound pressure at other listener positions.

5.6.3 Measurement validation

A common method for determining the validity of the measurement process is to compare the sound pressure measured at the reference position and the estimated, or synthesised, sound pressure obtained from the summation of all panel contributions. Figure 5.8 shows very similar results, especially between 50 Hz and 500 Hz, providing evidence of the successful performance of the measurement methodology.

Three factors are mainly responsible for the small discrepancies at higher frequencies: the variability between different measurements, the frequency limitations of the source used and the influence of the operator body. As shown in Figure 5.7, the reference pressure varies substantially at higher frequencies, which implies that the evaluated structure was exposed to slightly different excitation loads during the data acquisition process. Lack of stationarity between different measurements increases then the total estimation error. Furthermore, the sound source used during the transfer function measurements only has an omni-directional radiation pattern below 500 Hz. Directional radiation characteristics of the source above that frequency can decrease the quality of the acoustic

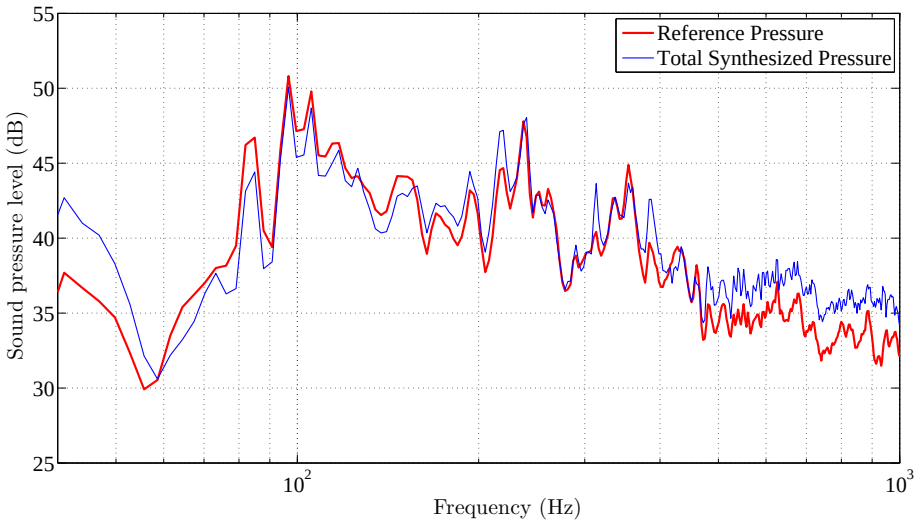

FIGURE 5.8: Comparison of the measured and synthesised reference sound pressure.

transfer functions. In addition, the operator body becomes an acoustic obstacle when wavelength is short, which may have a significant impact at high frequencies.

On the other hand, the estimation error induced by the measurement variance should be smaller at low frequencies since the reference sound pressure presents fairly consistent results. The manipulation noise [24] and spectral estimation errors may be responsible for the mismatch found. The use of scanning techniques implies assessing short time series which can yield significant spectral estimation errors at low frequencies [115].

5.6.4 Analysis of results

The acquisition of data using a sound intensity p-u probe in operational conditions and with a VVS provides detailed information about not only the vibrating structure under assessment but also the acoustic environment. The investigation procedure can be undertaken as follows: spatial discretisation of the scanning data, source localisation, analysis of the transfer functions and visualisation of pressure contribution maps.

Sound localisation maps are useful to determine the origin of the noise at certain problematic frequency regions. As shown in Figure 5.8, it was found that the average sound pressure level perceived at the reference position is maximum at 95 Hz. As such, the data analysis is focused upon this frequency region. The assessment of the car's ceiling is of particular interest due to its high excitation with respect to other areas and its proximity to the reference position. Figure 5.9 shows results of the different investigation stages of the ceiling at 95 Hz.

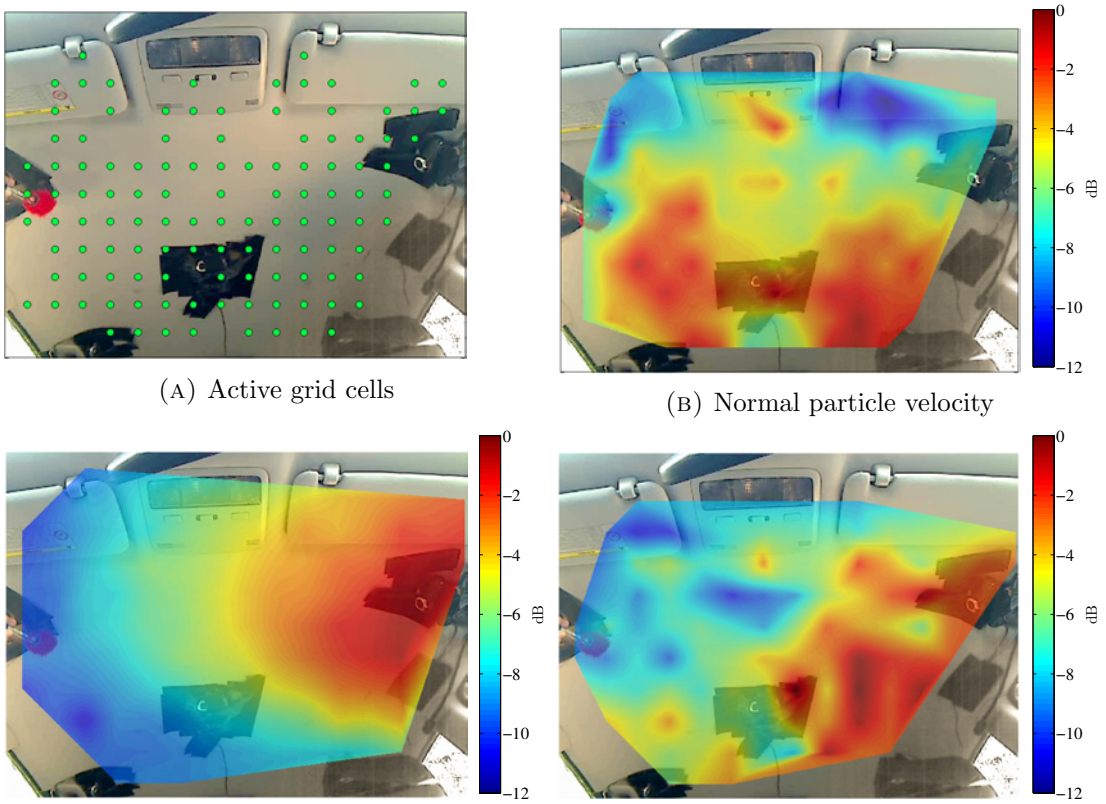

(A) Active grid cells

(B) Normal particle velocity

(C) Acoustic transfer function

(D) Sound pressure contribution

FIGURE 5.9: Measurement results of the car's ceiling at 95 Hz each normalized to its highest value.

Firstly, the recorded signals were segmented according to the position of the probe by applying the grid discretisation algorithm (see Section 3.2.1). In Figure 5.9 (A), the green dots represent the active points of the grid, previously denoted as $\boldsymbol{\Upsilon}_{\mathbf{m,n}}$, which have associated signal segments from both operational and transfer function measurements. This discretisation method enables the combination of several measurements provided that the camera position remains constant during the data acquisition process. Camera miss-alignments with the normal axis of the measured surface can potentially have an impact on the reconstruction of the total sound pressure. Further research should be undertaken to define the errors introduced by tracking and discretisation in the proposed scan-based panel contribution methodology.

The normal particle velocity shown in Figure 5.9 (B) reveals a symmetric excitation pattern which is most likely due to an operational resonant mode of the car's ceiling. Notably, the sound map shows a large dynamic range despite the low frequency assessed. As demonstrated in Chapter 4, the direct visualisation of the normal particle velocity near a vibrating surface offers a useful approach for localising noise sources due to its frequency-independent resolution and robust signal-to-noise ratio.

In complex environments such as a car interior, it is important to understand the acoustic effects caused by the cavity itself. An acoustic mode can largely amplify local excitations that in a near-field map may not seem problematic. Figure 5.9 (C) illustrates the transfer function map between the VVS and the sound pressure measured near the ceiling. The transfer function between these two quantities defines how the normal particle velocity emitted by the surface is related to the sound pressure perceived at the reference position, i.e. a spatial weighting factor. As can be seen, the sound map shows a progressive decay as the distance from the reference position (located at the driver's seat, on the bottom right hand side of the image) is increased. In this case, there is no evidence of a particular effect caused by the cabin interior.

The outcome of a transfer path analysis method is the computation of the pressure contribution of different parts of the structure, which ultimately enables the ranking of identified sound sources. The implementation of Equation 5.8 for a single grid cell results in the local contribution of a specific area. Figure 5.9 (D) presents the sound pressure contribution map of the car's ceiling. This colormap is the result of weighting the excitation input of the structure with the propagation paths. Since the panel normal particle velocity was far greater than sound pressure at the assessed frequency, the "hard-wall" assumption was suitable to express the contribution map as the combination of normal particle velocity and transfer functions. It should be noted that sound contribution maps do not consider the effect of partially-correlated neighbouring sources since every grid point is computed individually. However, the preserved relative phase term plays an important role when the contributions of multiple panels are added, hence during the calculation of the sound pressure at the reference position.

In addition, the contributions of different areas have been computed in order to rank the noise sources distributed across the cabin interior. Figure 5.10 shows the source ranking for the 95 Hz peak using the linear pressure contribution values on a percentage scale. As can be seen, the ceiling is the dominant noise source, followed by the driver's door and the trunk door. The large differences between contributions suggest that the application of acoustic treatment to the car's ceiling could result into a substantial reduction of the noise perceived at the reference position.

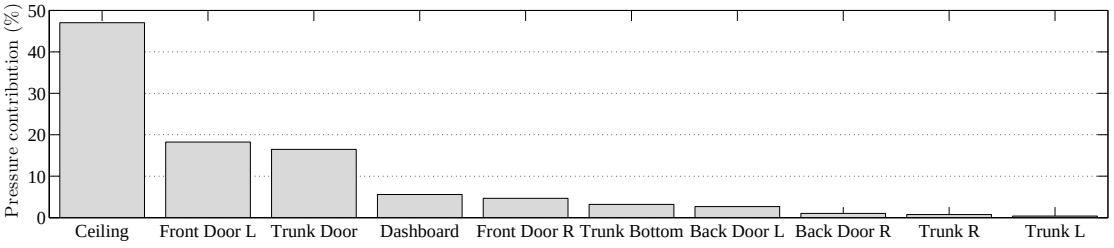

FIGURE 5.10: Example of source ranking of different areas at 95 Hz.

5.7 Comparison of scanning panel contribution analysis with current solutions

Most conventional panel contribution techniques are highly time consuming due to the high number of measurement points involved. In contrast, manual sweeps of a single probe, as performed with the proposed method, can acquire measurement data more quickly and therefore speed up the testing procedure. This methodology requires only one day for performing both reciprocal transfer functions and operational radiation measurements across a car interior.

The cost of the measurement equipment is another crucial factor that differentiates the proposed method from conventional solutions. Not only the large number of transducers but also the multichannel acquisition hardware required by array-based solutions raise the cost of other systems. In contrast, the scanning method involves few sensors and acquisition channels.

The main problems of conventional scanning techniques is the requirement for time stationary conditions. However, although some industrial applications assess transient or impulsive noise, most problems can be studied using stationary conditions.

Events such as accidentally touching the surface or producing noise while the probe is moving, are inherent to the measurement technique. Nevertheless, they can be detected and avoided during the post-processing stage.

The lack of an absolute probe tracking system yields positioning errors if the distance between probe and surface is not maintained. Furthermore, some panels (such as the drivers footwell) cannot be measured easily due to the lack of a clear line of sight. The incorporation of a novel three dimensional positioning system could solve most errors introduced by the current tracking procedure.

Fixed point measurements often suffer from large discretisation errors; choosing a set of fixed positions involves a high risk of missing sound sources or acoustic leakages. Moreover, the resolution of techniques such as acoustic holography or beamforming often encounter strong frequency limitations due to the measurement conditions and the algorithms applied, especially in the lower frequency range. The spatial resolution of the sound maps obtained with the proposed scanning method is high, frequency independent, and can be modified according to the measurement data.

5.8 Summary

A novel scan-based measurement technique for performing panel contribution analysis has been introduced. The proposed method involves far less measurement time and costs than traditional array based techniques. The theoretical foundations of the measurement technique have been reviewed along with the fundamentals of conventional methods. A practical case, a car interior, has been evaluated using the presented measurement methodology. The similarity between the estimated and measured sound pressure at the listener's position demonstrates the accuracy of the method. It should be noted that good results are obtained even at low frequencies, which most conventional measurement methods are not able to assess.

Normal particle velocity maps have been proven useful for studying the excitation distribution regardless of the frequency range of interest. On the other hand, transfer function mapping has been used to reveal amplification or attenuation effects caused by the geometry and properties of an acoustic environment. Finally, pressure contribution calculations enabled the ranking of detected sound sources; this information can be used for deciding where to apply acoustic treatments to reduce the noise perceived at an specific location.

Chapter 6

Virtual Phased Arrays

6.1 Introduction

There are many applications which require the utilisation of microphone arrays in order to localise sound sources. However, the number of sensors required to achieve reliable results is often prohibitive, particularly if the frequency range of interest is wide. Furthermore, the measurement resolution would depend upon the number of transducers used and their respective positions (the geometry of the array). If the array consists of too many sensors, it becomes acoustically significant, biasing the characterisation of the sound field.

A "Virtual Phased Array" approach can be taken to avoid many practical constraints of conventional multichannel systems, assuming the sound field is time stationary. The proposed technique enables the characterisation of a measurement area as a set of "virtual transducers" with a rather simple measurement system. A single moving sensor is used to acquire data continuously across the space whilst a static reference microphone records the event. The acoustic signal is later split into blocks which have different associated spatial positions. Each block, or segment of the recorded signal, represents an element of the virtual phased array. The phase estimation is computed relative to the fixed reference sensor. The use of a single moving sensor avoids array calibration issues and limitations derived from using fixed array geometry. This measurement method can potentially address many common problems due to its low cost and straightforward acquisition process.

The idea of creating synthetic or virtual arrays using a limited number of sensors has also been explored in other disciplines, most being focused upon enhancing the possibilities of conventional radars (Synthetic Aperture Radar or SAR) [155, 156] and sonar systems

(Synthetic Aperture Sonar or SAS) [157, 158]. The majority of methods developed for SAS and SAR share common characteristics which differ from the proposed noise localisation technique; they are active systems based on the coherent addition of many pings across the space [159], whereas the presented approach is based upon passive synchronisation via a fixed reference sensor.

In previous works by the author, virtual phased arrays have been shown to work remarkably well in laboratory conditions for mid-high frequencies [32] with multiple beamforming algorithms [160]. The performance of virtual phased arrays has also been tested successfully at lower frequencies in the surroundings of a gas plant [22, 33]. Furthermore, this novel technology has been proved suitable for evaluating complex noise sources in a wide frequency range, for instance in static tests of vehicle noise [15]. In addition, several deconvolution methods have been adapted and tested for virtual phased arrays, achieving improvements in spatial resolution, dynamic range and accuracy [34]. The work presented in the following sections is based upon the aforementioned publications, compiling the theoretical and experimental foundations of VPA developed thus far.

This chapter presents the theoretical basis for localising sound sources using only one or two fixed microphones and a moving sensor. The beamforming algorithms delay-and-sum, MUSIC and least squares are adapted to VPA. Furthermore, the beamformer output has been significantly enhanced by applying deconvolution techniques. A novel iterative algorithm is proposed and compared with well established deconvolution methods via simulations. Next, a practical implementation of the technique is suggested and evaluated for several experimental scenarios. In addition, the advantages and disadvantages of the technique are discussed considering its theoretical and practical limitations.

6.2 Foundations of VPA

The theoretical basis of the proposed measurement technique is studied in this section. It has been divided into two parts: an introduction to the method used to preserve the relative phase information of the sound field; and a description of the synthesis process required to generate the cross covariance matrix.

6.2.1 Relative phase information

It is common practice acquiring phase information at multiple positions using sensor arrays to maintain time synchronism. The absolute synchronisation of data acquired at different time intervals is only possible when dealing with strictly deterministic signals

and therefore it is unsuitable for most practical cases [116]. Nevertheless, if the sound field can be assumed time stationary, relative phase variations can be characterised at different time instances, also enabling the use of scanning techniques for assessing spatial phase distribution. The relative phase differences between any pair of points in the sound field can be obtained by calculating their cross-spectrum or transfer function, due to the resulting expressions remain constant during time. It is therefore convenient to study the sound field produced by a point source in order to gain a better understanding of this concept. The complex pressure at any point in a sound field caused by a pulsating sphere at a distance r can be defined as [111]

$$p(r,t) = \frac{A}{r}\, e^{j(\omega t - kr)} \tag{6.1}$$

where A is determined by the source features, as shown below, k is the wavenumber, ω is the frequency of the sinusoidal movement and r is the distance from the centre of the sphere. Consider a sphere of radius a, vibrating radially with complex speed $U_o e^{j\omega t}$, where the displacement of the surface is much less than the radius, $U_o/\omega << a$. The acoustic pressure of the fluid in contact with the sphere is given by Equation 6.1 evaluated at $r = a$. The pressure at the surface of the source can be defined as[1]

$$p(a,t) = Z_0 U_0 cos(\theta_a)\, e^{j(\omega t - ka + \theta_a)} \tag{6.2}$$

where Z_0 is the characteristic acoustic impedance of the medium ($\rho\, c_0$), and since $\theta_a = \coth(ka)$, it is a function of the ratio between source distance and wavelength. Comparing Equation 6.1 and Equation 6.2, it can be inferred that A is temporally and spatially independent, and it can be expressed as such

$$A = Z_0 U_0 a cos(\theta_a)\, e^{j(ka + \theta_a)} \tag{6.3}$$

The relative phase difference between two points $\mathbf{x}$ and $\mathbf{y}$ can be obtained by calculating the product between the Fourier Transform of pressure at one point $p(\mathbf{y},\omega)$ and the complex conjugate Fourier Transform of the pressure at the other point $p^*(\mathbf{x},\omega)$, i.e.

$$p^*(\mathbf{x},\omega)p(\mathbf{y},\omega) = \frac{A^2}{r_x r_y}\, e^{jk(r_x - r_y)} \tag{6.4}$$

where r_x and r_y are the distances between the sound source and positions $\mathbf{x}$ and $\mathbf{y}$, respectively. Equation 6.4 illustrates that the phase information is now only dependent upon the wavenumber k and the difference in distance between the two points $(r_x - r_y)$. So far, arbitrary signals have been considered in the derivation but for real scenarios it

[1]This is consistent regarding small amplitude variations of linear acoustics

would be necessary to deal with random signals of finite length [116]. One way to obtain relative phase information between two data segments of length T is by computing their cross-power spectral density (CPSD) [161]. The CPSD between two sound pressure signals can be defined as

$$S_{xy}(\omega) = \lim_{T\to\infty} \frac{E\left[p^*(\mathbf{x},\omega)p(\mathbf{y},\omega)\right]}{T} \tag{6.5}$$

where $E[.]$ denotes the expected value. As shown in Equation 6.5, phase information is preserved by computing the CPSD. Relative phase depends upon frequency and the difference in distance between the points and the sound source. In order to apply Equation 6.5 to scanning techniques it is necessary to reformulate the problem considering a fixed transducer and a sensor that changes position during time $\mathbf{x}(t)$. The discretisation of the measurement data introduced in Section 3.2 enables the fragmentation of continuous signals to compute the CPSD of a set of points in a space which will have associated magnitude and relative phase values, thus creating a set of "virtual phased transducers". In summary, it has been shown that relative phase changes in a sound field can be mapped by taking the cross-power spectral density estimates between two transducers: one at a fixed position and the other scanning an area of the sound field.

6.2.2 Covariance matrix synthesis

The covariance matrix (also called the cross-spectral matrix or spectral matrix) is essential for many powerful source localisation techniques based on random matrix theory [91, 93, 94]. A base of statistically independent components comprising the recorded dataset can be established via the eigenvalue decomposition of the covariance matrix. This can be used to distinguish between signal subspace (high eigenvalues) and noise subspace (low eigenvalues).

The covariance matrix is commonly calculated using data synchronously acquired. For an array of pressure microphones such as $\mathbf{p}(\omega) = [p(\mathbf{x}_1,\omega), p(\mathbf{x}_2,\omega), ..., p(\mathbf{x}_L,\omega)]^T$, the corresponding covariance matrix can be defined as

$$\mathbf{C}(\omega) = E\left[\mathbf{p}(\omega)\mathbf{p}(\omega)^H\right] = \begin{bmatrix} S_{x_1x_1}(\omega) & ... & S_{x_1x_L}(\omega) \\ \vdots & \ddots & \vdots \\ S_{x_Lx_1}(\omega) & ... & S_{x_Lx_L}(\omega) \end{bmatrix} \tag{6.6}$$

Conventional scan-based measurement methods are not compatible with Equation 6.6 since information is not acquired at different positions simultaneously. However, as shown in Section 6.2.1, cross-spectra calculations between a fixed and a moving sensor

allows the relative phase distribution of the sound field to be gathered. Reformulating Equation 6.5 into vector form, for L virtual transducers yields

$$\mathbf{S}_{\mathbf{x_i}\,\mathbf{y}}(\omega) = [S_{x_1\,y}(\omega) \quad S_{x_2\,y}(\omega) \;\ldots\; S_{x_L\,y}(\omega)]^T \tag{6.7}$$

If the position of the reference sensor coincides with one of the array elements, such as $\mathbf{y} = \mathbf{x}_1$, then it can be inferred that the transfer function vector $\mathbf{S}_{\mathbf{x_i}\,\mathbf{x_1}}(\omega)$ and its conjugated form will equal a row and column of the covariance matrix. The lack of cross-spectral terms between each transducer position prevents undertaking a direct reconstruction of $\mathbf{C}(\omega)$ using only transfer functions between a moving and fixed sensor. However, if far field conditions are satisfied, the covariance matrix $\mathbf{C}(\omega)$ is guaranteed to be Hermitian. Such matrix structure allows for the reconstruction of the full covariance matrix by using its symmetric properties for planar square or rectangular array geometries with equally spaced elements[2]. Figure 6.1 illustrates the structure of the covariance matrix obtained with a 3×3 square planar array in ideal far field conditions.

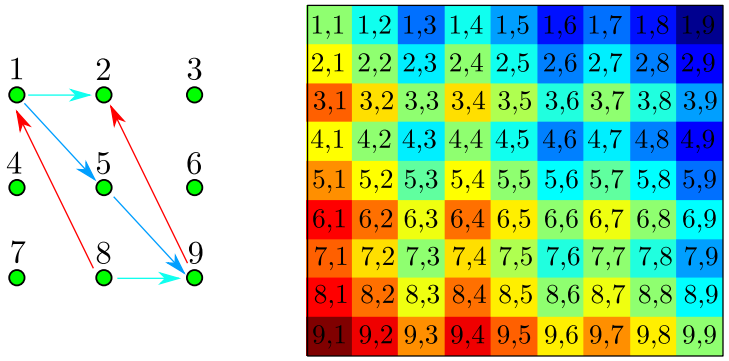

FIGURE 6.1: Sketch of a 3 x 3 square planar array (left) and its corresponding covariance matrix (right) representing the delay between the different element positions (green dots) with colours.

The arrows between the array elements represent the relative time delay between element pairs. On the right hand side, each term of the covariance matrix is displayed with a colour corresponding to its phase content. As shown, the matrix follows a repetitive pattern, 3×3 block Toeplitz matrix with 3×3 Toeplitz blocks, i.e. a Toeplitz-block-Toeplitz (TBT) matrix. There is a lot of redundant information in such a matrix structure since

$$S_{x_i x_j}(\omega) = S_{x_q x_l}(\omega) \;\; / \;\; \mathbf{x}_i - \mathbf{x}_j = \mathbf{x}_q - \mathbf{x}_l \tag{6.8}$$

In the particular case presented in Figure 6.1, the above expression can be applied to show that for instance $S_{x_9 x_2}(\omega) = S_{x_8 x_1}(\omega) = S^*_{x_1 x_8}(\omega) = S^*_{x_2 x_9}(\omega)$. It is therefore possible to reconstruct the whole matrix by using the unique components following a

[2] A discussion regarding the error implication of the far field assumption is covered in [32]

TBT pattern; information that can be gathered using only a single reference sensor at one of the corners of the array.

In conclusion, it has been shown that a square or rectangular planar VPA geometry with a reference sensor enables the synthesis of a full rank covariance matrix under far field measurement conditions. Further research should be undertaken to expand this theory for arrays with irregular geometries.

6.3 Source localisation and DOA algorithms

One common application for acoustic sensor arrays is the direction of arrival (DOA) estimation of propagating wavefronts for the localisation of noise sources. Generally, array geometry information is used in combination with the processed signals recorded by each sensor in order to create spatially discriminating filters [94]. This spatial filtering operation is also known as beamforming. In this section several frequency domain beamforming methods compatible with VPA are studied.

6.3.1 Delay-and-sum beamforming

Conventional delay-and-sum beamforming algorithms steer a beam to a particular direction by computing a properly weighted sum of the individual sensor signals. As such, this procedure results in the addition of signals coming from the direction of focus, maximising the energy of the beamformer output whilst signals from other directions are attenuated.

Asynchronous time acquisition performed with virtual phased arrays implicitly constrains the range of applicable localisation techniques to frequency domain beamforming methods. A compatible delay-and-sum algorithm can be defined as

$$B(\boldsymbol{\sigma}, \omega) = \frac{1}{L} \sum_{i=1}^{L} w_i S_{x_i\, y}(\omega) e^{j\phi(\boldsymbol{\sigma}, \omega)} \tag{6.9}$$

where L is the total number of virtual transducer positions covered by the moving sensor, w_i is a weighting factor applied to each cross-spectrum and $\phi(\boldsymbol{\sigma}, \omega)$ is a phase term which allows the beamformer to be focused toward a certain direction $\boldsymbol{\sigma}$. If the distance to the source is known beforehand, it is possible to express $\phi(\boldsymbol{\sigma}, \omega)$ as a function of the wavelength k and the separation differences between source and sensors $(r_{x_i} - r_y)$. In

addition, an attenuation term can be added to quantify the sound pressure emitted

$$B_{NF}(\omega) = \frac{1}{L}\sum_{i=1}^{L} w_i S_{x_i y}(\omega) r_{x_i} r_y e^{jk(r_{x_i} - r_y)} \tag{6.10}$$

It is impossible to provide sound pressure information at the source if the distance is unknown. However, if the array is sufficiently far away, the resulting sampled wavefronts can be regarded as plane waves. Therefore, it is feasible to estimate the location of the noise sources for far field conditions by defining $\phi(\boldsymbol{\sigma}, \omega)$ as the scalar product between the moving sensor position $\mathbf{x_i}$ and a unitary vector $\zeta^{\boldsymbol{\sigma}}$, oriented to the direction $\boldsymbol{\sigma}$ [91]

$$B_{FF}(\omega) = \frac{1}{L}\sum_{i=1}^{L} w_i S_{x_i y}(\omega) e^{jk(\zeta^{\boldsymbol{\sigma}} \cdot \mathbf{x}_i)} \tag{6.11}$$

Beamforming maps can be obtained by evaluating B_{FF} for different directions of propagation $\zeta^{\boldsymbol{\sigma}}$. Several coordinate systems can be implemented depending on the array and source geometry [91, 162]. Spherical coordinates have been found to be the most suitable for combining a background image and the beamformer output without using prior information of the sound sources. Consequently, most of the source localisation maps presented in this chapter express the results in terms of azimuth angle θ and elevation angle φ.

6.3.2 MUSIC

The term Multiple Signal Classification (MUSIC) is used to describe experimental and theoretical high resolution algorithms that provide asymptotically unbiased estimates for a variety of applications [163–165]. This section focusses upon the special case concerning the determination of the direction of arrival of multiple wavefronts.

MUSIC is a subspace based method that relies on the eigen-decomposition of the covariance matrix. The orthogonal properties of this approach allows for a signal subspace that contains information about S uncorrelated sources received by the array to be distinguish from a noise subspace describing the low energy components of the signals. Following [91], the covariance matrix $\mathbf{C}(\omega)$ can be modelled as

$$\mathbf{C}(\omega) = \mathbf{V_s}\,\mathbf{A_s}\,\mathbf{V_s}^H + \sigma_n^2 \mathbf{I} \tag{6.12}$$

where $\mathbf{V_s} = [\mathbf{v}(\boldsymbol{\sigma}_1), \mathbf{v}(\boldsymbol{\sigma}_2), \mathbf{v}(\boldsymbol{\sigma}_3), ..., \mathbf{v}(\boldsymbol{\sigma}_S)]$ is an array steering matrix of size $L \times S$, σ_n^2 is the noise variance, $\mathbf{I}$ is the identity matrix of size $L \times L$ and $\mathbf{A_s}(\omega)$ is an $S \times S$ matrix that contains the signal eigenvalues. In practice, the covariance matrix of the

signal subspace ($\mathbf{V_s}\,\mathbf{C_s}\,\mathbf{V_s}^H$) is not directly available from measurements and it must be estimated from the covariance matrix of the data. The eigen-decomposition of $\mathbf{C}$ results in a steering vector $\mathbf{V} = [\mathbf{V_s}\ \mathbf{V_n}]$ that has S eigenvectors which describe the signal subspace and $L - S$ which form the noise subspace as such

$$\mathbf{V_n} = [\mathbf{v}(\boldsymbol{\sigma}_{S+1}), \mathbf{v}(\boldsymbol{\sigma}_{S+2}), \mathbf{v}(\boldsymbol{\sigma}_{S+3}), ..., \mathbf{v}(\boldsymbol{\sigma}_L)] \tag{6.13}$$

The noise subspace eigenvectors are orthogonal to array steering vectors at the angles of arrivals $\boldsymbol{\sigma}_1, \boldsymbol{\sigma}_2, \boldsymbol{\sigma}_3, ..., \boldsymbol{\sigma}_S$. Therefore, the DOA can be estimated using the orthogonal property between the signal steering vectors and the eigenvectors of the noise subspace $\mathbf{V_n}$. The MUSIC pseudo-spectrum is given as

$$P_{MUSIC}(\boldsymbol{\sigma}) = \frac{1}{|\mathbf{v}(\boldsymbol{\sigma})^H \mathbf{V_n} \mathbf{V_n}^H \mathbf{v}(\boldsymbol{\sigma})|} \tag{6.14}$$

The last expression does not give a quantitative estimation of the sound sources but exhibits peaks in the vicinity of the true DOAs [93]. The use of an orthogonal basis implies that only uncorrelated sound sources are appropriately modelled. If signals are partially correlated, the vectors which describe the principal directions of variance of the data are no longer orthogonal[3], and, as a result, the covariance matrix becomes singular. Therefore, the performance of the conventional MUSIC algorithm degrades significantly depending upon the degree of correlation among sources.

6.3.3 Least Squares Beamformer

The least-squares (LS) criterion is a well-known method which can be used, for instance, to design FIR filters [166], 2D-filters [167] or beamforming algorithms [168]. In this section a review of the problem is given along with an expression for implementing a beamforming technique based on a least-squares solution.

A general model of the sound field produced by S sources perceived at L array element positions can be formulated as follows

$$\mathbf{Y} = \mathbf{Hq} - \sigma_n^2 \mathbf{W_n} \tag{6.15}$$

where $\mathbf{H} = [\mathbf{h}(\boldsymbol{\sigma}_1), \mathbf{h}(\boldsymbol{\sigma}_2), \mathbf{h}(\boldsymbol{\sigma}_3), ..., \mathbf{h}(\boldsymbol{\sigma}_L)]$ is an $L \times S$ array mixing matrix, $\mathbf{q} = [q_1, q_2, q_3, ..., q_S]^T$ is a $S \times 1$ vector that contains the source features and σ_n^2 is the variance of the background noise $\mathbf{W_n}$. The algorithm provides an approach to obtain the

[3]The correlation coefficient between two sources can be explained as the cosine of the angle between the two vectors which describe the principle directions of variance of the data.

DOA information contained in $\mathbf{H}$ by measuring the error between certain propagation models and the acquired dataset. A cost function Ψ that quantifies the estimation error can be defined as

$$\Psi = (\mathbf{Y} - \mathbf{H}\,\mathbf{q})^H(\mathbf{Y} - \mathbf{H}\,\mathbf{q}) \tag{6.16}$$

Next Ψ can be derived with respect to $\mathbf{q}$ to find the minimum of the cost function, i.e.

$$\frac{\mathrm{d}\Psi}{\mathrm{d}\mathbf{q}} = 2\mathbf{H}^H\mathbf{H}\,\mathbf{q} - 2\mathbf{H}^H\mathbf{Y} = 0 \rightarrow \mathbf{q} = (\mathbf{H}^H\mathbf{H})^{-1}\mathbf{H}^H\mathbf{Y} \tag{6.17}$$

Consequently, Equation 6.17 presents an optimal solution for the source features which is only dependent upon the measured data and the hypothetical positions of the sources. It is important to calculate the most likely solution, and as such a Least-Square expression is computed for each direction of arrival. The output of the least square beamformer is then defined as

$$S_{LS} = \frac{1}{\min|\mathbf{Y} - \mathbf{H}(\mathbf{H}^H\mathbf{H})^{-1}\mathbf{H}^H\mathbf{Y}|} \tag{6.18}$$

6.4 Deconvolution algorithms for VPA

The spatial resolution, signal-to-noise ratio and dynamic range can be enhanced by using deconvolution algorithms. In this section, two conventional deconvolution methods are reviewed and a novel approach, the Iterative Sidelobe Cleaner Algorithm (ISCA), based on the work previously presented in [34] is introduced.

6.4.1 Fundamentals of iterative algorithms

The beamformig output can be related to the sources present in the sound field by means of the beamformer's point-spread function (PSF). The PSF, defined as the beamformer response to a point source with unit strength at an arbitrary position, determines the characteristics of the beamformer in terms of shape of the main beam and side lobes [169, 170].

In the presence of several uncorrelated sound sources, the signal perceived at a position $\mathbf{x}$ can be modelled as

$$y(\mathbf{x}) = \sum_{s=1}^{S} q(\mathbf{x}_s)H(\mathbf{x}|\mathbf{x}_s) \tag{6.19}$$

where q is the source distribution, $H(\mathbf{x}|\mathbf{x}_s)$ is the PSF at the array ($\mathbf{x} = [\mathbf{x}_1, \mathbf{x}_2, ...\mathbf{x}_L]$) due to a point source located at position ($\mathbf{x}_s$); s being the source index defined by $s = 1, 2, ..., S$. This relationship makes the recovery of the source distribution from

the measured beamformer map and the beamformer's PSF possible, by means of a deconvolution procedure, implying that the distribution of sound sources must be non-negative ($q(\mathbf{x}_s) \geq 0$). This is an inverse problem, which in matrix notation can be rewritten as

$$\mathbf{Y} = \mathbf{Hq} \tag{6.20}$$

where the components of the vectors $\mathbf{Y}$ and $\mathbf{q}$ are $Y(\mathbf{x})$ and $q(\mathbf{x}_s)$. Each vector has a length L, corresponding to the total number of measurement points. On the other hand, $\mathbf{H}$ is an $L \times L$ matrix that contains the PSF for one source located at a particular position $\mathbf{x}_s$ in each column.

6.4.2 DAMAS

In 2004, Brooks and Humphreys [169] suggested a method to solve the inverse problem presented in Equation 6.19 and Equation 6.20 in order to recover the position and the strength of acoustic sources. The method, the called Deconvolution Approach for the Mapping of Acoustic Sources (DAMAS), is based on an iterative algorithm.

The first step of the algorithm is the initialisation of the iteration index, $n = 0$, and the choice of an estimate of q, $q_i^{(0)}$. Typically this value is set to zero for the entire region of interest,

$$q_i^{(0)} = 0, \qquad i = 1, ..., L \tag{6.21}$$

Then the estimate of the source distribution is computed as

$$q_i^{(n+1)} = \max\left(q_i^{(n)} - \frac{r_i^{(n)}}{H_{ii}}, 0\right) \tag{6.22}$$

where $r_i^{(n)}$ can be considered as the residual of the i-th component in the step n defined as

$$r_i^{(n)} = \sum_{j=1}^{i-1} H_{ij} q_j^{(n+1)} + \sum_{j=i}^{L} H_{ij} q_j^{(n)} - Y_i \tag{6.23}$$

were H_{ij}, Y_i and $q_i^{(n)}$ are the components of the matrix $\mathbf{H}$, and the vectors $\mathbf{Y}$ and $\mathbf{q^{(n)}}$, respectively.

Once the iteration index is incremented, the steps given by Equation 6.22 and Equation 6.23 are repeated at each iteration until the source distribution $\mathbf{q}$ converges. Note that although the result converges to a certain value, this method does not guarantee

the exact solution [171]. It is common to make use of the residual presented in Equation 6.23 for analysing the convergence. If $q_i^{(n)}$ converges to the exact solution then the residual $r_i^{(n)}$ tends to zero when the number of iterations n is increased.

This procedure makes it possible to not only localise sound sources, but also to determine their strength. This is achieved by summing the mean-squared values of the recovered sound distribution over the region of interest.

6.4.3 Non-Negative Least Squares (NNLS)

Non-Negative Least Squares is a well established deconvolution technique, originally proposed by Lawson and Hanson in 1974 [172]. The method algebraically solves the deconvolution problem in Equation 6.20 by minimising the square sum of the residuals, subject to the condition that there are no sources of negative strength ($\mathbf{q} \geq 0$), making it robust. The method is well defined in the sense that if a solution exists, convergence is guaranteed.

A gradient approach is studied in this section, in which no matrix factorisations are required, as described in [171]. The NNLS algorithm aims to minimise the squared sum

$$||\mathbf{Hq} - \mathbf{Y}||_2 \tag{6.24}$$

A brief overview of the steps for the gradient type implementation is given below; a more detailed description can be found in [171]. Firstly, a residual vector is estimated from a given solution $\mathbf{q}^{(n)}$, based upon which the gradient of the residual vector $\mathbf{w}^{(n)}$ is calculated, and the projected gradient $\tilde{\mathbf{w}}^{(n)}$ is used to define a path through the solution space given by $\mathbf{q}^{(n)}$. Then the auxiliary vector is obtained as

$$\mathbf{s}^{(n)} = \mathbf{q}^{(n)} + \lambda \tilde{\mathbf{w}}^{(n)} \tag{6.25}$$

where λ is a step factor that enables to find the minimum value of Equation 6.24, which represents the optimal location along the search path. Given this minimum value, the iteration step is finalised by applying the non-negative constraint

$$q_i^{(n+1)} = \max(s_i^{(n)}, 0) \tag{6.26}$$

yielding the values of the solution vector used in the subsequent iterations.

6.4.4 Iterative Sidelobe Cleaner Algorithm (ISCA)

The combination of a robust localisation algorithm with an iterative approach for enhancing the dynamic range of the beamformer output has lead to the development of the Iterative Sidelobe Cleaner Algorithm (ISCA). This deconvolution method is based upon the reconstruction of the measurement data from a set of synthetic sound sources via an adaptive approach. The application of a delay-and-sum beamforming algorithm to the superposition of both original and synthetic signals results in a reduction of the energy maximum previously found. This process has a direct impact on the beamforming results dynamic range, since the energy of the real source is directly decreased as well as the residual sidelobes. Ghost sources and any masking effect produced by the presence of strong sidelobes are progressively reduced by applying this procedure. The processing limits of ISCA are determined by an imposed dynamic range constraint. The algorithm removes energy iteratively within a dynamic range established by the user.

Similar to other deconvolution algorithms, the first step is to initialise the iteration index, $n = 0$, and choose an estimate of q, $\mathbf{q}^{(0)}$. Typically, this value is set to zero for the entire region of interest,

$$\mathbf{q}^{(0)} = 0 \tag{6.27}$$

In addition, an estimate of the cross-spectra perceived by the virtual array is initialised with the measurement data

$$\hat{S}^{(0)}_{x_i\,y} = S_{x_i\,y} \tag{6.28}$$

where $S_{x_i\,y}$ denotes the cross-spectrum between the signal at the fixed reference position $\mathbf{y}$ and the moving sensor $\mathbf{x_i}$.

In the first stage, a conventional delay-and-sum beamformer is applied to the acquired data following Equation 6.10. Next, the maximum of the beamforming output is used to extract information about the main excitation point

$$\psi^{(n)}(\mathbf{x}) = \max\left(\mathbf{B_{NF}}^{(n)}\right) \tag{6.29}$$

A negative synthetic source with a fraction of the power found at the maximum of the beamformer output is then introduced as such

$$q^{(n+1)}(\mathbf{x}) = q^{(n)}(\mathbf{x}) - \beta\psi^{(n)}(\mathbf{x}) \tag{6.30}$$

where β is an adaptive parameter which controls the amplitude assigned to the synthetic sources in each iteration. This factor is defined by the gradient of the error, i.e.

$$\beta = \begin{cases} \epsilon_0 & n = 0 \\ e_{RMS}^{(n-1)} - e_{RMS}^{(n)} & n \geq 1 \end{cases} \tag{6.31}$$

where $\epsilon_0 \in (0, 1)$ is a constant value used when there is not enough data to calculate the gradient and e_{RMS} represents the 2-norm between the original beamforming map and the synthesised solution, thus

$$e_{RMS} = ||\mathbf{Hq} - \mathbf{Y}||_2 \tag{6.32}$$

As the error between the the original and synthetic beamforming output decreases, the step parameter β is also proportionally reduced. Once the clean source map $\mathbf{q}^{(n)}$ has been updated, the data can be propagated from the source location to the array plane, hence

$$\xi_i^{(n)} = \frac{-\beta\psi^{(n)}(\mathbf{x})}{r_{x_i} r_y} e^{jk(r_{x_i} - r_y)} \tag{6.33}$$

Since the excitation sources have been assumed to be uncorrelated, it is then possible to directly add the original measured data to the synthetic sound field created

$$\hat{S}_{x_i\,y}^{(n+1)} = \hat{S}_{x_i\,y}^{(n)} + \xi_i^{(n)} \tag{6.34}$$

Although the method was designed to enhance source localisation maps obtained with a VPA, the approach presented in this section could be generalised for multichannel phased array systems. In this case, the covariance matrix would be the updated term in each iteration instead of the cross-spectral estimates, similar to the approach followed by CLEAN-SC [173]. Further research on this topic could be undertaken in future work.

6.5 Simulations

The implementation of the fundamental principles introduced so far allows for the performance of virtual phased arrays to be assessed from a theoretical point of view. This section is divided in two parts: firstly, the direction of arrival (DOA) obtained with a VPA and a multichannel phased array are compared; next, the deconvolution algorithms presented above are tested under several conditions.

6.5.1 Relative phase information for DOA estimation

Three pulsating monopole sources have been modelled in free field conditions with a sinusoidal excitation $q(t) = \omega^{-1}\sin(\omega t)$, for frequencies of 200, 400 and 800 Hz. Letting the fixed reference sensor be at the origin, the sources were positioned at 0°, 20° and 40° azimuth. A 2 m wide measurement area was evaluated using a sensor moving at 0.1 m/s and a phased array of 40 equally spaced elements. The distance between the source plane and the measurement area was set to 10 metres. Figure 6.2 illustrates the geometry of the simulation undertaken.

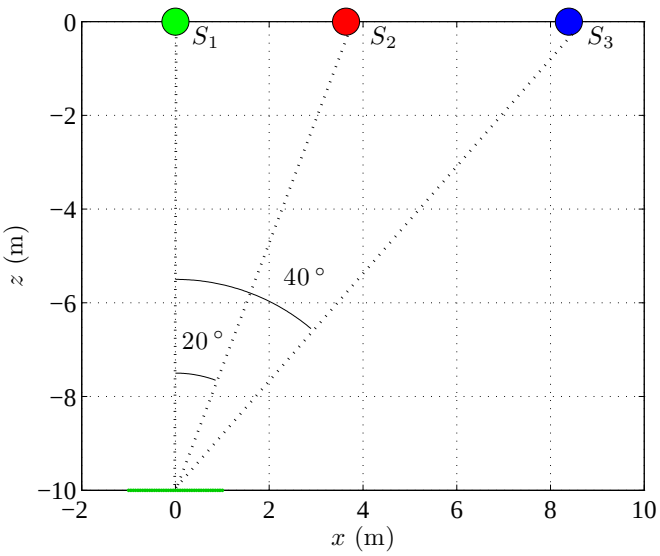

FIGURE 6.2: Schematic view of the simulation environment. The sensor array and sound sources are represented by a green line and circular markers, respectively.

The acoustic signal received by each microphone was computed by using a monopole model (Equation 6.1) for each source and then applying the superposition principle, i.e. adding individual source contributions. The delay-and-sum beamforming algorithm has been directly applied using the data from the static microphone array. On the other hand, the theory introduced in Section 3.3.2 was used to simulate the sound perceived by the moving sensor, signal that was divided into 40 blocks of 0.5 seconds length, associating each of those blocks to a position of the measurement area. Next, it was possible to apply the beamforming algorithm using the CPSD between the elements that constitute the virtual phased array and a reference sensor located at the origin. Figure 6.3 presents the obtained results in terms of beamforming output and phase estimation.

It can be seen in Figure 6.3 that the simulation gives almost identical results either using data from a static array or a virtual phased array. Furthermore, the maxima of the

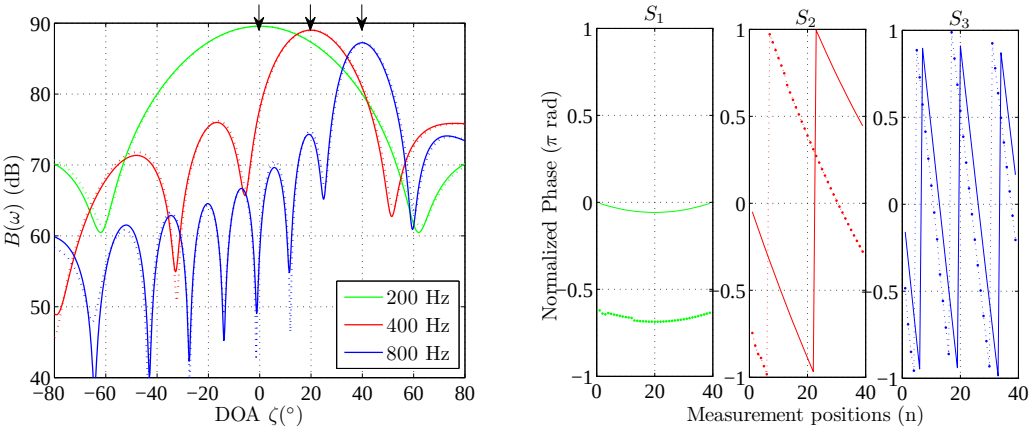

FIGURE 6.3: Comparison of the beamformer output (left) and phase estimation (right) of data acquired with a static microphone array (solid line) and a virtual phased array (dotted line) for several frequencies. The arrows above the left figure indicate the real position of the sound sources.

beamforming output perfectly match the theoretical location of the individual sources in all cases (0, 20 and 40 degrees). Furthermore, regarding the phase estimations (right hand side of Figure 6.3), the relative phase (dotted line) follows the same pattern as the absolute phase, independent of frequency or source position. There is however a constant offset between the relative and absolute phase caused by the propagation delay from the source to the reference sensor. Nevertheless, it does not affect the beamforming results since this difference remains constant during the scanning process.

6.5.2 Deconvolution algorithms

Three deconvolution methods are studied in this section under various simulation conditions. Comparisons with conventional delay-and-sum beamforming are used to illustrate the advantages provided by the different deconvolution algorithms. The geometry of the simulation environment is common for all the tests: a square array of 441 elements[4] regularly distributed across and a 2 m × 2 m area and a set of six uncorrelated point sources radiating at a frequency of 1 kHz located 30 m from the plane. The individual source positions are shown in Table 6.1.

	Q_1	Q_2	Q_3	Q_4	Q_5	Q_6
Azimuth (°)	30	10	0	-10	-20	15
Elevation (°)	-20	10	0	10	0	0

TABLE 6.1: Location of sound sources used in the simulations.

[4]Even though the total number of transducers seems excessively large, this choice was based on the amount of virtual transducers which is easily achievable using a VPA approach [22, 32].

An area of 40 metres (horizontal) by 30 metres (vertical) of potential source positions was evaluated using a regular grid of 1225 points. Figure 6.4 presents a sketch of the simulated scenario.

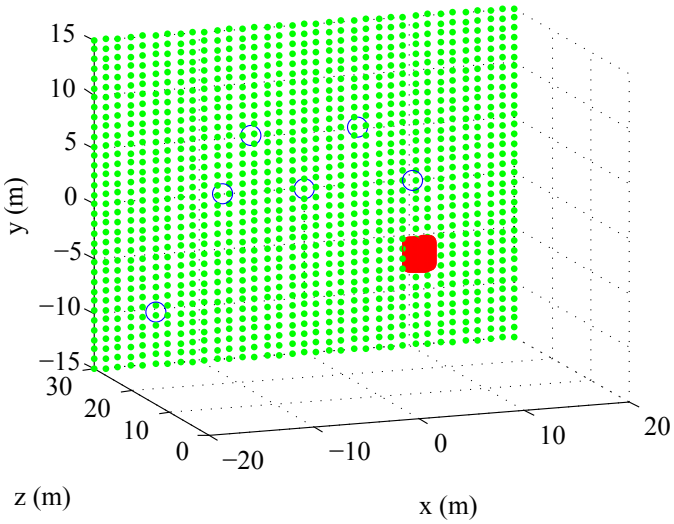

FIGURE 6.4: Geometry of the simulated scenario. Evaluated source positions are plotted in green, array sensor positions are represented by red dots and the location of the noise sources are shown by blue circular markers.

All DAMAS and NNLS results presented in this section were computed after 10000 iterations. The localisation maps obtained with ISCA were computed until the maximum level of the beamforming output was reduced by 10 dB, which corresponds to 138 iterations for the first experiment, 90 for the second and 109 for the last test.

6.5.2.1 Convergence of ISCA

One of the key features of iterative algorithms is the the ratio of convergence toward an optimal solution. It is therefore necessary to study the behaviour of the method when it is used under different sound field characteristics. A first order gradient algorithm (also known as steepest descent) was implemented in order to control the effort applied for each iteration. The cost function used to extract the gradient toward the optimal solution was based upon the difference between the initial data and the result of applying sound propagation models to a clean map of synthetic sources. The root-mean-square (RMS) value is reduced as the clean map improves with each step, hence reducing the synthetic source strength added with every iteration. The left hand side of Figure 6.5 shows how the cost function, the error between the “clean” map and the original beamforming output, is iteratively reduced for several source conditions. The power of multiple point sources was varied between 0, 3, 6 and 9 dB range.

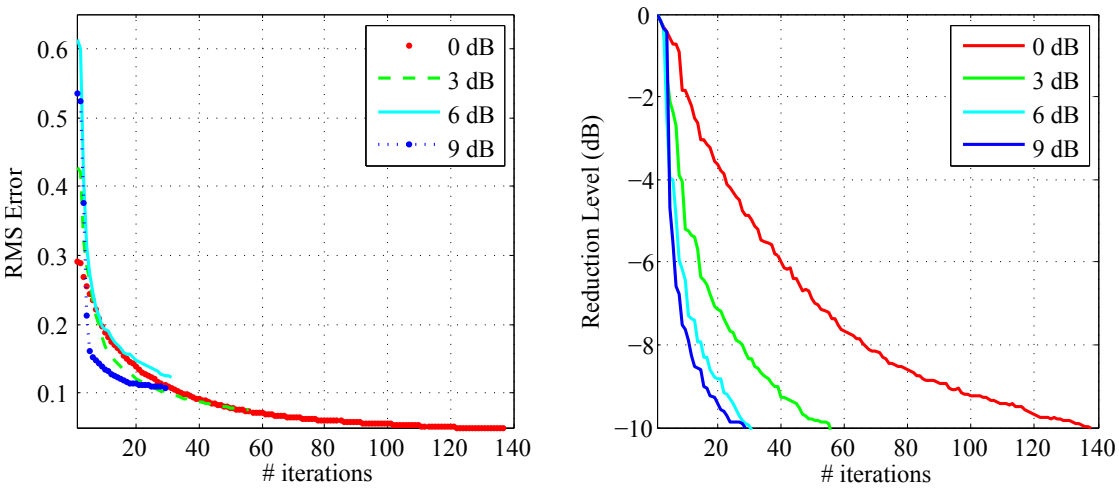

FIGURE 6.5: Convergence of the method for different source strength ranges.

As shown, the highest reductions are achieved during the first steps of the process. Furthermore, the number of iterations required to reduce the energy of a beamforming map by 10 dB depends directly upon the nature of the sound field. In the presence of sources with equal source strength the algorithm needs a relatively long time to converge. In contrast, when the source strength between them differs significantly, it is possible to minimise the energy more rapidly. Therefore, it can be concluded that the convergence of the algorithm depends upon the strength range of the excitation sources.

6.5.2.2 Localisation of sources with equal strength

An initial simulation case was used to test the performance of the different deconvolution algorithms. The six sources described at the beginning of this section were set to an equal source strength level of 90 dB. Noise was ignored for this simulation and consequently, even the source grid and real source location were matched to minimise the localisation error. Figure 6.6 presents a comparison of conventional beamforming CBF (top left), DAMAS (top right), NNLS (bottom left), and the proposed algorithm ISCA (bottom right).

As expected, the three iterative deconvolution methods are able to achieve a spatial resolution far better than the conventional delay-and-sum beamforming. It is apparent from Figure 6.6 that all methods resolve most source positions accurately. Only DAMAS produces a significant drift for the localisation of source number 1. This algorithm also presents several weak ghost sources distributed across the output map. Both ISCA and NNLS lead to similar localisation maps, although the accuracy of ISCA appears to be slightly better in terms of spatial resolution and energy spread.

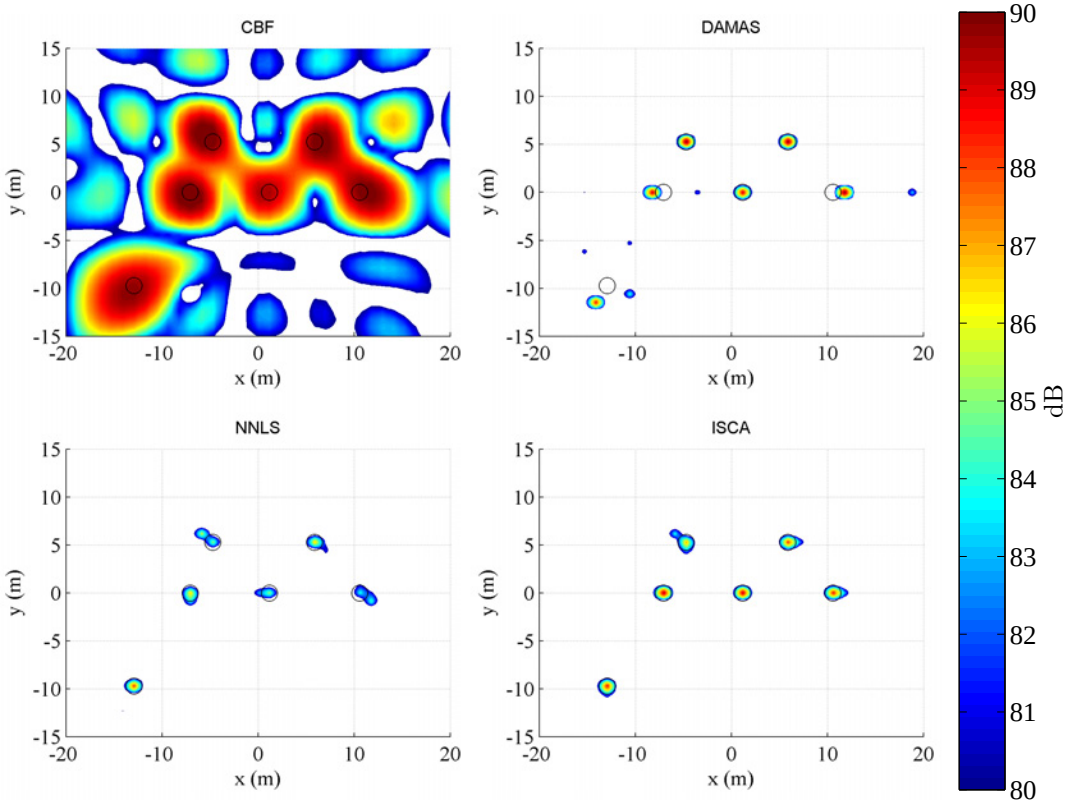

FIGURE 6.6: Comparison of several algorithms for localising multiple uncorrelated sources of equal source strength. The actual positions of the sources are indicated by circles.

6.5.2.3 Localisation of sources with multiple strengths

A second simulation scenario was studied for sources that have different excitation levels. The source strengths were distributed along a 6 dB range. The aim of this test was to evaluate the ability to detect sound sources that were originally masked by sidelobes in the conventional beamforming map. Table 6.2 gives the assigned strengths.

	Q_1	Q_2	Q_3	Q_4	Q_5	Q_6
Source Strength (dB)	85	86	87	88	89	90

TABLE 6.2: Source strengths of the sound sources used in the simulation scenario.

As in the previous section, noise was not added to the input data. Figure 6.7 illustrates a comparison of conventional delay-and-sum beamforming CBF, DAMAS, NNLS, and ISCA for multiple source excitations with different source strengths. The representation range has been expanded with respect to the previous results since the range of the excitation sources is larger in this experiment.

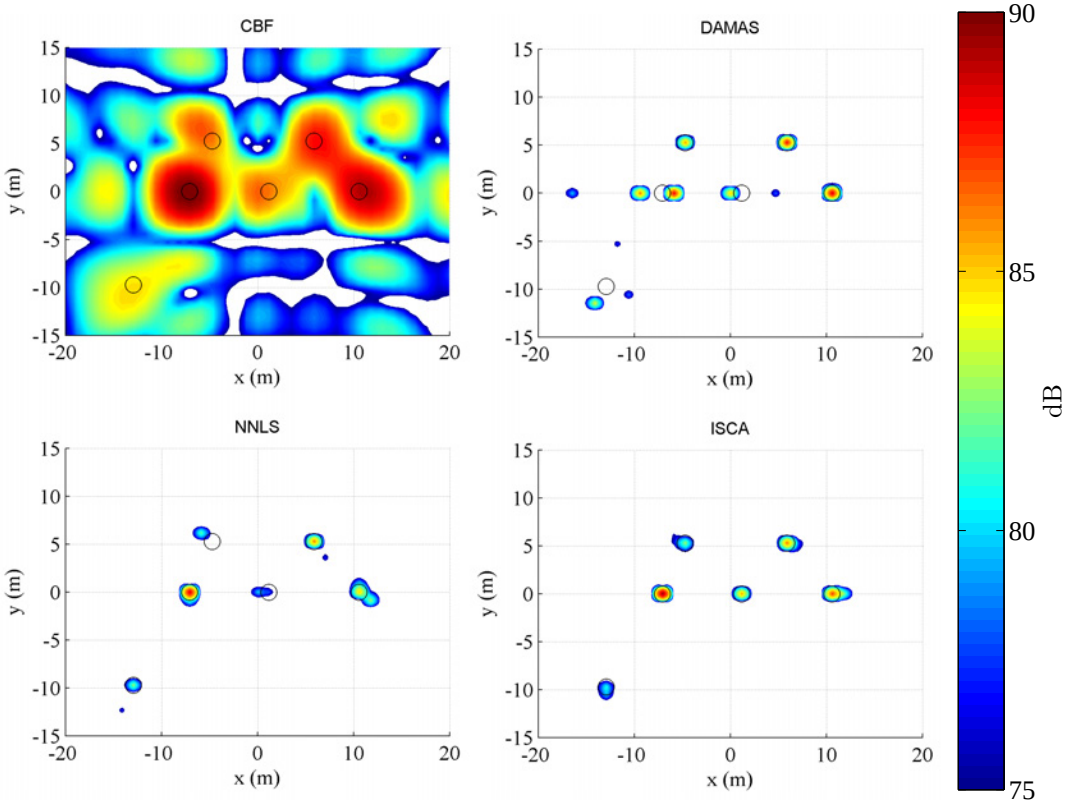

FIGURE 6.7: Comparison of several algorithms for localising multiple uncorrelated sources for which the power is distributed along a 6 dB range. The actual positions of the sources are indicated by circles.

DAMAS presents some difficulties when the excitation range is expanded. The number and power of the ghost sources is greater with respect to the previous test. In contrast, the performance of NNLS and ISCA are very similar to the results previously obtained. However, in this second experiment NNLS presents some drift in the location estimation of two of the sources. On the other hand, ISCA is able to produce a clear localisation map without the presence of ghost sources, although the energy seems to be slightly more spread out around the true source location than NNLS.

6.5.2.4 Localisation of sources including noise

The two previously presented simulations evaluate the performance of each algorithm in simple conditions. Nonetheless, this is not representative of a real case scenario. Experimental errors caused by spectral estimation, lack of excitation stationarity or the presence of background noise were disregarded thus far. It is therefore necessary to include an additional step in the simulations which allows the robustness of the beamforming algorithms to be assessed when the data deviates from ideal conditions. To achieve this, the location of the sources was modified to avoid a matching grid between

beamforming observation points and real source locations. In addition, random complex error has been added to the sound pressure perceived by each virtual array transducer. The variance of the error has been limited to 50 percent of the original received sound pressure (signal to noise ratio of 6 dB). Figure 6.8 shows the assessed array output before and after adding noise.

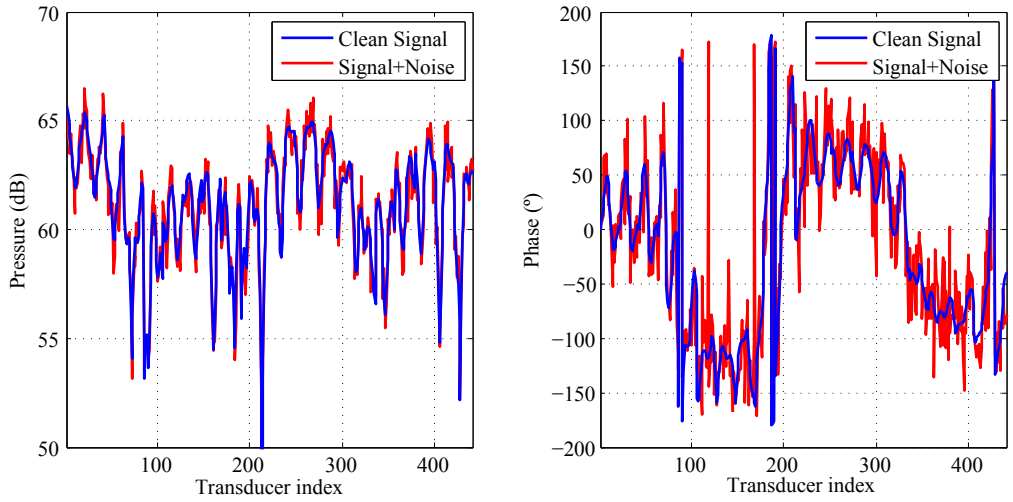

FIGURE 6.8: Signal received by the virtual array in terms of magnitude (left) and phase (right).

Furthermore, Figure 6.9 illustrates the results of CBF, DAMAS, NNLS, and ISCA when the sources introduced in the previous simulation are assessed including noise. As shown, despite the severe noise added to the array signal, the deconvolution algorithms are able to provide similar solutions to the ones found in previous experiments. The appearance of additional ghost sources is noticeable in DAMAS and NNLS but not in ISCA. On the other hand, the use of a non-matching grid together with the inclusion of random noise seems to cause a slight drift in the estimated source locations affecting all three algorithms.

The robustness of ISCA can be attributed to the fact that only the range of data with the best signal to noise ratio is used to compute the clean source map. In the simulation presented above, the original energy of the beamforming output was iteratively reduced by 10 dB, mainly over the excitation maxima. In contrast, NNLS and DAMAS tend to converge to a numerically optimal solution using the complete dataset available. Therefore, the accuracy of these methods is slightly more biased by the presence of noise than the proposed algorithm.

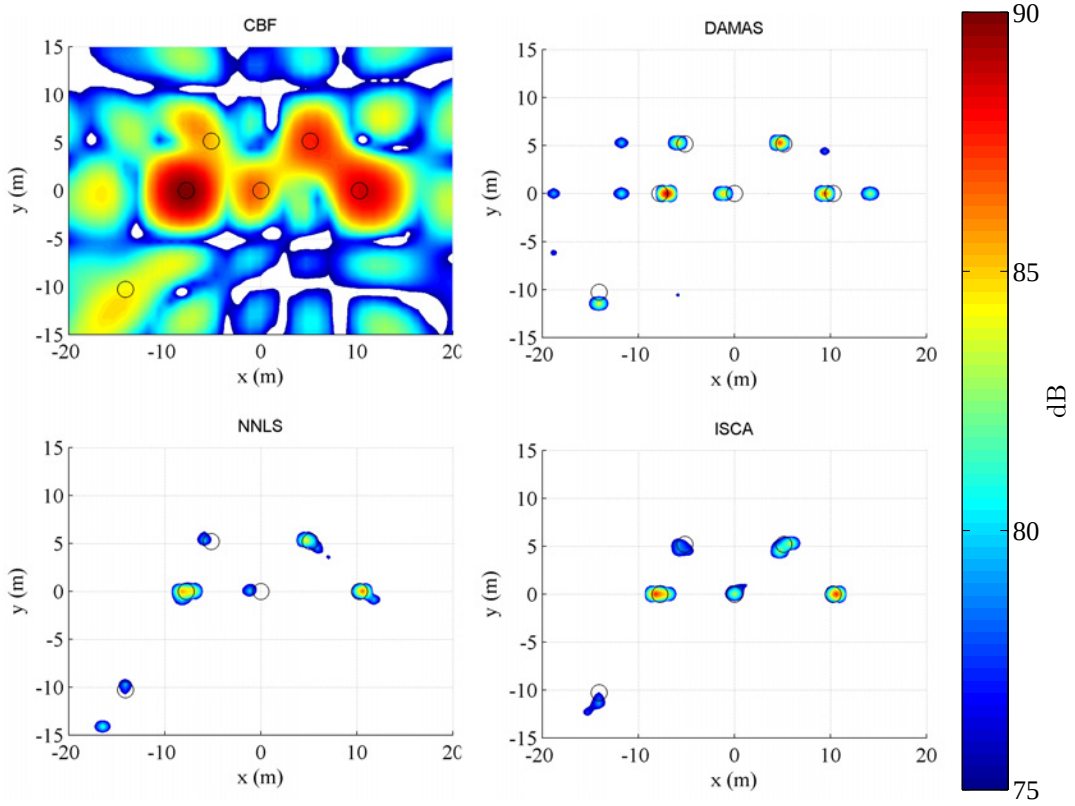

FIGURE 6.9: Comparison of several algorithms for localising multiple uncorrelated sources including random spectral estimation error.

6.6 Practical implementation

A set of validation experiments have been undertaken in several measurement scenarios for both low and high frequency sources [15, 22, 32–34, 160]. This section provides a detailed description of the measurement methodology and VPA configuration, along with an overview of the experimental results found so far.

6.6.1 Measurement methodology and VPA configuration

Although the measurement process of VPA is very similar to the "Scan&Paint" method introduced in Chapter 3, additional steps are required to ensure the reliability of the beamforming output. The application of a positional discrimination filter and the selection of a spatial discretisation algorithm that suits the frequency range of interest are the main aspects to take into account.

The creation of a VPA begins by performing scanning measurements across a planar region that determines the location of the virtual array. The continuous acquired signal is then fragmented by applying the regular grid discretisation introduced in Section 3.2.1.

The selection of the grid becomes crucial to the performance of any source localisation algorithm applied afterwards. The size of each grid cell should be smaller than half of the shortest wavelength assessed in order to avoid spatial aliasing. On the other hand, the grid span establishes the lowest frequency limit, it should contain at least half of the longest wavelength to be localised.

Once appropriate frequency limits are defined, the measurement dataset performance can be estimated by following the routine suggested in Figure 6.10.

FIGURE 6.10: Evaluation procedure of a VPA grid.

Firstly, a regular grid is coupled with the tracking data, storing grid cells covered during scanning. Each signal segment is delimited by the time instances of entering and leaving a grid cell. Assessing variable length signals may eventually cause misleading spectral estimations if the time series are too short. Therefore, a threshold of minimum signal length per cell is recommended to prevent this problem.

VPAs have all data linked to a shared reference via cross-spectral estimates. The asynchronous acquisition of time series at different locations constrains this technique to the use of processing methods mainly in the frequency domain. Common practice for determining the quality of a cross-spectrum, or a transfer function, is to compute the coherence between the assessed signals (see Equation 3.66). This function establishes a way of measuring the degree of the linear relationship between two signals, producing values near unity when they are linearly related. As such, it is good practice to neglect cross-spectral estimates when the coherence between the signals is lower than a certain threshold. In order to implement this cross-spectral quality control in VPA, the grid configuration obtained above is filtered using a positional discrimination algorithm[5]. This process is based on removing grid cells when the coherence is below a certain value. According to [118], the spatial coherence function of any source in non-anechoic conditions changes in proportion to its wavelength. Consequently, the resulting VPA grid changes depending upon the evaluated frequency, reducing the number of virtual transducers mainly for higher frequencies.

The grid positions that have a good coherence relationship with the reference sensor and sufficiently long time series are considered "active grid cells". The theoretical performance of the virtual array geometry can be evaluated in terms of spatial resolution,

[5]An additional application for the positional discrimination algorithm is presented in Appendix B

energy spreading, aliasing and potential ghost sources derived from the directivity pattern. All this information can be inferred from calculations of the point spread functions (PSF), as shown in Figure 6.11. These patterns were obtained by computing the beamforming response when a point source is placed in front of an array with an arbitrary geometry.

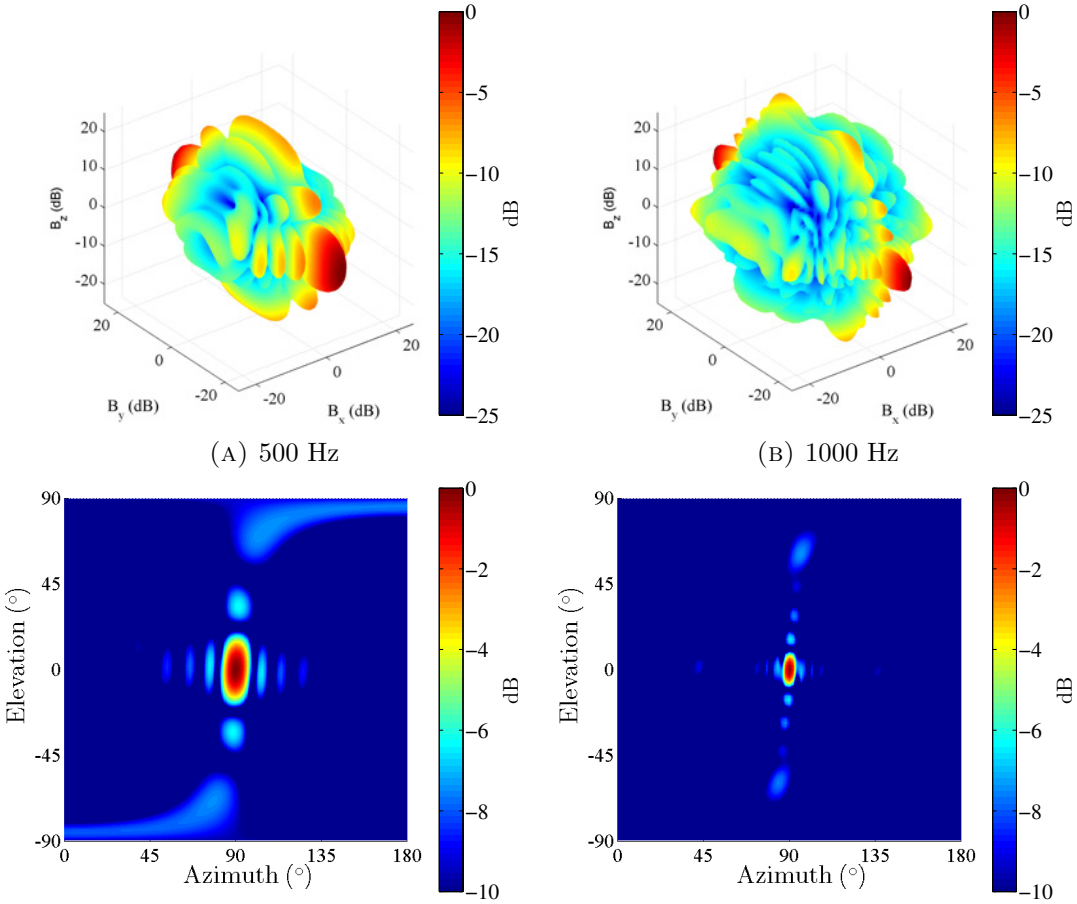

(A) 500 Hz (B) 1000 Hz

(C) 500 Hz (D) 1000 Hz

FIGURE 6.11: Virtual phased array PSF at 500 Hz (A) and 1 kHz (B) and 2D graph of the point spread function (PSF) at 500 Hz (C) and 1 kHz (D).

In summary, the performance of a VPA geometry can be evaluated by coupling tracking information together with a discretisation grid, next discarding unrepresentative positions and then calculating the PSF.

6.6.2 Instrumentation and experimental setup

All scanning measurements shown in this section were carried out using a Microflown *p-u* probe comprised of a sound pressure microphone and particle velocity transducer. Two free-field GRAS microphones were used as reference sound pressure sensors placed at fixed locations in the measurement plane. In addition, a "Logitech Webcam Pro

9000" camera was utilised to film the scanning process. Figure 6.12 shows pictures of the three different experimental cases assessed: low frequency noise localisation around a gas plant (Grijpskerk, the Netherlands), mid-high frequency source localisation inside a small anechoic chamber (Southampton, UK) and broadband sound characterisation of exterior car noise (Arnhem, the Netherlands).

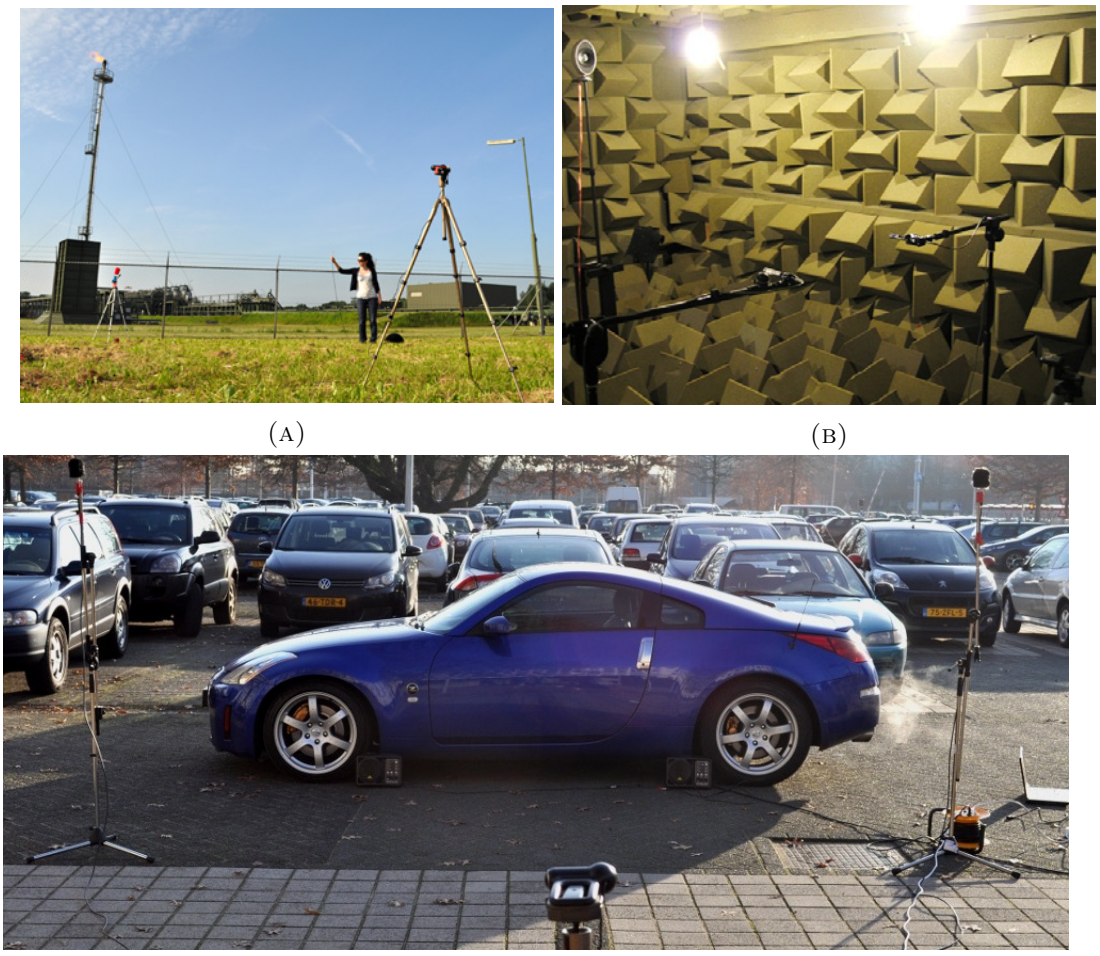

(A) (B)

(C)

FIGURE 6.12: Pictures of the assessed measurement scenarios: outdoors experiments (left and bottom) and small anechoic chamber test (right)

The low frequency noise experiment (Figure 6.12-A) was performed across a total surface of 6 m (horizontal) by 2 m (vertical) at a position over 100 m from the source. The measurement time taken for the presented experiment was about 4 minutes. Grid cells of 0.25 m were chosen to create an array of 85 active virtual transducers.

In the second experiment (Figure 6.12-B), two KEF KHT 3005 loudspeakers were excited with broadband white noise while an area of 0.5 m (horizontal) by 0.35 m (vertical) was measured with a 3 m separation between plane and sources. Three different 3 minutes scans were undertaken and averaged. The three tests were discretised using a grid cell size of 0.03 m, resulting in a VPA of 118 active elements.

The sound field generated by a Nissan 350z (Figure 6.12-C) with the engine running in stationary conditions of 3000 RPM was evaluated by measuring a plane of 4 metres (horizontal) and 2 m (vertical) at a distance of 4 m from the vehicle. A single sweep measurement was carried out over approximately 4 minutes. In this case, a discretisation grid of 0.2 m cell width was used, resulting in an array of 175 active virtual transducers.

6.6.3 Data analysis

Before studying the accuracy of the DOA estimations in detail, it is necessary to focus initially on the reliability of the data. Figure 6.13 (left) provides an example spectrogram of the moving sensor along with a 360° localisation map of the outdoor experiment in the gas plant facility. The assessment of the spectral variations across time and space is a direct and effective approach for detecting loud manipulation noise during scanning measurements. Otherwise, undesired transient noise would be taken into account, decreasing the accuracy of the DOA estimations. Consequently, time blocks containing any disturbance were disregarded in the post-processing stage.

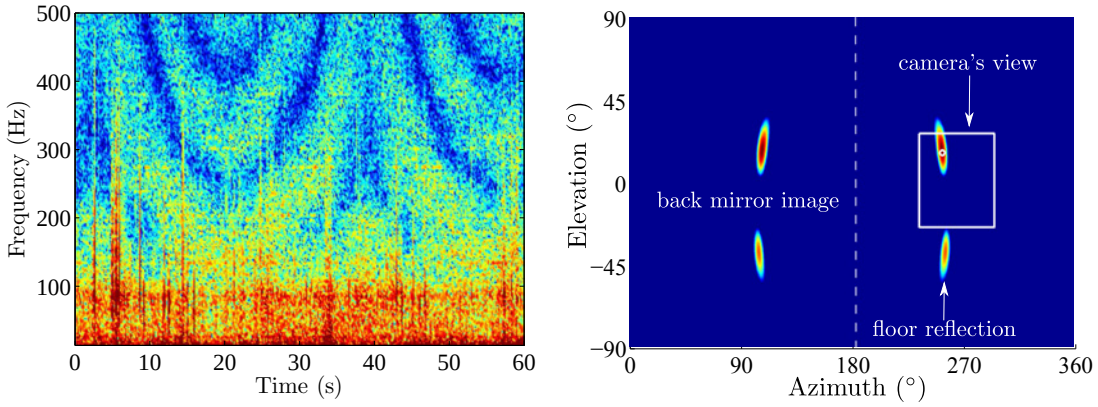

FIGURE 6.13: Spectrogram sample of the scanning sensor (left) and 360° localisation map of the outdoor measurement (right)

The 360° localisation map shown on the right hand side of Figure 6.13 reveals secondary sources present in the measurement environment. As can be seen, the main noise source can be located within the limits of the camera view, but it also shows a symmetric source at a negative elevation angle caused by the floor reflection. In addition, a back mirror image is shown at azimuth angles between 180° and 360°, an inherent effect of planar array geometries. Further research should explore the ability to distinguish front and back propagation based upon the assessment of the relative phase between the particle velocity sensor and the pressure transducer contained in a p-u probe.

6.6.4 Sound localisation maps

The localisation maps measured in the surrounding facilities of a gas plant (Figure 6.12-A) are shown in this section. In the case studied, a flare stack was identified as the a priori dominant noise source in the area. Figure 6.14 presents several source localisation maps for different frequency regions using a delay-and-sum beamforming approach.

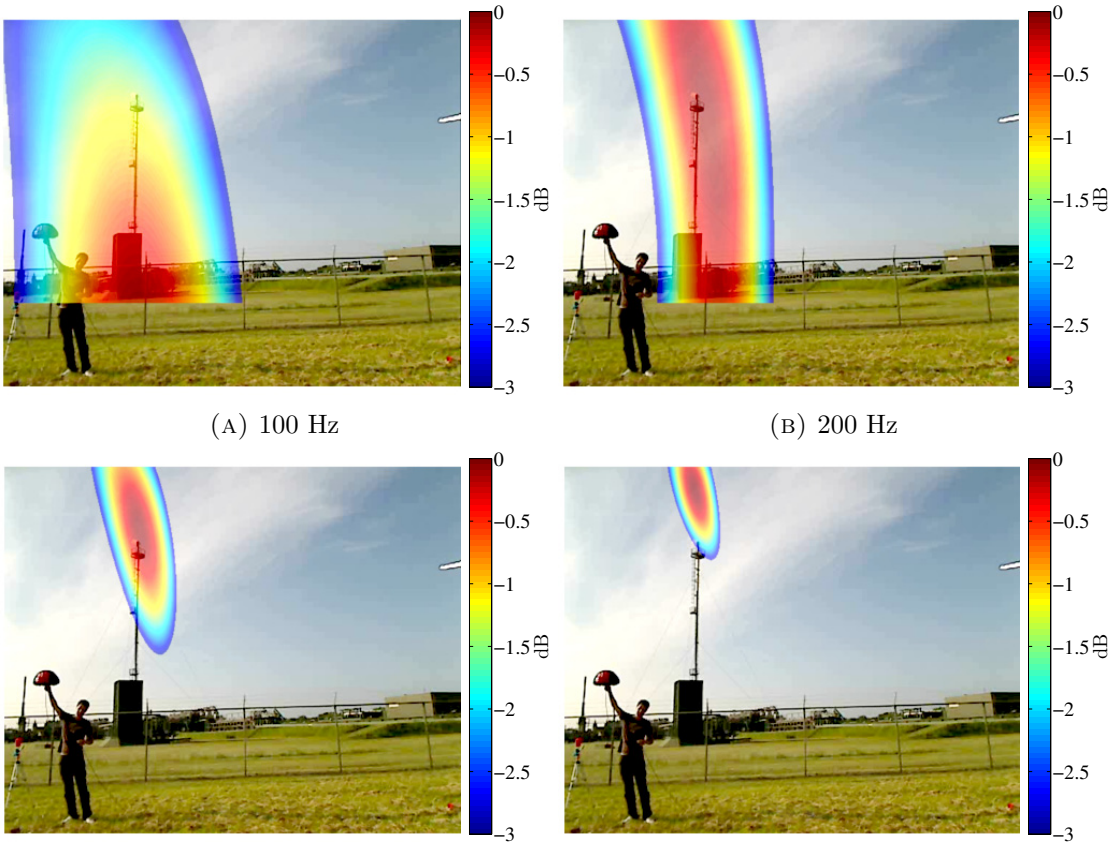

(A) 100 Hz (B) 200 Hz

(C) 400 Hz (D) 600 Hz

FIGURE 6.14: Sum-and-delay beamforming localisation maps at several frequencies.

A minor correction was applied (5 degree offset) in order solve the misalignment between the camera axis and the normal axis measurement plane. It is shown that localisation in the azimuth axis gives good estimates even at low frequencies. In contrast, the elevation of the noise source was not as accurate at low frequencies, mainly due to the limited height of the virtual array (2 m). As mentioned above, the number of transducers and the total effective length of the array are asymmetrical, leading to better results for azimuth than for elevation estimations. Therefore, a larger measurement area along the vertical axis should be covered in order to improve the elevation estimation at lower frequencies.

6.6.5 DOA estimation

The measurement accuracy of the experiments shown in Figure 6.12-A and B was assessed throughout the calculation of the norm between the DOA, provided by the different source localisation algorithms, and the real position of the sound sources. The locations of the loudspeakers in the anechoic chamber test were carefully adjusted beforehand. Nonetheless, the dominant noise source for the outdoor measurements was assumed to be located at the flare stack. The position of this noise source was calculated using satellite pictures along with a map of the area as described in [22].

A performance comparison between different beamforming algorithms for the gas plant and anechoic chamber experiments are shown in Figure 6.15. On the left hand side, the localisation errors of the flare stack are shown from 100 Hz to 700 Hz. Both beamforming algorithms used in this experiment give similar estimation errors, least-squares providing the lowest error. In this case, some grid cells of the measurement plane were excluded due to low coherence with the reference sensors, preventing the reconstruction of the covariance matrix required to compute the MUSIC algorithm.

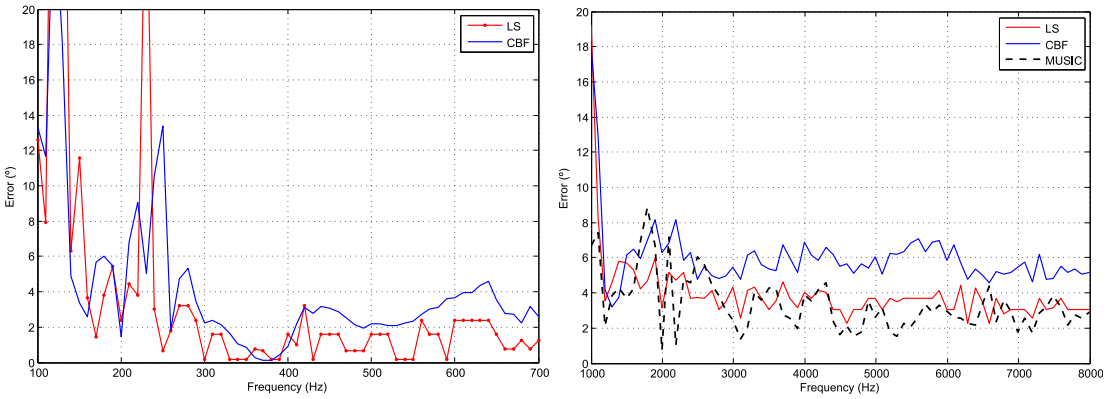

FIGURE 6.15: Error between estimated and real source location for the outdoor test (left) and the anechoic chamber experiment (right)

On the right hand side of Figure 6.15 the error curves of the anechoic chamber experiment are displayed, focused on the localisation of high frequency sources (1 kHz to 8 kHz). Results show good performance using all DOA algorithms, although conventional delay-and-sum beamforming presents the largest error. These results provide experimental evidence to show that localisation algorithms based on the data covariance matrix are also suitable for VPA providing a regular array geometry is used.

6.6.6 Near-field pressure mapping versus VPA

Near-field scanning measurements allow for the comparison of sound pressure distribution and beamforming output of the VPA. Sound pressure mapping is focused on visualising a slice of the sound field produced by a combination of several noise sources distributed across the car body, such as the engine, exhaust or ventilation system. On the other hand, beamforming algorithms allocate and quantify those noise sources directly but do not aim to reconstruct the sound field (issues covered by acoustic holography). Consequently, the results presented in this section, albeit related, have a dissimilar nature and hence must be compared carefully. Firstly, the left hand side of Figure 6.16 focuses on comparing broadband high frequency sound maps when the noise is mainly produced by the engine whilst the presence of exhaust noise is insignificant, i.e. between 600 Hz and 1500 Hz. Furthermore, the right hand side of Figure 6.16 illustrates lower frequencies, around 150 Hz, where initial resonance occurs. The colour scale dynamic range of both methods has been adjusted in order to be able to compare the current figures. Results obtained using VPA have been normalised to show a maximum level difference of 3dB, avoiding the presence of any sidelobes or "ghost-sources" in the beamforming map. Near-field sound pressure maps have been adjusted to display levels with a dynamic range of 10 dB.

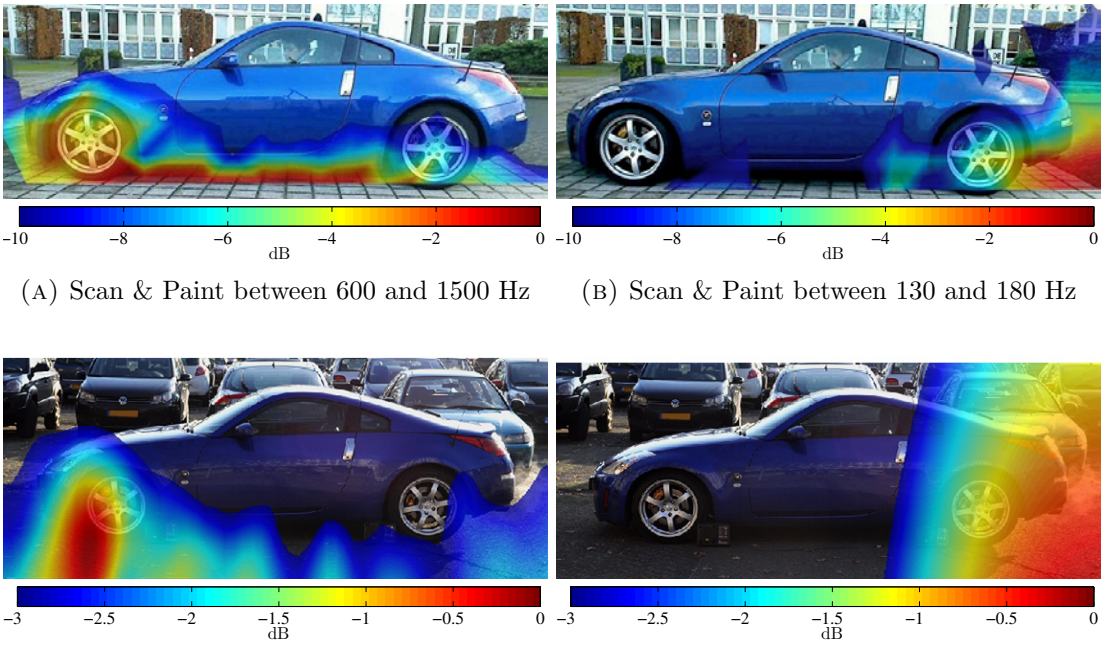

(A) Scan & Paint between 600 and 1500 Hz (B) Scan & Paint between 130 and 180 Hz

(C) VPA between 600 and 1500 Hz (D) VPA between 130 and 180 Hz

FIGURE 6.16: Comparison of VPA output (bottom figures) and nearfield sound pressure map (top figures), each normalized to its highest value.

The comparison of near-field sound pressure maps and VPA results provides evidence of a similar source localisation performance. An understanding of the location of the

noise sources can be gained by mapping acoustic variations near a sound source, which is exactly the information that beamforming techniques aim to provide. Conventional array sytems are highly limited when assessing low frequencies because the size of the array must be proportional to the wavelength. VPA avoids this constraint because there are no physical transducers distributed across a large area, data is acquired by freely scanning across a plane in the space. It is therefore expected to be able to assess noise sources accurately even below 200 Hz, as shown in Figure 6.16. In addition, experimental evidence has been provided showing that the method can also work remarkably well at mid and high frequency ranges, giving a good match between near-field scanning and VPA beamforming maps. The main discrepancy appears around the bottom body area, where the pressure is high in the near-field but not for VPA. This phenomenon is likely due to most of the noise being produced by the engine at which the VPA is pointed and it generates sound which travels through the tire and bottom body to reach the measured near-field plane. Therefore, although there is a slight discrepancy between the two maps, it is expected if we assume the mid-high frequency noise is caused mainly by the engine itself.

6.7 Comparison of different beamforming techniques for VPA

Three different beamforming techniques have been studied experimentally: delay-and-sum beamforming, MUSIC and Least-Squares. Theoretical and practical limitations, computational time and accuracy are the main attributes that should be evaluated in order to understand which one is the most suitable algorithm for an specific case.

Delay-and-sum beamforming is a non-parametric method which does not require prior information of the measurement scenario. The simplicity of the method is one of its major advantages, allows for the computation of beamforming maps very quickly. It only requires the use of a fixed reference transducer for the acquisition of relative phase information. Nevertheless, the accuracy and resolution of the technique has been shown to be worse than more complex methods [91, 174].

The MUSIC algorithm results in high-resolution source localisation maps suitable for locating uncorrelated noise sources. The practical cases studied show that this method can achieve very accurate results in a relatively short time. However, it is a parametric method which requires the establishment of a limit between signal and noise subspaces, and for VPA, it also requires square or rectangular array geometries. It is also worth remarking that far field conditions have been assumed for the synthesis of the covariance

matrix in order to use its symmetric properties as the key of the reconstruction process. The impact of this assumption has been studied in [32], showing that a distance greater than 3 m between source and measurement plane yields an estimation error smaller than 2°. Furthermore, the implementation of this technique requires the use of two static reference sensors for reconstructing the covariance matrix. In summary, this method offers a fast, high resolution and relatively accurate approach to locating uncorrelated sound sources but it may be not suitable for every measurement scenario.

Using a Least-Square approach to find the direction of arrival of propagating wavefronts gives the optimal solution for a measured dataset. Furthermore, no assumptions are made concerning the correlation of the sound sources or the far field conditions. As shown on the right hand side of Figure 6.15, the error and its variance across the spectra is very low, leading to the most accurate results. Similar to conventional delay-and-sum beamforming, only a static sensor is required. The problem of this parametric method comes from its high computational load and slow calculation process. The algorithm is based on inverting a matrix which size depends on the number of sources and the number of field points evaluated. The number of iterations needed for producing each beamforming map at a single frequency is proportional to N^{2S} where N is the number of field points and S is the number of sound sources. This limits the use of the algorithm for scenarios with few dominant noise sources.

In conclusion, delay-and-sum beamforming provides a fast and reasonably accurate solution without additional instrumentation requirements. Advanced techniques such as MUSIC or Least-Squares may achieve more accurate results but they have strong drawbacks in terms of measurement conditions and computational time respectively. The use of deconvolution methods in combination with source localisation algorithms, such as delay-and-sum beamforming, has proved very promising in a simulated free-field environment (see Section 6.5.2) and it should be explored further in order to obtain experimental evidence for the successful combination of these two approaches.

6.8 Large multichannel arrays versus VPA

One of the main problems of most conventional beamforming arrays is the cost of the measurement equipment. Not only the large number of transducers but also the multichannel acquisition systems raise costs remarkably.

The amount of time required to set up the instrumentation and perform measurements is always an important issue. Manual sweeps of a single probe are a fast procedure to obtain information across a sound field. The measurements presented in this chapter

were undertaken in less than 15 minutes, which is a reasonable time for obtaining a solution to a noise localisation problem. There are several commercial systems which are also portable and easy to set-up; however, their frequency range is very limited, especially in the low frequency region due to their reduced dimensions.

The flexibility of virtual phased arrays is one of its prime advantages versus multichannel solutions. The proposed method enables the scanning of very small areas, for high frequency assessments, or large planes, for localising low frequency sources. In contrast, multichannel arrays have a set of transducers distributed along a fixed structure which is usually difficult to modify, making it infeasible to optimise the array geometry for a frequency range of interest.

The design process of the VPA introduces an unusual step when evaluating source localisation algorithms: the geometry of the array can be modified and refined at a post-processing stage. This is certainly a very useful feature since it is possible to maximise and control the performance of the virtual transducer array after the measurements have been performed. A series of spatial filters have been designed in order to neglect positions which can introduce error into the location estimation a priori (such as positions with low coherence to the reference sensor or short time signals). In addition, the absence of physical fixed positions results in reductions in discretisation error and spatial aliasing.

The assessment of sound fields created by partially-correlated sound sources may decrease the quality of the phase estimates due to coherence drops between signals of the fixed and moving transducer. A detailed investigation of this concept is out of the scope of this work, but it should be investigated further to clarify the limitations it can potentially impose.

6.9 Summary

A novel measurement methodology for localising noise sources has been introduced. When the sound field is time stationary, it has been demonstrated that the number of transducers can be dramatically reduced to two sensors: one static reference and one moving sensor. The theoretical background, design process of a virtual transducer array and the in-field performance of the method have been examined in detail. Despite the minimalistic character of the proposed approach, the accuracy and resolution of VPA has proved comparable to that of large microphone arrays.

Three different beamforming algorithms have been derived and implemented for VPA. Delay-and-sum beamforming was found to be a fast and fairly accurate technique with

low instrumentation requirements, whilst MUSIC or Least-Squares are able to produce better results but are very demanding in terms of measurement conditions and computational time, respectively. The small error found between estimated and real noise source location provides clear evidence of the successful implementation of the methodology. It is important to highlight the similar results even at lower frequencies, which commercial multichannel solutions are not able to assess due to size limitations of the arrays.

In addition, several deconvolution methods have been adapted to VPAs and tested for source localisation purposes. Spatial resolution, dynamic range and accuracy improvements are achieved by applying deconvolution techniques to a conventional delay-and-sum beamforming output. A novel iterative sidelobe cancellation algorithm (ISCA) has been introduced and validated against conventional deconvolution methods such as DAMAS and NNLS. Noise localisation experiments for multiple uncorrelated sources have been simulated under different excitation conditions, with and without including noise in the virtual array data. It has been shown that the performance of the novel method proposed exceeds conventional iterative deconvolution algorithms due to the nature of the investigation process: ISCA mainly interacts with the data at the points where the energy is maximised along a limited dynamic range. Alternatively, NNLS and DAMAS seek the solution of the system algebraically, converging towards an answer which best fits the complete dataset. This argument is supported by the simulation results, providing clear evidence of the robustness and accuracy of ISCA, even in the presence of severe measurement noise.

Chapter 7

Conclusions and Recommendations

7.1 Summary of the main conclusions

This study contributes to the development of sound visualisation methods, powerful tools that aid in the understanding of a great variety of noise, vibration and harshness problems. It is shown that the employment of sound imaging techniques has played an important role in the development of acoustics throughout history. Numerous acoustic apparatus and measurement methods have evolved into the widely used measurement techniques currently available. The lack of straightforward, fast and cost effective sound visualisation methods have triggered the development of the work presented in this thesis. As a result, "Scan & Paint" is proposed as a simple, flexible and effective acoustic imaging tool that can be used in combination with several processing methods for studying a wide range of sound and vibration phenomena in both qualitative and quantitative terms.

The theoretical and practical foundations of "Scan & Paint" are introduced along with several fundamental principles common to scan-based techniques. As shown, the evaluation of the Doppler effect and the time-domain formulation of the sound field perceived by a moving sensor provide a detailed description of data acquired by a scanning procedure. In addition, a statistical assessment of the implemented methodology has lead to the derivation of novel analytical expressions for the bias and variance error of scanning measurements, allowing for a quantitative evaluation of spectral estimation errors.

The foundations of direct mapping methods are also explored. The spatial resolution of sound pressure and normal particle velocity mapping are derived, demonstrating

that the visualisation of particle velocity is more suitable for revealing closely spaced noise sources. Moreover, experimental evidence using both one dimensional and three dimensional acoustic mapping are proved to be useful for machine diagnostics, vibro-acoustic characterisation and sound radiation problems in real-life conditions.

A scan-based panel contribution analysis method based on the direct acquisition of sound pressure and acoustic particle velocity using a p-u intensity probe is introduced. The practical evaluation is focused on the study of a vehicle compartment, showing that the proposed method involves far less measurement time and costs than traditional techniques. The validation of the method provided good results especially in low frequencies, where most of the conventional methods are unable to assess. Furthermore, a complete investigation of the results in terms of particle velocity, transfer function and pressure contribution mapping are given, demonstrating the capabilities of these visual representations for a detailed study of the acoustic behaviour of a complex environment. In addition, pressure contribution calculations are utilised to rank the sound sources detected, information that can be used to decide where to apply acoustic treatments in order to reduce the noise perceived at an specific location.

A "Virtual Phased Array" approach is introduced and validated as a novel broadband source localisation technique for assessing noise problems under stationary conditions from both a theoretical and practical point of view. It is shown that low scanning speeds do not have a significant influence on the accuracy of the localisation maps. Assessing a time stationary sound field, the introduced measurement technique reduces the number of transducers, measurement time and cost of conventional microphone arrays whilst maximise the flexibility of the measurement procedure. Furthermore, several deconvolution methods are adapted and tested for VPAs for source localisation purposes. Spatial resolution, dynamic range and accuracy improvements are achieved by applying deconvolution techniques to the conventional beamforming output. A novel iterative sidelobe cancellation algorithm (ISCA) is introduced and validated against conventional deconvolution methods, showing that the performance of ISCA exceeds other iterative deconvolution algorithms due to the nature of the investigation process: it mainly interacts with the data at the points where the energy is maximised along a limited dynamic range. In addition, successful experimental validation tests are described. It is important to highlight that good results are obtained even at lower frequencies, which commercial multichannel solutions are not able to assess due to size limitations of the arrays.

7.2 Recommendations for future work

The work reported in this thesis opens the door to many questions and possible further improvements of the proposed methods. Some suggestions for future research, and topics that have not been investigated, are listed below:

- The lack of an absolute probe tracking system yields positioning errors if the distance between probe and surface is not maintained. The use of a novel three dimensional positioning system could solve most errors introduced by the current tracking procedure.
- The effects of measuring close to non-rigid materials have not been assessed. Further investigation would provide a better understanding of the contribution of external noise sources in the mapping of sound pressure and particle velocity under such conditions.
- The presence of multiple correlated or partially-correlated sound sources reduces the spatial coherence and therefore the quality of transfer function estimates between reference and scanning sensors. It is suggested to investigate the use of multiple reference transducers for improving the accuracy of the relative phase reconstruction process of panel contribution analysis and VPA.
- It is recommended to study the relative phase between the particle velocity sensor and the pressure transducer contained in a p-u probe in order to distinguish between front and back propagation of a VPA.
- A synthesis technique to reconstruct a full rank covariance matrix has been developed based upon the use of a square or rectangular planar VPA geometry. This could be extended also for irregular array geometries.
- The use of deconvolution methods in combination with source localisation algorithms, such as delay-and-sum beamforming, has been proven to be very promising in a simulated free-field environment. The application of deconvolution methods should also be studied with experimental data in order to define the practical limitations of the proposed approach.
- The ISCA deconvolution algorithm introduced for VPA should be generalised for multichannel phased array systems. In that case, the covariance matrix would be the updated term in each iteration instead of the cross-spectral estimates, similar to the approach followed by CLEAN-SC [173].

Appendix A

Sound power measurements

The sound power of a machine or device provides a general description of its acoustic output. Sound intensity based methods determine this quantity by integrating the normal sound intensity over an area enclosing the noise source. Current ISO standards solely regulate the use of *p-p* intensity probes. A *p-p* probe consists of two paired pressure microphones that approximate sound intensity by combining the average pressure and pressure gradient. Sound pressure is strongly affected by the measurement conditions, especially in reverberant environments or the presence of background noise, which can significantly constrain the accuracy of intensity estimations. As a result, regulations define a set of parameters or "field indicators" to guarantee the validity of measurements and control the uncertainty limits of the estimated sound power level. Alternatively, it is possible to directly obtain sound intensity from the sound pressure and particle velocity acquired using *p-u* probes. However the measurement methodology that support this approach has not yet been established. This appendix adapts the current measurement standards for the use of *p-u* intensity probes. A corresponding field indicator that determines the accuracy of the computed estimations is suggested.

A.1 Introduction

Sound power is one of the main characteristics defining the acoustic output of a noise source. This quantity has a fundamental role in many practical applications since it allows for the estimating of the acoustic impact of a machine or device in its operational environment. Furthermore, it is often used for benchmarking products from different suppliers. Although sound power is commonly used "as a quantitative label of acoustic output" [117], it is not completely independent of the measurement environment [121].

There are many standardised methods to determine sound power based upon sound pressure measurements in free-field conditions (ISO series 3744-3746), sound pressure measurements in a reverberant field (ISO series 3741-3743) and sound intensity measurements (ISO 9614-1, 9614-2 and 9614-3). The main limitation of pressure-based methods is the necessity to perform tests in special measurement rooms, either anechoic or reverberant chambers. Difficulties are often encountered when the test object cannot be placed in an controlled environment, possibly due to its large size, heavy weight or a requirement to operate coupled with another device. In contrast, sound intensity techniques can be used *in-situ* providing that certain measurement conditions are met, regulated by the field indicators.

Sound intensity is the time averaged product of sound pressure and particle velocity. These two quantities can be directly acquired using a *p-u* probe comprising a microphone and a particle velocity sensor (also known as a Microflown), or estimated via indirect methods[1], using a *p-p* probe to approximate acoustic particle velocity from the gradient between two microphones. Multiple research articles have been published exploring the fundamental differences between these two sound intensity measurement principles [132, 176, 177]. Nonetheless, both the IEC standard on instruments for the measurement of sound intensity [178] and the corresponding North American ANSI standard [179] only regulate the use of pressure-based solutions. The lack of calibrated acoustic particle velocity sensors at the time when the standards were proposed may be the main reason for the absence of a *p-u* measurement standard. However, a full-bandwidth calibration procedure has already been established [180], enabling *p-u* probes to be utilised for the localisation, quantification and ranking of sound sources, even in conditions where *p-p* probe cannot be used due to high levels of background noise or reverberation [133].

This appendix outlines the theoretical basis of sound intensity methods using both *p-p* and *p-u* probes for the estimation of sound power based on the work published in [181]. Furthermore, the standardised measurement procedure is expanded to include sound intensity *p-u* probes, introducing a new field indicator which accounts for the measurement error of a direct sound intensity approach.

A.2 Sound power estimation

Sound power is commonly used as a quantitative description of the acoustic output of a device [117]. It is defined by the integral of the normal intensity over the radiating

[1] A novel indirect method based on particle velocity measurements has recently been introduced for the estimation of sound power [175]

noise surface, i.e.

$$\Pi = \int_S I_n dS \tag{A.1}$$

where I_n is the active normal intensity described as [182]

$$I_n =< p\, u_n >_t = \frac{1}{2}\mathrm{Re}\{p\, u_n^*\} \tag{A.2}$$

where p is sound pressure, u_n is normal particle velocity and $< \, . \, >_t$ indicates time averaging. Taking into account the measurement errors introduced by the acquisition of sound intensity gives

$$\hat{\Pi} = \Pi \left(1 + \int_S b[\hat{I}_n]\right) \tag{A.3}$$

where Π is the "pure" sound power unaffected by any errors, $\hat{\Pi}$ denotes its biased estimate and $b[\hat{I}_n]$ is the bias of the sound intensity estimations. This last term depends upon the measurement principle used to acquire sound intensity: directly using a *p-u* probe, or indirectly with a *p-p* probe (two pressure microphones). Note that random errors are not considered in Equation A.3, thus spatial positioning errors, electrical noise, etc, are disregarded.

A.2.1 Direct intensity estimation

Equation A.2 can be directly calculated from the sound pressure and acoustic particle velocity acquired using *p-u* probes without any further assumptions or approximation. The measurement error introduced depends upon the reactivity of the sound field and the calibration of the probe [183]

$$\hat{I}_n = \frac{1}{2}\mathrm{Re}\{p\hat{u}_n^*\} = \frac{1}{2}\mathrm{Re}\{pu_n^* e^{j\varphi_{ue}}\} = I_n \left(1 - \varphi_{ue}\frac{J_n}{I_n}\right) = I_n(1 + b[\hat{I}_n]) \tag{A.4}$$

where φ_{ue} is a small phase error introduced during the calibration procedure and J_n is the reactive intensity, defined as

$$J_n = \frac{1}{2}\mathrm{Im}\{pu_n^*\} \tag{A.5}$$

A.2.2 Indirect intensity estimation

Sound intensity can be estimated by measuring sound pressure at two closely spaced positions using the "p-p measurement principle". Two fundamental quantities define the intensity at one point: sound pressure and acoustic particle velocity. Whereas the former can be easily calculated as the average of the two pressure signals, the latter is

obtained by a finite-difference approximation to the pressure gradient in Euler's equation of motion [132], hence

$$\hat{I}_n \simeq \frac{1}{2\rho\Delta r}\left\langle (p_1(t)+p_2(t))\int_{-\infty}^{t}[p_1(\tau)-p_2(\tau)]\,d\tau\right\rangle_t \tag{A.6}$$

where $\langle . \rangle_t$ denotes an time average operation, ρ is the density of air and Δr is the separation between the two microphones. Scattering and diffraction, instrumentation phase mismatch and finite difference approximation are the main limitations of this measurement approach. It can be shown that a small phase mismatch error gives rise to a bias error that can be approximated by

$$\hat{I}_n \simeq I_n - \frac{\varphi_{pe}}{k\Delta r}\frac{|p|^2}{\rho c} = I_n\left(1-\frac{\varphi_{pe}}{k\Delta r}\frac{|p|^2/\rho c}{I_n}\right) = I_n(1+b[\hat{I}_n]) \tag{A.7}$$

where k is the wave number and c is the speed of sound. This expression shows that the bias error $b[\hat{I}_n]$ is inversely proportional to the frequency and the microphone separation distance whilst being proportional to the ratio of absolute square sound pressure to sound intensity.

A.3 Field indicators

"Field indicators" are a set of parameters suggested by standards to assess measurement conditions and ultimately judge the quality of the produced results. They are calculated from acquired data, accounting for errors introduced not only by the measurement instrumentation but also by the testing environment.

A.3.1 Temporal variability indicator (F_1)

The temporal variability indicator is used to check the stationarity of the sound field within the measured segment by evaluating a series of short time average intensity estimates.

$$F_1 = \frac{1}{I_n}\sqrt{\frac{1}{M-1}\sum_{k=1}^{M}(I_{nk}-\overline{I_n})^2} \tag{A.8}$$

where $\overline{I_n}$ is the arithmetic average of I_n calculated from M short time averages I_{nk}. The criterion for this indicator is given in the standard as $F_1 \leq 0.6$. Being a statistical concept, this indicator is valid for both direct and indirect methods.

A.3.2 Surface pressure-intensity indicator (F_2)

The purpose of surface pressure-intensity indicator is to limit the bias error due to instrument phase mismatch. It is calculated by taking the difference in decibels between arithmetic averages of *unsigned intensity* and pressure levels. It is defined as:

$$F_2 = \overline{L_p} - \overline{L_{|I_n|}} = 10\log\left(\frac{|p|^2/\rho c}{I_n}\right) = \delta_{pI} \tag{A.9}$$

where

$$\overline{L_p} = 10\lg\left(\frac{1}{N}\sum_{i=1}^{N} 10^{0.1L_{pi}}\right),\ \overline{L_{|I_n|}} = 10\lg\left(\frac{1}{N}\sum_{i=1}^{N}|I_{ni}|/I_0\right) \tag{A.10}$$

Note that F_2 is equal to the pressure-to-intensity index δ_{pI}. There are two criteria regarding this indicator:$F_2 < L_d$, implying $\delta_{pI} < \delta_{pI_0} - K$ where K is bias error factor given in the ISO standard, the other is related with F_3 and given in the next section.

A.3.3 Negative partial power indicator (F_3)

This indicator is essentially the same as F_2 except the arithmetic average is evaluated using *signed intensity* so $\overline{L_{|I_n|}}$ becomes $\overline{L_{I_n}}$ whereby

$$\overline{L_{I_n}} = 10\lg\left|\frac{1}{N}\sum_{i=1}^{N} I_{ni}/I_0\right| \tag{A.11}$$

The criterion regarding F_2 and F_3 is given as $F_3 - F_2 \leq 3dB$. This is a measure of the ratio between partial sound power entering and leaving the segment.

A.3.4 Field non-uniformity indicator (F_4)

The field non-uniformity indicator is the normalised variance of segment intensity values. It is the spatial variance across the defined surface and used to control the minimum number of segments necessary, thus restricting the uncertainty of the spatial mean estimates within acceptable limits. It is defined as:

$$F_4 = \frac{1}{\overline{I_n}}\sqrt{\frac{1}{N-1}\sum_{i=1}^{N}(I_{ni} - \overline{I_n})^2} \tag{A.12}$$

where $\overline{I_n}$ is the arithmetic average of I_n using N segment measurements I_{nk}. The criterion of this indicator is defined in the ISO 9614-1 as $N > CF_4^2$. N indicates the number of segments defined and C depends on grade of accuracy. F_4 is applicable for both direct and indirect intensity methods.

A.3.5 Reactivity error indicator (F_5)

The reactivity error indicator is directly associated with the phase relation between pressure and velocity. The indicator can be defined as:

$$F_5 = \left| 10 \lg \left(1 - \varphi_{ue} \frac{|\overline{J_n}|}{|\overline{I_n}|} \right) \right| \tag{A.13}$$

where F_5 is the ratio of reactive to active intensity in logarithmic form and φ_{ue} is approximately 0.035 radians (2°) for the piston-on-a-sphere calibration procedure [180]. If this indicator has a large value then even a small phase mismatch φ_{ue} could cause considerable bias error (See equation A.7). The criterion for $F5$ is given as $F_5 < 2s$ where s is defined in the ISO standard in terms of octave bands and engineering accuracy. Note that this criterion replaces F_2 and F_3 for controlling the bias errors introduced by the use of p-u probes.

A.4 Sound power estimation with *p-p* and *p-u* probes

An experimental example is shown in this section. The sound power of a loudspeaker measured in an anechoich chamber and a room with noise is computed following Equation A.1 and can be seen in Figure A.1. It should be noted that very similar results are obtained using either p-p or p-u probes in both testing environments, regardless of the fundamental differences between acoustic transducers, calibration procedure or data acquisition equipment. The small discrepancies between curves were most likely due to experimental errors introduced during the measurement process, such as probe misalignments or slight variations of loudspeaker signal.

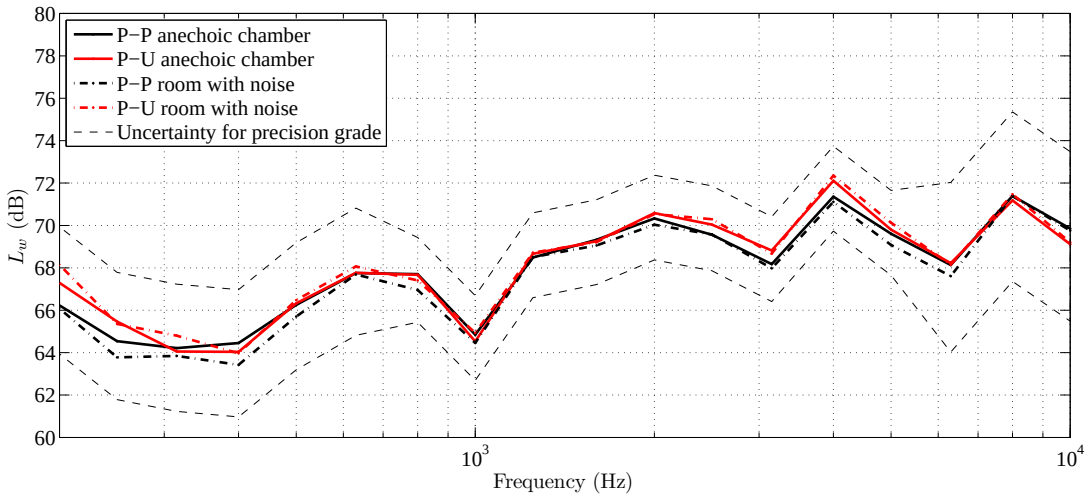

FIGURE A.1: Sound power of a loudspeaker source, measured with a p-p and a p-u probes in two different measurement scenarios.

Appendix B

Mapping non-stationary sound fields

Scanning techniques can significantly reduce the number of sensors required to obtain the acoustic characteristics of a time-stationary sound field. However, excitation changes during the data acquisition process are traditionally disregarded. This appendix presents a new method for assessing non-stationary sound fields based upon the computation of transfer functions between a scanning transducer and a reference sensor positioned near the excitation source [17, 25, 184]. A frequency dependent spatial discrimination filter is applied to select the active measurement positions. The proposed method has been developed to estimate musical instrument radiation patterns.

B.1 Introduction

Directivity patters play an important role on virtual acoustics, especially for the computation of room auralisations [185]. The assessment of musical instrument radiation patterns is a classic example that shall be evaluated in non-stationary conditions. There are no standard regulations regarding the measurement procedure required to characterise such acoustic sources mainly due to practical difficulties. Therefore, the development of a technique which allows for the characterisation of sound radiated by non-stationary sources in a fast and efficient way is particularly valuable.

Scanning methods are proven to minimise the measurement time and cost, but typically constrained to mapping stationary sound fields. In the literature of near-field acoustic holography (NAH), several signal processing techniques have been proposed to overcome some problems derived from the source degree of time stationary [186–188]. Most

techniques require complicated and time consuming measurement procedures, involving multiple reference sensors and scanning microphone arrays. In contrast, the proposed method aims to provide a simple approach for obtaining sound radiation patterns using a single reference sensor and a scanning transducer.

B.2 Theory

The problem addressed in this appendix is shown in Figure B.1: a sound pressure microphone is moved across a plane located at a distance R whilst a reference sensor is placed near the musical instrument.

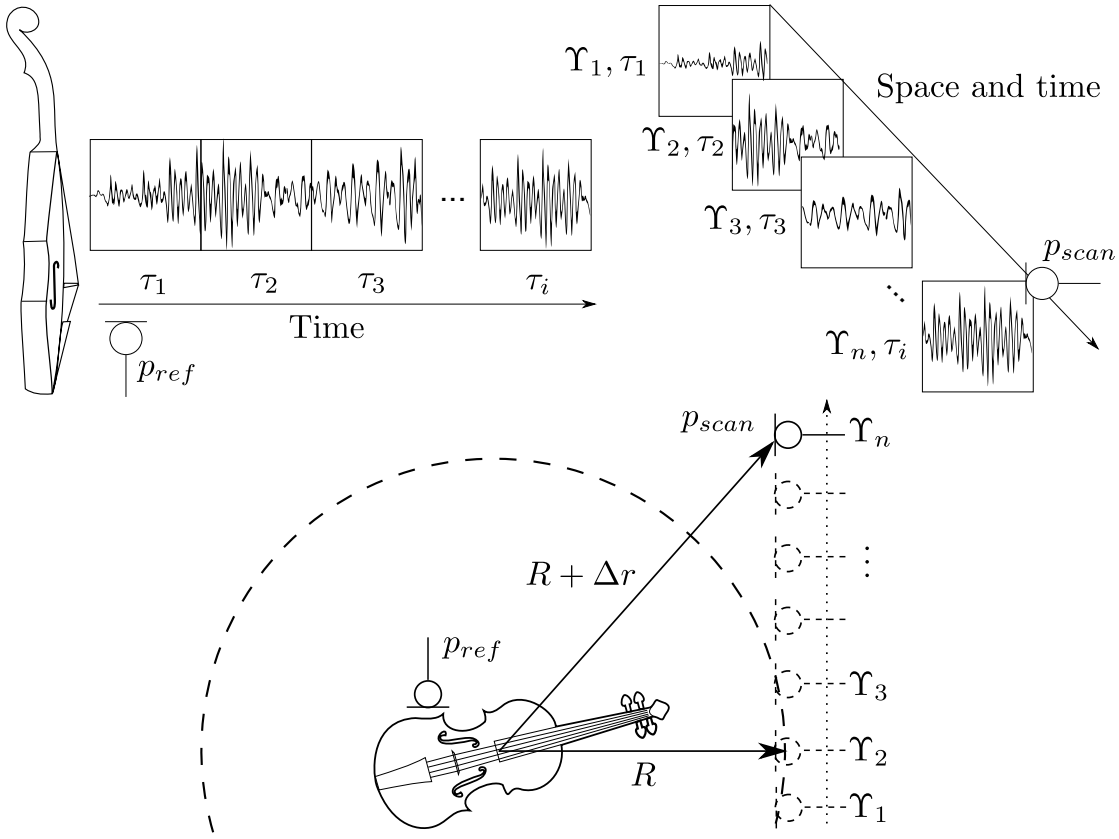

FIGURE B.1: Sketch of the assessed problem

According to the principles of Equivalent Source Methods (ESM) reviewed in Section 5.2.4, any complex sound source can be approximated by a set of monopole sources. The sound pressure generated by the superposition of two or more closely distributed monopoles in a free field space can be expressed as

$$p(r, \theta, \varphi, t) \approx \frac{A(\omega)}{r} D(\theta, \varphi) e^{j(\omega t - kr)} \tag{B.1}$$

where A is a complex time independent term which depends upon the source characteristics such as volume velocity, specific acoustic impedance and wavenumber; ω is the angular frequency; r is the distance between source centre and measurement position; and $D(\theta, \varphi)$ is a directivity term which can take arbitrary values for different radiation angles of azimuth (θ) and elevation (φ). Evaluating the above expression for a simple source such as a pulsating sphere, $D(\theta, \varphi)$ simplifies to unity for all angles. Assessing a baffled circular piston, D(θ, φ) would then be composed by first order Bessel functions [111]. In contrast, musical instruments cannot be described using general analytical expressions and consequently measurement procedures are key to their characterisation.

The sound pressure perceived at any point of the sound field can be obtained by evaluating Equation B.1. In the case studied, the pressure at the fixed reference transducer located at $[r', \theta', \varphi']$ can be defined as such:

$$p_{ref}(t) = p(r', \theta', \varphi', t) \approx \frac{A(\omega)}{r'} D(\theta', \varphi') e^{j(\omega t - k\, r')} \tag{B.2}$$

Directivity patterns define the acoustic radiation behaviour for different azimuth and elevation angles. However, as shown in Figure B.1, the scanning sensor is moved across a plane, which implies that the separation to the source r changes during the data acquisition process. The acquired pressure signals shall be then modified to calculate the equivalent sound pressure received across a spherical surface of radius R, i.e.

$$p_{sph}(\theta, \varphi, t) \approx p(R + \Delta r, \theta, \varphi, t) \left(\frac{R + \Delta r}{R} \right) e^{j\Delta r} \tag{B.3}$$

where Δr represents the euclidean distance between the measurement position and its projection on the sphere. Figure B.2 shows an example of the sound field produced by a monopole source measured in 6 equidistant planes and the corresponding directivity pattern obtained after correcting the data.

A time independent expression that captures the sound radiation characteristics can be obtained by computing the transfer function estimator H_1 between the acquired signals defined in Equation B.2 and Equation B.3, hence

$$H_1(\theta, \varphi, \omega) = \frac{S_{p_{ref} p_{sph}}}{S_{p_{ref} p_{ref}}} = D(\theta, \varphi) \left(\frac{r'}{D(\theta', \varphi') R} \right) e^{-jk(R - \Delta r - r')} \tag{B.4}$$

where $S_{p_{ref} p_{sph}}$ is the cross-power spectral density between p_{ref} and p_{sph} and $S_{p_{ref} p_{ref}}$ is the auto-spectral density of p_{ref}. The influence of the reference sensor position remains constant for all positions scanned with the moving sensor. It can therefore be shown that the transfer function estimator H_1 could be understood as a scaled version of the

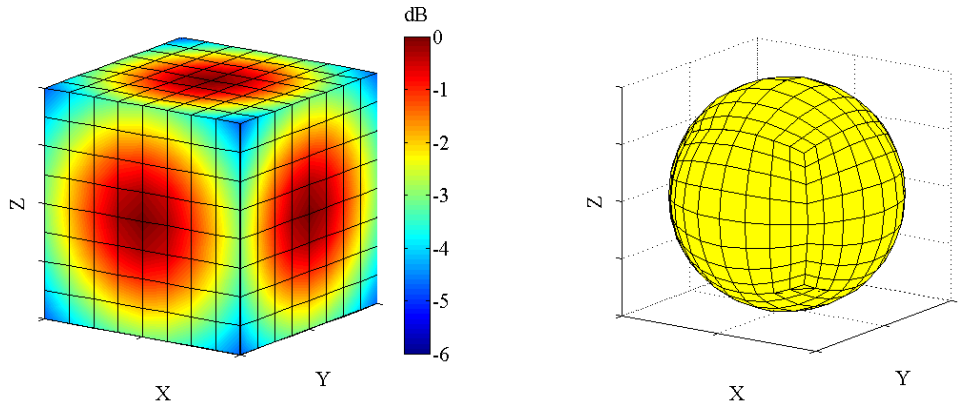

FIGURE B.2: Example of a monopole radiattion measurements transformed to a spherical directivity pattern

directivity term $D(\theta, \varphi)$, i.e.

$$H_1(\theta, \varphi, \omega) = D(\theta, \varphi)\gamma(\omega) \tag{B.5}$$

where $\gamma(\omega)$ is a scaling factor which depends upon the reference sensor position, sphere radius R and source characteristics. Equation B.5 shows that the computation of the transfer function between the reference and scanning signals yields a time independent expression for calculating the directivity of a sound source. This fundamental property enables using scanning techniques even though the excitation is non stationary. Furthermore, representations of the transfer function variations across the space are directly related to the sound source radiation patterns.

The lack of excitation during the data acquisition process can lead to erroneous estimations. Similar to VPA, a positional discrimination algorithm can be applied to select the active spatial positions. In this case, the valid data segments are selected depending on the spectral content of the reference sensor by defining a constrained dynamic range. Consequently, positions with insufficient excitation are disregarded in the analysis. This yields an irregular spatial grid which size changes depending on frequency. Figure B.3 shows an sketch of the process.

In summary, it has been shown analytically that the transfer functions between a fixed and a moving transducer yields a time independent ratio which contains information related to the source directivity.

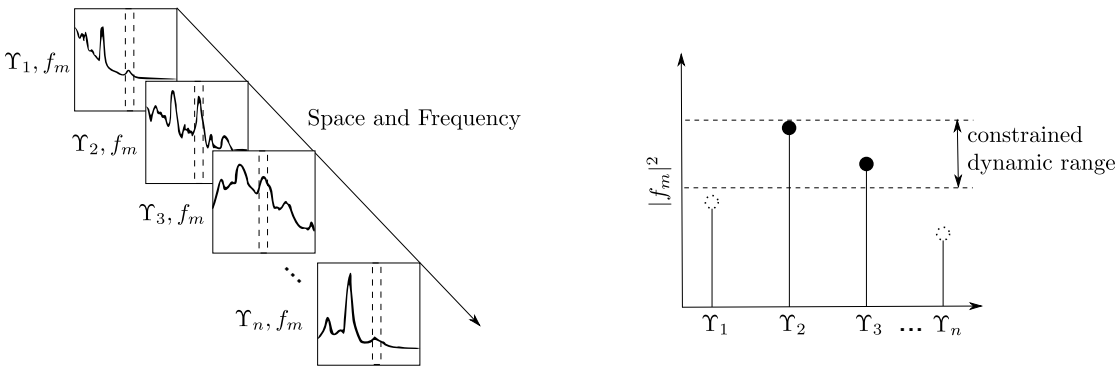

FIGURE B.3: Diagram of the positional discrimination procedure

B.3 Experimental evaluation

This section presents an overview of the results previously presented in [17, 25, 184], the characterisation of a violin sound radiation.

B.3.1 Non-stationary mapping

This first measurement example is focused on the direct sound mapping of a musical instrument. Figure B.4 shows the acoustic radiation of a violin. The continuously changing sound field was assessed as if data were acquired in stationary conditions due to the computation of transfer functions across the measurement plane in combination with the positional discrimination filter. As a result, a smooth radiation pattern is obtained with a maximum over the area where the strings were bowed.

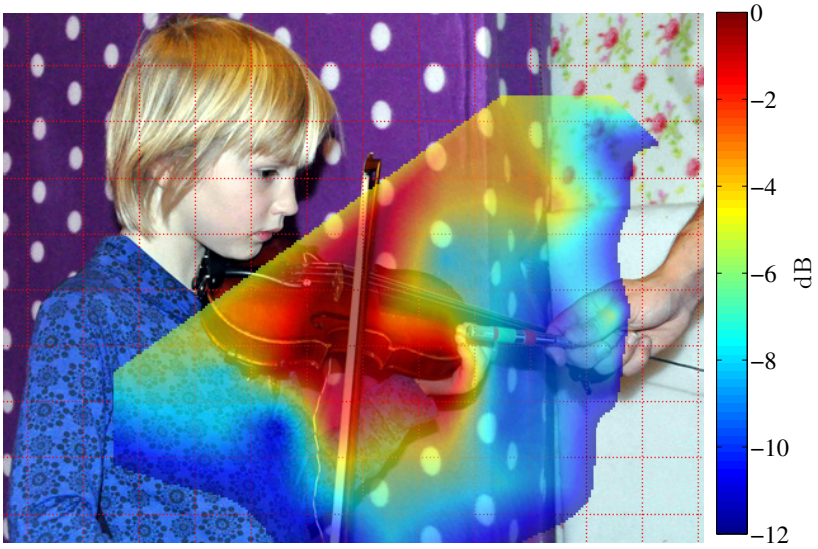

FIGURE B.4: Direct sound radiation mapping of a violin at 1340 Hz.

B.3.2 Directivity patterns

A set of measurements were performed in a large anechoic chamber at the ISVR (Southampton, UK) in order to achieve the free-field conditions required to apply Equation B.3. The sound radiation of a violin was characterised by moving a microphone across a plane of two metres horizontally by two metres vertically located one metre away from the musical instrument. The musician was turned around the radiation centre for the front, left, right and back plane and then she had to perform lying on a table in order to capture the top and bottom radiation. A traditional music piece was played during the data acquisition process. The time expended in each scan was about 4 minutes.

Figure B.5 presents a picture of the experimental setup along with a spectrogram sample extracted from one the recordings. As can be seen, measurements were performed under non time stationary condition since short time segments of the excitation signal present very different spectral characteristics.

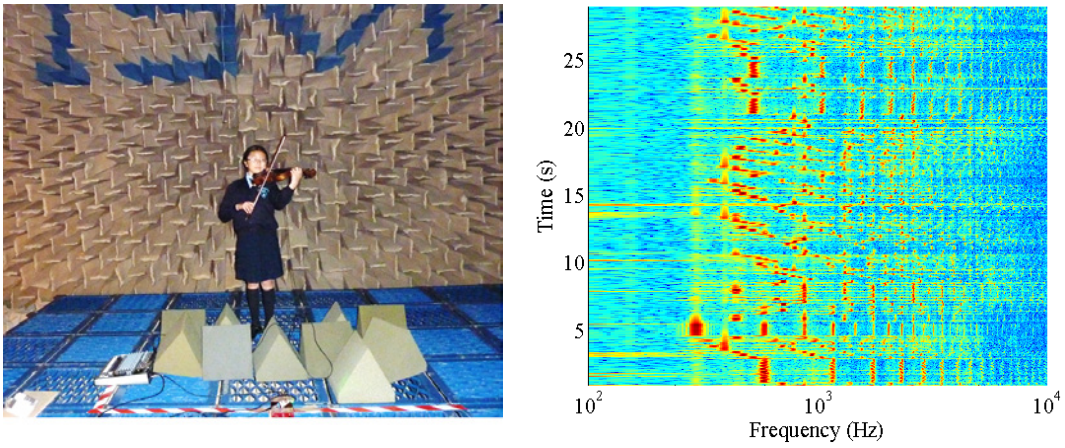

FIGURE B.5: Experimental measurement setup (left) and spectrogram sample (right)

One method for displaying 3D directivity patterns is the use of multiple colourmaps. Such figures give a direct feedback about radiation maxima but they may not be sufficiently clear. It is also common practice to use polar coordinates scaling the radius of the point aimed to represent according to the measured value. Figure B.6 illustrates the two representation methods showing the violin radiation pattern at 1260 Hz.

Furthremore, Figure B.7 presents several examples of the measured directivity patterns at several third octave frequency bands: 315 Hz, 500 Hz, 1000 Hz and 1588 Hz. The x plane represents the frontal measurement plane; therefore, only the frontal, top and righ sides can be seen in the given figures. According to the measurement results, the violin has an omnidirectional behaviour at the lower frequency bands. In contrast, as frequency

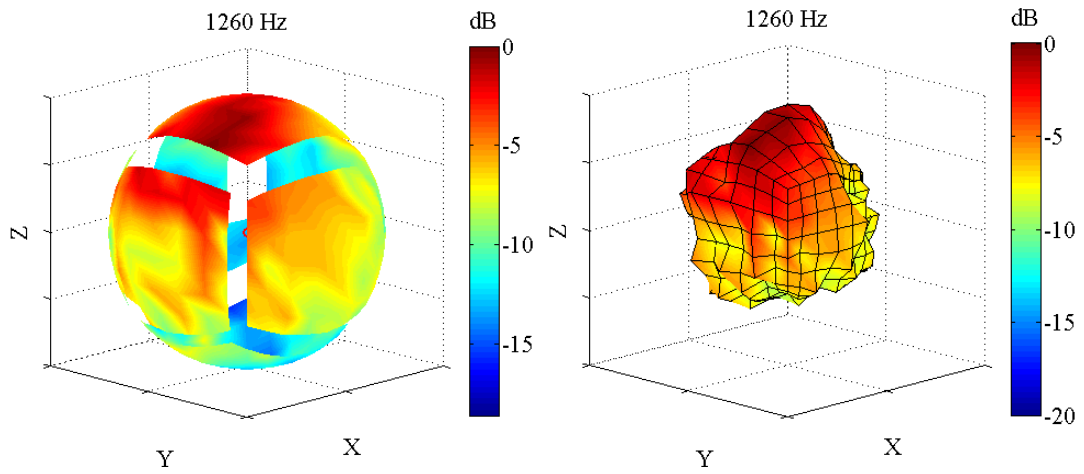

FIGURE B.6: Example of a monopole radiattion measurements transformed to spherical directivity pattern

increases, the directivity patterns change dramatically, moving the main radiation lobe from the front of the musician to the side, depending on the frequency band assessed.

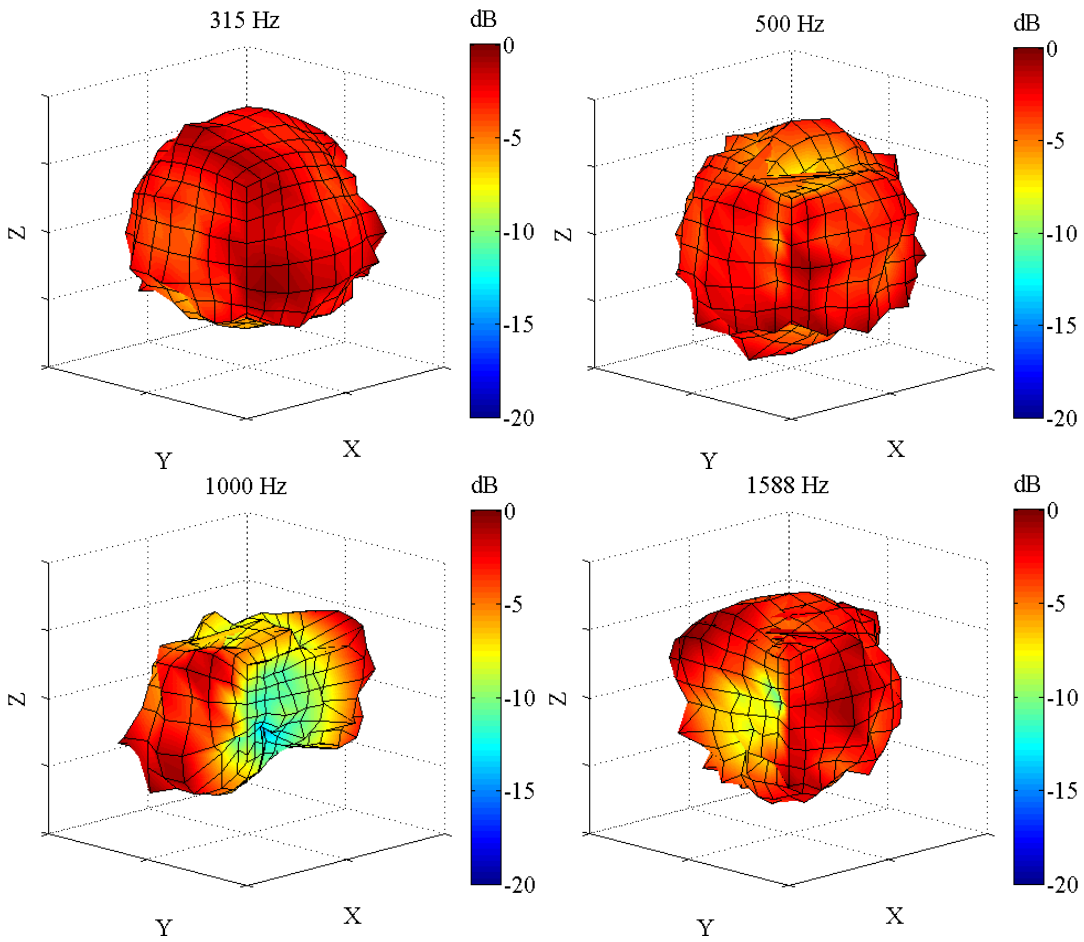

FIGURE B.7: Directivity patterns of a violin at third octave bands of 500 Hz (top left), 1000 Hz (top right), 1260 Hz (bottom left) and 1588 Hz (bottom right) [dB]

Appendix C

Scanning Operational Deflection Shapes

Under specific conditions, structural vibrations can be acoustically measured using particle velocity sensors located near a vibrating structure. Relative phase information can also be acquired by using a static reference sensor. The combination of scanning particle velocity measurements and relative phase information enables to study operational deflection shapes (ODS) in a fast and efficient way. A theoretical basis of the measurement principle is presented in this appendix along with an experimental example evaluated with the proposed method.

C.1 Introduction

Understanding the dynamic behaviour of a machine is crucial for controlling noise, vibrations, fatigue or wear problems. Obtaining a visual representation of structural deflections may lead to discover which optimal modifications could improve the assessed design. The characterisation of the Operational Deflection Shapes (ODS) is one of the most common methods for studying the vibro-acoustic properties of a device working in an stationary regime [189–191] since it provides an observation, or visualisation, of its forced motion.

The most widespread techniques for testing Operational Deflection Shapes are based on step-by-step or simultaneous measurements using accelerometers. Nonetheless, attaching transducers to a vibrating structure may not be always possible. This fact has increased the popularity of non-contact solutions such as Laser Doppler Vibrometry (LDV) [192]. LDV systems allow for fast acquisition of a high number of measurements

with a good spatial resolution. However, the excessive price and setup complexity of current commercial systems limit the use of LDV for most common applications.

Alternatively, acoustic particle velocity sensors have been proven suitable for measuring non-contact vibrations [193, 194]. Several studies have revealed the potential of p-u probes for measuring structural vibrations with step-by-step techniques [129, 195–198] but there was no evidence about the viability of measuring ODSs using p-u probes via scanning methods. This appendix explores the use of Scan & Paint for measuring the ODSs of a vibrating structure in stationary conditions, based on the work previously introduced by the author in [19, 21]. The foundations of the method are given along with experimental evidence on the performance of the measurement technique.

C.2 Background Theory

Two fundamental aspects are covered in this section: the capability of particle velocity sensors for performing non-contact vibration measurements and the importance of measuring Operation Deflection Shapes for vibroacoustic applications.

C.2.1 Particle velocity sensors for vibro-acoustic applications

The following derivation follows the work of de Bree et. al. introduced in [129, 195]. It begins by studying the definition of the Helmholtz wave equation in terms of velocity potential $\Psi(r)$, i.e.

$$\bigtriangledown^2 \Psi + k^2 \Psi = 0 \tag{C.1}$$

where $\bigtriangledown^2$ is equivalent to the Laplace operator and k is the wave number $(2\pi f/c_0)$. A description of the sound field near a vibrating surface can be obtained by evaluating Equation (C.1) with the following boundary conditions:

$$\begin{cases} u_n = \partial\Psi/\partial_n & \text{if } r = 0 \\ \\ \Psi \propto e^{jkr}/r & \text{if } r \to \infty \end{cases} \tag{C.2}$$

where r is the distance to the vibrating surface; ∂/∂_n is the normal derivative and u_n is the normal component of the particle velocity. The observable acoustic values, sound pressure p and particle velocity $\mathbf{u}$, are connected with the potential as such:

$$\mathbf{u} = \bigtriangledown\Psi \quad , \quad p = -j\omega\rho\Psi \tag{C.3}$$

where $\bigtriangledown$ represents the gradient operator and ρ is the density of the medium (air).

According to [129], it is possible to establish a region between the vibrating surface and the beginning to the conventionally called "near-field" where Equation C.1 is reduced to the Laplace equation for incompressible fluids. In order to derive this expression it is necessary to perform a Taylor series expansion of the velocity potential term $\Psi(r)$ in the vicinity of the surface and then only consider sound waves of wavelength (λ) much larger than the spatial wavelength which defines the vibrating surface (L_{eff}). In summary, it can be shown that the sound field at a distance r from a vibrating surface can be considered to be in the "very near-field" if the two following conditions are met:

$$\begin{cases} r << L_{eff}/2\pi & \text{condition (I)} \\ \\ \lambda >> L_{eff} & \text{condition (II)} \end{cases} \tag{C.4}$$

In the very near-field, the normal component of the particle velocity equals the structural velocity of the vibrating surface with neglectable error. These considerations are the basis of non-contact vibration measurements using particle velocity sensors. An important issue is related to the estimation of the very near-field size along the normal direction to the surface. To verify this condition, r should be at least two orders of magnitude smaller than $L_{eff}/2\pi$. Nevertheless, it should be noted that the effective wavelength related to the vibrating surface changes with frequency depending on the mode index. For a simple geometry, such as a rectangular panel of dimensions L_x by L_y, L_{eff} can be defined as such:

$$L_{eff} = \sqrt{\left(\frac{L_x}{n_x}\right)^2 + \left(\frac{L_y}{n_y}\right)^2} \tag{C.5}$$

where n_x and n_y are the mode indexes for the x and y axis, respectively. This means that the measurement distance range that allow for the direct acquisition of structural vibrations using a particle velocity sensor is reduced according to the panel size and mode index as well as increasing the frequency.

C.2.2 Operational Deflection Shapes

Operational Deflection Shapes (ODSs) are representations of the relative motion of a vibrating device, which describe the dynamic behaviour of a component, machine or structure. According to [199], and ODS could be understood as "the picture which is seen using a stroboscope, large, fast and powerful enough to freeze the object at a desired frequency, if the eyes of the observer are strong enough to resolve the (probably) very small deformations."

An ODS can be defined from any forced motion, either at a moment in time, or at a specific frequency. Conventionally, an ODS is computed from a set of sampled time domain responses of accelerometers acquired simultaneously or using pairs of frequency domain data sets. Alternatively, acoustic particle velocity sensors are also suitable for such measurements providing the transducer is located in the vicinity of the vibrating surface, in the very near field [129, 195]. A detailed overview of the most widespread ODS measurement methods, both in time and frequency domain, can be found in [190].

Operational Deflection Shapes can be predicted from analytical models (modal analysis) by defining the boundary conditions and operating forces, providing that these terms are measurable in the assessed scenario. In the latter, it has become possible to use particle velocity transducers in the areas of experimental modal analysis (EMA) [198] and operational modal analysis (OMA) [200] thanks to the so-called very near field assumption described above. If, however, the objective is to study a particular structure under one or a few specific conditions, a direct ODS measurement is faster, simpler, and more accurate than analytical predictions [199]. No errors are introduced derived from geometry problems, wrong boundaries conditions or linearity issues.

In practice, the input excitations are often unknown and therefore the ODS have to be computed using "ODS FRF measurements". The measurement procedure is based upon the asynchronous acquisition of data, either step-by-step or by scan-based methods, but it requires a fixed reference sensor for linking all the acquired data. The main limitation of this method is that the data acquired with both transducers must be linearly related (high values of coherence between the two signals), otherwise the resulting ODS may not correspond with the real dynamic behaviour of the element.

Each ODS FRF is formed by replacing the magnitude of each cross-spectra between the moving and static sensor with the auto-spectra of the scanning transducer. The phase of the cross-spectra is preserved as the phase of the ODS FRF. The new term obtained contains the magnitude of each point across the vibration surface, and the phase relative to the fixed reference position.

C.3 Experimental evaluation

This section presents an overview of the experiments presented in [19, 21]. Two measurement methods are compared: step-by-step measurements attaching accelerometers to a vibrating surface; and Scan & Paint measurements using a p-u intensity probe moved near the plate (less than 5 centimetres away).

C.3.1 Measurement setup

A measurement rig was designed and built to simulate the flow induced vibration and noise radiation from a car window due to the turbulent wake produced by the wing mirror. Turbulences are convected downstream causing surface pressure fluctuations on the side window that produce vibration and ultimately noise. This excitation, despite its random nature, is time-stationary whilst maintaining the flow speed constant. As a result, a stationary broadband excitation source is achieved. Measurements were performed in the subsonic open jet anechoic wind tunnel located at the ISVR (Southampton, UK) where a very low noise and low turbulent flow of up to 150 km/h can be produced [201]. A constant flow speed of 144 km/h was used in the experiments presented below. Figure C.1 shows a front and rear picture of the experimental setup.

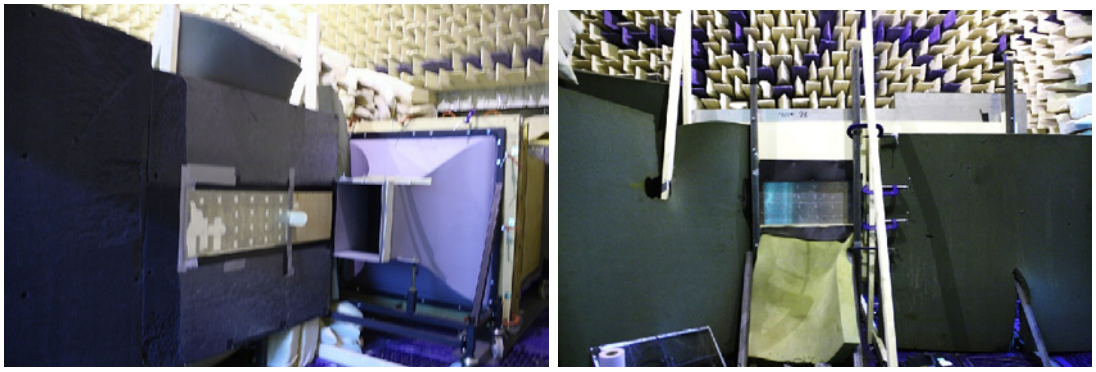

FIGURE C.1: Front (left) and rear (right) view of the experimental setup.

Practical difficulties prevented the installation of a real car window; instead, an aluminium plate with similar dynamic properties was studied. The plate was attached to a rigid frame so as to achieve an idealised zero displacement boundary condition at the edges. The test panel was mounted on an acoustic baffle for minimising the noise generated by flow interaction with the panel edges and diffraction effects. Furthermore, the wing mirror was substituted by a half cylinder. The object was placed just before the upstream edge of the aluminium panel and aligned with the central axis of the nozzle for ensuring that it was located inside the jet core.

C.3.2 Surface velocity spectra

The use of the Scan & Paint grid discretisation method introduced in Chapter 3 allows for the direct comparison of step-by-step and scanning measurements. Figure C.2 presents the surface velocity spectra obtained with both methods at two different positions.

Results are very similar from 90 Hz to 500 Hz. However, the scanning method overestimates the structural vibrations at very low frequencies probably caused by poor

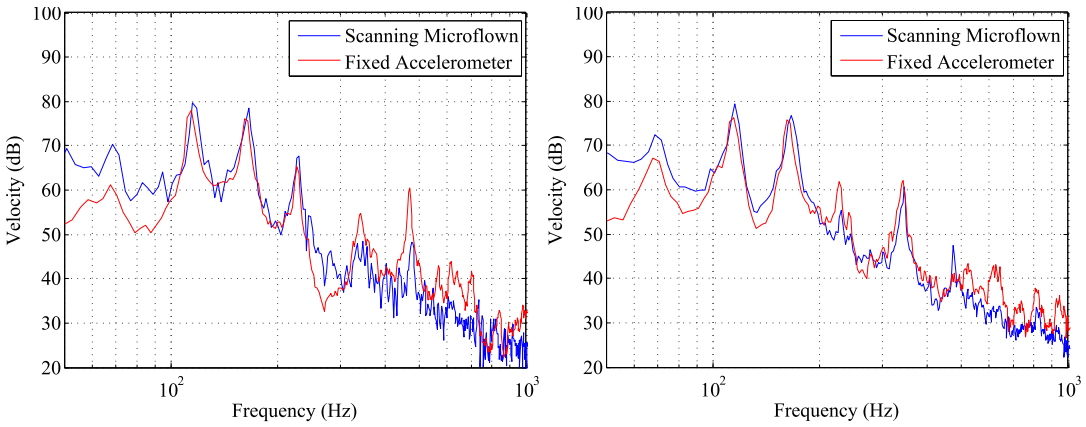

FIGURE C.2: Comparison of surface particle velocity at two different positions

signal-to-noise ratio in the presence of high flow speed leaked through the panel framework. It should be noted that the higher assessable frequency depends upon the spatial wavelength L_{eff} associated with the vibrating panel and the measurement distance between panel and transducer. These boundaries can be estimated according to the theory given in Section C.2.1. For the case studied, the high frequency limit of the scan-based measurement method was approximately at 450 Hz.

C.3.3 Direct panel velocity mapping

The direct mapping of surface velocity is an intuitive approach for comparing two different measurement methods. Figure C.3 shows the results achieved at four operational resonant frequencies. The results are very similar below 200 Hz. However, the vibration patterns significantly differ at higher frequencies probably induced by the spatial resolution differences between both methods. The number of measurement positions of the step-by-step method determines the total time required for the test. Therefore, a decision have to be made considering the maximum assessable frequency and the total measurement time. It should be noted that the data acquisition process of the step-by-step measurements took about an hour, whereas Scan & Paint measurements were performed in about 4 minutes.

C.3.4 Operational Deflection Shapes

As have been pointed out in Section C.2.2, Operational Deflection Shapes (ODS) illustrate the dynamic behaviour of a structure or a vibrating plate. It is interesting to focus the analysis on the spectral excitation frequencies that cause operational resonances. At

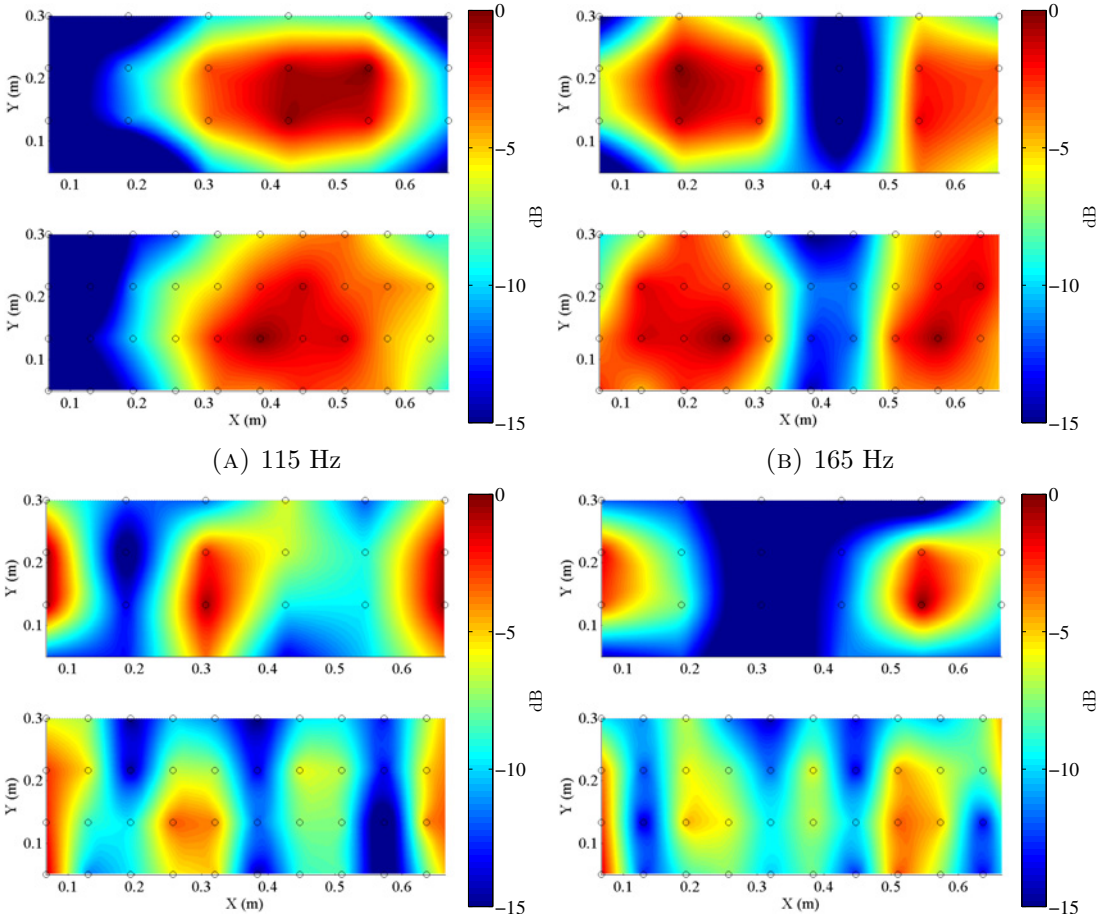

(A) 115 Hz (B) 165 Hz

(C) 342 Hz (D) 470 Hz

FIGURE C.3: Panel velocity mapping with step-by-step measurements using accelerometers (top of each sub-figure) and scanning measurements using a p-u probe (bottom of each sub-figure).

these specific frequencies, which conventionally are very close to the natural modes of the structure, the input excitation energy is highly amplified.

Figure C.4 shows the ODSs at the first four resonant frequencies which coincide with the horizontal modes of the vibrating panel. Particle velocity plots are presented with relative phase information linked to a fixed accelerometer that was attached to the surface (ODS FRF). These results show very clear ODSs, supporting the potential of using p-u intensity probes in combination with scan-based measurement methodologies for vibro-acoustics applications.

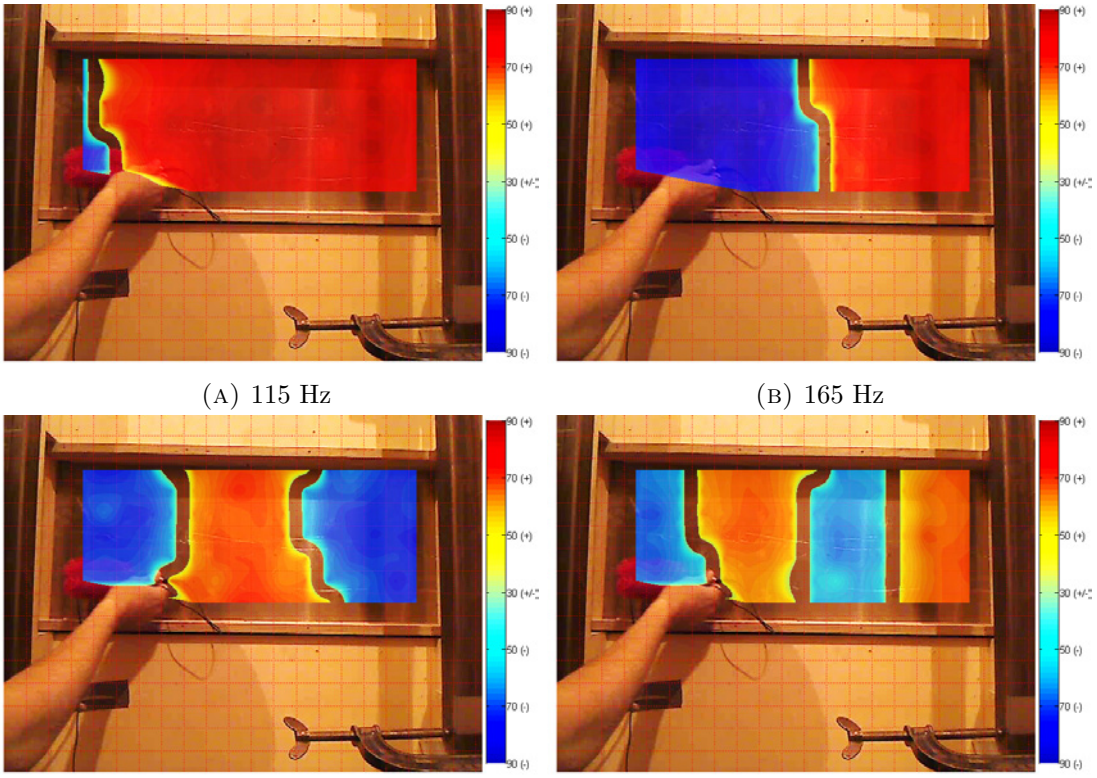

(A) 115 Hz (B) 165 Hz

(C) 230 Hz (D) 342 Hz

FIGURE C.4: Operational deflection shapes of a vibrating plate obtained with scanning measurements using a p-u probe.

Bibliography

[1] W. Kock, *Seeing sound.* Wiley-Interscience, 1971.

[2] I. Newton, *Opticks: Or, A Treatise of the Reflections, Refractions, Inflections and Colours of Light.* W. Innys, 1704.

[3] G. S. Settles, *Schlieren and Shadowgraph Techniques: Visualizing Phenomena in Transparent Media.* Experimental Fluid Mechanics, Springer, 2001.

[4] M. Josephson, *Edison: a biography.* McGraw-Hill paperbacks, McGraw-Hill, 1959.

[5] Y.-H. Kim, "Sound visualization and manipulation: theories and applications," *Noise News International*, vol. 20(1), pp. 8–25, 2012.

[6] R. Beyer, *Sounds of Our Times: Two Hundred Years of Acoustics.* Springer Verlag GMBH, 1999.

[7] J. Hald, "STSF - a unique technique for scan-based near-field acoustics holography without restrictions on coherence," tech. rep., Bruel & Kjaer, 1989.

[8] H.-S. Kwon and Y.-H. Kim, "Moving frame technique for planar acoustic holography," *The Journal of the Acoustical Society of America*, vol. 103, no. 4, pp. 1734–1741, 1998.

[9] S.-H. Park and Y.-H. Kim, "An improved moving frame acoustic holography for coherent bandlimited noise," *The Journal of the Acoustical Society of America*, vol. 104, no. 6, pp. 3179–3189, 1998.

[10] S.-H. Park and Y.-H. Kim, "Effects of the speed of moving noise sources on the sound visualization by means of moving frame acoustic holography," *The Journal of the Acoustical Society of America*, vol. 108, no. 6, pp. 2719–2728, 2000.

[11] S.-H. Park and Y.-H. Kim, "Visualization of pass-by noise by means of moving frame acoustic holography," *The Journal of the Acoustical Society of America*, vol. 110, no. 5, pp. 2326–2339, 2001.

[12] M. Lee and J. S. Bolton, "Scan-based near-field acoustical holography and partial field decomposition in the presence of noise and source level variation," *The Journal of the Acoustical Society of America*, vol. 119, no. 1, pp. 382–393, 2006.

[13] E. Lumnitzer and Z. Farkaovsk, "New methods for improving of the product quality in the automotive industry," *Researches and Applications in Mechanical Engineering (RAME)*, vol. 2 (1), pp. 23–29, 2013.

[14] D. Fernandez Comesaña, J. Wind, and H.-E. de Bree, "A scanning method for source visualization and transfer path analysis using a single probe," in *SAE International*, 2011.

[15] D. Fernandez Comesaña, B. Zajamsek, A. Grosso, and K. R. Holland, "Assessing vehicle exterior noise using a virtual phased array (VPA)," in *Proceedings of SAE 2013 Noise and Vibration Conference and Exhibition Technical Papers*, SAE International, May 2013.

[16] D. Fernandez Comesaña, D. G. Escribano, H.-E. de Bree, and K. R. Holland, "Evaluacion y deteccion de perdidas de aislamiento acustico en edificacion," in *Tecniacustica 2011*, September 2011.

[17] D. Fernandez Comesaña, T. Takeuchi, S. M. Cervera, and K. R. Holland, "Measuring musical instruments directivity patterns with scanning techniques," in *19th International Conference of Noise and Vibration*, July 2012.

[18] D. Fernandez Comesaña, A. Grosso, and K. R. Holland, "Loudspeaker cabinet characterization using a particle-velocity based scanning method," in *AIA-DAGA 2013*, March 2013.

[19] D. Fernandez Comesaña, E. Latorre Iglesias, M. G. Smith, and H.-E. de Bree, "Experimental characterization of a car window excited by turbulent flow using scanning sound intensity techniques," in *Proceedings of the Internoise 2012/ASME NCAD Meeting*, American Society of Mechanical Engineers, August 2012.

[20] E. Tijs, H.-E. de Bree, and S. Steltenpool, "Scan & paint: a novel sound visualization technique," in *Internoise*, 2010.

[21] D. Fernandez Comesaña, E. Latorre Iglesias, H.-E. D. Bree, J. Wind, K. Holland, and M. Smith, "Measuring operational deflection shapes with a scanning P-U probe," in *19th International Congress on Sound and Vibration*, 2012.

[22] D. Fernandez Comesaña, J. Wind, H.-E. de Bree, and K. R. Holland, "Virtual Arrays, a novel broadband source localization technique," in *Noise and Vibration: Emerging Methods (NOVEM 2012)*, April 2012.

[23] D. Fernandez Comesaña and S. Steltenpool, "Mapping stationary sound fields using scanning techniques the fundamentals of scan & paint," in *20th International Congress on Sound and Vibration*, July 2013.

[24] D. Fernandez Comesaña, J. Wind, A. Grosso, and K. Holland, "Performance evaluation of P-P and P-U intensity probes using a scanning method," in *ICSV*, 2011.

[25] D. Fernandez Comesaña, S. Morales Cervera, T. Takeuchi, and K. R. Holland, "Measuring under non stationary conditions with scanning techniques," in *Noise and Vibration: Emerging Methods (NOVEM 2012)*, April 2012.

[26] A. Grosso, D. Fernandez Comesaña, and H.-E. de Bree, "Further development of the PNCA: new panel noise contribution reference-related (PNCAR)," *SAE International Journal of Passenger Cars- Mechanical Systems*, vol. 5, p. 6, June 2012.

[27] D. Fernandez Comesaña, D. G. Escribano, and H.-E. de Bree, "Helicopter cabin interior noise assessment using Scan & Paint Transfer Path Analysis," in *European Rotorcraft Forum*, September 2012.

[28] D. Fernandez Comesaña, K. R. Holland, J. Wind, and H.-E. de Bree, "Comparison of inverse methods and particle velocity based techniques for transfer path analysis," in *Acoustics 2012*, April 2012.

[29] D. Fernandez Comesaña, A. Grosso, H.-E. de Bree, J. Wind, and K. R. Holland, "Further development of velocity-based airborne tpa: scan & paint tpa as a fast tool for sound source ranking," in *7th International Styrian Noise, Vibration & Harshness Congress: The European Automotive Noise Conference*, June 2012.

[30] D. Fernandez Comesaña, E. Tijs, P. Cats, and D. Cook, "Visualization of acoustic intensity vector fields using scanning measurement techniques," in *Internoise 2013*, September 2013.

[31] P. Cats, E. Tijs, and D. Fernandez Comesana, "Exploration of the differences between a pressure-velocity based in situ absorption measurement method and the standardized reverberant room method," *Proceedings of Meetings on Acoustics*, vol. 19, no. 015140, pp. 1–9, 2013.

[32] D. Fernandez Comesaña, J. Wind, K. Holland, and A. Grosso, "Far field source localization using two transducers: a Virtual Array approach," in *18th International Congress of Sound and Vibration*, 2011.

[33] D. Fernandez Comesaña, D. Garcia Escribano, and H.-E. de Bree, "Virtual Phased Arrays: nueva técnica de medida para localización de fuentes de ruido," *Revista de acustica*, vol. 44, no. 1-2, pp. 3–9, 2013.

[34] D. Fernandez Comesaña, E. Fernandez Grande, E. Tiana Roig, and K. R. Holland, "A novel deconvolution beamforming algorithm for virtual phased arrays," in *Internoise 2013*, September 2013.

[35] R. Lindsay, *Acoustics: historical and philosophical development.* Benchmark papers in acoustics, Dowden, Hutchinson and Ross, 1972.

[36] E. Chladni, *Entdeckungen Über Die Theorie Des Klanges, Etc.* Breitkopf & Härtel, 1787.

[37] J. Loudon, "A century of progress in acoustics," *Science*, vol. 14(365), pp. 987–95, 1901.

[38] E. Chladni, *Die akustik.* Breitkopf & Härtel, 1830.

[39] T. Rossing, *Springer Handbook of Acoustics.* Springer handbooks, Springer, 2007.

[40] J. Tyndall, *Sound: A Course of Eight Lectures Delivered at The Royal Institution of Great Britain.* Longmans, Green, and Company, 1867.

[41] L. Beranek, *Acoustic measurements.* J. Wiley, 1949.

[42] B. Bowers, I. of Electrical Engineers, and S. M. G. Britain), *Sir Charles Wheatstone Frs: 1802-1875.* History of technology series, Institution of Electrical Engineers, 2001.

[43] H. von Helmholtz, *On the Sensations of Tone.* Peter Smith, 1862.

[44] J. A. Lissajous, "Mémoire sur l'étude optique des mouvements vibratoires," *Annales de Chimie et de Physique*, vol. 51, pp. 147–231, 1857.

[45] R. Koenig, *Catalogue des appareils d'acoustique.* Harvard University, 1865.

[46] A. Kundt, *Annalen der Physik*, pp. 497–523. No. v. 127, J. A. Barth, 1866.

[47] J. Tyndall, *Sound: A course of eight lectures delivered at the Royal Institution of Great Britain.* D. Appleton and co., 1873.

[48] A. H. Davis, "The analogy between ripples and acoustical wave phenomena," *Proceedings of the Physical Society of London*, vol. 38, no. 1, p. 234, 1925.

[49] D. Pantalony, *Altered Sensations: Rudolph Koenig's Acoustical Workshop in Nineteenth-Century Paris.* Archimedes (Dordrecht, Netherlands), Springer, 2009.

[50] H. Miller, *Acoustical measurements: methods and instrumentation.* Benchmark papers in acoustics, Hutchinson Ross Pub. Co., 1982.

[51] A. Toepler, "Optical studies with the schlieren method," in *Acoustical Measurements: Methods and Instrumentation* (H. B. Miller, ed.), Stroudsburg: Hutchinson Ross, 1982.

[52] P. Krechl and S. Engemann, "August Toepler - the first who visualized shock waves," *Shock Waves*, vol. 5, pp. 1–18, 1995.

[53] A. Toepler, "Observations with a new optical method," *Ostwalds Klassiker der exakten Wissenschaften*, vol. 157, pp. 5–6, 1906.

[54] A. Toepler, "Optischen studien nach der methode der schlierenbeobachtung," *Poggendorfs Annalen der Physik und Chemie*, vol. 131, pp. 33–55, 1867.

[55] E. Mach and J. Sommer, "Ueber die fortpflanzungsgeschwindigkeit von explosionsschallwellen," *Sitzungsb. d. k. Acad. d. Wiss. Math. Naturw. Cl. Wien*, vol. 75, pp. 101–130, 1877.

[56] J. Marat, *Recherches physiques sur le feu.* chez Cl. Ant. Jombert, 1780.

[57] V. Dvorak, "On a new, simple method of observing schlieren," *Annals of Physics*, vol. 9, pp. 502–511, 1880.

[58] A. L. Foley and W. H. Souder, "A new method of photographing sound waves," *Physical Review*, vol. 35, pp. 373–386, 1912.

[59] W. C. Sabine, "Architectural acoustics," *Eng. Rec.*, vol. 38, pp. 520–522, 1898.

[60] W. C. Sabine, "Theater acoustics," *The American Architect*, vol. 104, p. 257ff, 1913.

[61] W. C. Sabine, "Architectural acoustics," *Journal of the Franklin Institute*, vol. 179, no. 1, pp. 1 – 20, 1915.

[62] J. S. Russell, "Report on waves," in *14th meeting of the British Association for the Advancement of Science*, vol. 311, p. 390, 1844.

[63] W. H. Eccles, "The new acoustics," *Proceedings of the Physical Society*, vol. 41, no. 1, p. 231, 1928.

[64] W. Kock, *Sound Waves and Light Waves.* Anchor science study series, Anchor Books, 1965.

[65] H. Jenny, *Cymatics: A Study of Wave Phenomena and Vibration.* MACROmedia Publishing, 2001.

[66] M. C. M. Wright, "A short history of bad acoustics," *The Journal of the Acoustical Society of America*, vol. 120, no. 4, pp. 1807–1815, 2006.

[67] J. D'Angelo, *The Healing Power of the Human Voice: Mantras, Chants, and Seed Sounds for Health and Harmony.* Inner Traditions/Bear, 2005.

[68] D. Gabor, "A new microscopic principle," *Nature*, vol. 161, pp. 777–778, 1948.

[69] G. M. Brown, R. M. Grant, and G. W. Stroke, "Theory of holographic interferometry," *The Journal of the Acoustical Society of America*, vol. 45, no. 5, pp. 1166–1179, 1969.

[70] R. L. Powell and K. A. Stetson, "Interferometric vibration analysis by wavefront reconstruction," *Journal of the Optical Society of America*, vol. 55 (12), pp. 1593–1597, 1965.

[71] K. A. Haines and B. P. Hildebrand, "Surface-deformation measurement using the wavefront reconstruction technique," *Applied Optics*, vol. 5(4), pp. 595–602, 1966.

[72] C. M. Hutchins, K. A. Stetson, and P. A. Taylor, "Clarification of free plate tap tones by holographic interferometry. the acoustics of violin plates," *Catgut Acoustical Society Newsletter*, vol. 16, pp. 15–23, 1971.

[73] E. N. Leith and J. Upatnieks, "Reconstructed wavefronts and communication theory," *J. Opt. Soc. Am.*, vol. 52, pp. 1123–1128, Oct 1962.

[74] W. E. Kock, "Hologram television," *Proceedings of the IEEE*, vol. 54, no. 2, pp. 331–331, 1966.

[75] E. G. Williams, J. D. Maynard, and E. Skudrzyk, "Sound source reconstructions using a microphone array," *The Journal of the Acoustical Society of America*, vol. 68, no. 1, pp. 340–344, 1980.

[76] E. G. Williams and J. D. Maynard, "Holography imaging without the wavelength resolution limit," *Physical Review Letters*, vol. 45, pp. 554–557, August 1980.

[77] J. D. Maynard, E. G. Williams, and Y. Lee, "Nearfield acoustic holography: I. theory of generalized holography and the development of NAH," *The Journal of the Acoustical Society of America*, vol. 78, no. 4, pp. 1395–1413, 1985.

[78] W. A. Veronesi and J. D. Maynard, "Nearfield acoustic holography (NAH) ii. holographic reconstruction algorithms and computer implementation," *The Journal of the Acoustical Society of America*, vol. 81, no. 5, pp. 1307–1322, 1987.

[79] W. A. Veronesi and J. D. Maynard, "Digital holographic reconstruction of sources with arbitrarily shaped surfaces," *The Journal of the Acoustical Society of America*, vol. 85, no. 2, pp. 588–598, 1989.

[80] E. Fernandez Grande and F. Jacobsen, *Near-field acoustic holography with sound pressure and particle velocity measurements.* DTU Electrical Engineering, 2012.

[81] A. Torras Rosell, S. Barrera Figueroa, and F. Jacobsen, "The versatility of the acousto-optic measuring principle in characterizing sound fields," in *Proceedings of the Institute of Acoustics*, vol. 35, pp. 242–250, 2013.

[82] D. Royer and O. Casula, "Quantitative imaging of transient acoustic fields by optical heterodyne interferometry," in *Ultrasonics Symposium, 1994. Proceedings., 1994 IEEE*, vol. 2, pp. 1153–1162 vol.2, 1994.

[83] T. A. Pitts and J. F. Greenleaf, "Three-dimensional optical measurement of instantaneous pressure," *The Journal of the Acoustical Society of America*, vol. 108, no. 6, pp. 2873–2883, 2000.

[84] J. M. Buick, J. A. Cosgrove, P.-A. Douissard, C. A. Greated, and B. Gilabert, "Application of the acousto-optic effect to pressure measurements in ultrasound fields in water using a laser vibrometer," *Review of Scientific Instruments*, vol. 75, no. 10, pp. 3203–3207, 2004.

[85] Y. Oikawa, M. Goto, Y. Ikeda, T. Takizawa, and Y. Yamasaki, "Sound field measurements based on reconstruction from laser projections," in *Acoustics, Speech, and Signal Processing, 2005. Proceedings. (ICASSP '05). IEEE International Conference on*, vol. 4, pp. iv/661–iv/664 Vol. 4, 2005.

[86] T. Sakoda and Y. Sonoda, "Visualization of sound field with uniform phase distribution using laser beam microphone coupled with computerized tomography method," *Acoustical science and technology*, vol. 29, pp. 295–299, jul 2008.

[87] Y. Oikawa, T. Hasegawa, Y. Ouchi, Y. Yamasaki, and Y. Ikeda, "Visualization of sound field and sound source vibration using laser measurement method," in *20th International Congress on Acoustics*, 2010.

[88] A. Torras Rosell, S. Barrera Figueroa, and F. Jacobsen, "An acousto-optic beamformer," *Acoustical Society of America. Journal*, vol. 132, no. 1, pp. 144–149, 2012.

[89] A. Torras Rosell, E. Fernandez Grande, F. Jacobsen, and S. Barrera Figueroa, "Investigating the use of the acousto-optic effect for acoustic holography," in *InterNoise 2012*, 2012.

[90] A. Torras Rosell, S. Barrera Figueroa, and F. Jacobsen, "Sound field reconstruction using acousto-optic tomography," *The Journal of the Acoustical Society of America*, vol. 131, no. 5, pp. 3786–3793, 2012.

[91] D. Johnson and D. Dudgeon, *Array signal processing: concepts and techniques.* Prentice-Hall signal processing series, P T R Prentice Hall, 1993.

[92] J. Billingsley and R. Kinns, "The acoustic telescope," *Journal of Sound and Vibration*, vol. 48, no. 4, pp. 485 – 510, 1976.

[93] H. Krim and M. Viberg, "Two decades of array signal processing research: the parametric approach," *Signal Processing Magazine, IEEE*, vol. 13, no. 4, pp. 67–94, 1996.

[94] D. Manolakis, V. Ingle, and S. Kogon, *Statistical and adaptive signal processing: spectral estimation, signal modeling, adaptive filtering, and array processing.* McGraw-Hill series in electrical and computer engineering: Computer engineering, McGraw-Hill, 2000.

[95] K. R. Holland and P. A. Nelson, "An experimental comparison of the focused beamformer and the inverse method for the characterisation of acoustic sources in ideal and non-ideal acoustic environments," *Journal of Sound and Vibration*, vol. 331, no. 20, pp. 4425–4437, 2012.

[96] M. Kac, "Can one hear the shape of a drum?," *The American Mathematical Monthly*, vol. 73(4), pp. 1–23, 1966.

[97] D. B. Barker and M. E. Fourney, "Measuring fluid velocities with speckle patterns," *Opt. Lett.*, vol. 1, pp. 135–137, Oct 1977.

[98] R. J. Adrian, "Particle-imaging techniques for experimental fluid mechanics," *Annual Review of Fluid Mechanics*, vol. 23, no. 1, pp. 261–304, 1991.

[99] A. Tonddast-Navaei, *Acoustic Particle-Image Velocimetry.* PhD thesis, The Open University, 2005.

[100] A. Fischer, E. Sauvage, and I. Roehle, "Acoustic piv: Measurement of the acoustic particle velocity using synchronized PIV-technique," *The Journal of the Acoustical Society of America*, vol. 123, no. 5, pp. 3130–3130, 2008.

[101] A. Fischer, F. Bake, and A. Bassetti, "The acoustic-particle velocity in the vicinity of a liner: a PIV-CAA comparison," in *19th AIAA/CEAS Aeroacoustics Conference*, 2013.

[102] M. J. Hargather, G. S. Settles, and M. J. Madalis, "Schlieren imaging of loud sounds and weak shock waves in air near the limit of visibility," *Shock Waves*, vol. 20, no. 1, pp. 9–17, 2010.

[103] W. Merzkirch, *Flow Visualization.* Academic Press, 1987.

[104] H. Kleine, "Filming the invisible - time resolved visualization of compressible flows," *The European Physical Journal Special Topics*, vol. 182, no. 1, pp. 3–34, 2010.

[105] F. Alvi and L. Cattafesta, "The art and science of flow control - case studies using flow visualization methods," *The European Physical Journal Special Topics*, vol. 182, no. 1, pp. 97–112, 2010.

[106] J. Hald and K. B. Ginn, "Spatial Transformation of Sound Fields: principle, instrumentation and applications," in *Acoustic Intensity Symposium*, 1987.

[107] J. Hald, "Development of stsf with emphasis on the influence of bandwidth," in *Noise-Con Proceedings*, vol. 88, pp. 529–536, 1988.

[108] M. Crocker, *Handbook of Noise and Vibration Control.* Wiley InterScience, Wiley, 2007.

[109] J. B. Schneider, "Understanding the Finite-Difference Time-Domain method," 2010.

[110] D. Fernandez Comesaña, "Mapping stationary sound fields," Master's thesis, Institute of Sound and Vibration Research, December 2010.

[111] L. E. Kinsler, A. R. Frey, A. B. Coppens, and J. V. Sanders, *Fundamentals of acoustics.* Wiley, 2000.

[112] J. Wind, *Acoustic source localization : exploring theory and practice.* PhD thesis, University of Twente, Enschede, November 2009.

[113] A. T. de Hoop, "Electromagnetic radiation from moving, pulsed source distributions: The 3D time-domain relativistic doppler effect," *Wave Motion*, vol. 46, no. 1, pp. 74 – 77, 2009.

[114] C. Camier, J.-F. Blais, R. Lapointe, and A. Berry, "A time-domain analysis of 3D non-uniform moving acoustic sources: application to source identification and absolute quantification via beamforming," in *Berlin Beamforming Conference*, 2012.

[115] J. Bendat and A. Piersol, *Random Data: Analysis and Measurement Procedures.* Wiley Series in Probability and Statistics, Wiley, 2011.

[116] D. Percival and A. Walden, *Spectral Analysis for Physical Applications.* Cambridge University Press, 1993.

[117] F. Fahy, *Sound Intensity.* E & FN Spon, 1995.

[118] J. Bendat and A. Piersol, *Engineering applications of correlation and spectral analysis.* J. Wiley, 1993.

[119] F. Jacobsen, "Random errors in sound power determination based upon intensity measurement," *J. Sound Vib.*, vol. 131, pp. 475–87, 1989.

[120] H.-E. de Bree and W. F. Druyvesteyn, "A particle velocity sensor to measure the sound from a structure in the presence of background noise," in *Forum Acusticum*, 2005.

[121] F. Jacobsen and P. Juhl, *Fundamentals of General Linear Acoustics.* Wiley, 2013.

[122] K. Beissner, "On the plane wave approximation of acoustic intensity," *The Journal of the Acoustical Society of America*, vol. 71, no. 6, pp. 1406–1411, 1982.

[123] V. Jaud and F. Jacobsen, "Calibration of p-u intensity probes," in *Euronoise 2006*, 2006.

[124] G. Williams, *Fourier Acoustics: Sound Radiation and Nearfield Acoustical Holography.* Academic Press, 1999.

[125] F. Jacobsen and V. Jaud, "A note on the calibration of pressure-velocity sound intensity probes," *The Journal of the Acoustical Society of America*, vol. 120, no. 2, pp. 830–837, 2006.

[126] H.-E. de Bree, "The microflown e-book," 2011.

[127] F. Jacobsen and D. tekniske højskole. Laboratoriet for akustik, *The Diffuse Sound Field: Statistical Considerations Concerning the Reverberant Field in the Steady State.* Lyngby. Technical university of Denmark, Acoustics laboratory. Report, Acoustics Laboratory, Technical University of Denmark, 1979.

[128] N. Jacobson, *Basic Algebra I.* Basic Algebra, Dover Publications, Incorporated, 2009.

[129] H.-E. de Bree, V. B. Svetovoy, R. Raangs, and R. Visser, "The very near field. theory, simulations and measurements of sound pressure and particle velocity in the very near field.," in *11th ICSV*, 2004.

[130] S. Weyna, "Acoustic flow visualization based on the particle velocity measurements," in *Forum Acousticum*, 2005.

[131] W. F. Druyvesteyn and H. E. de Bree, "A new sound intensity probe comparison with the pair of pressure microphones intensity probe," *J. Audio Eng. Soc*, vol. 48, no. 1/2, pp. 49–56, 2000.

[132] F. Jacobsen and H.-E. de Bree, "A comparison of two different sound intensity measurement principles," *J. Acoust. Soc. Am.*, vol. 118, no. 3, pp. 1510–1517, 2005.

[133] F. Jacobsen and H.-E. D. Bree, "Measurement of sound intensity: P-u probes versus p-p probes," in *NOVEM*, 2005.

[134] J. Borwick, *Loudspeaker and Headphone Handbook.* Focal Press, 2001.

[135] P. R. Newell and K. R. Holland, *Loudspeakers: For Music Recording And Reproduction.* Focal Press, 2007.

[136] Rolls-Royce Ltd, *The jet engine.* Rolls-Royce, 2005.

[137] O. Wolff, "Fast panel noise contribution analysis using large pu sensor arrays," in *Proceedings of Internoise*, 2007.

[138] F. X. Magrans, "Method of measuring transmission paths," *Journal of Sound and Vibration*, vol. 74 (3), pp. 321–330, 1981.

[139] C. Bertolini, J. Horak, M. Mantovani, and G. L. Sinno, "Interior panel contribution based on pressure-velocity mapping and acoustic transfer functions combined with the simulation of the sound package," in *Internoise 2011*, 2011.

[140] S. Sorenson, "Investigation of different techniques for quantifying automotive panel noise radiation," in *SAE Technical Paper 951267*, 1995.

[141] M. Boyle, R. Gault, R. Cooper, and J. Wang, "Modelling correlated and uncorrelated sound sources," in *Collaborative Product and Service Life Cycle Management for a Sustainable World* (R. Curran, S.-Y. Chou, and A. Trappey, eds.), Advanced Concurrent Engineering, pp. 173–181, Springer London, 2008.

[142] K. Wyckaert and A. H. van der, "Operational analysis, transfer path analysis, modal analysis: Tools to understand road noise problems in cars," in *Proceedings of SAE Noise and Vibration Conference*, 1995.

[143] K. R. Holland and F. J. Fahy, "An investigation into spatial sampling criteria for use in vibroacoustic reciprocity," *Noise Control Engineering Journal*, vol. 45(5), pp. 217–221, 1997.

[144] LMS, "Transfer path analysis, the qualification and quantification of vibro-acoustic transfer paths," tech. rep., LMS Application Note, 2005.

[145] J. W. Verheij, "Reciprocity method for quantification of airborne sound transfer from machinery," in *International congress on recent developments in air and structure borne sound and vibration*, 1992.

[146] C.-X. Bi and J. Stuart Bolton, "An equivalent source technique for recovering the free sound field in a noisy environment," *The Journal of the Acoustical Society of America*, vol. 131, no. 2, pp. 1260–1270, 2012.

[147] J. W. Verheij, "Inverse and reciprocity methods for machinery noise source characterization and sound path quantification," *International Journal of Acoustics and Vibration*, vol. 2(1), pp. 11–20, 1997.

[148] J. Rondeau, A. Duval, G. Deshayes, M. Lassalas, H.-E. de Bree, and S. Chaigne, "Vehicle acoustic synthesis method: Improving acquisition time by using p-u probes," in *SAE Technical Paper 2005-01-2444*, 2005.

[149] A. Duval, J. Rondeau, L. Bischoff, C. Morgenstern, G. Deshayes, and L. Gagliardini, "Vehicle acoustic synthesis method 2nd generation: New developments with p-u probes allowing to simulate unsteady operative conditions like run-ups," in *SAE Technical Paper 2007-01-2271*, 2007.

[150] L. K. Natarajan, S. Mylavarapu, and S. Wu, "Panel contribution analysis for the interior region of a complex structure using the Helmholtz equation least squares method.," *The Journal of the Acoustical Society of America*, vol. 129, no. 4, pp. 2415–2415, 2011.

[151] S. F. Wu and L. Kumar Natarajan, "Panel acoustic contribution analysis," *The Journal of the Acoustical Society of America*, vol. 133, no. 2, pp. 799–809, 2013.

[152] J. Hald, M. Tsuchiya, and M. Kimura, "Panel contribution analysis using a volume velocity source and a double layer array with the SONAH algorithm," in *Internoise*, 2006.

[153] J. Hald and J. Morkholt, "Panel contribution analysis in a vehicle cabin using a dual layer handheld array with integrated position measurement," *SAE Int. J. Passeng. Cars- Mech. Syst*, vol. 2(1), pp. 1458–1469, 2009.

[154] J. Wind, H.-E. de Bree, and X. B., "3D sound source localization and sound mapping using a p-u sensor array," in *Proceedings of CEAS-AIAA*, 2010.

[155] C. Wiley, "Synthetic aperture radars," *Aerospace and Electronic Systems, IEEE Transactions on*, vol. AES-21, no. 3, pp. 440–443, 1985.

[156] J. C. Curlander and R. N. McDonough, *Synthetic aperture radar- Systems and signal processing.* John Wiley & Sons, 1991.

[157] L. J. Cutrona, "Comparison of sonar system performance achievable using synthetic-aperture techniques with the performance achievable by more conventional means," *The Journal of the Acoustical Society of America*, vol. 58, no. 8, pp. 336–346, 1975.

[158] L. J. Cutrona, "Additional characteristics of synthetic-aperture sonar systems and a further comparison with nonsynthetic-aperture sonar systems," *The Journal of the Acoustical Society of America*, vol. 61, no. 5, pp. 1213–1217, 1977.

[159] M. P. Hayes and P. T. Gough, "Synthetic aperture sonar: a review of current status," *Oceanic Engineering, IEEE Journal of*, vol. 34, no. 3, pp. 207–224, 2009.

[160] D. Fernandez Comesaña, K. R. Holland, J. Wind, and H.-E. de Bree, "Adapting beamforming techniques for virtual sensor arrays," in *Berlin Beamforming Conference*, 2012.

[161] K. Shin and P. Hammond, *Fundamentals of Signal Processing for Sound and Vibration Engineers.* Wiley, 2008.

[162] A. Xenaki, F. Jacobsen, E. Tiana-Roig, and E. F. Grande, "Improving the resolution of beamforming measurements on wind turbines," in *Proceedings of 20th International Congress on Acoustics, ICA*, 2010.

[163] R. O. Schmidt, "Multiple emiter location and signal parameter estimation," in *Proceedings RADC Spectral Estimation Workshop*, Oct. 1979.

[164] R. Schmidt, "Multiple emitter location and signal parameter estimation," *Antennas and Propagation, IEEE Transactions on*, vol. 34, pp. 276–280, Mar 1986.

[165] M. Hayes, *Statistical digital signal processing and modeling.* John Wiley & Sons, 1996.

[166] W.-S. Lu and A. Antoniou, "Design of digital filters and filter banks by optimization: a state of the art review," in *Proceedings of the European Signal Processing Conference (EUSIPCO)*, 2000.

[167] S.-C. Pei and J.-J. Shyu, "2-D FIR eigenfilters: a least-squares approach," *IEEE Trans. Circuits Systems*, vol. 37(1), pp. 24–34, 1990.

[168] S. Doclo and M. Moonen, "Design of far-field and near-field broadband beamformers using eigenfilters," *Signal Processing*, vol. 83, pp. 2641–2673, 2003.

[169] T. F. Brooks and W. M. Humphreys, "A deconvolution approach for the mapping of acoustic sources (DAMAS) determined from phased microphone arrays," *Journal of Sound and Vibration*, vol. 294, no. 4, pp. 856–879, 2006.

[170] R. Dougherty, "Extension of DAMAS and benefits and limitations of deconvolution in beamforming," in *Proceedings of the 11th AIAA/CEAS Aeroacoustics Conference*, vol. 3, pp. 2036–2048, 2005.

[171] K. Ehrenfried and L. Koop, "Comparison of iterative deconvolution algorithms for the mapping of acoustic sources," *AIAA journal*, vol. 45, no. 7, pp. 1584–1595, 2007.

[172] C. Lawson and R. Hanson, *Solving Least Squares Problems.* Classics in applied mathematics, Society for Industrial and Applied Mathematics, 1974.

[173] P. Sijtsma, "CLEAN based on spatial source coherence," *International Journal of Aeroacoustics*, vol. 6, no. 4, pp. 357–374, 2007.

[174] H. Van Trees, *Detection, Estimation, and Modulation Theory, Optimum Array Processing.* Detection, Estimation, and Modulation Theory, Wiley, 2004.

[175] D. Fernandez Comesaña, E. Tijs, and D. Kim, "Direct sound radiation testing on a mounted car engine," in *iSNVH*, 2014.

[176] E. Tijs, N. A., and H.-E. de Bree, "verification of p-u intensity calculation," in *Novem*, 2009.

[177] W. F. Druyvesteyn and H. E. de Bree, "A new sound intensity probe: Comparison to the Bruel & Kjaer p-p probe," in *Audio Eng. Soc. Conv. 104*, 1998.

[178] IEC, "Instruments for the measurement of sound intensity. measurements with pairs of pressure sensing microphones," 1993.

[179] American National Standard ANSI, "Instruments for the measurement of sound intensity," 1996.

[180] T. G. H. Basten and H.-E. de Bree, "Full bandwidth calibration procedure for acoustic probes containing a pressure and particle velocity sensor," *J. Acoust. Soc. Am.*, vol. 127, no. 1, pp. 264–270, 2010.

[181] D. Fernandez Comesaña, B. O. Peksel, and H.-E. de Bree, "Expanding the sound power measurement criteria for sound intensity p-u probes," in *21th International Congress on Sound and Vibration*, July 2014.

[182] F. Jacobsen, "Sound intensity and its measurement and applications," tech. rep., Technical University of Denmark, 2011.

[183] F. Jacobsen, "Spatial sampling errors in sound power estimation based upon intensity," *J. Sound Vib.*, vol. 145, pp. 129–149, 1991.

[184] D. Fernandez Comesaña, H.-E. de Bree, J. Wind, and K. Holland, "Characterising radiation patterns of non-stationary sound sources with scanning techniques," in *DAGA*, 2012.

[185] S. Morales-Cervera, "Virtual reality system for musical performance practice," Master's thesis, Institute of Sound and Vibration Research, 2011.

[186] J. Hald, "Non-stationary stsf," tech. rep., Bruel & Kjaer, 2000.

[187] M. Lee and J. S. Bolton, "Scan-based near field acoustical holography and partial field decomposition in the presence of noise and source level variation," *Journal of the Acoustical Society of America*, vol. 119, pp. 382–393, 2005.

[188] H.-S. Kwon, Y.-J. Kim, and J. S. Bolton, "Compensation for source nonstationarity in multireference, scan-based near-field acoustical holography," *Journal of the Acoustical Society of America*, vol. 113, pp. 360–368, 2003.

[189] M. H. Richardson, "Is it a mode shape or an operating deflection shape?," *Sound and Vibration*, vol. 31(1), pp. 54–61, 1997.

[190] B. J. Schwarz and M. H. Richardson, "Introduction to operating deflection shapes," in *CSI Reliability Week*, 1999.

[191] B. J. Schwarz and M. H. Richardson, "Experimental modal analysis," in *CSI Reliability Week*, 1999.

[192] W. Bae, Y. Kyong, J. Dayou, K.-H. Park, and S. Wang, "Scaling the operating deflection shapes obtained from scanning laser doppler vibrometer," *Journal of Nondestructive Evaluation*, vol. 30 (2), pp. 91–98, 2011.

[193] H.-E. de Bree, P. Leussink, T. Korthorst, H. Jansen, T. S. J. Lammerink, and M. Elwenspoek, "The microflown: a novel device for measuring acoustic flows," *Sensors and Actuators*, vol. 54, pp. 552–557, 1996.

[194] H.-E. de Bree, "An overview of microflown technologies," *Acta Acustica united with Acustica*, vol. 89, pp. 163–172, 2003.

[195] H.-E. de Bree, V. B. Svetovoy, and R. Visser, "The very near field ii: an introduction to very near field holography," in *SAE*, 2005.

[196] L. Soria, V. C. Belgiovine, P. Aarnoutse, H. V. der Auweraer, and K. Janssens, "Experimental analysis of the very near field produced by different acoustic sources," in *ISMA*, 2010.

[197] R. Raangs, *Exploring the use of the Microflown*. PhD thesis, University of Twente, 2005.

[198] E. Pierro, E. Mucchi, and A. Vecchio, "Using p-u probes for the experimental vibro-acoustical modal analysis of a helicopter," in *ISMA*, 2008.

[199] O. Dossing, "Structural stroboscopy - measurement of operational deflection shapes," *Sound and Vibration Magazine*, vol. 1, pp. 18–24, 1988.

[200] E. Pierro, E. Mucchi, L. Soria, and A. Vecchio, "EMA and OMA techniques for vibro-acoustically coupledsystems: the example of a helicopter cabin," in *IOMAC 09 - 3rd International Operational Modal Analysis Conference*, 2009.

[201] T. P. Chong, P. Joseph, and P. Davies, "Design and performance of an open jet wind tunnel for aero-acoustic measurement," *Applied Acoustics*, vol. 70, no. 4, pp. 605–614, 2009.